The University of Osaka
Institutional Knowledge Archive

Title	The Transient Electron Emission Phenomena from Metal Surfaces under the Effect of High Electric Field
Author(s)	塩田, 忠
Citation	大阪大学, 2000, 博士論文
Version Type	VoR
URL	https://doi.org/10.11501/3169347
rights	
Note	

The University of Osaka Institutional Knowledge Archive : OUKA

https://ir.library.osaka-u.ac.jp/

The University of Osaka

工博 7419

The Transient Electron Emission Phenomena from Metal Surfaces under the Effect of High Electric Field

Tadashi Shiota

The Transient Electron Emission Phenomena from Metal Surfaces under the Effect of High Electric Field

(強電界により生じる金属表面からの非定常電子放射現象に関する研究)

Tadashi Shiota

Department of Material and Life Science
Graduate School of Engineering
Osaka University

Preface

The exoemission phenomena were discovered for almost century ago. A number of researches on exoemission have been performed only from the macroscopic point of view, and none of them have dealt with exoemission from the microscopic point of view. This is somewhat unreasonable, since many of recent investigations in surface science were based upon the microscopic nature of surfaces. This thesis focuses the microscopic aspects of the exoemission from metal surfaces. The attitude of this research is unique in the exoemission research.

In order to investigate exoemission from the microscopic point of view, the experiments using the surface analytical techniques with atomic resolution, *i.e.*, field emission microscopy and field ion microscopy, were carried out. The obtained results were interpreted based on the computational results using the first-principles calculation, which was applied to exoemission study for the first time. The exoemission was successfully related to the dynamics of the surfaces, such as diffusion, oxidation, defect formation, and gas adsorption.

This pioneering work in exoemission will be a milestone of the exoemission works, and I am sure that this work will contribute to developing the application of exoemission as well as to the fundamental research on exoemission.

Tadashi Shiota

Tadashi Shiota

Osaka, Japan

January, 2000

Contents

Chapter 1

Introduction

Today, electron emission from a solid surface is one of the most famous physical phenomena and widely applied to a variety of the technology or engineering fields. In the field of surface analysis, the electron emission phenomenon plays an important role. Auger electron spectroscopy (AES) and X-ray photoelectron spectroscopy (XPS) are the methods to analyze the surface status from the energy distribution of electrons emitted from the surface. Also, electron gun is one of the most popular applications of electron emission phenomenon, and has been widely used in vacuum tube, cathode ray tube (CRT), electron beam lithography as well as surface analysis methods such as low-energy electron diffraction (LEED), electron energy loss spectroscopy (EELS), electron probe microanalysis (EPMA) and so on. Therefore, electron emission phenomena from variety kinds of semiconductors, superconductors as well as metals have been investigated to produce the electron beam with high brightness and high stability.

The electron emission phenomena are categorized into thermionic emission, photoemission, field emission, secondary electron emission and so on, and the systematic study on each emission phenomenon has been carried out in detail. Thermionic emission and photoemission occur when the energy higher than the work function of a solid surface is introduced. Theoretical backgrounds of these phenomena were given by Richardson [1] and Einstein [2], respectively. On the other hand, when the potential barrier of a surface becomes narrowed by a high electric field applied to a solid surface, electrons are also emitted to outside of the metal by the tunneling effect. This electron emission phenomenon has been recognized as field emission, and was explained theoretically by Fowler and Nordheim [3]. Moreover, secondary electron emission, which is induced by high-energy electron or ion bombardment [4], has also been widely studied. Besides these four electron emission phenomena, the transient electron emission, which can not be explained by any simple process described above, was sometimes observed at the many kinds of surfaces. This phenomenon has been called "exoelectron emission".

Curie and Rutherfod, who were very famous nuclear physicists, discovered the anomalous emission from the solids placed near Ra or Th. This seems to be the first discovery of exoelectron emission. Also, in 1897, Russell observed the fact that a scratched Zn surface liberated electrons, and this emission phenomenon was called "Russell effect". However, the detailed research on such phenomena had not been carried out. The first report of exoelectron emission was made by Mclenann in 1902. He studied the electron emission from CaF_2:Mn activated by electron beam irradiation when the specimen was heated [5]. In 1935, Tanaka observed that electrons were continued to be counted by Geiger-Müller (GM) counter, even after electron beam irradiation was stopped [6]. This observation was first discovery of exoelectron emission in Japan, and he was a pioneer of Japanese exoelectron emission researchers. The results of systematic investigations on exoelectron emission were reported by Kramer in 1949 [7]. He showed that low-energy electrons were emitted from metals or ion crystals when the surface was suffered by mechanical treatment, light irradiation or annealing treatment. The emission phenomena could not be explained by the simple energy transfer process. In the experiment on electron emission from wood metal reported by Kramer, it was indicated that no electron emission was detected during melting process of the wood metal, while burst of electron emission was detected during solidification process. Since this transient emission phenomenon was only observed during the solidification, this electron emission was considered to be related to exothermic reaction. The word of "exoelectron emission" was named after the exothermisity. Later, the temporal electron emissions activated by photons or electric field were observed as well as such a thermally activated electron emission. These electron emissions have been categorized in the exoelectron emission, and were classified by the method of stimuli; thermally-stimulated exoelectron emission (TSEE), photo- (optically-) stimulated exoelectron emission (PSEE (OSEE)) and field-stimulated exoelectron mission (FSEE). However, the term of "exoemission" was decided to be used on behalf of "exoelectron emission" at the 11th international symposium on exoelectron emission and its applications held in Glucholazy, Poland. Because temporal emission of negative ions [8], photons [9], neutral particles and positive ions [10] as well as electrons were included in the same emission category. Namely, exoemission is now used as a comprehensive term to denominate the nonstationary charged or non-charged particle emission phenomena, appearing only from emitters (metallic as well as nonmetallic) after some prior treatment (irradiation, deformation, etc.). They were accompanying the relaxation of the perturbed states [11].

The research on exoemission has been carried out almost a century long since it was firstly discovered. Many applications of exoemission to a variety of scientific/engineering fields have been studied; surface analysis, phase transition, deformation or destruction of solids and so on. Especially, in the fields of dosimetery and surface analysis, exoemission has been investigated intensively. The application of thermally-stimulated exoemission (TSE) to dosimetery was first suggested by Kramer in 1957. A number of investigations have been carried out to develop exoemission dosimeter (EED) [12-20] as shown in the Section 2.1. It is recognized that the layer, which is sensitive to the dose of radiation, is thinner than that of thermoluminescence dosimeter (TLD) which is commonly used today. Therefore, EED is considered to be more sensitive to measure α-, β- and γ-rays. However, the property of TSE is affected by fabrication process of EED and the pre-treatment of the EED devices. Thus, EED device has not been commercially available. On the other hand, photo-stimulated exoemission (PSE) has been studied as a non-destructive method for detecting surface cracks or defects [21-25]. However, these attempts seem not to be very successive. This is mainly because the emission mechanisms of PSE are not fully understood and the PSE phenomena can not be interpreted in detail.

In contrast, field-stimulated exoemission (FSE), which have been investigated on Al surfaces by our research group [26-30], is one of the exoemissions induced by a high electric field applied to the specimen surface, and has some characteristic features different from the other exoemissions as follows:

- One can deal with the excitation and the emission processes of exoelectrons individually because field-stimulated exoelectrons are emitted without the external energy like field emission. Therefore, the analysis of FSE is easily achieved compared with TSE or PSE. This is the advantage to clarify the exoemission mechanism.

- The specimen is a sharp tip in order to apply a high electric field to the surface. The tip specimen is also applicable to field ion microscopy (FIM) and field emission microscopy (FEM). Using FIM an FEM, one can obtain the data regarding the atomic arrangement and the electronic state at the tip surface with a high spatial resolution. Hence, combination of FIM/FEM techniques with FSE may allow us to identify the exoemission sites with an atomic resolution.

The purpose of this study is to identify the exoemission sites and to construct the emission model. For this purpose, W (tungsten) was chosen as a specimen because W was relatively easily imaged by FIM and FEM. The experimental results are summarized in chapters 3 ~ 5. In chapter 3, a fundamental question upon exoemission was investigated; whether or not a clean surface liberates FSE ? Since the exoemission from W surface has not been reported, FSE from W surface was investigated as the first step of this project. Then, the experimental conditions to emit exoelectrons were studied in detail, and the possible emission mechanism was proposed finally.

In chapter 4, the relationship between FSE and gas adsorption was focused. The effects of adsorption of hydrogen, oxygen and water at W surfaces, which has been considered to be one of origins of exoemission, were studied.

In chapter 5, the relationship between FSE and surface imperfection was studied; the FSE from the sputtered W surfaces was investigated in order to elucidate the role of surface defects.

On the other hand, recent improvement in computational science has made it possible to calculate the electronic structures not only for a bulk, but also for a variety of surfaces non-empirically. On the Si(001) or Si(111) surfaces, the reconstruction mechanism were proposed from the results of non-empirical calculations [31,32], and the adsorption site of oxygen, which coincides with the experimental result, was also determined [33]. The reconstructed surface structures of the transition metals such as W, Mo and Cr were computed by the first-principles calculational studies and the results were consistent with those obtained experimentally [34,35]. Although many computational studies in the surface science have been reported, no computational studies have been made with regard to exoemission. The first-principles calculation technique provides the electronic structure of the surface, and it will also be valuable for understanding the origins of exoelectron traps and for constructing emission models of exoelectrons.

In this study, the first-principles calculation method was applied to the exoemission study for the first time. In chapter 6, electronic structures of the clean and oxygen-adsorbed Al (001) surfaces were calculated by the first-principles calculation using ultrasoft pseudopotentials. A possible emission mechanism of exoelectrons from the Al surfaces in the early stage of oxidation was proposed based both on the computational results obtained in this study and on experimental results reported previously [27]. The electronic structures of the Al (001) surfaces with surface defects and steps were also calculated. From the computational results, a role of surface detects and steps on FSE from Al tips was discussed.

In chapter 7, the experimental and computational results obtained in this study are summarized, and the roadmap to the future research plans is indicated.

References

[1] "*The Emission of Electricity from Hot Bodies*"; O. W. Richardson, (Longmans Green and Company, London, 1921)

[2] "*Uber einen die Erzeugung und Verwandlung des Lichtes betreffenden heuristischen Gesichtspunkt*"; A. Einstein, Annalen der Physik, vol. 17 (1905) 132 ~ 148.

[3] "*Electron Emission in Intense Electric Fields*"; R. H. Fowler and L. W. Nordheim, Proceedings of the Royal Society of London Series A, vol. 119 no. 781 (1928) 173 ~181.

[4] "*Ion Bombardment of Solids*"; G. Carter and J. S. Colligon, (Heinemann Educational Books Ltd., London, 1968).

[5] "*On a Kind of Radioactivity Imparted to Certain Salts by Cathode Rays*"; J. Mclenann, The London Edinburgh and Dublin Philosophical and Journal of Science Series 6, vol. 3 no. 14 (1902) 195 ~ 203.

[6] "*After Effect of Aluminum Bombarded by Electrons*"; M. Tanaka, Physical Review, vol. 48 (1935) 916.

[7] "*Spitzenzahler und Zahlrohr bei Metallographischen ober Flachen-unter Suchungen*"; J. Kramer, Zeitschrift fur Physik, vol. 125 (1949) 739 ~ 756.

[8] "*The discrimination of Charged Particles during Exo-Electron Emission*"; P. Gordan, A. Scharmann and J. Seibert, Physica Status Solidi, vol. 33 (1969) K97.

[9] "*Photon Emission during Chemisorption of Oxygen on Al and Mg Surfaces*"; B. Kasemo, Physical Review Letters, vol. 32 no. 20 (1974) 1114 ~ 1117.

[10] "*Spontaneous Emission of Charged Particles and Photons During Tensile Deformation of Oxide-Covered Metals under Ultra-High-Vacuum Conditions*"; B. Rosenblum, Journal of Applied Physics, vol. 48 no. 12 (1977) 5262 ~ 5273.

[11] "*Spectral and Temporal Characteristics of Photostimulated Exoemission from Coldworked Metals*"; H. Käämbre, V. Bichevin, V. Sammelselg, H. Kelle, E. Asari and O. Saks, Applied Surface Science, vol. 136 (1998) 55 ~ 61.

[12] "*Diamond Detectors in Relative Dosimetry of Photon, Electron and Proton Radiation Fields*"; V. S. Khrunov, S. S. Martynov, S. M. Vatnitsky, I. A. Ermakov, V. I. Fominych, D. L. Karlin, A. M. Chervjakov and Yu. V. Tarbeyev, Radiation Protection Dosimetry,

vol. 33 no. 1-4 (1990) 155 ~ 157.

[13] "*Dependence of the TSEE of β ray irradiated BeO Thin Film Detectors on the Properties of Surrounding Materials*"; M. Petel, J. L. Chartier, C. Itie, H. Kessler, W. Kreigseis and A. Scharmann, Radiation Protection Dosimetry, vol. 33 no. 1-4 (1990) 307 ~ 310.

[14] "*Fast Reader for Thermostimulated Exoelectron Dosemeters Used for β ray Routine Dosimetry*"; M. Petel, J. Barthe, W. Kreigseis, G. Portal, A. Scharmann and G. Shiriex, Radiation Protection Dosimetry, vol. 33 no. 1-4 (1990) 311 ~ 314.

[15] "*Measurement of Skin Dose with TSEE from BeO*"; M. Aoki, S. Okabe, M. Nishikawa and T. Nishikawa, Radiation Protection Dosimetry, vol. 33 no. 1-4 (1990) 315 ~ 317.

[16] "*TSEE and TL β ray Dosimetry*"; L. Hobzova and J. Novotny, Radiation Protection Dosimetry, vol. 33 no. 1-4 (1990) 319 ~ 321.

[17] "*Response of TSEE Dosimeters of Foil-Covered BeO Thin Films to β Radiation*"; W. Kriegseis, H. Kessler, K. Rauber and M. Petel, Radiation Protection Dosimetry, vol. 39 no. 1-3 (1991) 127 ~ 130.

[18] "*TL and TSEE Techniques for Skin Dose Measurements*"; G. Uchrin, Radiation Protection Dosimetry, vol. 39 no.1-3 (1991) 131 ~ 134.

[19] "*Combined Aluminium Oxide TSEE-TL Detectors for Skin Dosimetry*"; M. S. Akselrod and V. S. Kortov, Radiation Protection Dosimetry, vol. 39 no. 1-3 (1991) 135 ~ 138.

[20] "*The Effect of Secondary Electrons on the Photon Energy Response of TL and TSEE Detectors Used for β and Photon Dosimetry*"; E. Piesch, B. Burghardt, S. Goldbach and M. Vilgis, Radiation Protection Dosimetry, vol. 39 no. 1-3 (1991) 187 ~ 190.

[21] "*Measurement of Surface Fatigue Damage by Using Photostimulated Exoelectron Emission*"; S. Yamamoto; Japanese Journal of Applied Physics, vol. 16 no. 12 (1977) 2157 ~ 2163.

[22] "*Versatile Photostimulated Exoelectron Microscope and Its Application*"; S. Yamamoto, H. Yokokawa and H. Hashimoto, Japanese Journal of Applied Physics Supplement, vol. 24-4 (1985) 277 ~ 280.

[23] "*Autoradiography of Fatigue Fracture in Aluminum*"; J. C. Grosskreutz, Journal of Applied Physics, vol. 33 no. 18 (1962) 2653 ~ 2655

[24] "*Photostimulated Exoelectron Emission from Slip Lines: A New Microscopy of Metal*

Deformation"; W. J. Baxter and S. R. Rouze, Journal of Applied Physics, vol. 44 no. 10 (1973) 4400 ~ 4404.

[25] "*Photoemission Electron Microscopy of Oxide Fracture at Slip*"; W. J. Baxter and S. R. Rouze, Journal of Applied Physics, vol. 16 no. 6 (1975) 2429 ~ 2432.

[26] "*Field-Stimulated Exoelectron Emission from 99.9999% Pure Al*"; M. Tagawa, S. Takenobu, N. Ohmae and M. Umeno, Applied Physics Letters, vol. 53 no. 7 (1988) 626 ~ 627.

[27] "*The Trap-Level of Exoelectron and Field-Stimulated Exoelectron Emission of High Purity Al*"; M. Tagawa, M. Umeno, N. Ohmae and S. Takenobu, Japanese Journal of Tribology, vol. 34 no. 10 (1989) 1175 ~ 1184.

[28] "*Distribution of Trap Levels in Field-Stimulated Exoelectron Emission*"; M. Tagawa, K. Tsuzuki, M. Mori, N. Ohmae and M. Umeno, Applied Physics Letters, vol. 61 no. 12 (1992) 1471 ~ 1473.

[29] "*Influence of Oxygen Adsorption on Field-Stimulated Exoelectron Emission from High-Purity Aluminum*"; M. Tagawa, M. Mori, N. Ohmae and M. Umeno, Applied Surface Science, vol. 72 (1993) 259 ~ 265.

[30] "*Temperature Dependence of the Field-Stimulated Exoelectron Emission*"; M. Mori, E. Ogawa, M. Tagawa, N. Ohmae and M. Umeno, Applied Surface Science vol. 76/77 (1994) 21 ~ 25.

[31] "*Electronic States of Si(100) Reconstructed Surfaces*"; Z. Zhu, N. Shima and M. Tsukada, Physical Review B, vol. 40 no. 17 (1989) 11868 ~ 11879.

[32] "*Self-Consistent Pseudopotential Calculations for Si (111)*"; M. Schluter, J. R. Chelikowsky, S. G. Louie and M. L. Cohen, Physical Review B, vol. 12 no. 10 (1975) 4200 ~ 4204.

[33] "*Atomic and Electronic Sructures of Oxygen-Adsorbed Si(001) Surfaces*"; T. Uchiyama and M. Tsukada, Physical Review B, vol. 53 no. 12 (1996) 7917 ~ 7922.

[34] "*Electronic Origin of the Surface Reconstruction of the (001) Surface of Cr, Mo and W*"; I. Terakura, Surface Science, vol. 103 no. 1 (1981) 103 ~ 117.

[35] "*Electronic Origin of the Surface Reconstruction and Relaxation of the (001) Surface of Mo and W*"; I. Terakura, K. Terakura and N. Hamada, Surface Science, vol. 111 no. 3 (1981) 479 ~ 491.

Chapter 2

Overview of the Exoemission Phenomena

2.1 Thermally-Stimulated Exoemission

The first discovery of thermally-stimulated exoemission (TSE) was reported by Mclenann in 1902 [1], which was also the first report on exoemission. He found that the emission intensity of electrons from CaF_2:Mn, which was irradiated by electron beam, indicated a glow curve similar to that of thermoluminescence (TL) while the specimen was heated. Thus, TSE signal can be detected by simply heating from the specimen which experienced the pre-treatment, such as electron bombardment, X-ray irradiation, mechanical deformation and so on. Because of such a simple detection method of TSE, the TSE research occupies a large part of the exoemission studies.

The TSE phenomenon was reported on metals, oxides, insulators and semiconductors. It was observed by Hieslmair that the TSE glow curves from Al, Cu, Zn and Fe, which were activated by X-ray irradiation, showed peaks at 160 and 260 ℃ for all materials [2]. Scharmann also observed the similar glow curve of TSE from β-ray irradiated Al, and concluded that TSE was emitted from the electron-trapping level formed in the oxide layers by the β-ray irradiation [3]. On the other hand, Haxel et al. detected TSE from the abraded metals and suggested that the peak position of TSE glow curve depended on the adsorption state of oxygen [4]. Many of these experimental results suggested that the adsorbed layer on the metal surface played a crucial role on TSE. In contrast, it was reported that the phase transitions were accompanied with TSE in the cases of metal alloys such as Fe-Mn [5] and semiconductor surfaces such as Si [6]. Thus, TSE phenomena have also been observed even without relating to the adsorbed layer.

TSE from ionic crystals has been studied by many researchers. Brunsmann [7] and Samuelsson [8] observed TSE from LiF. It was also confirmed that the energy of electrons from LiF through TSE process depended on the orientation of crystal plane [9]. TSE from

NaCl, which was irradiated by electron beam at 100 K, and from NaF [10], were also studied. It was concluded from these TSE studies that TSE from ionic crystals was strongly related to the color centers formed in the crystals by the pretreatments [11,12].

There have been a number of reports on TSE from metal oxides as well as ion crystals. Huzimura observed that the peak of TSE glow curve from MgO was located at 110 ℃ [13]. Regarding TSE from MgO, it was found that the peak position of the TSE glow curve did not change in an atmosphere Q-gas and in vacuum of 1.3 x 10^{-5} Pa [14] and that the intensity of the peak was decreased by the pre-annealing treatment at 700 ℃ in air. Besides the investigations of TSE from MgO, the studies on the TSE properties from BeO [15,16] and Al_2O_3 [17,18] have also been performed in order to apply TSE to dosimetry. From these many researches about TSE from oxides, it is believed that vacancies of oxygen in the oxide work for electron traps and TSE is originated from such traps.

From the analysis of a glow curve, one can obtain parameters such as the trap level energy *E*, the frequency factor ν and so on, which are necessary to clarify the TSE mechanism. The theory of TL for a single trap provided by Randall [19,20] has been applied as a basic model of TSE. According to this theory, temperature dependence of TSE intensity *(I(T))* was expressed by the following equation;

$$I(T) = I_0 \exp\left[-\frac{\nu}{\beta} \int_{T_0}^{T} \exp(-E/kT) dT \right] \times \exp(-E/kT) \qquad (2\text{-}1)$$

where ν, β, T, E and k are the frequency factor, the heating rate, the sample temperature, the trap level energy and the Boltzmann's constant, respectively. On the basis of the equation (2-1), a variety of methods were proposed for estimating *E* and ν. In the initial rise method, *E* can be calculated from a slope of the straight line in the graph of *log(I(T))* versus *1/T*. The methods to obtain *E* directly from the peak temperature in TSE glow curve are the maximum [21] and the differential analysis [22] methods. Besides these methods, wide variety of methods have been proposed; the heating rate method, the half width method [23,24], the integral glow curve method [25,26], the asymptotic estimation method [27], the curve fitting method [28] and so on. Moreover, there have been some attempts to estimate the electron affinity of the solid, which is the difference between vacuum level and conduction band, from the peak positions of TSE and TL or TSE [29].

In order to explain the emission properties of TSE, a variety of emission models have been proposed. The following models were constructed based on the analysis of TSE glow curves;

- Physico-Chemical Model; Physico-chemical model was proposed by Krylova in 1973 [30]. According to this model, adsorbates such as water molecules on a surface are excited, and ions or radicals are formed. When the recombination occurs, the excess energy is transferred to electrons to emit.
- Trap and Auger Model; Color centers formed in an ionic crystal by the radiation dose act as electron traps. In trap model, electrons are emitted from the electron traps by the thermal activation process. On the other hand, in Auger model, electrons are liberated by receiving the excess energy when a color center recombines an electron.

However, it was reported that the energy of electrons from KCl:Ti through TSE process reached several tens eV [31], and the electron emission with such a high energy can not be explained by the former two models. The following two models have been proposed to explain the high electron energy of TSE:

- Patch Field Model; At the oxide surface, the local surface potential is different in location because of its low electric conductivity. Therefore, the electric field induced by such a difference in surface potential accelerates electrons, and electrons received high energies. This model was proposed by Brunsmann in 1977 [32].
- Space Charge Model; When cracks are introduced in the oxide layer by the deformation or electron beam irradiation, positively and negatively charged areas (space charge areas) are induced at the cracks. The space charge in the crack gives rise to a high electric field, and electrons can be emitted under the effect of such a high electric field [33]. This model can be mostly applied to TSE from the brittle insulator surfaces.

Huzimura observed that TSE from MgO decreased by the adsorption of Ar or Ne at room temperature, and it was supposed that TSE was contributed by a strong electric field induced at the oxide surface [34]. This experimental result supports the two models described above.

Many studies on application of TSE, as well as the fundamental studies, have been performed by many research groups. Especially, in the field of radiation dosimetry, it has been recognized that the TSE dosimeter is highly sensitive to β-, γ- and X-rays compared with conventional thermoluminescence dosimeter (TLD). The application of TSE to dosimetry was proposed firstly by Kramer, and it was demonstrated by Scharmann [35] and Petel [36] that BeO TSE dosimeter had a high sensitivity to X- and γ-rays. However, the TSE dosimeters consisted of BeO [15,16], Al_2O_3 [17,18] or $Li_2B_4O_7$ [37] have a disadvantage in the linearity in their properties. Therefore, the investigations to increase the linearity of TSE devices are ongoing research topics.

2.2 Photo-Stimulated Exoemission

When the light with energy lower than the photoemission threshold of the surface illuminates the mechanically damaged surface, a temporal electron emission is sometimes observed. This phenomenon is called “Photo-Stimulated Exoemission (PSE)”. Veerman pointed out in 1969 that there was a clear correlation between cracks formed on Al surface and PSE intensity [38]. Figure 2-1 (a) shows the photograph of a crack on Al surface formed by fatigue. When this Al surface was scanned by the light beam with diameter of several tens of micrometers, the electron emission from the crack was measured even though the energy of the light was lower than the work function of the Al surface. Figure 2-1 (b) is the results of electron emission from the crack. From the comparison of Figures 2-1 (a) and (b), it is obvious that PSE occurs at the surface crack. Therefore, PSE has been utilized to a non-destructive method to detect cracks or defects on the surface.

There have been a number of researches on PSE from the metal surfaces undergoing mechanical treatments. Baxter observed that PSE intensity was enhanced by the cracks on the metal surfaces [39]. Also, PSE took place on a polycrystalline Al surface deformed by fatigue, and it has been considered that PSE intensity was related to the density of slip-steps on the surface [40]. It was confirmed that PSE intensity was influenced by atmosphere, detection methods, deformation or destruction methods and so on, but especially the adsorption states of oxygen and thickness of oxide layer formed on the metal surfaces [40]. Thus, it has been suggested that oxidation or adsorption plays an important role on PSE

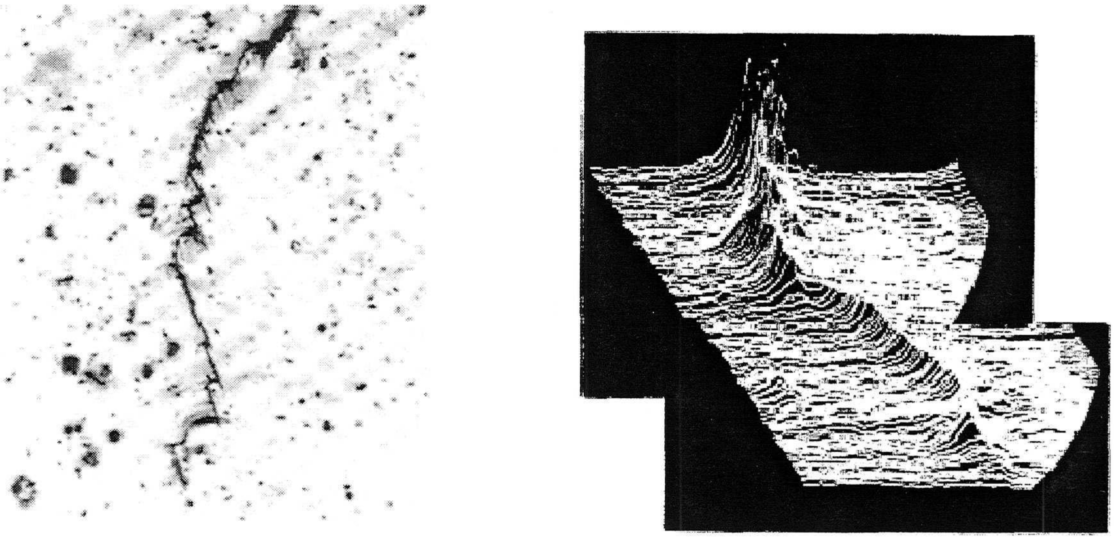

(a) Photograph (b) Exoemission image

Figure 2-1 Photograph and exoemission image on the Al surface with cracks. [38]

phenomena. The relationship between PSE phenomenon and adsorption of oxygen or water has been examined [41-44]. Moreover, it was also reported by Momose et al. that PSE was induced by the interaction of organic compounds with the metal surface [45,46]. Mori et al. discovered that materials of alloy or adsorbates affected PSE property [47]. It was also observed by Mori et al. that the energy distribution of exoelectrons in PSE was changed by a small amount of impurities, which could not be detected by X-ray diffraction [48]. They proposed PSE as a tool of analyzing the surface structure and the composition of the surface. Besides PSE from the surface, investigations on the PSE induced by crystallization have been performed by Gorecki et al. [49,50]. They observed that PSE and differential thermal analysis (DTA) had the same temperature dependence, and indicated that PSE was more sensitive analysis method to crystallization process than DTA. Recently, it was also reported that PSE took place on a variety of material surfaces such as clean semiconductor (Si) surfaces. Yamada et al. reported that photoelectrons at cleaved Si(111) 2x1 surfaces were detected, when the laser with an energy lower than photoemission threshold, and concluded that it was originated from the surface states induced by steps on the surface [51]. Thus, PSE is sensitive to the surface structure as well as adsorbates, and is

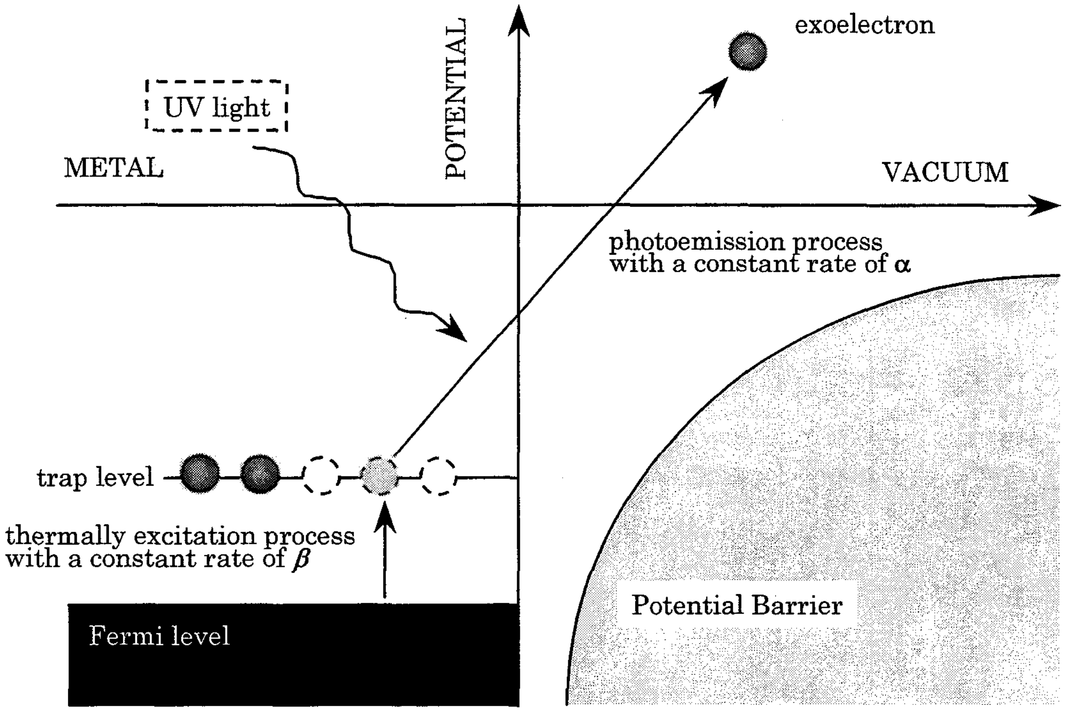

Figure 2-2 Two process model of PSE; electrons are pumped up to trap level, an then are emitted from traps with stimulation of UV light. [52]

also expected to be as a new surface analysis method.

Many emission mechanisms have been proposed to explain the PSE phenomena, and are classified roughly into two types of models. One type of the models considers an electron trap at the surface, and the other relates the absorption enhancement of light due to surface plasmon induced by cracks or defects. The two-process model proposed by Shigekawa et al. is one of the former models and it can quantitatively explain the PSE properties from scratched Al surfaces [52]. Figure 2-2 shows the concept of the two-process model. This model assumes that the PSE takes place through the two competing processes. One is the photoemission process by which electrons are emitted at a rate of α from the trap level, which is considered to be formed in a band gap of aluminum oxides [53]. The other is the supplement process of electrons at a rate of β from the valence band of Al to the trap level, which is considered to be due to the tunneling process or the thermal activation process. Shigekawa et al. observed the characteristic property of PSE from Al surfaces after scratching, and it was called "storage effect". The two-process model was introduced to explain the storage effect. Figures 2-3 (a) and (b) illustrate the typical storage

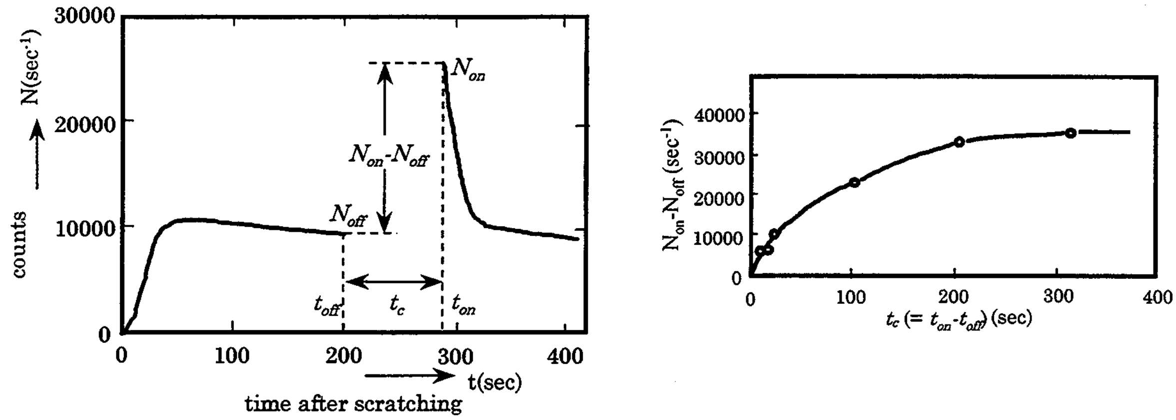

(a) emission property

(b) interruption period dependence of PSE intensity

Figure 2-3 Storage effect of PSE from the scratched Al surface. [52]

effect observed after scratching the Al surface. As shown in Figure 2-3 (a), the emission current from the scratched Al surface is enhanced temporally at the moment when the light started illuminating after the interruption period t_c, *i.e.*, $N_{on} - N_{off}$ in Figure 2-3 (a). Moreover, $N_{on} - N_{off}$ depends strongly on t_c as indicated in Figure 2-3 (b). According to the two-process model, $N_{on} - N_{off}$ can be described as a function of t_c by solving the rate equation as follows:

$$N_{on} - N_{off} = \frac{\alpha}{\alpha + \beta} S_0 [1 - \exp(-\beta t_c)] \qquad (2\text{-}2)$$

where S_0 is a number of total emission sites in a specimen. It can also be reproduced from this equation that $N_{on} - N_{off}$ increases with t_c and finally saturates, as shown in Figure 2-3 (b). Therefore, the parameters α, β and S_0 are estimated by fitting the equation (2-2) to the experimental result.

In contrast, it was confirmed by Buck et al. that the fatigue enhanced the intensity of photoelectrons with energies only near Fermi level [54]. Even though the breakup of the oxide layer by fatigue had been known to be a principal source of the fatigue-enhanced photoemission, it was concluded that the emission mechanism for the PSE observed by Buck et al. was not the case. This is because they confirmed that the fatigue enhancement of the photoelectron yield occurred from an ion-sputtered surface, that is, oxide-free surface. Hence, they proposed the new model to describe the PSE phenomena from Al surfaces induced by deformation. The model was based upon the slip-step-induced resonant absorption of incident *p*-polarized UV light by the surface plasmons [55]. The calculation regarding the absorption rate of the UV light was carried out on the oxidized Al surfaces. As a consequent, the absorption enhancement calculated by this model was in good agreement with the increase in the photoelectron yield, and could also reproduce the wavelength dependence of the fatigue-enhanced emission.

On the other hand, an attempt to obtain the spatial distribution of the surface damage has also been carried out using PSE microscope. Yamamoto observed the PSE images from the deformed Al surfaces stimulated by the UV light with energies lower than 4.0 eV and the time history of the images [56,57]. Figures 2-4 shows the results. It became clear from the comparison of the PSE image with SEM photograph that the bright areas in Figure 2-4 correspond to the slip-steps formed by the deformation. Therefore, it was concluded that the slip-steps were strongly related to the PSE phenomenon. Since the intensity of PSE decayed with time, it was also suggested that the freshness of the damage might be correlated to the PSE phenomenon. Baxter and Rouse have also investigated the PSE images from the deformed metal surfaces [58-60]. They concluded that PSE from the deformed surfaces

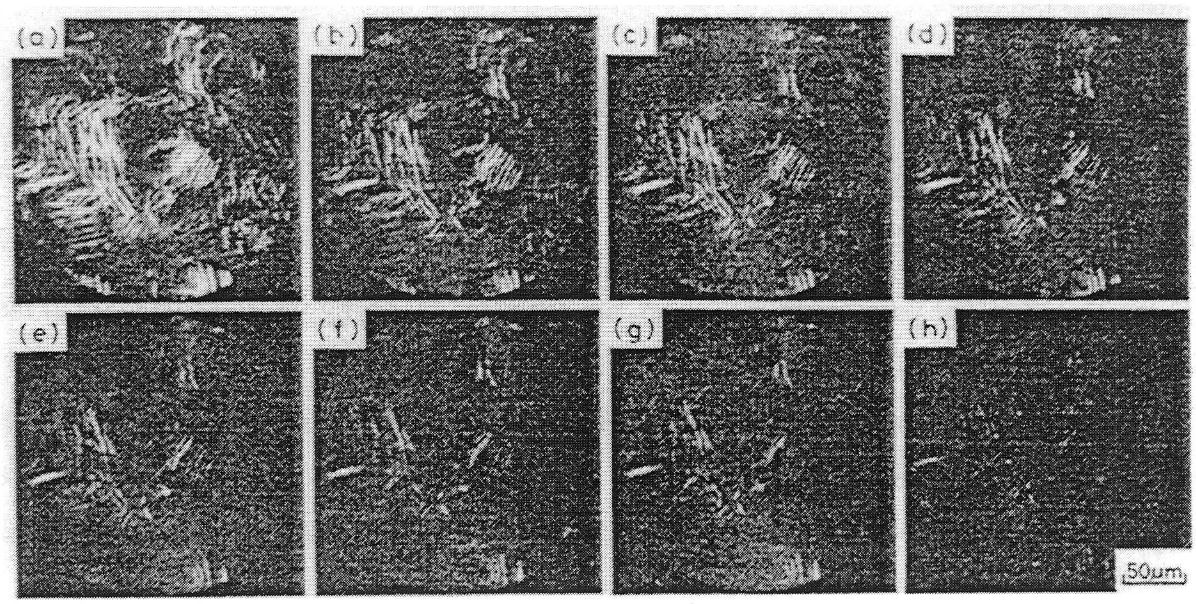

Figure 2-4 PSE image from the polycrystalline Al surface with cracks induced by deformation. PSE images were taken at 0, 1, 2, 3, 4, 5 and 24 hours after deformation, which are denoted by (a) ~ (h), respectively. [57]

was attributed to a decrease of work function due to destruction of oxide layer, and the PSE intensity was decayed by the re-oxidation of the destructed areas. However, as described above, PSE was also observed on the oxide-free Al surface. Thus, it is impossible to explain all PSE phenomena by only one model.

It is clear from the experimental results reviewed above that the cracks or defects on a metal surface induce or enhance PSE. Namely, the PSE image from the surface reflects the distribution of the surface cracks or defects. Therefore, for the industrial engineering purpose, the imaging of PSE is important as a non-destructive testing method to detect surface cracks or defects. However, the imaging of the PSE has not been established yet. That is the reason why the relationship between PSE properties and states of the surface has not been clarified quantitatively. In order to realize such a non-destructive testing method using PSE, the cracks or defects on the emitting surface will be identified with higher resolution, and quantitative discussions regarding the relationship between PSE and the surface state will be required.

2.3 Field-Stimulated Exoemission

When a high electric field is applied to a solid surface, an electron emission occurs due to the tunneling effect. This phenomenon has been theoretically described by Fowler and Nordheim as an electron emission from the conduction band of metals [61]. Robertson pointed out that the same type of emission phenomenon may be observed for exoelectrons, and he called this exoelectron emission as field-stimulated exoelectron emission (FSE or FSEE) [62]. This phenomenon was firstly discovered at borosilicate glass surface by Hibbert and co-workers [63]. It was reported that electron emission took place from

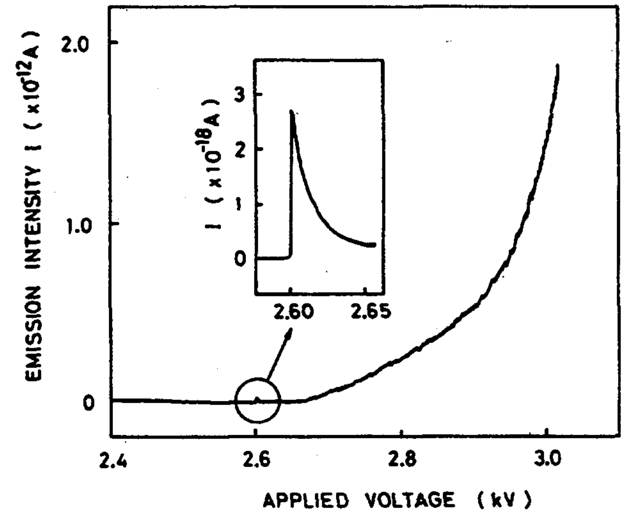

Figure 2-5 FSE peak before the onset of field emission of electrons. [65]

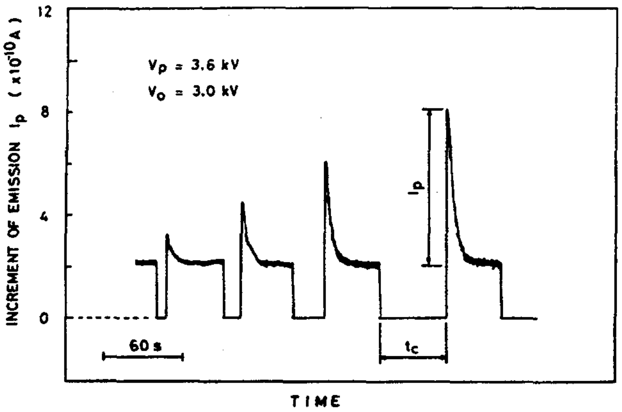

Figure 2-6 Storage effect of FSE peak. Increment of emission (I_p) is dependent on the interval of the applied voltage pulses (t_c). [65]

the active sites on borosilicate glass surface where an electric field of about 5 x 10^6 V/m was applied. The temperature dependence of the emission was examined, and it was found that energy of only 1.0 eV was required for this electron emission. They concluded that a model of field-enhanced thermionic emission (Schottky effect) from the emission active sites with low work function could explain the experimental results. Also, according to their further study with borosilicate glass, it was found that a temporal enhancement of emission current was observed when the voltage was applied as a voltage step from zero to the operating voltage [64]. It was also reported that the emission enhancement depended on the turn-off time of the voltage. This phenomenon is similar to the storage effect of PSE described in Section 2.2.

Robertson suggested in his review paper that it was possible that the emission phenomenon found by Hibbert et al. was not restricted to a borosilicate glass but would take place on many materials [62]. In 1989, similar emission phenomenon was discovered at the Al surface by Tagawa et al. [65]. They observed a small hump of electron emission at an applied voltage lower than field emission threshold from Al tip surfaces as seen in Figure 2-5. From a series of experiment using Al tips as a specimen, they discovered the emission properties of FSE from Al tips as follows:

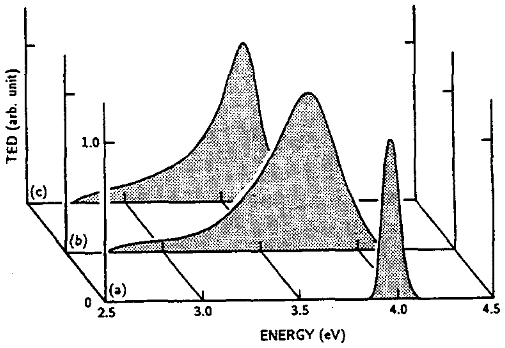

(a) 99.9999% Al tip
(b) 99.999% Al tip
(c) 99.99% Al tip

Figure 2-7 Total energy distribution of exoelectrons from the 99.9999%, 99.999% and 99.99% pure Al tips. [66]

1) FSE from Al tips indicated storage effect as shown in Figure 2-6. Therefore, FSE from Al tips would be explained by

the two-process model [65].

2) The energy distribution of exoelectron traps depended on the purity of Al tips as shown in Figure 2-7. These results showed that trap levels of exoelectrons on pure Al tips were formed at 0.2 eV above the Fermi level and the additional traps were attributed to the impurities on the tip surfaces [66].
3) Oxygen adsorption on Al tip surfaces caused the increase of FSE as shown in Figure 2-8. From the energy distribution of exoelectrons from the oxygen-adsorbed Al surfaces, it was concluded that chemisorbed and physisorbed oxygen atoms formed the exoelectron traps at -4.00 eV and -3.62 eV with respect to the vacuum level, respectively [67].
4) The FSE intensity decreased with increasing tip temperature in the temperature range between 300 and 380 K as shown in Figure 2-9, and it recovered after holding the tip at room temperature in UHV. These phenomena were considered to be due to hydrogen physisorption, which was main component of residual gas in UHV [68].

Since FSE was discovered within the last decade, the number of reports regarding FSE is limited. This fact would be due to the limitation on the sample used in FSE experiments, that is, the sample has to be a sharp tip as described above in order to apply a high electric field to the sample surface. Therefore, widely used techniques to analyze a solid surface, for example AES (Auger Electron Spectroscopy), XPS (X-ray Photoelectron Spectroscopy) and so on, can not be applied. However, field ion microscopy (FIM) and field emission

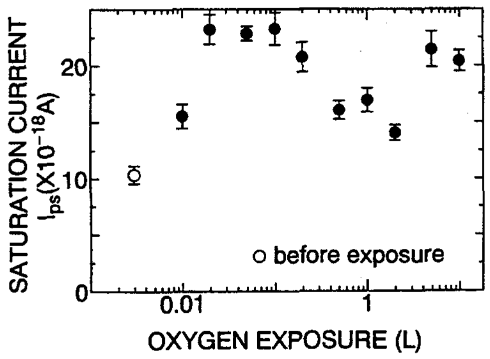

Figure 2-8 Change in saturation current of FSE with respect to oxygen exposures. [67]

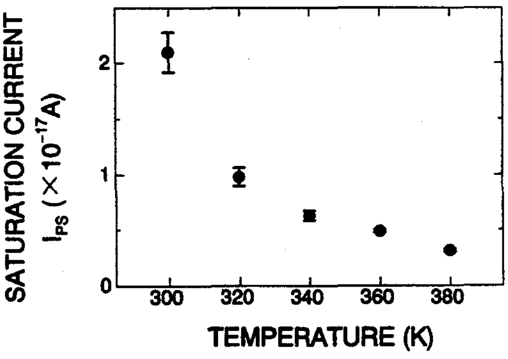

Figure 2-9 Change in saturation current of storage effect, I_{ps}, with the tip temperature at 320 ~ 380 K. [68]

microscopy (FEM) have been established as a method to evaluate the tip surface. These microcopies have an atomic resolution, especially using FIM, the atomic arrangement of the tip surface can be observed in a real space. By using FEM, the information on electronic structures such as the distribution in work function can be obtained with a extremely high resolution. If FIM and FEM are combined to FSE study, it is expected to clarify the spatial distribution of FSE, similar to FEM, and to identify the atomic arrangement of the electron-emitting surface by FIM. Therefore, the relationship between surface state and FSE can be discussed quantitatively, and the mechanism of exoemission will be able to be constructed. The study on FSE from metals has been performed only with Al surface. If comprehensive and detailed investigations regarding FSE from various kinds of metals will be performed, it is expected that the exoemission mechanism will be elucidated, and will be a great help to the application-oriented exoelectron studies.

2.4 Chemically-Stimulated Exoemission

Most of the exoemission phenomena need the stimulating energy such as heat or light to emit electrons, ions and photons. Besides these stimulating energies, the adsorption process of electronegative gas also triggers the exoemission phenomena. These emission phenomena have called "chemically-stimulated exoemission (CSE)", and first discovered by Thomson in 1905 [69]. CSE has been considered to be closely related to the non-adiabatic gas/surface reaction process, and the systematic research has been carried out regarding Mg + O_2 and alkali metals + O_2 systems.

The reactions of oxygen with Mg and MgO lead to the emission of photons as well as electrons. Lohff and Raether observed exoemission of negative particles from the abraded Mg surfaces [70], and concluded that oxygen played an important role of the exoemission [71]. Kasemo reported that the light emission, as well as negatively charged particle emission, took place during the oxidation of Mg [72]. It was suggested that the variation of the work function related to the exoemission of electrons and photons. In the system of MgO + O_2, exoemission of electrons and photons was also observed, similar to Mg+O_2

system. These exoemission phenomena including photons and electrons have been explained by the following emission mechanisms;

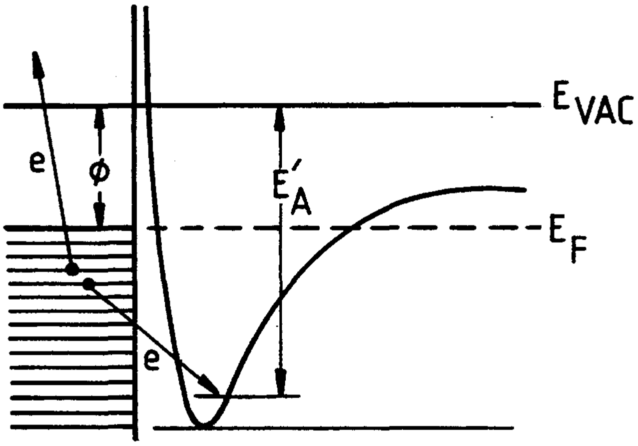

Figure 2-10 A simple energy level diagram to illustrate the model based upon Auger de-excitation process.

1) In the Mg + O_2 system; the electrons and photons are emitted by the excess energy $(E'_A - \phi)$ due to the Auger de-excitation process of the hole created below the Fermi level (E_F) during the reaction (see Figure 2-10) [73].
2) In the MgO + O_2 system; the excess energy comes from the recombination of F-centers, *i.e.*, oxygen vacancies in the oxide, and an electron which receive this excess energy are emitted [74].

On the other hand, it has been recognized that the oxidation of alkali metals accompanies electron emission [75-77]. Recently, the investigations regarding exoemission from Cs surface, which has the lowest work function among alkali metals, due to O_2 exposure were reported by Böttcher et al. The results obtained by their systematic experiments were

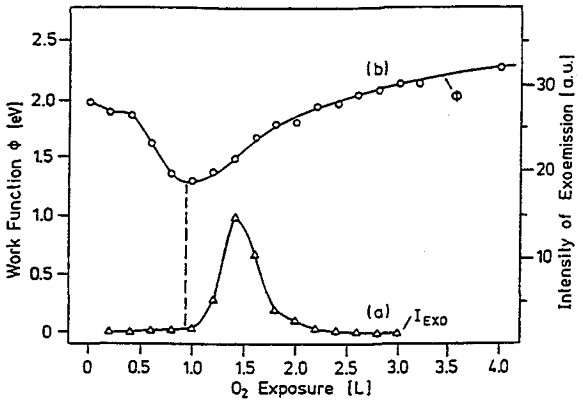

Figure 2-11 Variation of he current of exoelectrons (a) and the work function D curve (b) upon stepwise exposure of a Cs film with about 3 ML thickness at 220 K to an O_2 pressure of 4 x 10^{-7} Pa. [77]

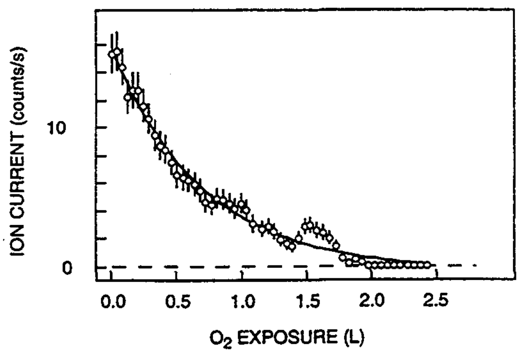

Figure 2-12 O$^-$ emission from a monolayer of Cs on Ru (0001) as a function O_2 exposure. The applied O_2 pressure was 10^{-6} Pa and the sample was kept at 200 K. [79]

reviewed by Greber [78]. Figure 2-11 shows the variation of work function and the exoemission intensity as a function of oxygen exposure [77]. From the comparison between the work function change and the exoemission intensity, it was suggested that a transformation from peroxide (Cs_2O_2) to superoxide (CsO_2) gave rise to the exoelectron emission. This conclusion was also supported by the experimental findings that O^- species as well as electrons were emitted from Cs surface only at the early stage of oxygen exposure as shown in Figure 2-12 [79]. During the oxidation of Cs surface, the different oxide structures were confirmed by low-energy electron diffraction (LEED), high-resolution electron energy loss spectroscopy (HREELS) and scanning tunneling microscopy (STM). Böttcher et al. indicated that several thermally-activated processes were involved in the formation of a Cs oxide layer and that exoemission was a suitable tool for the exploration of the kinetics of phase transformations. According to their reports on the exoemission from Cs surfaces during oxygen exposure, the emission mechanisms are summarized in Figure 2-13 and explained as follows: When oxygen molecule approaches to Cs surface, the charge transfer takes place between the Cs surface and the oxygen molecule (harpooning process). Because the image force lowers the affinity level of the molecule, which resonantly ionizes as soon as it crosses the Fermi level [80]. O_2^- thus formed comes closer to the surface, and the harpooning process occurs again. After the second electron transfer ($O_2^- \rightarrow O_2^{2-}$), the

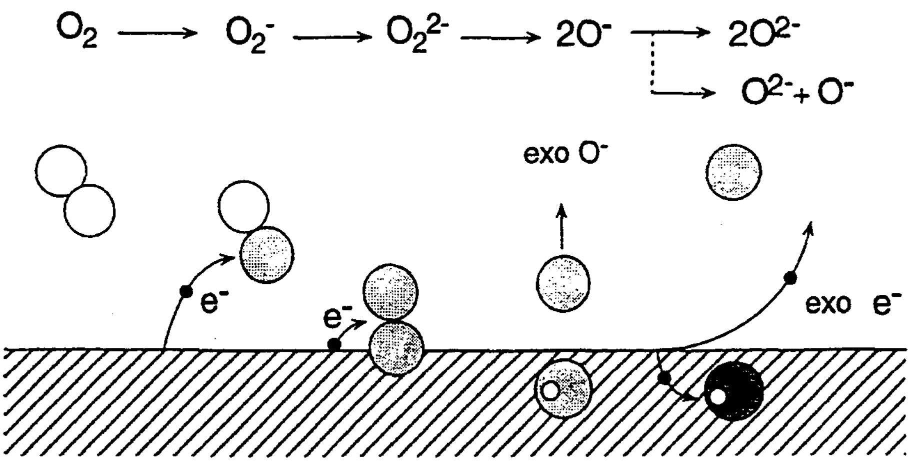

Figure 2-13 Model for harpooning and direct dissociation for oxygen accompanying exoemission of O^- and electrons. [78]

hot O_2^{2-} species bursts into two fragments. If the momentum of one of these fragments, O^-, is large enough and directed away from the surface, it may escape the Cs surface (O^- emission). The electron affinity of O^- will be lowered during approaching the surface, and when the electron affinity dives to the level deeper than the Fermi level of the Cs surface the exoelectron emission takes place due to Auger de-excitation process.

Thus, exoemission comprises additional information about the kinetics of the oxidation process. Therefore, the exoemission of non-adiabatic particles is considered to be an excellent probe for the study of adsorption dynamics.

2.5 Tribo- and Fract-Emission

When a solid surface is damaged by friction, it has been recognized that electrons, ions and/or photons are emitted from the frictional area or the surroundings. The schematics of these tribological processes accompanying the emission of particles are shown in Figure 2-14 [81]. This particle emission phenomenon has been known as a "tribo-emission (TRE)" [82,83]. It has been confirmed that TRE takes place from any surfaces of insulators, semiconductors and metals. The intensity of the TRE from an insulator surface is the high, while that from a metal surface is relatively low [84].

In the case of TRE from the insulator surface, the emission intensity shows the burst at the moment of the starting friction and the emission stops when the friction is completed [85]. The emission mechanism of the TRE from an insulator has been proposed as follows: A high electric field in

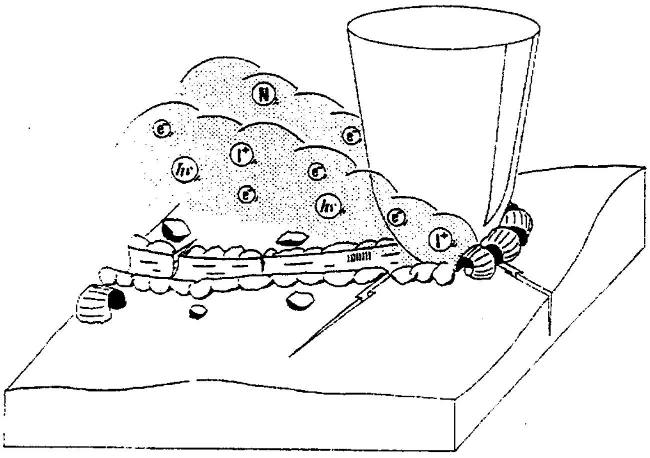

Figure 2-14 Schematic drawings of the particle emission during the tribological process. [81]

the order of 10^9 V/m is induced in the damaged region by friction or the surroundings due to charge separation [86]. When atmospheric gas molecules encounters in to such a high electric field, some of the gas molecules would be ionized. Electrons, ions and photons are thus formed, namely, plasma is induced in the frictional regions. Therefore, the emissions of such electrons, ions and/or photons are observed as TRE. This model is supported by the fact that the pressure of the surrounding gas strongly influences the TRE property [85].

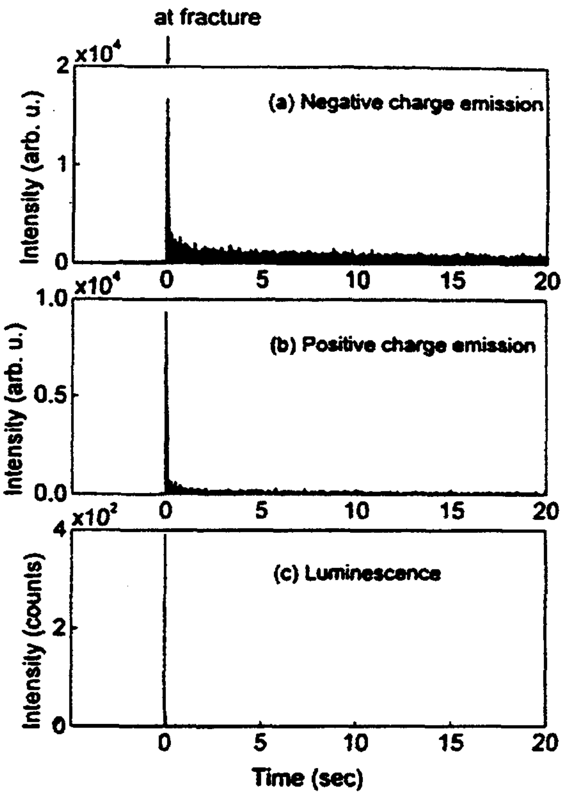

Figure 2-15 Fracto-emission from granite at 10^{-5} Pa. [89]

On the other hand, the TRE phenomenon from the metal surface has been explained by the different emission model. The adsorbates are removed and a flesh metal surface is activated by friction. When surrounding gas molecules react chemically with such a flesh surface, electrons may be emitted by receiving the excess energy in the chemical adsorption reaction through CSE process described in the previous Section 2.4. For example, a mechanical machining of Ni in N_2 atmosphere did not lead to appearance of TRE. In contrast, as soon as O_2 gas was introduced, the electron emission was promoted rapidly [85]. Furthermore, even when the cutting process was stopped, the electron emission was continued. This TRE phenomenon can be explained by the model based upon CSE at the flesh surface region formed due to friction [85].

Also, it has been recognized that the deformation or fracture of a solid is accompanied by the emissions of electrons, ions, photons, neutral particles and/or electromagnetic radiations. This emission phenomenon is called "Fracto-Emission (FRE)" [87,88]. Figure 2-15 shows the time response of the charged particle emission and the luminescence in the fracture of granite at 10^{-5} Pa reported by Kawaguchi [89]. Although no particle is detected before the fracture, the emission signal rises at the moment of the fraction. It is suggested by Kawaguchi that all the emission would be caused by the bond-breaking due to the fracture in the microscopic scale, that is, the energy released directly by the bond-breaking, and the excess energy would be used for the emission of electrons, charged particles and photons.

Furthermore, similar emission phenomena, but in a large scale, have been reported to occur prior to earthquakes, and the investigation to use these phenomena for the earthquake forecasts is performed intensively [90]. Several models of FRE, which is observed before earthquake, are proposed as follows:

1) Microfracture of rocks just before an earthquake causes emission of electrons, ions, and photons [91].
2) Large stress on quartz-containing rocks causes piezoelectric currents [92].
3) Heating of rocks by magma leads to TSE [93].

However, details of the mechanism have not been clarified yet. The investigations of the earthquake forecasts using FRE phenomena are in progress with a great interest.

References

[1] "*On a Kind of Radioactivity Imparted to Certain Salts by Cathode Rays*"; J. Mclenann, The London Edinburgh and Dublin Philosophical and Journal of Science Series 6, vol. 3 no. 14 (1902) 195 ~ 203.

[2] "*Zur Temperaturabhängingkeit der Röntgenstimulierten Exoelektronenemission*"; H. Hieslmair and H. Müller, Zeitschrift fur Physik, vol. 152 (1958) 642 ~ 654.

[3] "*Elektronennachemission und Photoomission von Aluminiumoberflächen*"; A. Sharmann, Zeitschrift fur Physik, vol. 183 (1965) 249 ~ 264.

[4] "*Die Elektronemission von Metalloberflächen als Nachwirkung einer Mechanischen Bearbeitung oder Glimmentladung*"; O. Haxel; Zeitschrift fur Physik, vol. 130 (1951) 109 ~ 123.

[5] "*Photostimulated Electron Emission from Thin Layers of Nickel and Nickel Oxide during Phase Transitions of the Second Kind*"; L. Bieracki, T. Górecki and B. Sujak, Acta Physica Polanica, vol. 32 (1967) 193 ~ 195.

[6] "*Exoemission and Phase Transitions on Real Crystal and Porous Silicon Surfaces*"; I. V. Krylova and A. G. Petrukhin, Semiconductor, vol. 30 no. 3 (1996) 231 ~ 237.

[7] "*Energy Distribution of Thermally Stimulated Exoelectrons by means of a Retarding Potential Difference Method*"; U. Brunsmann and A. Scharmann, Physica Status Solidi, vol. 26 no. 2 (1974) K123 ~ 126.

[8] "*High Resolution Studies of the Energy Distribution of Thermally Stimulated Exo-Electrons from LiF*"; L. I. Samuelsson, S. B. M. Hagstrom and C. A. Carlsson, Physica Status Solidi, vol. 20 no. 1 (1973) K79 ~ 81.

[9] "*Thermally Stimulated Exoelectron Emission from the (100), (110) and (111) Surfaces in Single Crystals*"; T. Kubozoe, Y. Watanabe, Y. Nakamura, S. Okabe and M. Aoki, Radiation Protection Dosimetry, vol. 4 no. 3-4 (1983) 257 ~ 259.

[10] "*Dose and Temperature Dependence of the Exoelectron Energy Distribution of LiF*"; U. Brunsmann, R. Huzimura and A. Scharmann, Physica Status Solidi, vol. 26 no. 2 (1974) K149 ~ 151.

[11] "*Exoelectron Emission, Phenomena and Parameters*"; A. Scharmann, Proceedings of 4th International Symposium on Exoelectron Emission and Dosimetry, Liblice, (1973)

12 ~29.

[12] “*A Possible Manifestation of Auger Processes in Thermostimulated Electron Emission*”; V. Bichevin and H. Käämbre, Physica Status Solidi A, vol. 4 no. 3 (1971) K235 ~ 243.

[13] “*Exoelectron Emission of $CaSO_4$ and MgO*”; R. Huzimura and Y. Yanagisawa, Ionics, vol. 7 (1983) 25 ~27.

[14] “*Thermal and Optical Stimulation Processes of V^- Centers in MgO Single Crystal*”; H. Nanto, I. Konishi, R. Kikuchi and M. Kawanishi, Oyo-Butsuri, vol. 48 no. 6 (1979) 545 ~ 551.

[15] “*Computation of the Energy and Angular Distribution of Exoelectrons by the Monte-Carlo Method*”; V. S. Kortov and P. P. Zolnikov; Physica Status Solidi, vol. 31 no. 1 (1975) 331 ~ 339.

[16] “*Field-Assisted Thermally Stimulated Exoelectron Emission from BeO*”; A. Scharmann and U. Weissler, Physica Status Solidi A, vol. 60 no. 1 (1980) 117 ~122.

[17] “*Intense Exoelectron Emission from Fine Particles of Al_2O_3 and its Dependence on the Conductivity of the Substrate Material*”; K. Kawabata, Physica Status Solidi A, vol. 78 no. 2 (1983) K127 ~ 130.

[18] “*TSEE Detection of α and very Soft β Radiations*”; L. Hobzova, M. Petel and Z. Spurny, Radiation Protection Dosimetry, vol. 4 no. 3-4 (1983) 137 ~139.

[19] “*Phosphorescence and Electron Traps 1. The Sturdy of Trap Distributions*”; J. T. Randall and M. H. F. Wilkins, Proceeding of the Royal Society of London Series A, vol. 184 (1945) 366 ~ 389.

[20] “*Phosphorescence and Electron Traps 2. The Interpretations of Long-Period Phosphorescence*”; J. T. Randall and M. H. F. Wilkins, Proceeding of the Royal Society of London Series A, vol. 184 (1945) 390 ~ 407.

[21] “*Light-induced Defect Studies in Hydrogenated Amorphous Silicon by Exoelectron Emission*”; R. S. Bhide, V. Manorama, S. K. Pawar, S. Babras, S. V. Bhoraskar and V. G. Bhide, Applied Physics Letters, vol. 57 no. 15 (1990) 1528 ~ 1530.

[22] “*Differential Analysis of TSC Spectra in GaAs Semi-Insulating Material*”; M. Castagne, J. Bonnafe, J. Romestan and J. P. Fillard, Journal of Physics C, vol. 13 no. 30 (1980) 5555 ~ 5563.

[23] "*Evaluation of Thermal Activation Energies from Glow Curves*"; A. Halperin and A. A. Braner, Physical Review, vol. 117 (1960) 408 ~ 415.

[24] "*On the Calculation of Activation Energies and Frequency Factors from Glow Curves*"; R. Chen, Journal of Applied Physics, vol. 40 no. 2 (1969) 570 ~ 584.

[25] "*Computation of the Exponential Trap Population Integral of Glow Curve Theory*"; W. L. Paterson, Journal of Computation Physics, vol. 7 (1971) 187 ~ 190.

[26] "*Thermally Stimulated Luminescence and Exoelectron Emission from Barium and Strontium Sulphate Doped with Europium*"; G. Holzapfel and M. Krystek, Physica Status Solidi A, vol. 37 no. 1 (1976) 303 ~ 312.

[27] "*On the Determination of the Trap Depths from Thermally Stimulated Currents. II*"; S. Maeta and F. Yoshida, Japanese Journal of Applied Physics, vol. 28 no. 9 (1989) 1712 ~ 1717.

[28] "*Numerical Curve Fitting for Calculating Glow Parameters*"; N. S. Mohan and R. Chen, Journal of Physics D : Applied Physics, vol. 3 no. 2 (1970) 243 ~ 247.

[29] "*Variation of the Energy and Intensity of Exoelectrons from BeO*"; V. S. Kortov, Physica Status Solidi A, vol. 19 no. 1 (1973) 59 ~ 66.

[30] "*The Physico-Chemical Nature of Exoelectron Emission*"; I. V. Krylova, Proceedings of 4th International Symposium on Exoelectron Emission and Dosimetry, liblice, (1973) 145 ~ 153.

[31] "*Energy Spectra of Thermally Stimulated Exoelectrons from KCl:Tl X-irradiated at 77K*"; M. Kamada, K. Yoshiara and K. Tsutsumi, Japanese Journal of Applied Physics, vol. 23 no.3 (1984) 286 ~ 290.

[32] "*A Simulation of the Maxwellian Exoelectron Energy Distributions with regard to Patch Fields*"; U. Brunsmann and A. Scharmann, Physica Status Solidi, vol. 42 no. 1 (1977) K79 ~ 81.

[33] "*The Mechanism of Exo-Electron Emission after Excitation with Electrons*"; J. Drenckhan, H. Gross and H. Glaefeke, Physica Status Solidi, vol. 22 no. 1 (1970) K51 ~ 54.

[34] "*TSEE Responses of Oxides to Energetic Ion Bombardment*"; R. Huzimura, S. Miyagawa, Y. Ato and M. Kawanishi, Japanese Journal of Applied Physics Supplement, vol. 24-4 (1985) 53 ~ 59.

[35] "*Characteristics of an Improved Proportional Counter for the Readout of TSEE Dosimeters*";A. Scharmann, G. Schmirler and W. Senger, Radiation Protection Dosimetry, vol. 4 no. 3-4 (1983) 160 ~ 163.

[36] "*Thermally Stimulated Exoelectron Emission from Lithium Fluoride for β and γ dosimetry*"; Y. Herbaut, A. R. Neto, M. Petel and G. Portal, Radiation Protection Dosimetry, vol. 4 no. 3-4 (1983) 140 ~ 143.

[37] "*TSEE and TL from Physically Processed Surface of Dosemeter Material*"; M. Kawanishi, R. Kikuchi, T. Yamamoto, T. Kubozoe, Y. Watanabe, S. Okabe and T. Kawamoto, Radiation Protection Dosimetry, vol. 6 no. 1-4 (1984) 213 ~ 216.

[38] "*Registration and Mapping of Plastically Deformed Metal Surfaces by Means of Photoelectrons*"; C. C. Veerman, Material Science Engineering, vol. 4 (1969) 329 ~ 342.

[39] "*The Detection of Fatigue Damage by Exoelectron Emission*"; W. J. Baxter, Journal of Applied Physics, vol. 44 no. 2 (1973) 608 ~ 610.

[40] "*Characterization of the Oxide Film of Aluminum by PSEE Measurement during Tensile Deformation*"; Y. Shinada, Ionics, vol. 7 (1983) 55 ~ 59.

[41] "*The Emission of Electrons from Aluminum Abraded in Atmospheres of Air, Oxygen, Nitrogen and Water Vapor*"; J. A. Ramsey, Surface Science, vol. 8 (1967) 313 ~ 322.

[42] "*The Relationship between Triboinduced Electron Emission and Adsorption Processes in the System* $Al\text{-}O\text{-}H_2O$"; E. Linke and K. Meyer, Surface Science, vol. 20 no. 2 (1970) 304 ~ 312.

[43] "*Triboinduced Electron Emission and Work Function Measurement in the System Aluminium-*O_2*-*H_2O *under UHV Conditions*"; E. Linke and D. Born, Proceedings of 4th International Symposium on Exoelectron Emission and Dosimetry, (1973) 159 ~ 161.

[44] "*Exoelectron Emission, Phenomena and Parameters*"; A. Scharmann, Proceedings of 4th International Symposium on Exoelectron Emission and Dosimetry, (1973) 12 ~ 29.

[45] "*Exoelectron Emission from Ground Aluminium Powder and its Relationship to the Adsorption of Oxygen, Water, and Some Organic Compounds*"; Y. Momose, Y. Iguchi and S. Ishii, Journal of Physical Chemistry, vol. 80 no. 12 (1976) 1329 ~ 1335.

[46] "*Exoelectron Emission from Metals Subjected to Friction and Wear, and its Relationship to the Adsorption of Oxygen, Water Vapor, and Some Other Gases*"; Y.

Momose and T. Namekawa, Journal of Physical Chemistry, vol. 82 no. 13 (1978) 1509 ~ 1515.

[47] "*Application of Exoelectron Phenomena to the Surface Characterization of Some Alloys*"; S. Mori, H. Kurosawa and Y. Tamai, Ionics, vol. 7 (1983) 32 ~ 34.

[48] "*A Study of the Structure of Some Aluminum Alloys by Exoelectron*"; S. Mori, H. Kurosawa and Y. Tamai, Ionics, vol. 7 (1983) 35 ~ 37.

[49] "*Applications of the Exoelectron Emission Technique in Physical Metallurgy*"; T. Górecki and C. Górecki, Radiation Protection Dosimetry, vol. 4 no. 3-4 (1983) 292 ~ 294.

[50] "*Photostimulated EEE Accompanying Structural Transformations in Metallic Glasses (Exoelectron Emission)*"; T. Górecki and C. Górecki, Japanese Journal of Applied Physics, vol. 24-4 (1985) 27 ~ 31.

[51] "*Low-Energy Laser Photoelectron Study of Defect States on Cleaved Si(111)2x1 Surfaces*"; M. Yamada, J. Kanasaki, N. Itoh and R. T. Williams, Surface Science vol. 349 (1996) L107 ~ 110.

[52] "*Two-Process Model of PSEE from Scratched Metals*"; H. Shigekawa and S. Hyodo, Applied Surface Science, vol. 22/23 (1985) 361 ~ 368.

[53] "*Intensity vs. Time Profiles of Photostimulated Exoelectron Emission from Scratched Aluminum*"; H. Shigekawa and S. Hyodo, Japanese Journal of Applied Physics, vol. 22 no. 10 (1983) 1493 ~ 1495.

[54] "*Deformation Enhanced Photoemission from Aluminum 1. Experimental Results*"; O. Buck, W. J. Pardee, F. J. Szalkowski and D. O. Thompson, Applied Physics, vol. 12 (1977) 301 ~ 310.

[55] "*Deformation Enhanced Photoemission from Aluminum 2. Theory of the Plasmon Resonance Mechanism*"; W. J. Pardee and O. Buck, Applied Physics, vol. 14 (1977) 367 ~ 375.

[56] "*A Versatile Photostimulated Exoelectron Emission Microscope as Applied to Observing Mechanical Damage on Aluminum Surfaces*"; S. Yamamoto, Japanese Journal of Applied Physics, vol. 20 (1981) 971 ~ 978.

[57] "*Photostimulated Exoelectron Emission Microscope Observation of Deformed Aluminum*"; S. Yamamoto, Ionics, vol. 7 (1983) 82 ~ 86 [in Japanese].

[58] "*Photostimulated Exoelectron Emission from Slip Lines: A New Microscopy of Metal Deformation*"; W. J. Baxter and S. R. Ouze, Journal of Applied Physic, vol. 44 no. 10 (1973) 4400 ~ 4404.

[59] "*Photoemission Electron Microscopy of Oxide Fracture at Slip Steps on Metals*"; W. J. Baxter and S. R. Ouze, Journal of Applied Physics, vol. 46 (1975) 2429 ~.

[60] "*The Effect of Oxide Thickness on Photostimulated Exoelectron Emission from Aluminum*"; W. J. Baxter and S. R. Ouze, Journal of Applied Physics, vol. 49 no. 7 (1978) 4233 ~ 4237.

[61] "*Electron Emission in Intense Electric Fields*"; R. H. Fowler and L. W. Nordheim, Proceedings of the Royal Society of London Series A, vol. 119 no. 781 (1928) 173 ~181.

[62] "*Exoelectron Emission from Solids*"; A. J. B. Robertson, International Journal of Electronics, vol. 51 (1981) 607 ~ 619.

[63] "*The Emission of Electrons from Glass Induced by a Strong Electric Field and the Mechanism of the Silent Electric Discharge*"; D. B. Hibbert and A. J. B. Robertson, Proceedings of the Royal Society of London A, vol. 349 (1976) 63 ~ 79.

[64] "*Field Stimulated Exoelectron Emission from Borosilicate Glass*"; T. M. Roberts and D. B. Hibbert, Nature, vol. 297 (1982) 42 ~ 43.

[65] "*Field-Stimulated Exoelectron Emission from 99.9999% Pure Al*"; M. Tagawa, S. Takenobu, N. Ohmae and M. Umeno, Applied Physics Letters, vol. 53 no. 7 (1988) 626 ~ 627.

[66] "*Distribution of Trap Levels in Field-Stimulated Exoelectron Emission*"; M. Tagawa, K. Tsuzuki, M. Mori, N. Ohmae and M. Umeno, Applied Physics. Letters, vol. 61 no. 12 (1992) 1471 ~ 1473.

[67] "*Influence of Oxygen Adsorption on Field-Stimulated Exoelectron Emission from High-Purity Aluminum*"; M. Tagawa, M. Mori, N. Ohmae and M. Umeno, Applied Surface Science, vol. 72 (1993) 259 ~ 265.

[68] "*Temperature Dependence of the Field-Stimulated Exoelectron Emission*"; M. Mori, E. Ogawa, M. Tagawa, N. Ohmae and M. Umeno, Applied Surface Science vol. 76/77 (1994) 21 ~ 25.

[69] "*On the Emission of Negative Corpuscles by the Alkali Metals*"; J. J. Thomson, The

London, Edinburgh and Dublin Philosophical Magazine and Journal of science Series 6, vol. 10 (1905) 584 ~ 590.

[70] "*Die Elektronenemission von Metalloberflächen nach Mechanischer Berbeitung*"; J. Lohff and H. Raether, Zeitschrift fur Physik, vol. 142 (1955) 310 ~ 320.

[71] "*Die Elektronenemission bei der Oxydation Mechanisch Bearbeiteter Metalloberflächen*"; J. Lohff, Zeitschrift fur Physik, vol. 146 (1956) 436 ~ 446.

[72] "*Photon Emission during Chemisorption of Oxygen on Al and Mg Surfaces*"; B. Kasemo, Physical Review Letters, vol. 32 no. 20 (1974) 1114 ~ 1117.

[73] "*Photon and Electron Emission as Indicators of Intermediate States in Surface Reactions*"; B. Kasemo, E. Tornquist, J. K. Norskov and B. I. Lundqvist, Surface Science, vol. 89 (1979) 554 ~ 565.

[74] "*Chemisorption Induced Luminescence from Color Centers*"; V. T. Coon, Surface Science, vol. 88 (1979) L42 ~ 50.

[75] "*Behavior of Cesium Oxide as a Low Work-Function Coating*"; J. J. Uebbing and L. W. James, Journal of Applied Physics, vol. 41 no. 11 (1970) 4505 ~ 4516.

[76] "*Initial Oxidation of Potassium at 77 and 295K*"; B. Kasemo and L. Walldén, Surface Science, vol. 75 (1978) L379 ~ 384.

[77] "*Nonadiabatic Surface Reaction: Mechanism of Electron Emission in the* $Cs+O_2$ *System*"; A. Böttcher, R. Imbeck, A. Morgante and G. Ertl, Physical Review Letters, vol. 65 no. 16 (1990) 2035 ~ 2037.

[78] "*Charge-Transfer Induced Particle Emission in Gas Surface Reactions*"; T. Greber, Surface Science Report, vol. 28 (1997) 1 ~ 64.

[79] "O^- *Escape During the Oxidation of Cesium*"; T. Greber, R. Grobecker, A. Morgante, A. Böttcher and G. Ertl, Physics Review Letters, vol. 70 no. 9 (1993) 1331 ~ 1334.

[80] "*A Model for Non-Adiabatic Coupling on Metals: the Sticking Problem*"; G. P. Brivio and T. B. Grimley, Surface Science, vol. 131 (1983) 475 ~ 490.

[81] "*Exoelectron Emission and Tribology*"; N. Ohmae, Hyoumenkagaku, vol. 9 (1988) 90 ~ 95.

[82] "*Triboemission of Charged Particles and Photons from Solid Surfaces During Frictional Damage*"; K. Nakayama, N. Suzuki and H. Hashimoto, Journal of Physics D: Applied Physics, vol. 25 (1992) 303 ~ 308.

[83] "*Triboemission of Charged Particles and Photons from Wearing Ceramic Surfaces in Various Gases*"; K. Nakayama and H. Hashimoto, Tribology Transaction, vol. 35 (1992) 643 ~ 650.

[84] "*Chemi-Emission of Electrons from Metal Surfaces in the Cutting Process due to Metal/Gas Interactions*"; K. Nakayama, J. A. Leiva and Y. Enomoto, Tribology International, vol. 28 no. 8 (1995) 507 ~ 516.

[85] "*Energy Distribution of Exoelectrons Emitted into Vacuum from Plastically Deformed, Oxide Covered Auminium at Low Temperatures*"; B. Sujak, A. Gieroszynski and E. K. Gieroszynska, Acta Physica Polanica A, vol. 46 (1974) 3 ~ 17.

[86] "*Triboemission*"; K. Nakayama, Journal of the Institute of Electrostatics Japan, vol. 15 no. 6 (1991) 421 ~425 [in Japanese].

[87] "*Fracto-Emission from Filled and Unfilled Polybutadiene*"; J. T. Dickinson and L. C. Jensen, Journal of Polymer Science Polymer Physics ed, vol. 23 (1985) 873 ~ 888.

[88] "*Fracto-Emission Accompanying Adhesive Failure between Rocket Propellent Constituents*"; J. T. Dickinson, L. C. Jensen, M. H. Miles and R. Yee, Journal of Applied Physics, vol. 62 (1987) 2965 ~ 2971.

[89] "*Fractoemission from Rocks*"; Y. Kawaguchi, Proceedings of 12th International Symposium on Exoelectron Emission and Applications, Polanica-Zdroj, (1997) 221 ~226.

[90] "*Emission of Electromagnetic Radiation Preceding the Ito Seismic Swarm of 1989*"; Y. Fujinawa and K. Takahashi, Nature, vol. 347 (1990) 376 ~ 378.

[91] "*Emission of Charged Particles from Indentation Fracture of Rock*"; Y. Enomoto and H. Hashimoto, Nature, vol. 346 (1990) 641 ~ 643.

[92] "*Electromagnetic Fault for Earthquake Lightning*"; M. Ikeya and S. Takaki, Japanese Journal of Applied Physics, vol. 35 (1996) L355 ~ 357.

[93] "*Exoelectron Emission: Possible Relation to Seismic Geo-Electromagnetic Activities as a Microscopic Aspect in Geotribology*"; Y. Enomoto, M. Akai, H. Hashimoto, S. Mori and Y. Asabe, Wear, vol. 168 (1993) 135 ~ 142.

Chapter 3

Field-Stimulated Exoemission from W Surfaces

3.1 Introduction

It has been recognized that exoemission relates to gas adsorption, oxidation, surface defects (for example dislocation or vacancy) and so on. Therefore, it has been considered that exoemission does not occur on the atomically flat and clean surfaces. Actually, it has been reported by several researchers that no exoemission was detected at a clean surface after an electron bombardment or abrasion in the UHV environment [1-4]. In contrast, it was reported that clean Al surfaces, scratched or ion-sputtered, liberated exoelectrons with illuminating the light of a proper energy (PSE) [5-8]. TSE due to a phase transition in age-hardened Al alloys was also discovered [9]. Therefore, the unified understanding of the exoelectrons from clean surfaces has not been obtained.

We have examined the emission properties of FSE from Al surface [10-14]. In the FSE experiments, the specimen is limited to be a sharp tip because of the necessity of applying the high electric field (~10^9 V/m) to the specimen surface. This limitation prevents FSE studies from applying to the well-characterized flat surfaces. However, FIM [15] and FEM [16] allow us to characterize the tip surface. These surface characterization techniques provide the information on the atomic arrangement of the topmost layer and the electronic structure near the Fermi level of the tip surface. By combining FIM and FEM with FSE studies, the FSE properties can be analyzed with relating surface defects and electronic states of the individual crystal planes with an atomic resolution in real space.

In this chapter, the emission property of FSE from W surfaces was studied with an atomic resolution using FIM and FEM. Even though the advantages of application of FIM/FEM to FSE study are clear, such studies have not been performed with Al tips, because of the difficulty to image Al tips with FIM/FEM. In contrast, W tips have widely been used to investigate dynamics or catalysis on the tip surfaces with FIM/FEM. This is the reason why the W tip was chosen as a sample in this study. In Sections 3.2 and 3.3, the principles of FEM and FIM are described in detail. In Section 3.4, the experimental apparatus and the procedures of sample preparation and of FSE measurement are explained. The experimental results on FSE from W surfaces are shown in Sections 3.5 and 3.6. The temperature and the applied voltage dependencies of FSE, surface reconstruction of W tip surface, the spatial distribution of FSE and the emission mechanism of FSE were also discussed.

3.2 Field Emission

3.2.1 Fowler-Nordheim Theory

The field emission, which has been discovered since the early 20th century [17], was theoretically established in 1920 by Fowler and Nordheim [18,19]. The Fowler-Nordheim theory (F-N theory) provides the theoretical description of electron emission from metal surfaces under the presence of high electric field.

The potential diagram of the interface between a metal surface and vacuum is shown in Figure 3-1. The potential energy of electrons, $V(x)$, as a function of the distance from the metal surface, x, is expressed by the equations (3-1) and (3-2).

$$x < 0 \qquad V(x) = -W_a \tag{3-1}$$

$$x > 0 \qquad V(x) = -eFx - \frac{e^2}{4x} \tag{3-2}$$

where $-W_a$, e and F represent the potential energy of the valence band bottom of the metal against vacuum level, the electric charge and the field strength, as shown in Figure 3-1. In the equation (3-2), terms of $-eFx$ and $-\frac{e^2}{4x}$ express the effect of the applied field and the image potential, respectively.

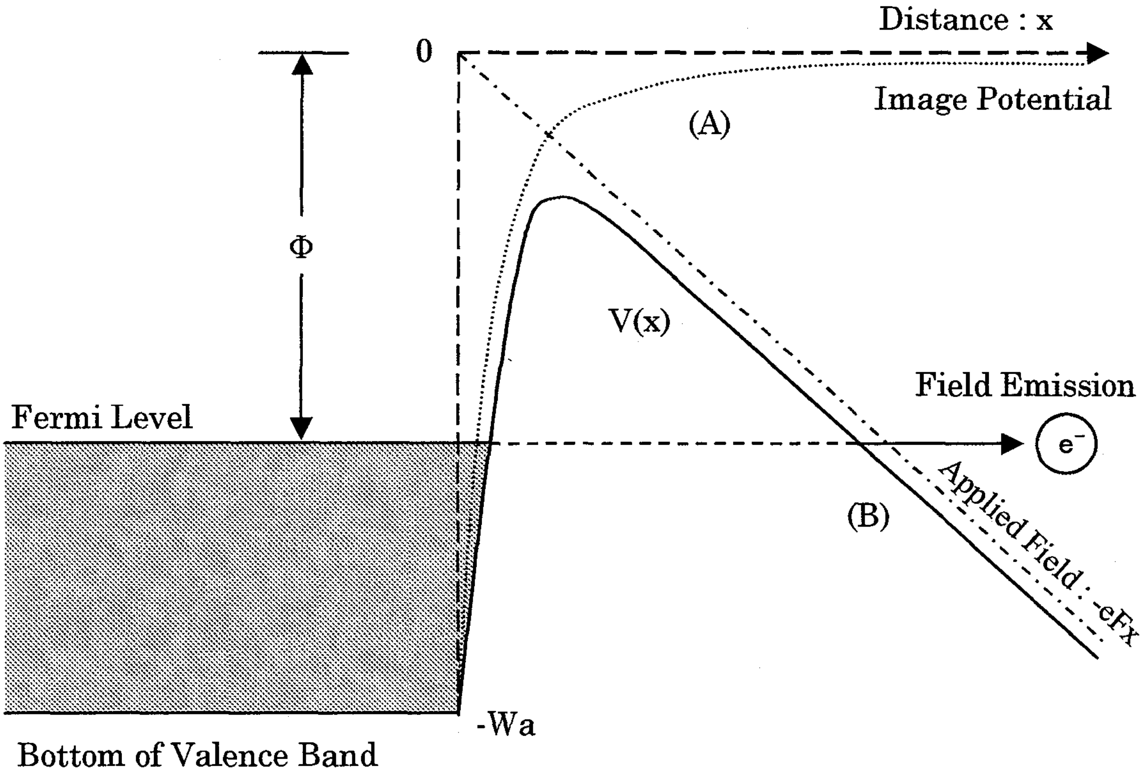

Figure 3-1 Potential diagram of the interface between a metal surface and vacuum under the presence of high electric field.

The total energy of electron, ε, with momentum, P_x, P_y, P_z and mass of m is expressed by the equation (3-3);

$$\varepsilon = \frac{P_x^2}{2m} + \frac{P_y^2}{2m} + \frac{P_z^2}{2m} + V(x) \qquad (3\text{-}3)$$

The number of electrons dn with energies from ε to $\varepsilon + d\varepsilon$ is based upon the Fermi statistics and expressed by the equation (3-4);

$$dn = \frac{2}{h^3} \frac{dP_x dP_y dP_z}{\exp\left(\frac{\varepsilon - \phi}{kT}\right) + 1} \qquad (3\text{-}4)$$

Moreover, the number of electrons with P_x going through a unit area perpendicular to x-axis per unit time is obtained as follows:

$$\begin{aligned} N(W)dW &= \int_{P_y=-\infty}^{\infty}\int_{P_z=-\infty}^{\infty}\frac{P_x}{m}\frac{2}{h^3}\frac{dP_x dP_y dP_z}{\exp\left(\frac{\varepsilon-\phi}{kT}\right)+1} \\ &= \frac{2}{h^3}dw\int_{\infty}^{\infty}\int_{-\infty}^{\infty}\frac{dP_y dP_z}{\exp\left(\frac{\varepsilon-\phi}{kT}\right)+1} \\ &= \frac{4\pi mkT}{h^3}\log\left[1+\exp\left(\frac{W-\phi}{kT}\right)\right]dW \end{aligned} \tag{3-5}$$

where W is represented by the equation (3-6);

$$W=\frac{P_x^2}{2m}+V(x) \tag{3-6}$$

The possibility that these electrons transmit the potential barrier (tunneling probability) $D(W)$, can be calculated by W. K. B. approximation as shown in the equation (3-7);

$$D(W)=\exp\left[-\int_{x_1}^{x_2}\sqrt{\frac{8m}{h^2}}\left(V(x)-W\right)dx\right] \tag{3-7}$$

where x_1 and x_2 $(x_1 < x_2)$ are the solutions of the equation $V(x)=\phi$ (ϕ:work function of the metal surface). Therefore, the number of electrons which transmit the potential barrier with energies from W to $W+dW$ and the emission current density are provided as the equations (3-8) and (3-9);

$$P(W)dW = D(W)N(W)dW \tag{3-8}$$

$$j=e\int_{W_a}^{\infty}P(W)dW \tag{3-9}$$

From the equations of (3-1) to (3-9), the emission current density at 0 K can be calculated as follows:

$$j_{T=0K}=\frac{1.54\times10^{-6}F^2}{\phi\cdot f_1}\exp\left(-6.83\times10^{7}\frac{\phi^{3/2}}{F}f_2\right)\quad\left(A/cm^2\right) \tag{3-10}$$

where F and ϕ are the field strength (V/cm) and work function (eV), and f_1 and f_2 are the correlation functions of F and ϕ. On applying a few kV to the tip surface, f_1 and f_2 are taken to be 0.8 ~ 0.9 and 1.02 ~ 1.03, respectively. When the temperature is not at 0 K, the equation (3-11) represents the field emission current density.

$$j_T = j_{T=0K}\left[1+\frac{1}{6}\times\left\{2.77\times10^4\frac{\phi^{1/2}}{F}\times T\cdot f_1\right\}^2+\cdots\right] \qquad (3\text{-}11)$$

However, when the electric field of 4 x 10^7 (V/cm) is applied to the W surface (work function of 4.5 eV), the field emission current densities at 300 K and 1000 K are 1.03 and 1.5 times higher than the current density at 0 K. Therefore, the use of equation (3-10) at room temperature provides good approximation.

In order to provide field emission, it is necessary to apply an electric field in the order of 10^{-9} V/m to the sample surface. Therefore, a sharp tip has been used as a sample. The strength of the electric field, *F*, applied to the tip surface is expressed by the following equation;

$$F=\frac{V}{\kappa R} \qquad (3\text{-}12)$$

where V, R and κ represent the applied voltage to the tip, the radius of curvature of the tip and the constant ($\kappa = 4 \sim 8$), respectively. Typical R of the tip used in this study is 10 ~ 100 nm. While the work function ϕ remains constant, the graph of $\ln(i/V^2)$ versus $1/V$, which is called F-N plot, gives a straight line according to the equations (3-10) and (3-12). One can calculate ϕ from the slope of the straight line, *S*(*F*), as shown in the equation (3-13),

$$S(F) = -6.83\kappa R\phi^{3/2} \qquad (3\text{-}13).$$

3.2.2 Field Emission Microscopy

When a high electric field is applied to the solid surface, electron emission occurs through the tunneling process. Field emission microscope (FEM) is a microscope which provides the spatial distribution of work function over the tip surface with a high resolution [20]. In the FEM observation, the high electric field of 2 ~ 5 x 10^9 V/m is usually applied to the solid surface. In order to apply such a high electric field, the sample is finished into a sharp tip. The emission current density of field emission reaches as high as 10^6 to 10^7 A/m^2. Electrons emitted from the metal surface are accelerated along with the line of electric force, because mass of electron is small. The electrons collide with the phosphor screen and then the field emission image, which reflects the electronic structure over the surface, can be observed on the screen. From Figure 3-2, the magnification of this image, M, is represented by the equation (3-14),

$$M = \frac{d}{\beta R} \tag{3-14}$$

where β is a constant depending on the tip/screen configuration and usually to be 1.3 ~ 2.0. When the radius of curvature of a tip (R) and the distance between tip and screen (d) are 50 nm and 10 cm, the magnification M is calculated to be one million.

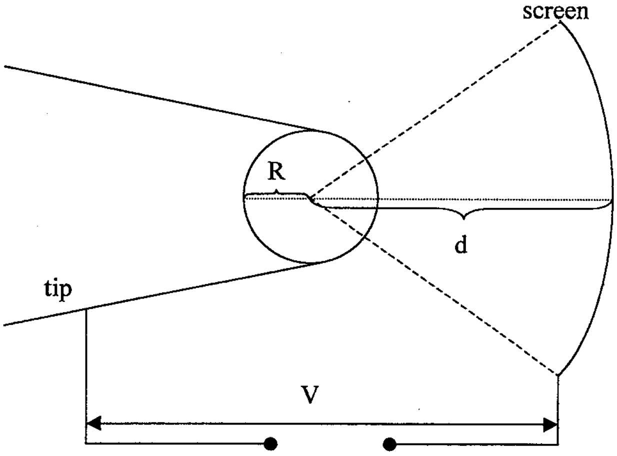

Figure 3-2 Magnification of FEM image.

The resolution of FEM, δ, is defined as a minimum distance $(\Delta y_t)_{\min}$ between two points on the tip surface can be distinguished on the FEM image $(\Delta y_s)_{\min}$ as follows:

$$\delta \equiv (\Delta y_t)_{\min} = (\Delta y_s)_{\min} \times M^{-1} \tag{3-15}$$

δ depends on the following factors;

1) y- and z-components of the initial velocity of electrons (Δy_{sv})
2) diffraction of electrons (Δy_{sd})

Δy_{sv} can be calculated from a momentum distribution on y-z plane by the equation (3-16).

$$\Delta y_{sv} = 2 v_p \tau \tag{3-16}$$

where $(v_p)^2$ and τ represent the mean square velocity of electrons on y-z plane and the flight time of electrons. The $(v_p)^2$ and τ are expressed as the equations (3-17) and (3-18), respectively.

$$(v_p)^2 = \frac{h}{2\pi}\frac{eF}{2m}(2m\phi)^{-2} \tag{3-17}$$

$$\tau = R\left(\frac{m}{2eV}\right)^{-2} \tag{3-18}$$

where, h: Planck's constant, e: elementary electric charge, F: field strength, ϕ: work function, m: mass of electron, V: applied voltage, respectively. In contrast, Δy_{sd} is led by Heisenberg's uncertainty principle, and is expressed in equation,

$$\Delta y_{sd} = \frac{h}{\pi}(2m\Delta y_t)^{-1}\tau \tag{3-19}$$

From these equations, the broadening of a bright spot on FEM image (Δy_s) is given as the equation (3-20).

$$\begin{aligned}(\Delta y_s)^2 &= (\Delta y_{sm})^2 + (\Delta y_{sv})^2 + (\Delta y_{sd})^2 \\ &= M^2(\Delta y_t)^2 + 4(v_p)^2\tau^2 + \left(\frac{h}{2\pi}\right)^2\frac{1}{m^2}(\Delta y_t)^{-2}\tau^2\end{aligned} \tag{3-20}$$

where Δy_{sm} indicates the contribution of the magnification to resolution. $(y_s)_{\min}$ can be obtained by calculating the lower limit of $(\Delta y_s)^2$ as a function of y_t,

$$(y_s)^2_{\min} = \frac{h}{\pi}\tau\frac{M}{m} + 4(v_p)^2\tau^2 \tag{3-21}$$

Using the equation (3-21), the resolution of FEM is expressed by the following equation;

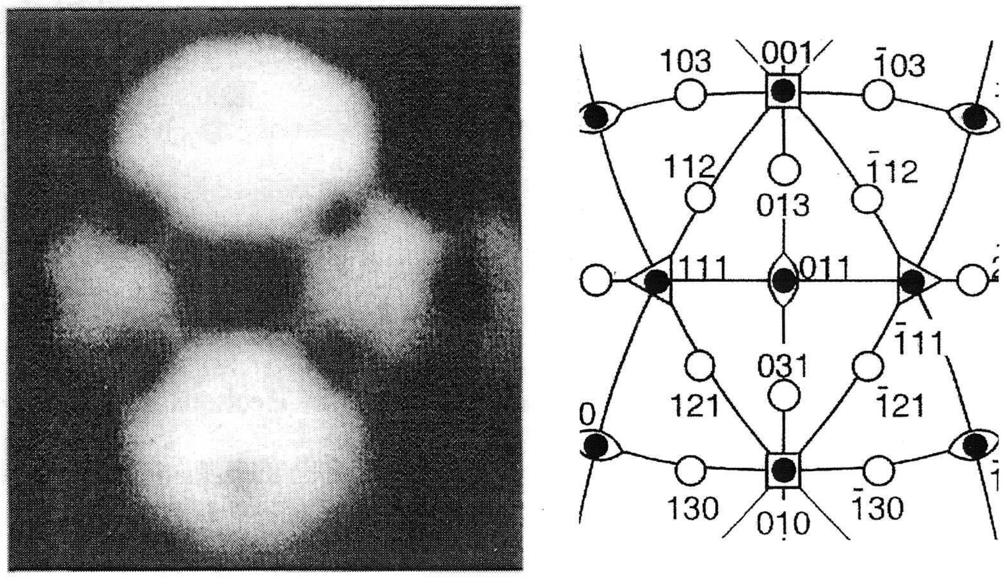

(a) FEM image (b) Stereographic projection

Figure 3-3 FEM image of the W [011] tip cleaned by flashing method at 2300 K, and stereographic projection of body-centered cubic (b.c.c) lattice with [011] orientation. [21]

$$\begin{aligned}\delta = \frac{(\Delta y_s)_{\min}}{M} &= \left\{ \frac{h\tau}{\pi m M} + \frac{4(v_p)^2\tau^2}{M^2} \right\}^{-1/2} \\ &= \sqrt{\frac{h\beta^2 r}{2\pi\kappa\sqrt{2m\phi}} \left\{ 1 + \frac{2\kappa}{\beta}\sqrt{\frac{\phi}{eV}} \right\}}\end{aligned} \tag{3-22}$$

According to this equation, the resolution of FEM can be estimated about 20 Å under the FEM experimental conditions.

Figure 3-3 (a) illustrates the FEM image of the W [110] tip cleaned by the annealing treatment at 2300 K [21]. The orientation of crystal plane can be determined by comparing the stereographic projection of body-centered cubic shown in Figure 3-3 (b). It is clearly observed that the FEM image reflects the distribution of work functions (Table 3-1) over the W tip surface.

Table 3-1 Work functions on the individual crystal planes

Crystal plane	Work function (eV)
Whole area	4.5
(110)	5.85
(111)	4.41
(112)	4.85
(100)	4.82
(310)	4.31
(210)	4.34
(211)	4.65~4.88

3.3 Field Ion Microscopy

3.3.1 Field Ionization

FIM uses a sharp tip as well as FEM, however, polarity of applying voltage is opposite to that of FEM. While a positive voltage is applied to the tip surface, the strength of the applied field to the surface is given by the equation (3-12), but the direction is opposite as shown in Figure 3-4. When a gas atom approaches to the tip surface, the positive electric field decreases the energy of an electron at ground state in the gas atom by eFx as shown in Figure 3-4. At the distance $x = x_c$, where eFx_c becomes equal to $I - \phi$ (I and ϕ are the ionization potential of a gas atom and the work function of a metal), the energy level of electron in the gas atom becomes equal to that of Fermi level of a metal surface. In the case that the potential barrier between the gas atom and metal surface is thin enough to transmit, the electron in the gas atom is transferred to the metal surface by the tunneling effect, and then the gas atom is ionized positively. This 'field ionization' takes place without the energy transfer, which is quite different from the other ionization processes such as photoionization or electron bombardment.

In the field ionization, the ionization probability (the tunneling probability of electron in the gas atom) becomes high when Heisenberg's uncertainty principle satisfies the following equation (3-23),

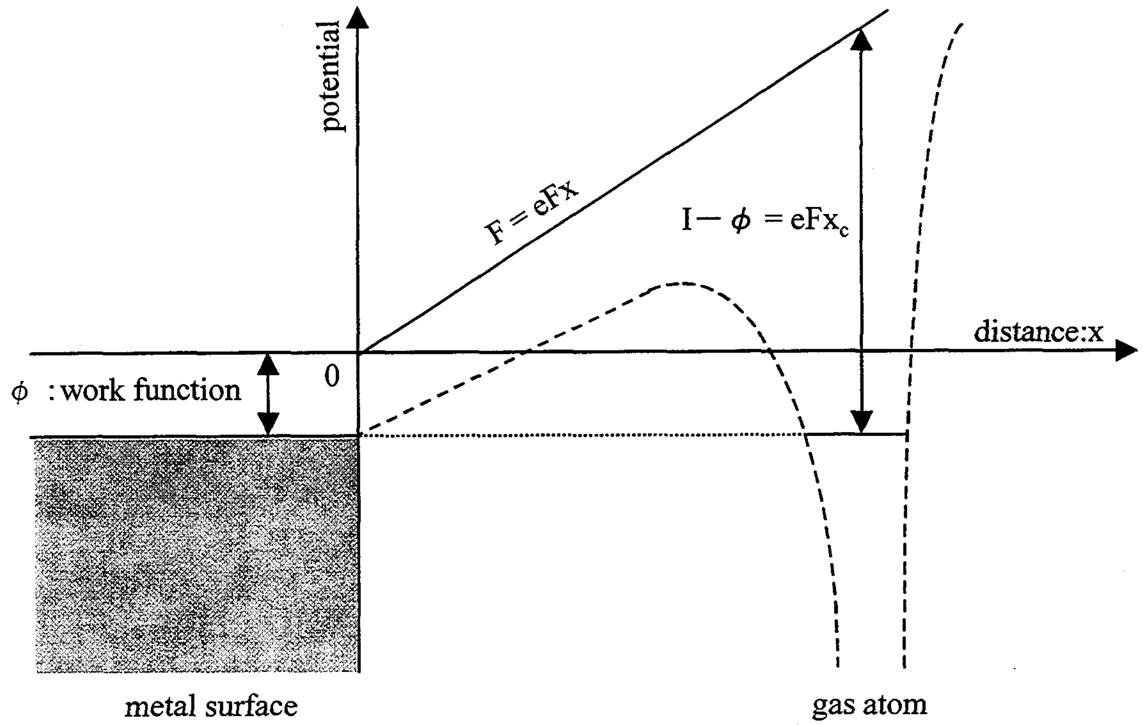

Figure 3-4 Field ionization process accompanied by the electron transfer through the tunneling effect.

$$\Delta x \cdot (2mE)^{1/2} \approx h \qquad (3\text{-}23)$$

where Δx and E represent uncertainty of the potential barrier position and the barrier height. When the distance between the metal surface and the gas atom is shorter than x_c, the potential barrier becomes thinner. However, electron in the gas atom can not be transferred to the metal, because the electronic state in the metal is occupied. Therefore, x_c is defined as a nearest distance of tunneling effect. From the equation (3-23), x_c is obtained as follows;

$$x_c = \frac{I - \phi}{eF} \qquad (3\text{-}24).$$

3.3.2 Field Evaporation

The applied electric field to the surface may also cause an ionization of a surface atom or an adsorbed atom. These ionized atoms are positively charged, so that the ions are removed from the surface since the positive voltage is applied to the surface. This desorption phenomenon is so-called "field evaporation" or "field desorption". The field evaporation is explained by the potential diagram shown in Figure 3-5. The horizontal axes indicate the distance between an adatom (*A-atom*) and substrate atom (*M-atom*), that is, zero in the horizontal axes mean these two atoms touch together. When both of *A*- and *M-atoms* are electrically neutral, the potential curves for these atoms are represented by the curve $M + A$. The adatom is stable at the position of r_0, and then the depth of potential, Λ, corresponds to the binding energy of these atoms. On the other hand, the curve $M^- + A^+$ represents the potential curve between M^- and A^+ ions. The $M^- + A^+$ curve is higher by $I_n - n\phi$ than $M + A$, where I_n and ϕ are the energy of ionization and work function of M. A high electric field, F, applied to the surface influences only for the potential $M^- + A^+$, and lowers energy by $neFx$ at the position with the distance of x. The dotted line $(M^- + A^+)_F$ indicates the potential curve between M^- and A^+ ions under such a high electric field. If F is large enough, both curves of $M + A$ and $(M^- + A^+)_F$ cross at the position $(r_0, -\Lambda)$. In the case of $x > r_0$, the potential curve $(M^- + A^+)_F$ becomes lower

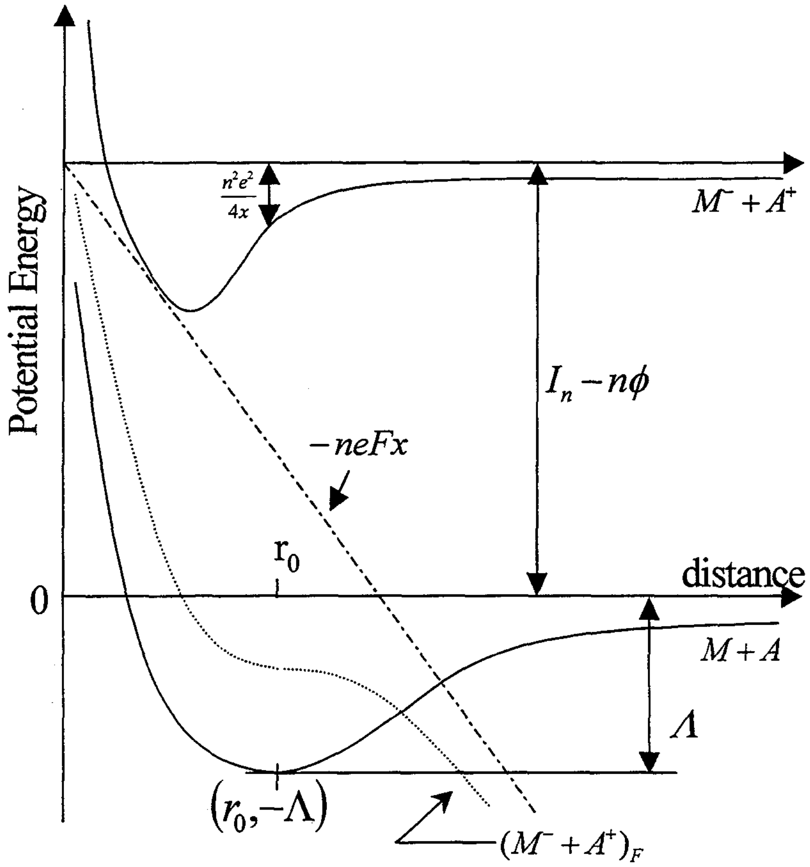

Figure 3-5 Potential diagram between *M* and *A* atoms under the presence of a positive high electric field.

than $M + A$. This fact means that ion is more stable than atom under the presence of a high electric field. When $(M^- + A^+)_F$ and $M + A$ curves cross at $x < r_0$, surface atom is ionized, feel the repulsive force from the surface, and remove from the surface. Since the potential curve $(M^- + A^+)_F$ includes the decrease of $\frac{n^2e^2}{4\pi\varepsilon_0(4x)}$ due to image potential, the condition that the $(M^- + A^+)_F$ curve passes the point $(r_0, -\Lambda)$ is

$$ner_0F + \frac{n^2e^2}{4\pi\varepsilon_0 \cdot 4r_0} = \Lambda + I_n - n\phi \qquad (3\text{-}25).$$

From this equation, the field strength required for field evaporation is expressed by the following equation;

$$F_n = \frac{\Lambda + I_n - n\phi}{ner_0} - \frac{0.36n^2}{r_0^2} \qquad (3\text{-}26).$$

Table 3-2 summarizes the electric field strength of the field evaporation calculated using the equation (3-26) and by the experiments [15].

By applying this technique, a contamination layer on the tip surface can be removed without a damage of the substrate region. Hence, field evaporation is used as a surface cleaning technique, and is the essential technique of the surface analysis of the outermost layer in atom probe.

Table 3-2 Field strength required for field evaporation on a variety of metals. Calculated values are obtained from the equation (3-26).

Metal	Calculated value (V/nm)	Experimental value (V/nm)
W	55.0	57.0
Mo	45.2	45.0
Fe	31.8	36.0
Ir	50.3	50.0
Pt	44.2	47.5
Au	48.5	35.0
Cu	43.0	30.0
Re	43.4	48.0
Si	31.7	30.0

3.3.3 FIM image

In FIM observation, He or Ne is introduced as an imaging gas into the FIM observation chamber. When a positive high electric field is applied to the tip surface, the He gas atom approached to the surface is field-ionized, and the ionized atom flies toward phosphor screen faced to the tip as shown in Figure 3-6. However, the field ionization probability shows the spatial distribution over the tip surface. Since the strength of the applied field is inversely proportional to the tip radius as indicated by the equation (3-12), the applied field concentrates at the kink-sites and ledge-sites as shown in Figure 3-7. He atoms are ionized at these sites and the bright spots at the screen reflect the distribution of these sites. Figure 3-8 (a) shows the FIM image of W [110] tip surface. Figure 3-8 (b) is the computer

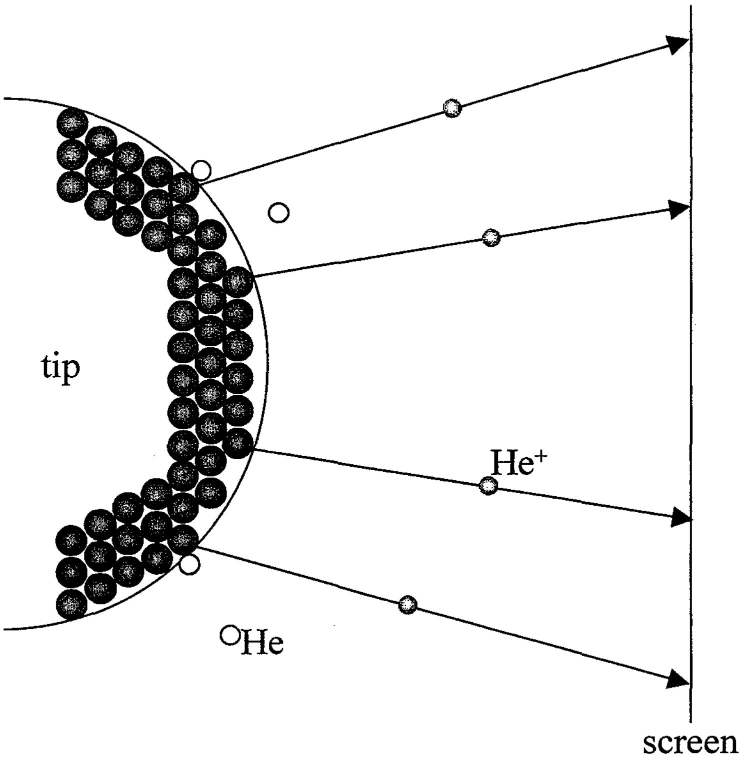

Figure 3-6 Principle of imaging in FIM. He is used as a imaging gas.

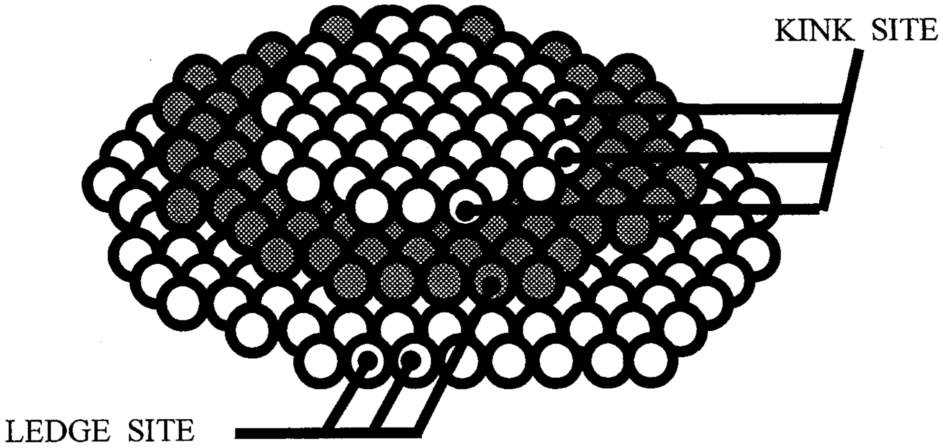

Figure 3-7 Atomic arrangement model of the tip surface.

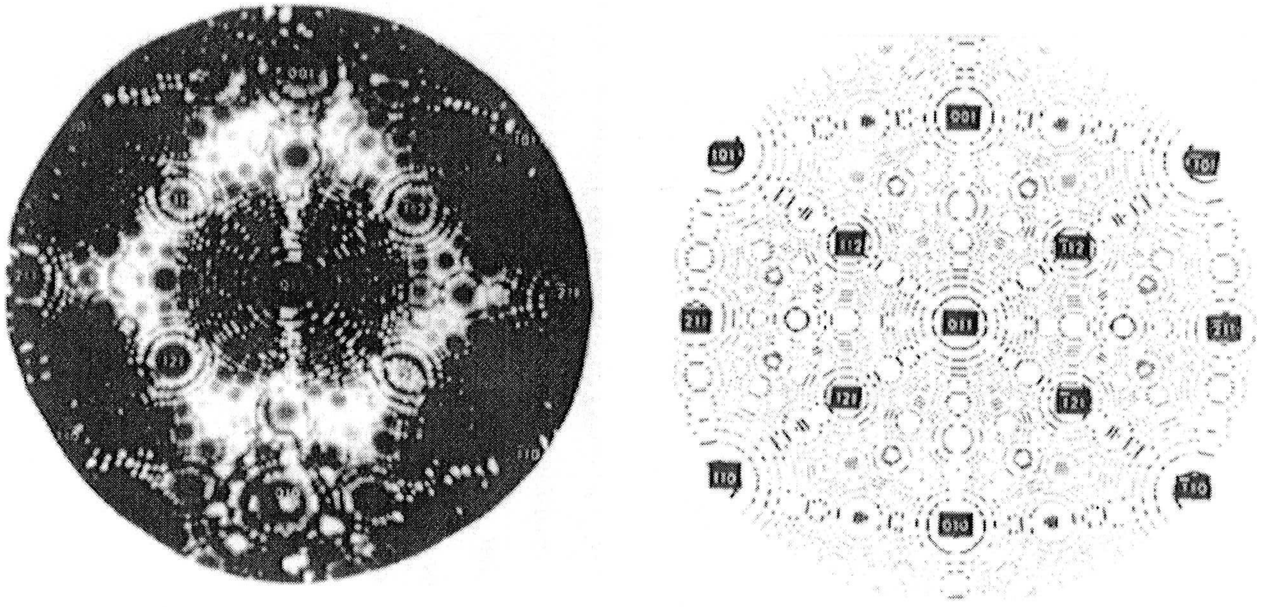

(a) FIM image

(b) computer simulation

Figure 3-8 FIM image of the W [011] tip surface (a) and the computer simulated FIM image of the ideal [011] tip surface (b).

simulation of the kink- and ledge-sites over the W [110] tip surface. The positions and symmetry of each crystal plane and atomic arrangement in the FIM image shows good agreement with the computer-simulated results. Moreover, since it is known that FIM image of W corresponds well to the stereographic projection of body-centered cubic with [110] orientation as shown in Figure 3-3 (b), the plane index can also be analyzed by the computer simulation.

Field ionized gas atoms have very small energy components normal to line of electric force because gas atoms loose their thermal energy by the collision with the tip surface where cooled by a He refrigerator. Therefore, the resolution of FIM becomes an atomic order and higher than that of FEM. The following equation expresses the spatial resolution [15];

$$\delta = \rho + \left\{ 4\left(\frac{\beta^2 r h^2}{2\kappa e m F} \right)^{1/2} + 16\left(\frac{\beta^2 r k T}{\kappa e F} \right) \right\}^{1/2} \qquad (3\text{-}27)$$

where ρ, m, k and T are the radius of a gas atom, the mass of a gas atom, Boltzmann's constant, and the tip temperature, respectively. From this equation, it is clear that the resolution depends greatly upon the tip temperature. When the tip temperature is 20 K, FIM can distinguish each atom on {112} crystal plane of W tip with the radius of 50 nm.

From a FIM image with an atomic resolution, the radius of curvature of a tip, R, can be obtained by counting the number of net plane rings between (hkl) and (h'k'l') crystal planes with the angle of θ. The principle of this method is shown in Figure 3-9. From this figure, R can be calculated by the following equation;

$$R = \frac{nS}{1-\cos\theta} \qquad (3\text{-}28).$$

This is the most accurate method to measure the radius of curvature of the FIM tips.

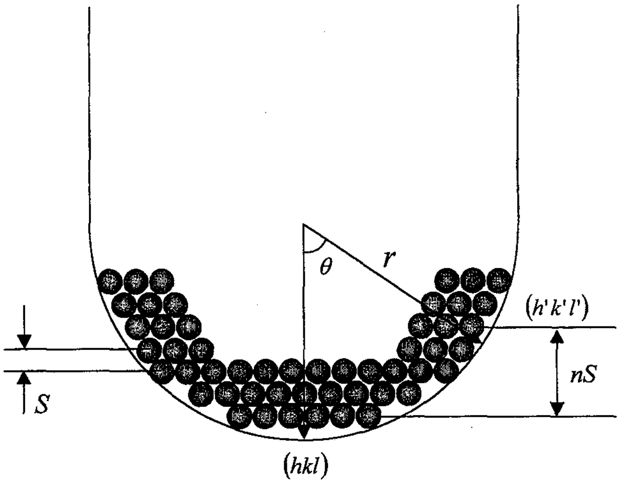

Figure 3-9 Principle of the ring counting method to determine the radius of curvature of a tip.

3.4 Experiments

3.4.1 Sample Preparation

The samples used in this study were finished into a sharp tip in order to apply a high electric field to the sample surface. In this study, the tip material was a high purity (99.95%) W-wire with a diameter of 60 μm. The W tip was spot-welded on a W-loop with a diameter of 200 μm as illustrated in Figure 3-10. One end of the tip was electropolished. Figure 3-11 and Table 3-3 show the apparatus and condition for electropolishing. The scanning electron microscope (SEM) image of the W tip thus prepared was demonstrated in Figure 3-12. Typical radius of curvature of a tip was several tens of nanometers. After electropolishing, the W tip was rinsed in ethyl alcohol and introduced into a vacuum chamber immediately.

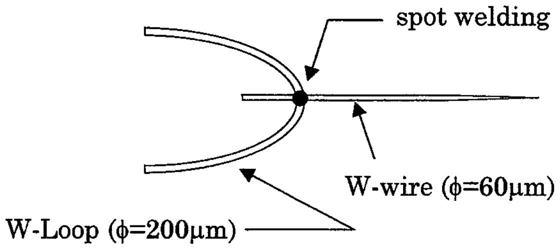

Figure 3-10 The configuration of a W tip used in this study.

Table 3-3 The condition for electropolishing the W tip.

Electrolyte	3% KOH
Voltage	DC 0~5V
temperature	Room Temp.

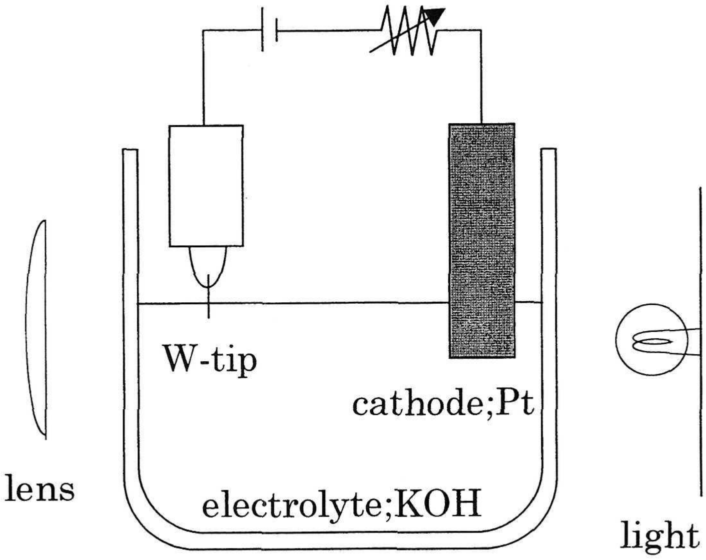

Figure 3-11 The setup for the electropolishing of the W tip

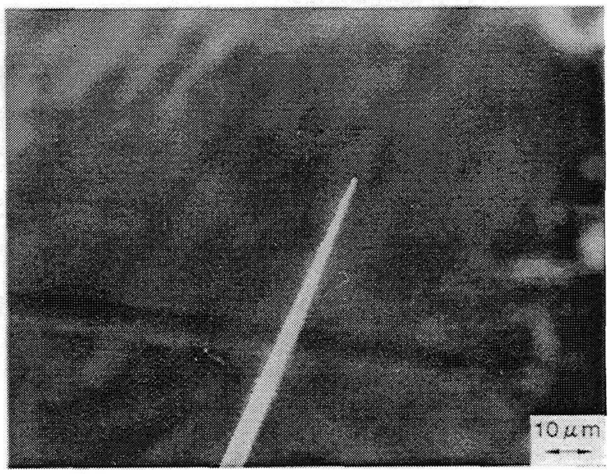

Figure 3-12 SEM image of the electropolished W tip.

3.4.2 Experimental Apparatus

The schematics of the experimental apparatus used in this study is illustrated in Figure 3-13. This apparatus was basically a conventional FIM facility. It consisted of two vacuum chambers, *i.e.*, the specimen preparation chamber and the FIM observation chamber. The specimen preparation chamber was evacuated by a 150 l/s turbo-molecular pump (TMP) and the vacuum pressure reached 2 x 10^{-6} Pa. Also, water vapor could be introduced into this chamber through valuable leak valve (VLV). While the FIM observation chamber, in which all FIM observations were carried out, was evacuated by a 300 l/s TMP, titanium getter pump, sputter ion pump and cryo pump. The ultimate pressure of this chamber attains lower than 1.6 x 10^{-8} Pa. In this FIM chamber, the pressure was measured by a cold cathode gauge instead of a nude ionization gauge in order to avoid uncertain effect of the desorption of gas from the vacuum gauge. Also, He, as an imaging gas of FIM, hydrogen and oxygen gases can be introduced into the chamber through VLVs. These two chambers

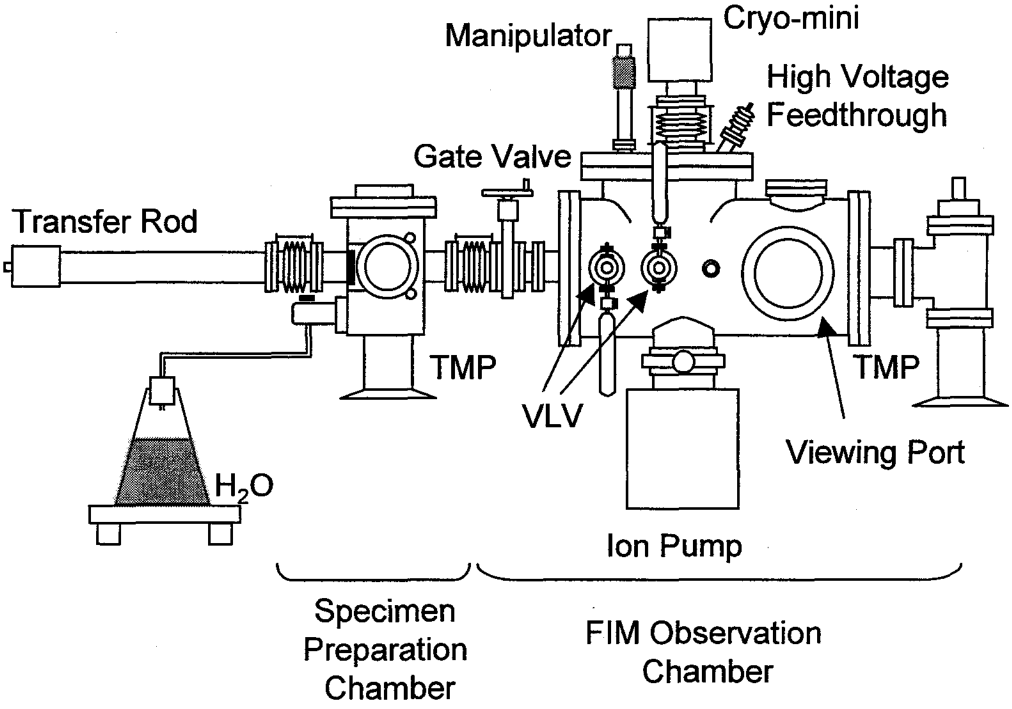

Figure 3-13 Schematics of the experimental apparatus.

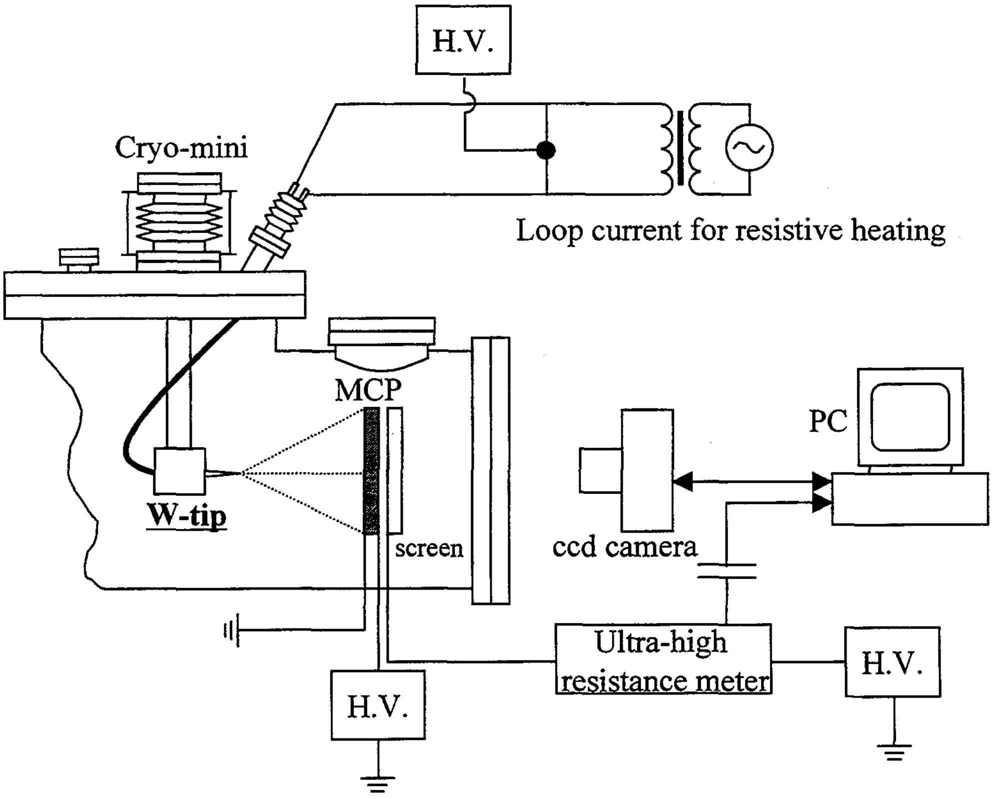

Figure 3-14 Schematic drawings of the measurement system of FIM/FEM images and emission current.

were separated by a gate valve, and the sample could be transferred using a vacuum transfer rod without breaking ultra high vacuum (UHV).

The systems to observe FIM/FEM image and to measure the emission current are illustrated in Figure 3-14. Ions or electrons emitted from the tip surface was amplified by a micro channel plate (MCP) and collected by a conductive phosphor screen. FIM or FEM images projected to the screen were captured by an electrically-cooled CCD camera and stored in PC. Also, the output current from the screen was recorded by PC with an ultrahigh resistance meter as an interface. The tip temperature was cooled down to 50 K by the closed-loop He refrigerating system and the tip temperature could be adjustable ranging from 50 to 1000 K by a resistive heating of W-loop with AC current. Before the FSE experiment, the relationship between heating current and tip temperature was measured using a type C thermocouple (W5%Re-W26%Re). The reference curve is shown in Figure 3-15.

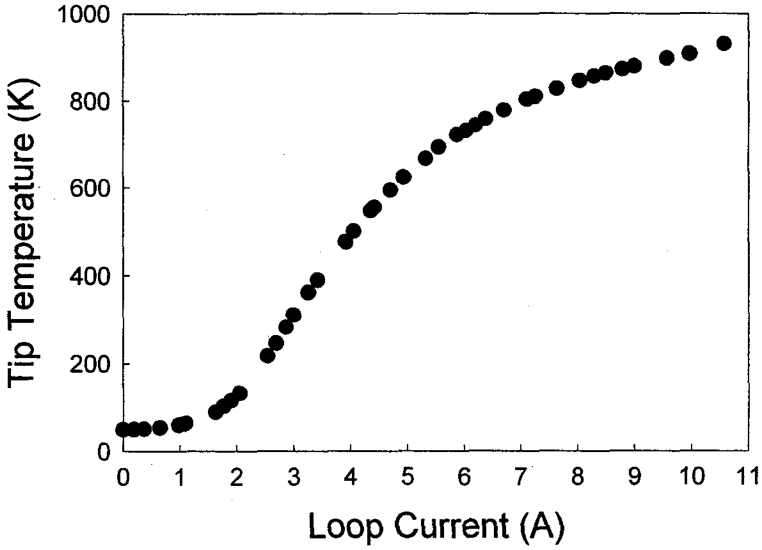

Figure 3-15 The relationship between the loop current for resistive heating and the tip temperature measured by a type C thermocouple.

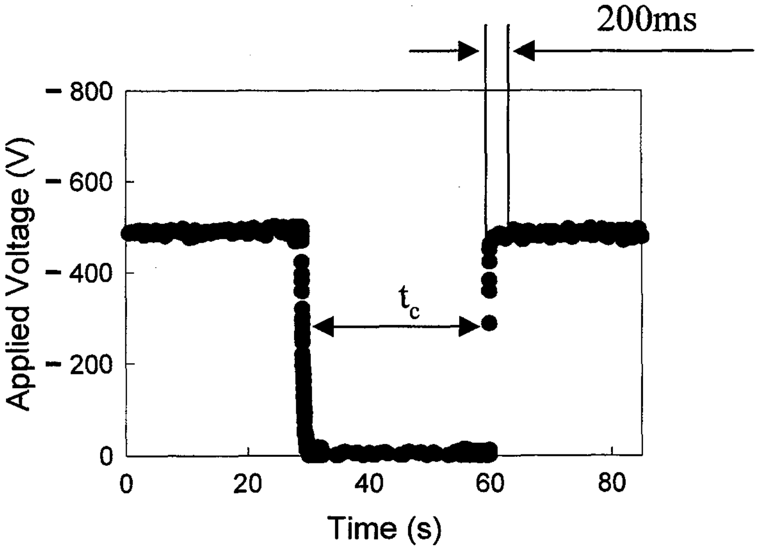

Figure 3-16 Voltage history in each run of the FSE experiment. No overshoot of the applied voltage is obvious.

3.4.3 FSE Measurement

In this study, a temporal enhancement of emission current due to the storage effect of exoelectrons, which was one of the FSE properties as described in Chapter 2, was used as a FSE signal. The measurement of FSE was performed by the following sequence;

1) A negative tip voltage was increased gradually until the field emission current reached 3 x 10^{-13} A;
2) The tip voltage was kept constant for 30 s and stability of field emission was confirmed;
3) The tip voltage was reduced to zero;
4) After the voltage interruption (t_c) of 30 s, the same tip voltage was reapplied.

The voltage history during this procedure is shown in Figure 3-16. As is shown in Figure 3-16, it was confirmed that the reapplied voltage was restored within 200 ms and no overshoot was observed.

3.5 FSE from an Ideal W Surface

Although there have been reported some investigations on exoemission from clean surfaces [1-4], the atomic arrangement of the surfaces was not characterized in these studies. Therefore, such a surface is not an ideal surface. In this study, whether or not FSE occurs at the ideal W surface (which means a well-ordered clean surface) was investigated. The measurements of FSE were performed in the temperatures between 50 and 400 K. Since it was reported that the atomic arrangement over the W tip surface was reconstructed due to surface diffusion at higher than 500 K [22], the maximum temperature on the measurements was determined to be 400 K. Before the experiment, the W tip surface was evaluated sufficiently by FIM and FEM. The W tip in the UHV chamber was cooled down to 50 K after the degas treatment at 800 ~ 900 K for several hours. Then, the tip was cleaned by field evaporation under the FIM observation. Figure 3-17 shows the FIM image of the W tip surface field-evaporated at 9.9 kV (field evaporation voltage: FEV). The He pressure was 1.3 x 10^{-4} Pa and the applied voltage during the FIM imaging was 8.0 kV (best image

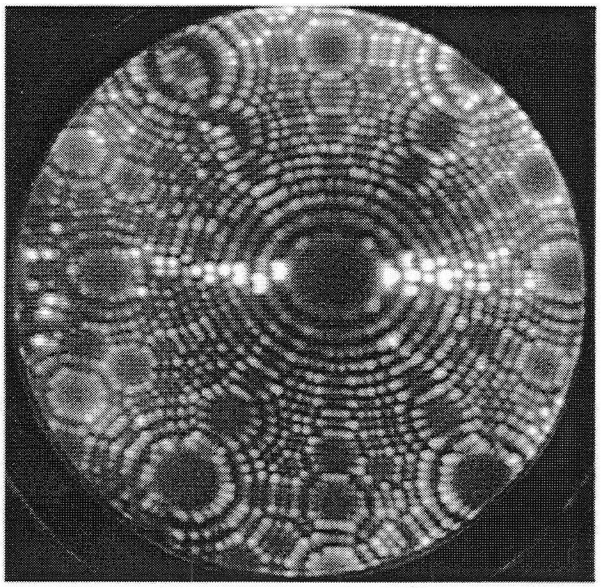

Figure 3-17 FIM image of an ideal W tip surface (FEV = 9.9 kV, BIV = 8.0 kV)

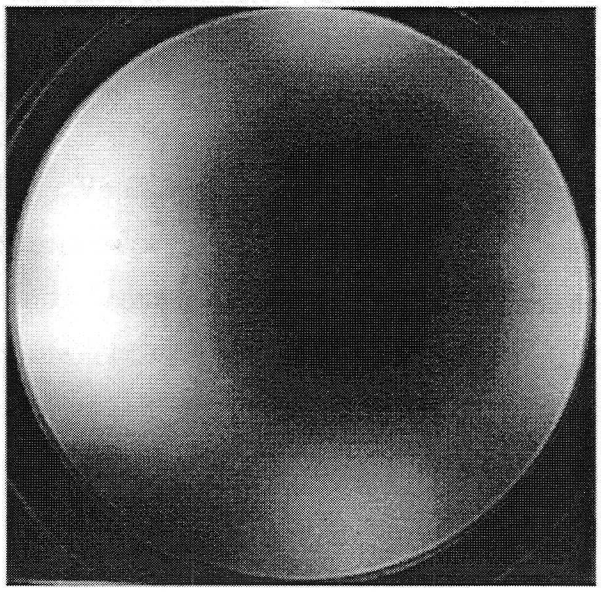

Figure 3-18 Corresponding FEM image of an ideal W surface (EV = -630V) with Figure 3-18. Dark area at the center of the screen is (011) plane

voltage: BIV). Few surface defects, for example vacancies, dislocations or adsorbates, were observed in the FIM image, and the net plane rings in the image agree well with those in computer simulation of the ideal surface of W (Figure 3-8 (b)). It was, therefore, confirmed from the FIM image that the W tip surface obtained after the field evaporation was clean and an atomic arrangement was also well-ordered. After obtaining an ideal W tip surface, He gas was evacuated under the application of FEV to the tip in order to avoid contamination on the surface. The pressure of the FIM observation chamber was restored lower than 1.6 x 10^{-8} Pa, and then FEM observation was performed at 50 K. Figure 3-18 indicates the FEM image of a clean W tip surface. It has been recognized that, when W [110] tip surface is clean, an FEM image with a two-fold symmetry is observed by FEM [15,21]. Since the FEM image of the W tip shown in Figure 3-18 has a two-fold symmetry, it was confirmed that the tip surface was kept clean during the FEM observation. In order to perform further evaluation of the W tip surface cleaned by the field evaporation, the work function over the tip surface was also estimated by the F-N plot described in Section 3.2.1. According to the equation (3-13), one can obtain the work function from the radius of curvature of the tip apex, *R*, and the slope of a straight line in the graph of F-N plot, $S(F)$. The mean value of *R* and $S(F)$ were obtainable from the number of net plane rings in the FIM image indicated by the equation (3-28) and from the F-N plot shown in Figure 3-19, respectively. Using $R = 25.8\ nm$ and $S(F) = -8.50 \times 10^3$, thus obtained, the mean work function over the W tip surface after the field evaporation was calculated to be 4.53 eV. This is in good agreement of the mean work function of a clean polycrystalline W surface reported previously [23]. From these results, it was concluded that the field-evaporated W tip surface was well-ordered, and the cleanliness of the tip was maintained during the FEM measurement.

The FSE properties from the ideal W tip surface were studied at 50 K. The measurements of emission properties from the ideal surface were conducted with the interruption period of the applied voltage, t_c, of 5 to 60 s. The results are shown in Figures 3-20. The enhancement of emission current due to the storage effect just after the voltage interruption was not observed. In the previous FSE study with Al tips, the emission property of FSE indicated a temperature dependence [13]. Therefore, the FSE properties from the W tip, whose surface was cleaned at 50 K, were also examined at t_c = 30 s in the

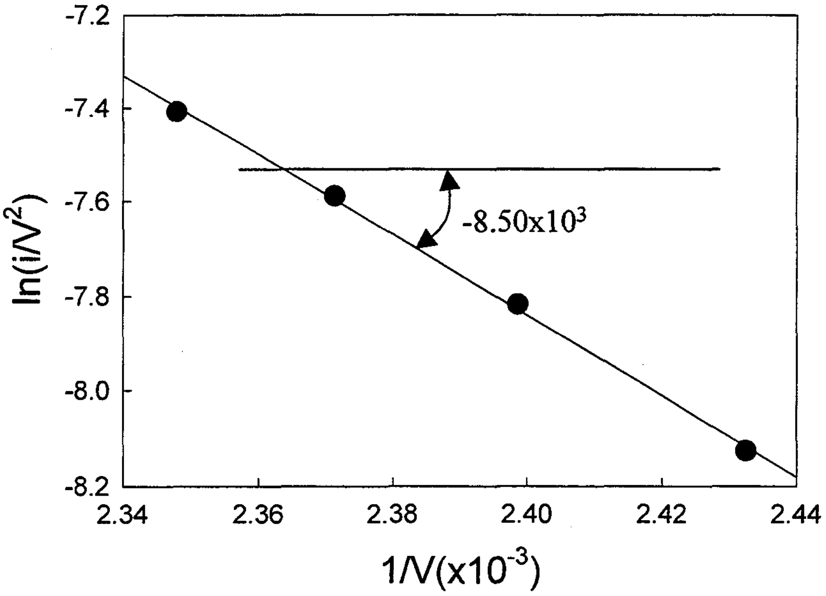

Figure 3-19 Typical F-N plot of a clean W tip measured at 50 K.

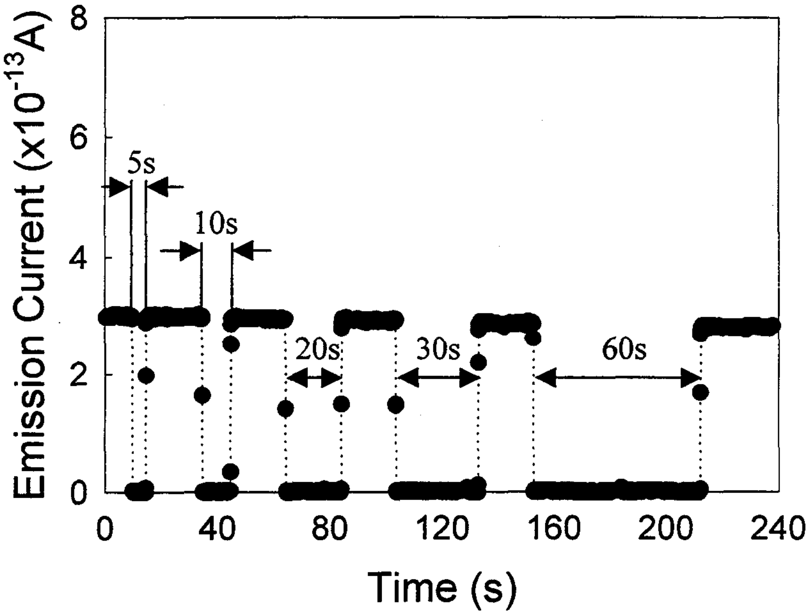

Figure 3-20 The measurement of FSE from an ideal W surface at t_c = 5 ~ 60 s.

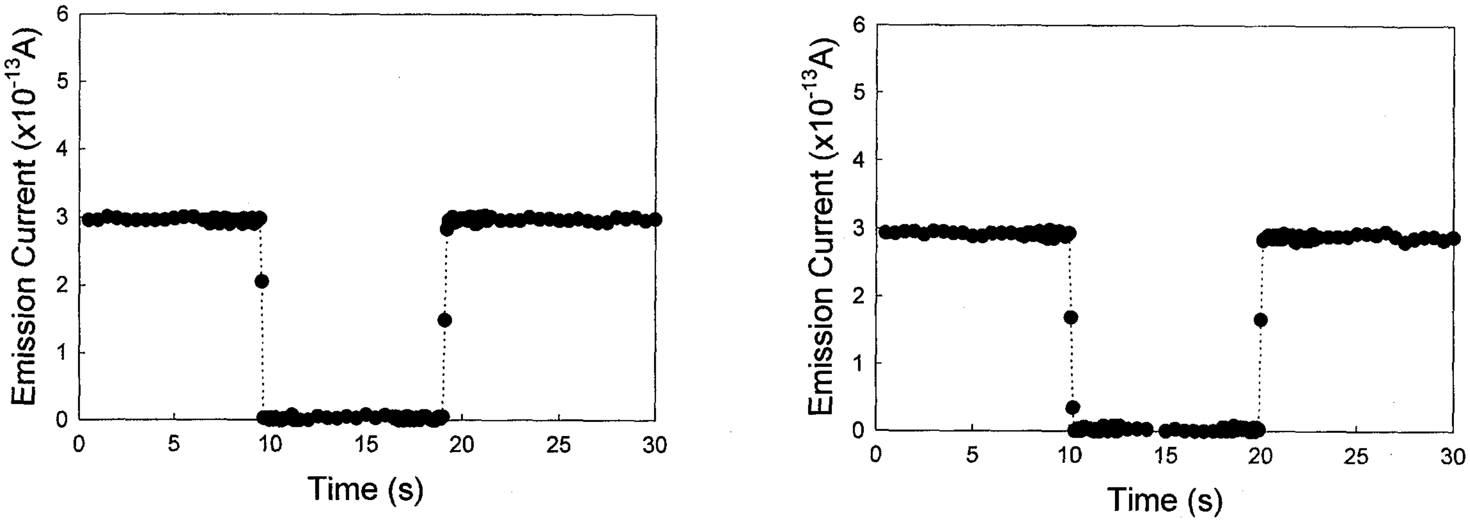

(a) 100 K

(b) 200 K

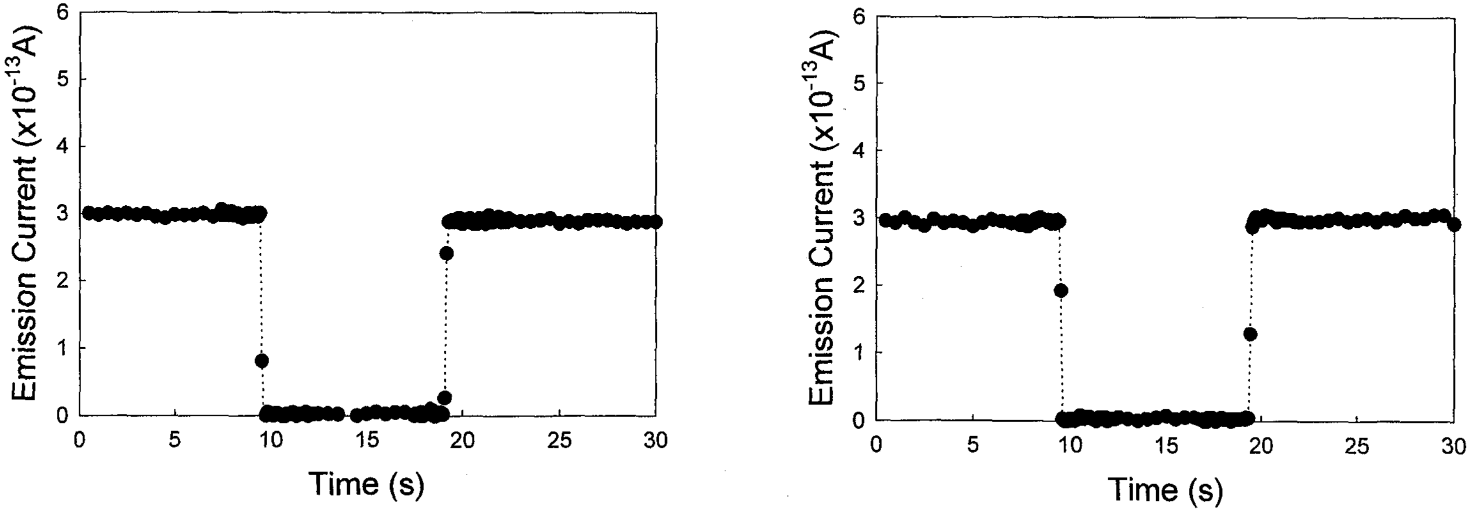

(c) 300 K

(d) 400 K

Figure 3-21 Emission properties from field-evaporated W tip measured at 100, 200, 300 and 400 K.

temperatures up to 400 K. Figures 3-21 (a) ~ (d) show the results of the experiments at 100, 200, 300 and 400 K, respectively. It is clear from these figures that no FSE signal was not detected in this temperature range. This result is consistent with the previous experimental result measured at 185 K reported in Ref. [24]. From these results, it was concluded that FSE does not take place at ideal (clean and well-ordered) W tip surfaces.

3.6 FSE from the Annealed W Surfaces

3.6.1 FSE from the W Surfaces Annealed at 800 K

The surface of a tip can be characterized by FIM and FEM with an atomic resolution as demonstrated in the previous section. Although this is one of the characteristic features in FSE studies, FIM and FEM can not image the atomic arrangement of all metal surfaces. Because W can be imaged relatively easily with FIM and FEM, and a number of investigations on adsorption phenomena [25-27], dynamics of surface diffusion [28-30], sputtering [31-33] and so on have been carried out with W tip surface in FIM and FEM studies. On the other hand, there has been no report on exoemission from W surfaces. As the first step of this study, whether or not FSE occurs at W tip surface was investigated.

The W tip used in this study was prepared by the field evaporation technique at 50 K during FIM observation, and then annealed at 800 K for 10 s in UHV. After annealing treatment, emission properties were measured at 50 and 300 K by the voltage history indicated in Figure 3-16. The results are shown in Figure 3-22. The open and filled circles represent the results measured at 50 and 300 K, respectively. As is seen in the Figure 3-22, a transient enhancement of the emission current (I_p), which has been considered as a FSE signal in FSE studies, was clearly observed at 300 K. The FSE signal decays to the steady-state level of 3 x 10^{-13} A within a few tens of seconds which is the contribution of the steady-state field emission. In contrast, at 50 K, the emission current immediately recovered to 3 x 10^{-13} A at the moment of reapplication of the tip voltage without any FSE signal.

In order to confirm reproducibility of the FSE phenomenon observed at 300 K, the

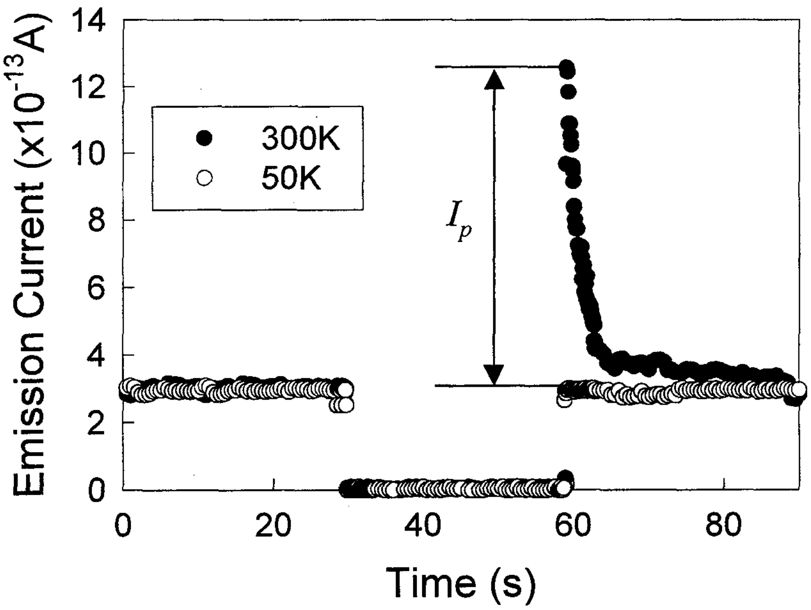

Figure 3-22 Emission properties of FSE from the annealed W tip measured at 50 and 300 K in the voltage history indicated in Figure 3-16.

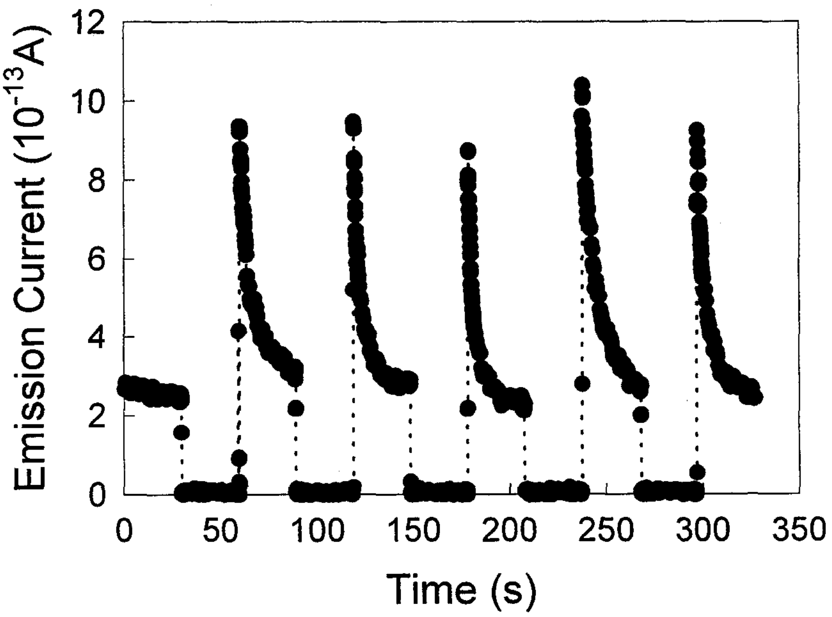

Figure 3-23 Emission current trace of the five continuous trials of FSE experiments at room temperature. The enhancement of emission (I_p) is measured as a FSE current.

same measurement was repeated five times. Figure 3-23 shows the results of the measurements. I_p was observed at every moment when the negative high voltage was reapplied (60, 120, 180 and 300 s in the abscissa). I_p distributed from 6.1 x 10^{-13} to 7.8 x 10^{-13} A, and the mean value was 6.8 x 10^{-13} A. Variation of the experimental data was within ±10% of its mean value. It was found from these results that the FSE phenomenon exhibited a good reproducibility. Also, as is shown in Figure 3-23, neither steady-state emission nor the peak values of I_p current show gradual decrease with the trials. This fact suggests that this phenomenon is independent of the H_2 or He positive ions that might be field adsorbed during the FSE observations.

The storage effect of FSE from W tips was also studied in this study, and the experimental results are indicated in Figure 3-24 (filled circle). In this figure, the experimental result on Al tips also is plotted in the same graph (open circle). One finds that I_p from W tips keeps almost constant over the interruption period from 5 to 120 s. In contrast, I_p from Al tips increases with interruption period and reaches the steady-state level at 6 x 10^{-16} A [11]. The minimum interruption period of 5 s was decided considering the cut-off and rise-up time of the high voltage supply, and it was the minimum interruption period that provides reliable result in the experimental setup used in this study. It is, thus, concluded that FSE on W tips does not show the storage effect which is characteristic to the FSE interpreted by the two step mechanism, while for Al tip the storage effect is clearly seen.

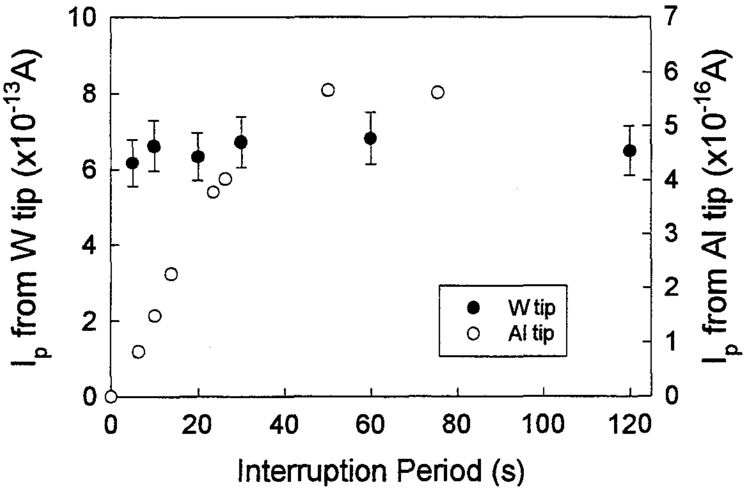

Figure 3-24 Interruption-period dependence of I_p on W and Al tips at room temperature; the filled and open circles indicate the experimental results on W (present study) and Al (Ref. [11]) tips, respectively.

3.6.2 Temperature Dependence of FSE

From Figure 3-22, it was obvious that FSE on W tip has a temperature dependence. In order to investigate the detail of the temperature dependence of FSE phenomenon on W tips, the relationship between I_p and the tip temperature was examined in the temperature range of 150 ~ 450 K. The results are shown in Figure 3-25. As shown in Figure 3-25, the FSE intensity shows a summit at 300 K, and disappears at the temperatures higher than 450 K or lower than 200 K. The emission properties of FSE on W tips presented in Figures 3-22 and 3-25 are similar to those observed in Al tips, *i.e.*, the increase of emission is observed at the moment of reapplication of the tip voltage [10], and it decreases with tip temperatures higher than 300 K [14]. However, we saw a difference with regard to the storage effect of FSE as described previously, that is, I_p from the W tips was independent of the interruption period of applied voltage. Since the interruption period dependence is essential to the two-process model, which explains FSE phenomenon from Al tips, it is necessary to consider new emission model or to modify the two-process model for describing the FSE phenomenon on W tips.

The variation of average work function over the tip surface was measured at the temperatures from 150 to 500 K where FSE intensity changes. According to the equations

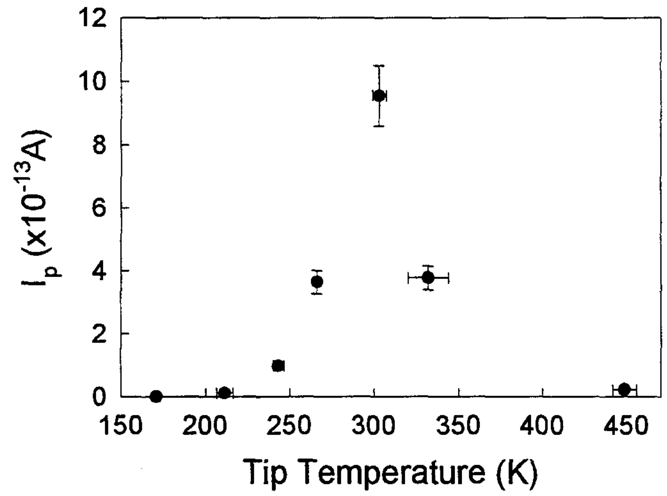

Figure 3-25 Temperature dependence of I_p on W tips in the temperature range from 150 to 450 K.

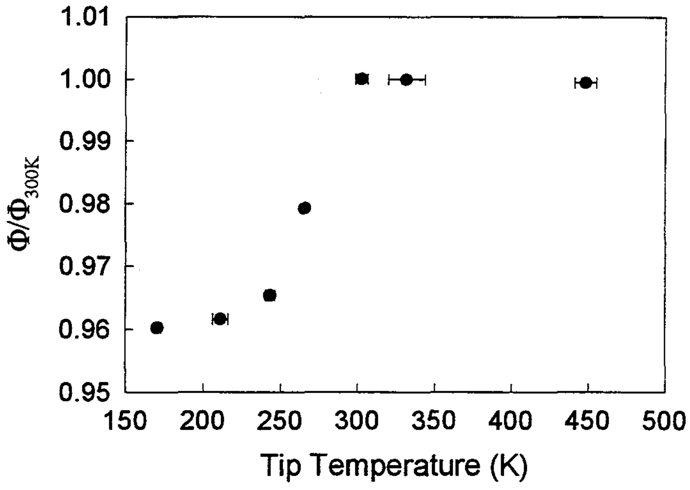

Figure 3-26 Average work function change over the W tip surface at temperatures between 150 and 450 K.

coverage during the experiment was estimated. The assumptions are as follows; (1) the residual gas was composed of H_2 molecule, (2) the sticking coefficient of H_2 on a clean W surface at 300 K was 0.24 [34], (3) it took 150 s to complete the experiment after the annealing. From this calculation, H_2 of 1.5 x 10^{13} atoms/cm^2 adsorbed on the W surface when the experiment was completed. The coverage of H_2 at the end of the FSE measurement was calculated to be as low as 0.01. In such a low coverage, it has been reported that the work function of the W surface was not affected by the H_2 adsorption [35]. Moreover, in order to confirm the contribution of H_2 adsorption to the FSE phenomenon, the effect of H_2 exposures on I_p was examined at 320 K. The experimental result is shown in Figure 5-6 in chapter 5. According to the discussion in chapter 5, H_2 adsorption tends to reduce I_p. Therefore, it seems reasonable to consider that FSE on W tips is not affected by the H_2 adsorption on the tip surface.

In contrast, LEED study showed that the surface reconstruction took place on the clean W{001} surfaces (close to W{013}) at the same temperature range that the work function change was observed in this study [36,37]. It was reported that the surface structure on W{001} surfaces changed gradually from an ordinary (1 x 1) to c(2 x 2) by cooling the surface temperature from 300 K, and c(2 x 2) occupied the entire W{001} surfaces at 200 K. The temperature range where the surface reconstruction occurs coincides with that of the FSE peak (Figure 3-25). It was also reported that this surface reconstruction was accompanied with the decrease of work function about 20 meV. Although the estimated decrease of work function in this study was somewhat larger than this value (180 meV), qualitatively similar work function change was measured in this study.

The LEED studies mentioned above are the experimental results in the absence of an electric field. In contrast, FSE is the phenomenon that occurs at the onset of high electric field; a transient phenomenon from the absence to the presence of the electric field in the order of a few V/nm. The effect of such a high electric field seems to be important to FSE phenomenon. Unfortunately not many modern literatures are available on the surface reconstruction of W under the presence of high electric field. Even so, Nishigaki et al. reported that the c(2 x 2) structure observed after the reconstruction on W{001} was caused by the field-induced effects [38]. Their FIM study indicated that the reconstruction of W{001} from ordinary (1 x 1) to c(2 x 2) occurred under the electric field; it occurred at the electric field strength of 60% of the evaporation field at 390 K as well as after the field evaporation at temperatures higher than 78 K. Also change in work function of W{013} and {012} surfaces at temperatures 78 ~ 400 K has been reported by Wysocki using FEM, and he concluded that the work function change was due to surface reconstruction [39]. Moreover, the surface reconstruction on {111} faces was also confirmed by Barwinski using scanning FEM (SFEM) [46]. Therefore, the surface reconstruction on {111} faces as well as {013}, {012} and {001} faces may be related to the FSE phenomenon. The relationship between the surface reconstruction and the FSE will be clarified from the experimental results of FEM/FIM observations. The spatial distribution of is discussed in Section 3.3.6.

In the temperature range between 200 and 300 K, where the surface reconstruction occurs, activation energy for movement of surface atoms along to the reconstruction seems to be quite low. Actually, almost zero activation energy on the movement of W atoms from (1 x 1) to c(2 x 2) positions were calculated by the first principle calculation [40,41]. Moreover, the FEM experiments indicated the reduction of nearly 10% in activation energy for self-migration by means of the application of the electric field in the order of 3 ~ 4 V/nm [42,43]. Therefore, it is likely to occur that the temperature-dependent surface reconstruction was triggered by the reapplication of the tip voltage (at the moment of onset of the electric field). Such phase transitions or structural changes were well-known as one of the origins of exoemission [44,45]. Also, unreasonable slow decay of I_p as an electron behavior (Figure 3-23) may be explained by the gradual progress of the structural transformation, for example from (1 x 1) to c(2 x 2) or vise versa.

3.6.3 Effect of Annealing Time and Temperature

The annealing treatment at 800 K for 10 s led to FSE as demonstrated in Figure 3-22. In order to obtain the FSE properties in detail, dependencies in annealing time and temperature were studied. The W tips cleaned by field evaporation at 50 K were annealed at 800 K for 600 and 7200 s. After the annealing treatments, FSE properties were measured at temperatures between 50 and 600 K by the method shown in Section 3.4.3. The results of the measurements are shown in Figure 3-27. The filled and open circles represent the experimental data measured at annealing time of 600 and 7200 s, respectively. As shown in Figure 3-27, both of the FSE intensities showed the summit at around 300 K, which are similar to that measured at annealing time of 10 s (see in Figure 3-25). Therefore, it is concluded that FSE does not depend on the annealing time.

The temperature dependence of FSE was also examined with the annealing temperatures at 300 to 965 K. In the first stage of this study, W tip was prepared by field evaporation. Then, the W tip was kept at 300 K for 60 s, and I_p was measured at the temperatures between 100 and 600 K. After the FSE measurement was completed, the annealing temperatures were gradually increased up to 965 K, and the FSE properties were measured repeatedly. The experimental results are shown in Figure 3-28. No FSE signal from the W tips annealed at the temperatures lower than 700 K was detected. However, FSE signals were measured at the W tips with the annealing temperatures at 825, 905 and 965 K. It was obvious from Figure 3-28 that the annealing temperature provides the shift of the FSE peak temperature, T_m, toward higher temperature. According to the report by Warwinski et al, a pyramid-like protrusion was formed on the (111) face of W tip surface by the annealing treatment at higher than 800 K [46]. It was also confirmed that the protrusion became sharp as the annealing temperature was increased. Since the annealing temperature required for appearance of the pyramid-like protrusion on the W (111) face coincides with that of FSE, it is also suggested that the protrusion on (111) face may relate to FSE phenomenon

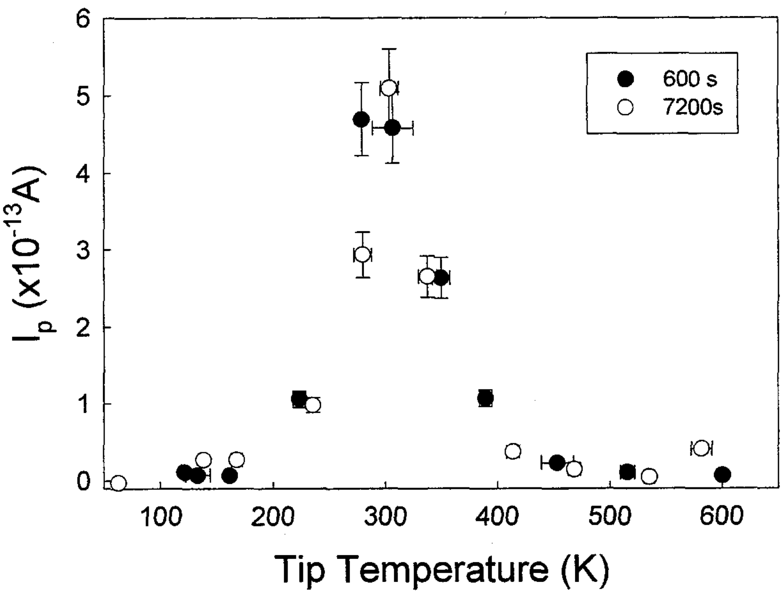

Figure 3-27 Dependence of I_p properties on the annealing time at 800 K; the filled and open circles show the results measured after the annealing treatment for 600 and 7200 s.

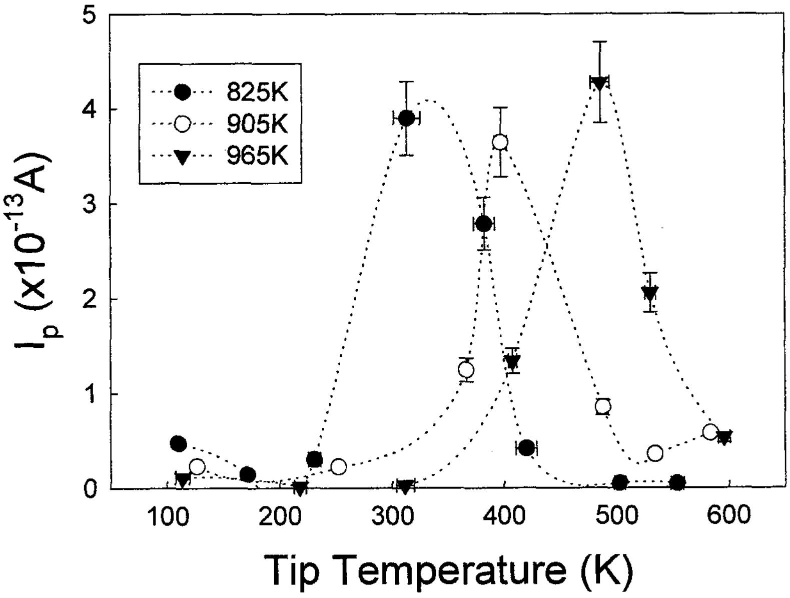

Figure 3-28 FSE properties from the W tips annealed at 825, 905 and 965 K measured at temperatures between 100 and 600 K

from W tips. If so, the shift of T_m would be considered to relate the shape of the protrusion.

3.6.4 Applied Voltage Dependence of FSE

The dependence of the applied voltage upon I_p was investigated. As the applied voltage to the tip becomes higher, electrons can be emitted from the deeper energy level. Therefore, it is expected that the investigation of the applied voltage dependence includes the information on the energy distribution of exoelectrons. Actually, the energy distribution of exoelectrons from Al tips was estimated from the applied voltage dependence of FSE [12,13].

The W tip used in this study was cleaned at 50 K by field evaporation, and annealed at 860 K for 600 s. Before the measurement of the applied voltage dependence, the FSE signals, I_p, from the annealed W tip surface was confirmed in the temperatures from 50 to 600 K. Figure 3-29 shows the result of the measurements. As is indicated in Figure 3-29, I_p was observed at the temperatures between 250 and 450 K, and I_p has the summit at around 350 K. This result was consistent with those in previous experiment (Figures 3-25 and 3-27). The negative voltage in the same time history was applied as shown in Figure 3-16, and the applied voltage was changed from -300 to -600 V. When the voltages higher than -600 V were applied to the tip, out gas from the phosphor screen caused significant increase of the pressure in the FIM chamber. The result of applied voltage dependence of I_p is indicated in Figure 3-30. Open and filled circles represent I_p and steady-state field emission current, respectively. The field emission current (filled circles) increased rapidly with increasing the applied voltage, as expected by the equation (3-29). In contrast, although the similar increase of I_p was obvious in the applied voltages lower than -450 V, difference in the rate of increase was observed in the applied voltage range higher than -500 V. It is found that I_p has different applied voltage dependence from stationary field emission, as well as temperature dependence described in Section 3.6.2. These preliminary data show the possibility of contribution of surface electronic states of W tips, which will not contribute to the steady-state field emission. Therefore, it would be necessary to propose the new emission model including change in surface states or surface electronic state due to the dynamics of movement of surface atoms for explaining the FSE phenomena from W tips.

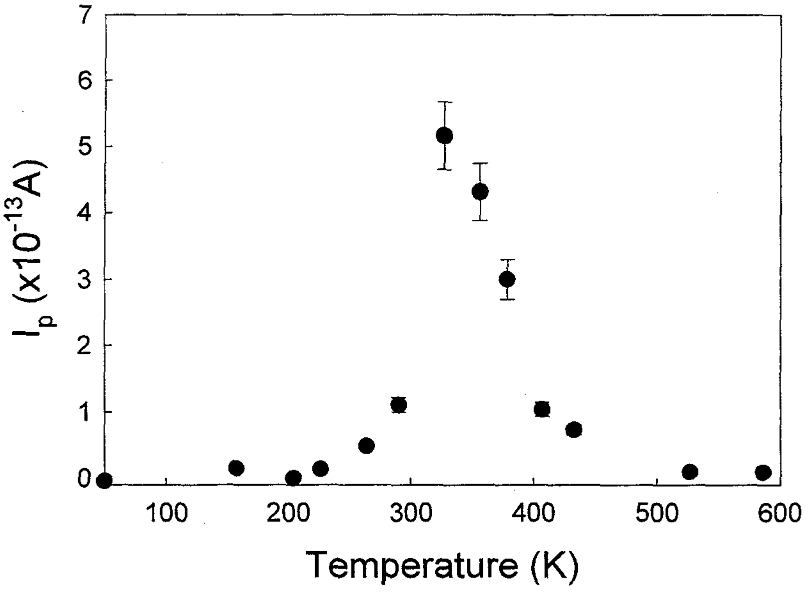

Figure 3-29 FSE property at temperatures between 50 and 600 K from the W tip annealed at 860 K.

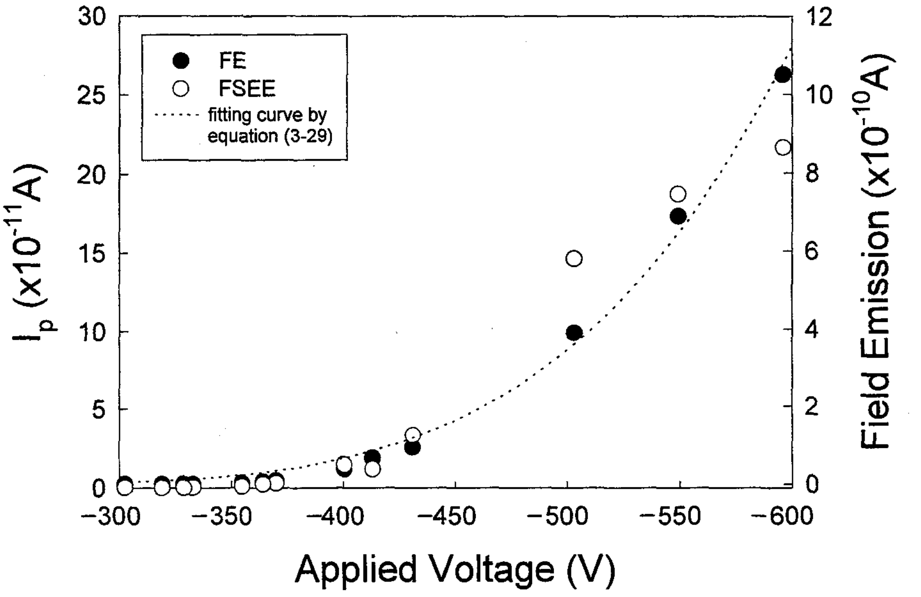

Figure 3-30 Applied voltage dependencies of I_p (open circle) and steady-state field emission current (filled circle) from the W tip annealed at 860 K. The measurements were carried out at 350 K.

3.6.5 Surface Reconstruction under High Electric Field

It was proved in Section 3.6.2 that the annealing treatment at the field-evaporated W tip surface led to the appearance of FSE. Also it was proposed that the changes of the surface structure on (031) or (111), as described in Sections 3.6.2 ~ 3.6.3 may relate to the FSE phenomenon. Therefore, in this section, the surface structural change induced by the annealing treatment and by the observation temperature were identified by FIM and FEM.

Prior to the FIM and FEM observations, the emission property from the W tip was confirmed. The W tip was prepared by field evaporation during FIM observation, and annealed at 880 K for 600 s. After the annealing treatment, FSE from the W tip was measured by the method described in Section 3.4.3 at temperatures from 50 to 550 K. The result is indicated in Figure 3-31. Filled and open circles represent the FSE intensity, I_p, and the relative work function change ϕ/ϕ_{50K}, respectively. The FSE property and the work function change with the tip temperature are consistent with the results shown in Sections 3.6.2 and 3.6.3. In order to characterize the surface structure of this W tip, the FIM and FEM observations are carried out.

Figures 3-32 (a) and (b) show the corresponding FIM and FEM images. The FIM image was taken at 50 K with BIV of 4.9 kV after field evaporation at FEV of 5.8 kV. In

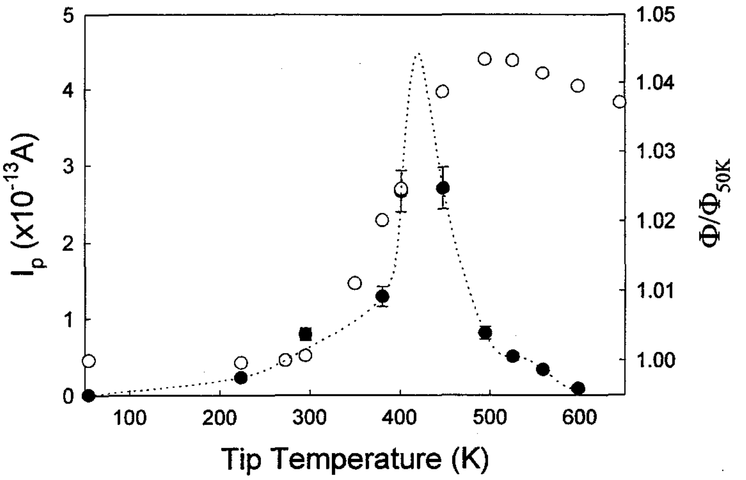

Figure 3-31 Temperature dependencies of I_p and the relative work function on the W tip surface after annealing at 880 K for 600 s.

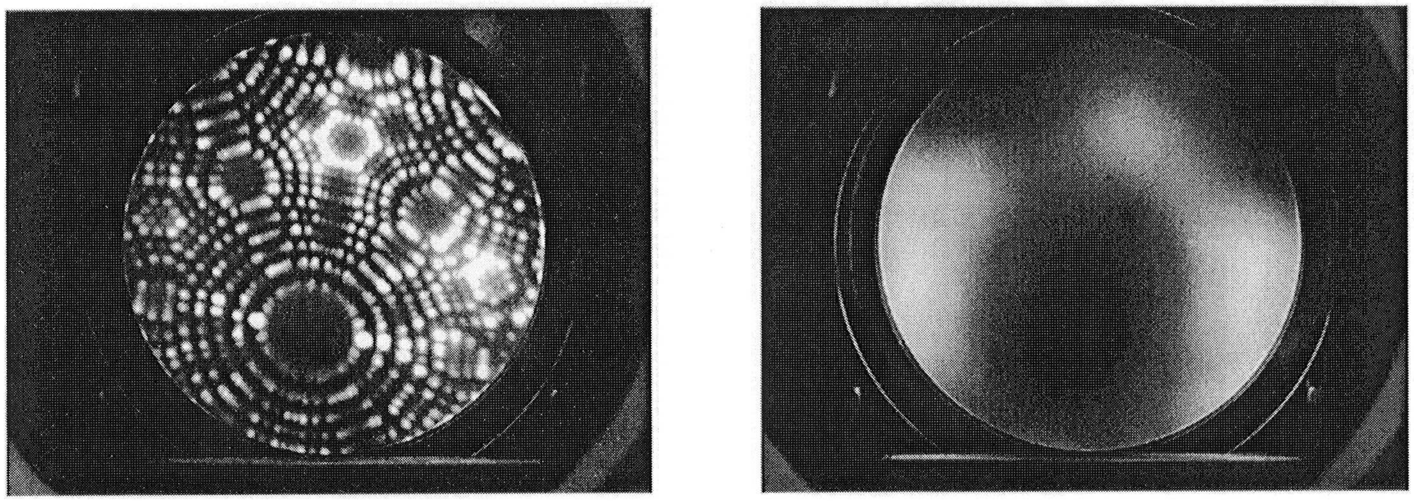

(a) FIM image
FEV:5.8kV
BIV:4.9kV

(b) EV:-314.1V
temp:50K

Figure 3-32 FIM and FEM images of the initial W tip surface prepared by field evaporation. Both observations were carried out at 50 K.

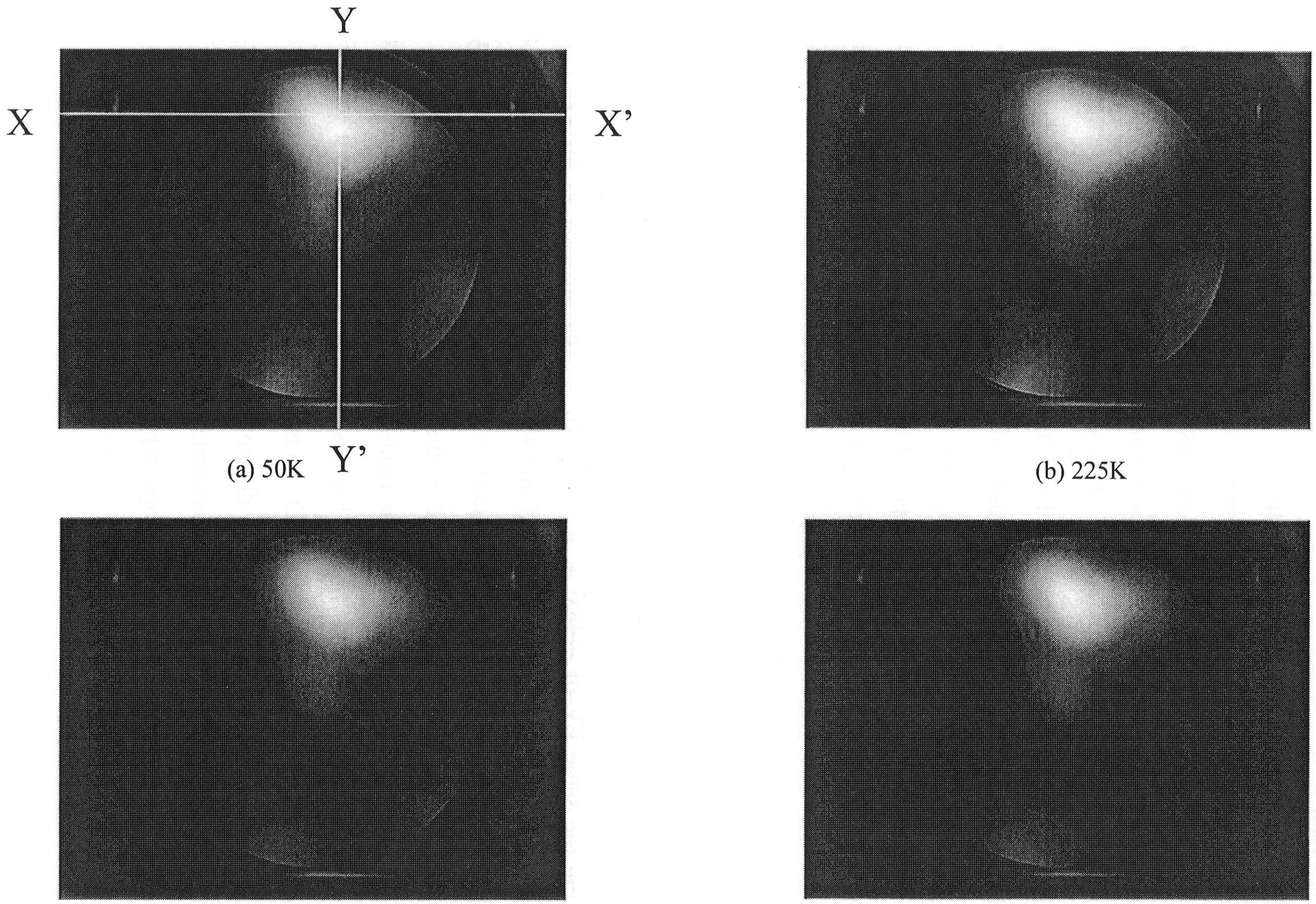

(a) 50K

(b) 225K

(c) 440K

(d) 630K

Figure 3-33 Variation of the FEM images of the W tip annealed at 880 K for 600 s with same EV of -448.6 V, when the tip temperature was increased from 50 to 630 K.

the FIM image (Figure 3-32 (a)), remarkable defects are not observed, and it is found that the atomic arrangement of the surface is well-ordered. The FEM image (Figure 3-32 (b)) was imaged at 50 K by applying the emission voltage (EV) of -314.1 V after the FIM observation. Since the FEM image shows a two-fold symmetry, it is also confirmed that the tip surface remains clean. This clean W tip was annealed at 880 K for 600 s, and the FEM observation of the tip surface followed at 50 K again. Even when the same EV of -341.4 V was applied to the tip, the FEM image did not appear. This fact clearly suggested that the tip apex became blunt. The EV was increased until FEM image appeared, and Figure 3-33 (a) was observed at 50 K with EV of -448.6 V. In this FEM image, the bright area with a three-fold symmetric structure appeared at the W (111) face. Note that only one (111) face was obvious in Figure 3-33. Barwinski et al. reported the reconstruction of the {111} faces on the W tip with the scanning FEM [39]. According to their report, after annealing the clean W tip at higher than 800 K for 30 s, the structure which showed three-fold symmetry arose on the {111} faces. It is considered that the similar phenomenon was observed in present study.

As the tip temperature increased, the change of the surface structure was observed by FEM. Figures 3-33 (b), (c) and (d) show the FEM images taken at 225, 440 and 630 K with applying the same EV of -448.6 V, respectively. The intensity of the FEM image seems to decrease at temperatures between 225 and 440 K, although all the FEM images keep the same three-fold symmetry. In order to clarify a temperature dependence of the intensity, the intensities along the cross sections denoted by the lines of X-X’ and Y-Y’ in Figure 3-33 (a) were measured. The measurement was made by counting the emission intensity in every pixel of CCD device on the line. Figures 3-34 (a) and (b) show a temperature dependence of the signal intensities in the CCD pixels along the X-X’ and Y-Y’ cross sections, respectively. The intensity at the W (111) did not change remarkably in the temperature range between 50 and 225 K, while it decreased rapidly at temperatures between 225 and 440 K. Moreover, the intensity of the FEM image kept constant at the tip temperatures higher than 440 K. This temperature dependence of the FEM intensity is in a good agreement with that of the applied voltage which is required for the emission current of 3 x 10^{-13} A (open circle in Figure 3-31).

Furthermore, the W tip surface, which was expected to have a pyramid protrusion, was

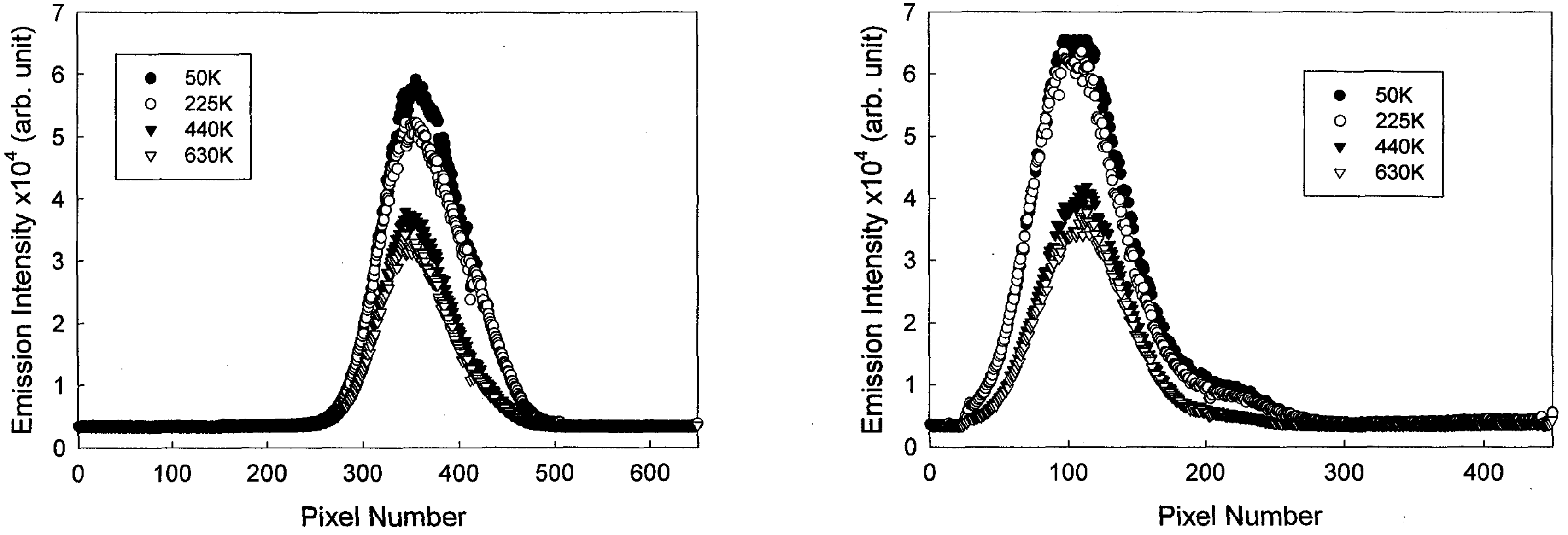

(a) X-X' Cross Section

(b) Y-Y' Cross Section

Figure 3-34 Temperature dependencies of FEM image intensities along the X-X' and Y-Y' cross sections in Figure 3-33 (a)

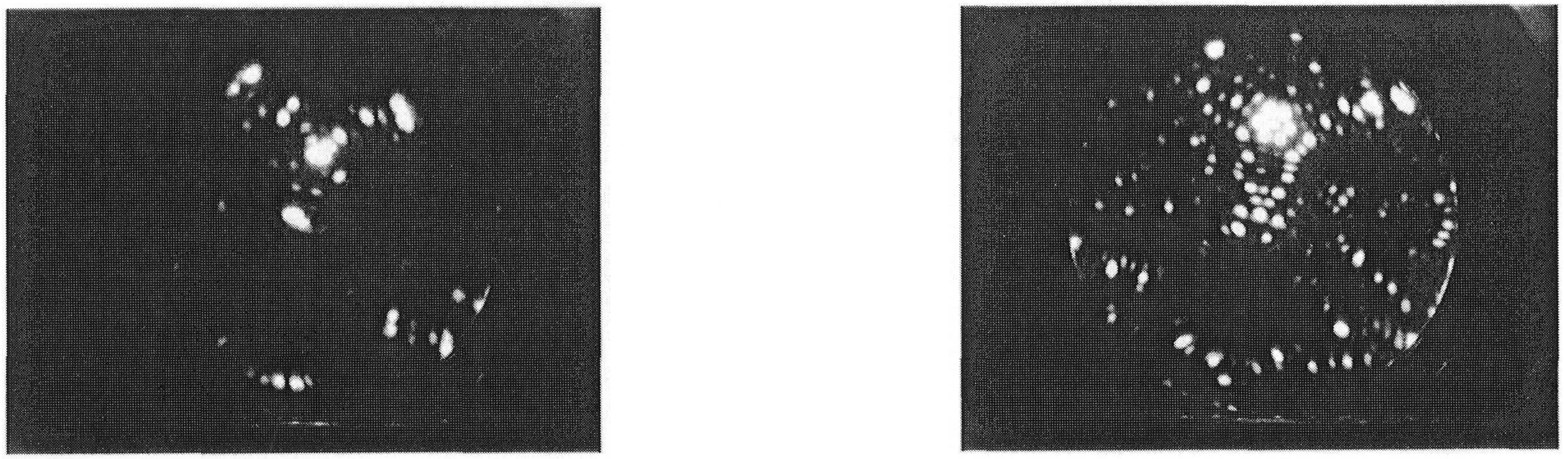

(a) FEV:3.7kV BIV:3.7kV

(b) FEV:4.7kV BIV:4.7kV

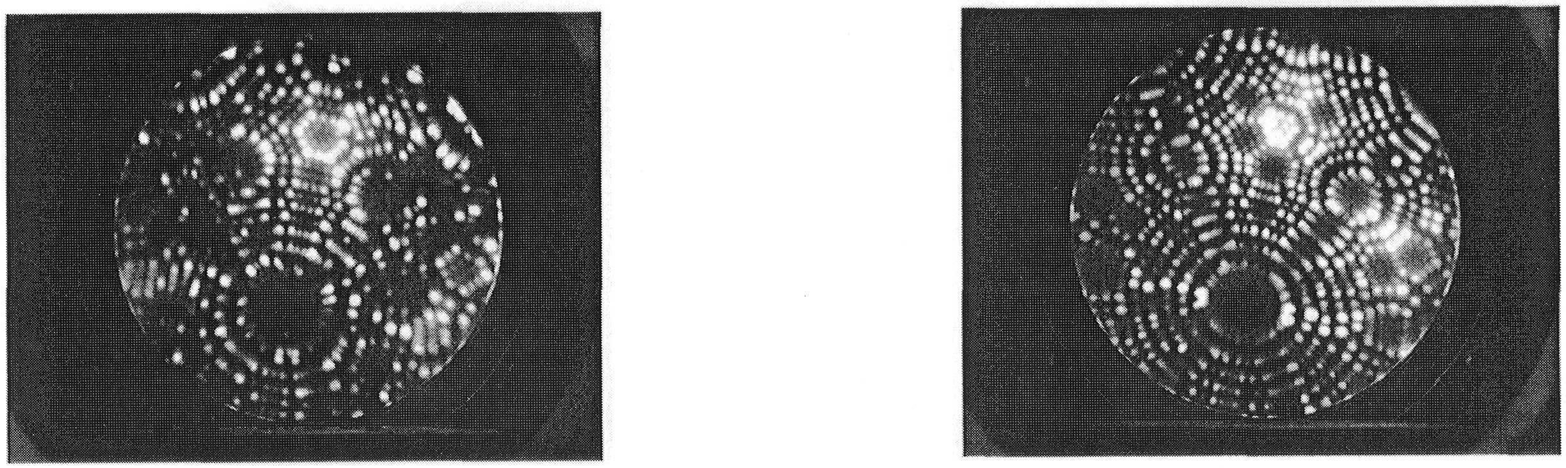

(c) FEV:5.5kV BIV:4.9kV

(d) FEV:6.1kV BIV:5.3kV

Figure 3-35 Characterization of the W tip surface annealed at 880 K for 600 s by FIM; FIM observations was carried out during the field evaporation process.

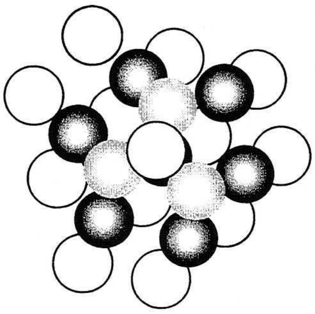

(a) pyramid structure of the (111) plane.

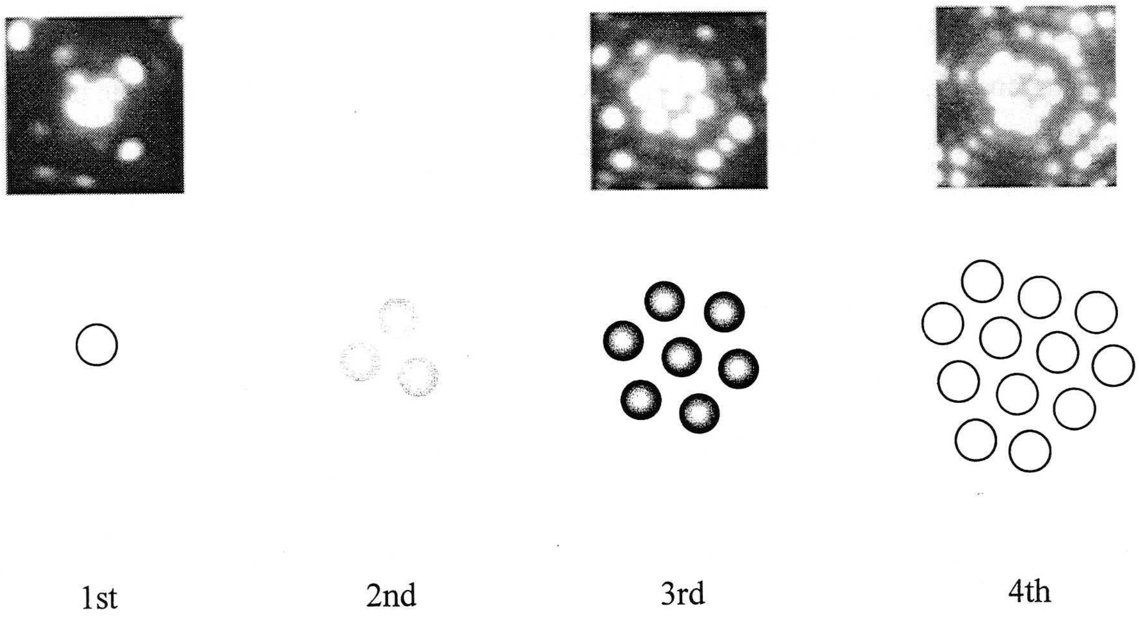

(b) atomic arrangement in the pyramid structure.

Figure 3-36 The model of the pyramid structure on (111) induced by the annealing treatment.

directly characterized by FIM. The results of the FIM observations are shown in Figure 3-35 (a) ~ (d). After the annealing treatment of the W tip was carried out at 880 K for 600 s, the tip temperature was cooled down to 50 K during FIM observation. As the positive applied voltage to the tip for field evaporation was increasing, the single bright spot appeared at first at a center of the (111) face, and the three-fold symmetric structure became visible (see Figure 3-35 (a)). This single bright spot means that the single-atom exists at the top of the (111) face. After the single atom was field-evaporated, the triangle structure consisted of three atoms was observed (not shown). By further field evaporation, the structure with seven atoms was obvious at the (111) face (see Figure 3-35 (b)). The recovery process to well-ordered atomic arrangement is shown in Figure 3-35 (c) and (d). From the FIM observations, it was concluded that the pyramid protrusion (Figure 3-36 (a)), in which structure was shown in Figure 3-36 (b), was formed at the (111) face due to the annealing treatment. Moreover, from FEM observations (Figure 3-33) and the change of the FE intensity on {111} faces (Figure 3-34), it is also considered that the height of the protrusion is rapidly lowered at the temperatures from 225 to 440 K.

3.6.6 Spatial Distribution of FSE

It was proposed in Sections 3.6.2 ~ 3.6.3 that the FSE from W tips with the annealing treatment higher than 800 K was related to the surface reconstruction. Also, in Section 3.6.5, the pyramid protrusion on (111) face of the W tip surface was confirmed after the annealing treatment. One of the characteristic features of FSE is that the spatial distribution of the FSE can be obtained using FEM as described in Section 2.3. Therefore, in this section, the spatial distribution of the FSE from W tips was measured.

Figure 3-37 shows the FIM image of the field-evaporated clean W tip used in this study. FEV and BIV were 6.5 and 5.5 kV, respectively. Then, the clean W tip was annealed at 800 K for 600 s. After the annealing treatment, the FEM image of the W tip was taken at 50 K with the negative voltage of -401.6 V (Figure 3-38). From the comparison of the FEM image with the FIM image shown in Figure 3-38, it was found that the bright area in Figure 3-38 was seen on the {111} face. This is because of the surface reconstruction at {111} by the annealing treatment as described in the previous Section 3.6.5.

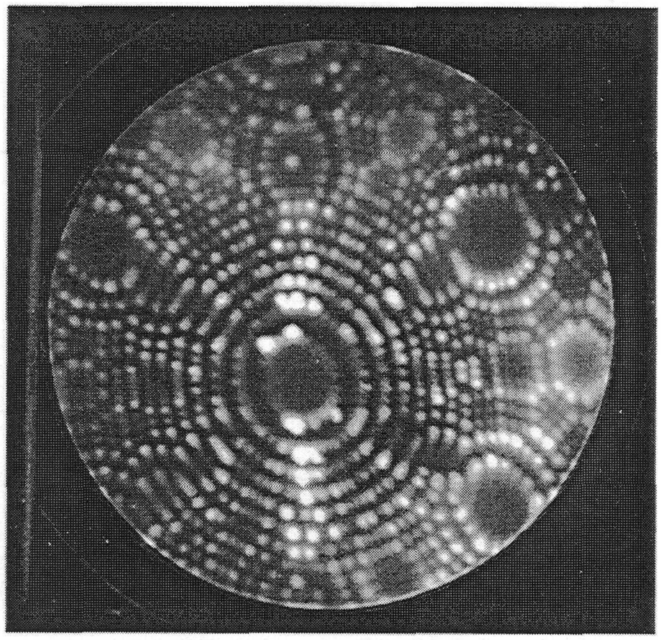

Figure 3-37 FIM image of the ideal W tip surface. (FEV=6.5kV, BIV=5.5kV)

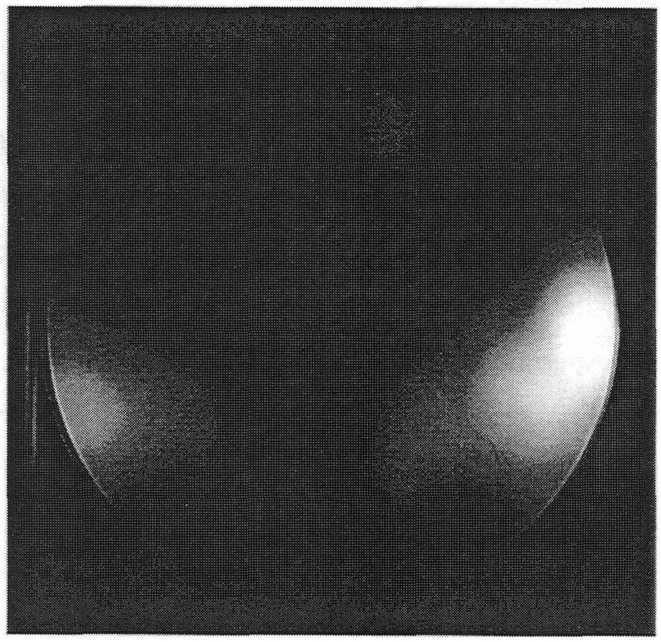

Figure 3-38 Corresponding FEM image of the W tip shown in Figure 3-37. (EV = -401.6V)

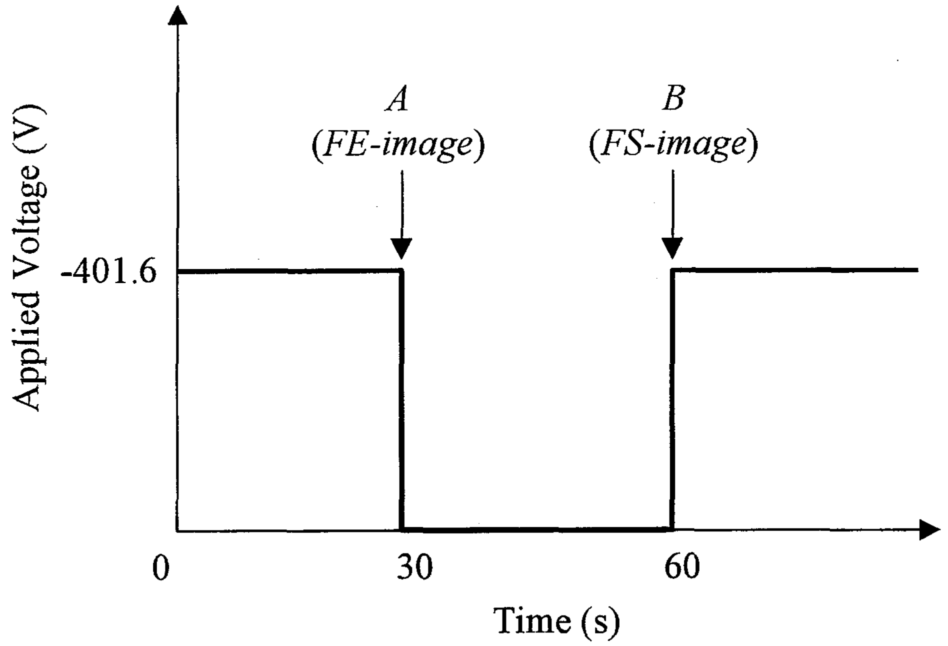

Figure 3-39 The time history of the applied voltage; the method to observe *FE-* and *FS- images*. *FSE-image* was obtained by subtracting *FE-image* from *FS-image*.

The spatial distribution of the FSE from this W tip surface was measured with the temperature range between 50 and 800 K. The same negative voltage of -401.6 V was applied to the tip in the time history shown in Figure 3-39 at every measuring temperature. The field emission (FE) and FSE + FE images were taken at the time denoted by *A* and *B* in Figure 3-39, and labeled "*FE-image*" and "*FS-image*", respectively. If the FSE occurs on the W tip surface, one can obtain the "*FSE-image*" by subtracting the *FE-image* from the *FS-image*. Since both of the images were captured by the electronically cooled CCD-camera, such a subtraction process can be carried out numerically. The temperature dependencies of *FSE-* and *FE-images*, thus obtained, were examined at temperatures between 50 and 800 K. Figure 3-40 shows the experimental result measured at temperatures between 50 and 500 K. Filled and open circles represent the total intensities of the *FSE-* and the *FE-images* thus calculated. The total intensity of *FE-image* decreased rapidly in the temperature between 200 and 330 K, and kept constant at higher than 330 K. This tendency of the total FE intensities reflects the variation of work function shown in Figure 3-26. Also, it is found that the FSE intensity showed the summit at around 300 K, which is in good agreement with the result on FSE current, I_p, indicated in Figure 3-25. From these results obtained by *FE-* and *FSE-images* in Figure 3-40, it was confirmed that FSE measured by the CCD device and

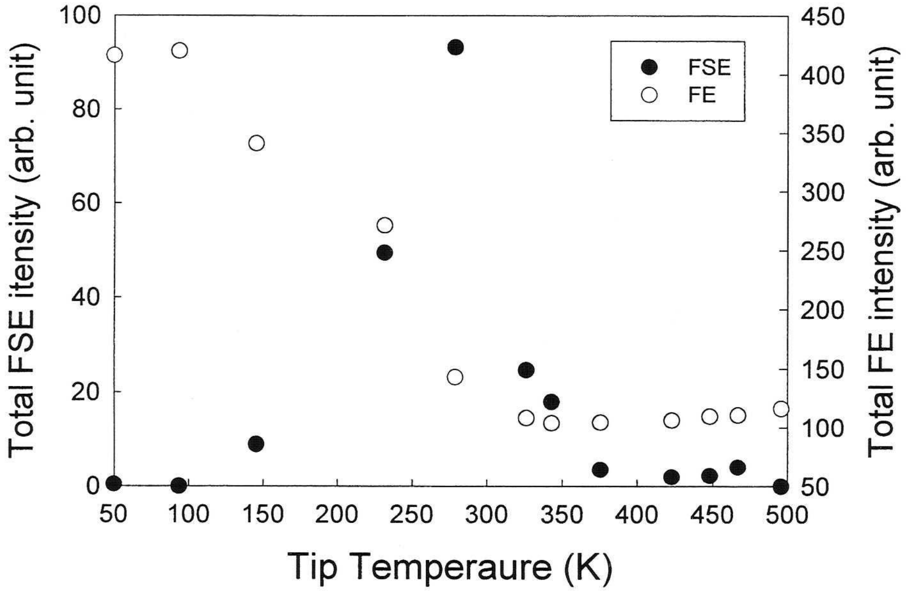

Figure 3-40 Temperature dependence of total *FSE-* and *FE-image* intensities from the annealed W tip.

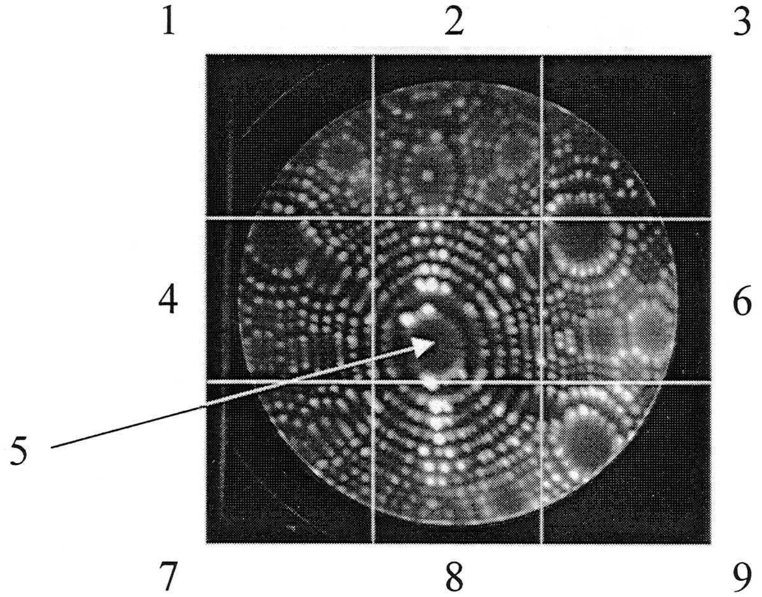

Figure 3-41 The division of the FSE images into nine areas. The intensity from each area was measured separately.

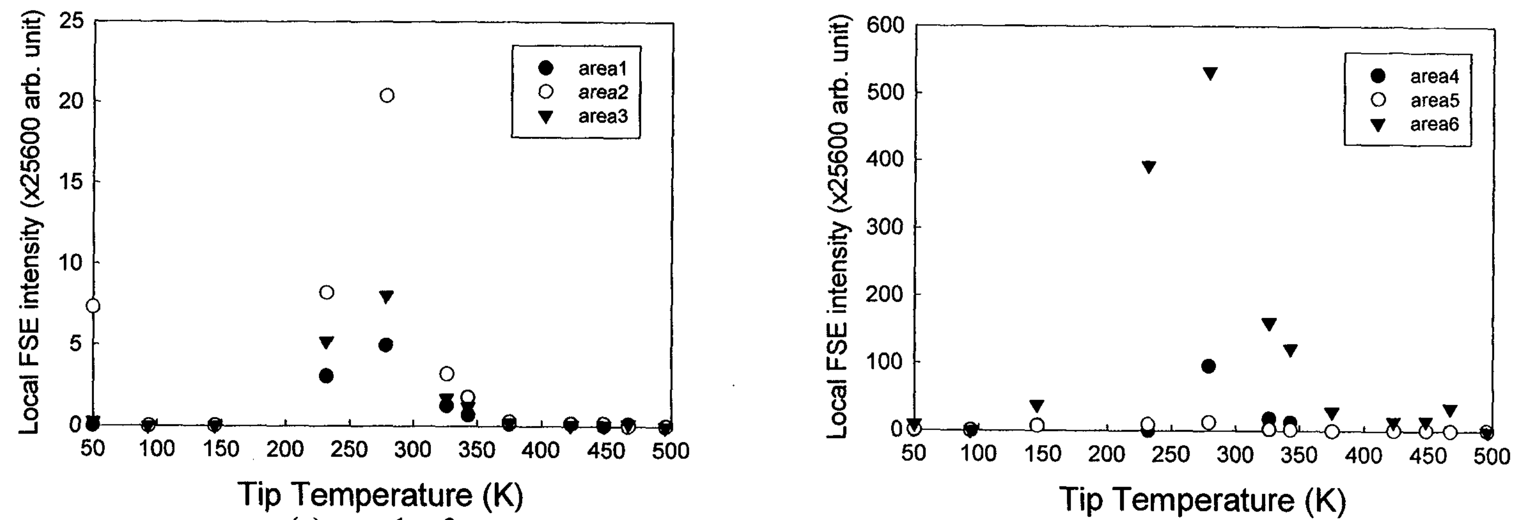

(a) area 1 ~ 3

(b) area 4 ~ 6

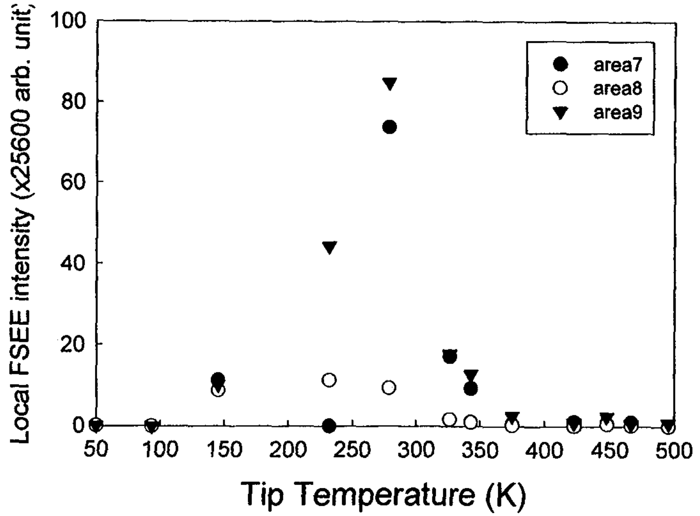

(c) area 7 ~ 9

Figure3-42 The local FSE intensities from the annealed W tip measured at temperatures between 50 and 500 K. Note that the scales of the vertical axes are different.

showed the same emission properties as described in Section 3.6.2. In order to analyze the spatial distribution of FSE in detail, each *FSE-image* was divided into nine areas as illustrated in Figure 3-41, and every area was labeled "*area 1*" ~ "*area 9*". Figures 3-42 (a), (b) and (c) show the temperature dependence of local FSE intensities at *areas 1 ~ 3*, *4 ~ 6* and *7 ~ 9*, respectively. It is obvious from Figures 3-42 (a) ~ (c) that all emission properties of FSE measured locally indicated the similar temperature dependence, that is, all the local FSE intensities have a peak at around 300 K. However, the strongest FSE signals were observed in *area 6* as is shown in Figure 3-42 (b), and the local FSE intensity of *area 6* at around 300 K is 6 ~ 100 times higher than those of the other areas. The second strongest FSE intensity was detected at the *areas 4*, *7* and *9*. By the comparison between Figure 3-37 (FIM image) and Figure 3-41, it is recognized that *area 6* involves (111) face, and its surroundings are included in *areas 4*, *7* and *9* as well as *area 6*. Actually, local FSE intensity from *area 4* and *6* (from {111} faces) measured was 75 % of total FSE intensity. Moreover, the sum of the local FSE intensities from *area 4*, *6*, *7* and *9* reaches 94 % of the total FSE intensity. Hence, it is concluded that FSE from (111) face and its surroundings govern the total FSE from the W tip surface at 300 K after the annealing treatment. In the previous Section 3.6.5, it was indicated that the pyramid protrusion was formed on the (111) face of the clean W tip surface due to the annealing treatment at 800 K. Therefore, the relationship between FSE and the surface reconstruction at {111} faces was strongly suspected. However, the FSE intensity from *area 2* is much lower than that of *area 6*, but clearly higher than its surroundings of *areas 1*, *3* and *5*. Since *area 2* involves (031) and (001) faces, there still be a possibility that FSE is also accompanied by the structural transformation of p(1x1) ↔ c(2x2) on (001) as proposed in Section 3.6.2.

3.6.7 Probable Emission Mechanism

From the discussion in the previous Section 3.6.6, it was clear that the pyramid protrusions were formed on {111} faces of the annealed W tip, and the reconstruction of such a protrusion was strongly related to FSE phenomenon from the W tip surfaces. The electronic structure of the surface depends strongly on the atomic arrangement of the surface. Therefore, the pyramid protrusion may induce the characteristic electronic structure.

Unfortunately, an electron energy spectrometer was not equipped with the experimental facility used in this study, and the electronic structure in the protrusion can not be measured directly. Binh et al. reported that the electronic structures both of macroscopic tips and of single-atom protrusion formed on a W <111> single crystal by using field-emission electron spectroscopy (FEES) [47]. Note that the "macroscopic tip" means the clean W tip prepared in the UHV chamber at ~3200K, and the "single-atom tip" does the nanoscale protrusion, which is ended by a single atom, formed by field-surface melting technique on the macroscopic tip surface. The total energy distribution (TED) spectra from (111) face of the macroscopic tip and of the single-atom tip are referred in Figures 3-43 (a) and (b). V_{app} indicates the applied voltage to the tip required for field emission during the measurement of TED. From the comparison between the TEDs shown in Figures 3-43 (a) and (b), it is obvious that the new peak labeled "Peak b" in Figure 3-43 (b) appears at 1.1 eV lower than Fermi level (E_F) in the TED spectrum of the single-atom tip. They interpreted the presence of these peaks, which is called "*b-peak*" in the following discussion, was due to the surface resonance bands localized at the topmost atom of the protrusion.

As is shown in Figure 3-22, FSE signal, I_p, was triggered by applying a negative high electric field. It was reported that such a high electric field reduced the potential barrier for surface diffusion [48] and gave rise to the field-induced compressive force [15]. According to the discussion in the Section 3.6.5, it was observed that the pyramid protrusion was formed on {111} faces of W tip surface by annealing at 800 K and the height of the protrusion was lowered when the temperature increased from 150 to 450 K. Both of the increase in the temperature and of the application of the high electric field provide the reduction of potential barrier required for surface diffusion. Therefore, it is supposed that the height of the protrusion with the electric field would be easier to be lowered without the electric field.

It is considered that the intensity of the additional peak in TED spectrum, "*b-peak*", shown in Figure 3-43 depends on the height of the pyramid protrusion, that is, the intensity of "*b-peak*" becomes higher, as the protrusion is shaper. The contribution of the "*b-peak*" to FSE was proposed and is explained in Figure 3-44. The "*b-peak*" heights during steady-state field emission (*region A* in Figure 3-44) and without a high electric field (*region B*) are defined as H_f and H_0, respectively. Note that $H_0>H_f$, because it was proposed in Section 3.6.5 that the high electric field applied to the tip surface lowered the height of the pyramid

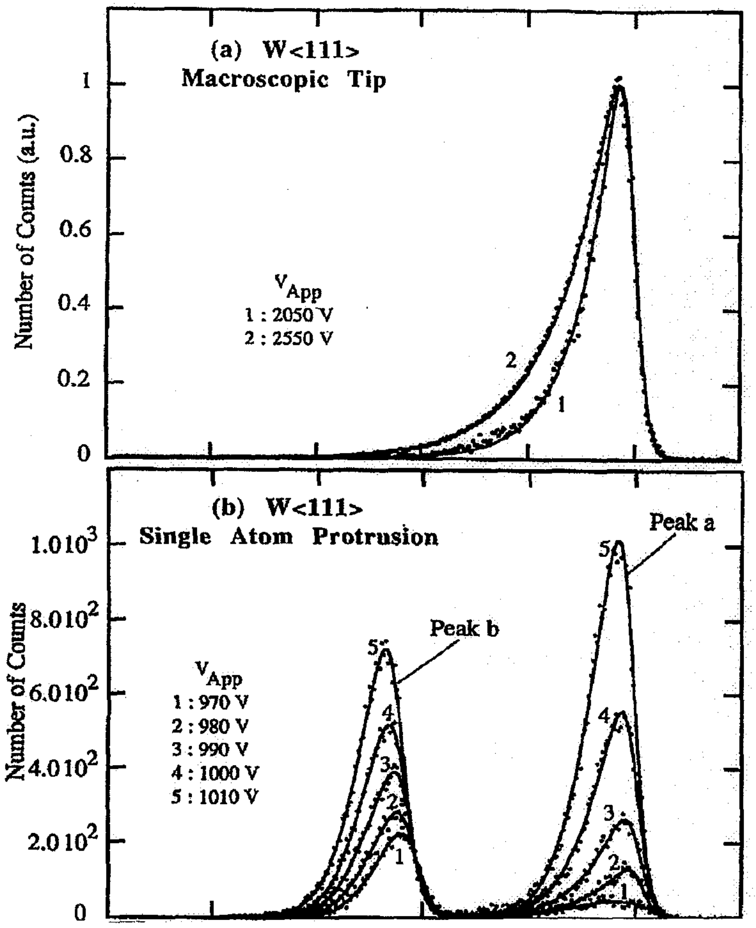

Figure 3-43 Experimental TED spectra measured at room temperature from a macroscopic tip (a) and a protrusion ending in a single-atom for various applied voltages (b). [47]

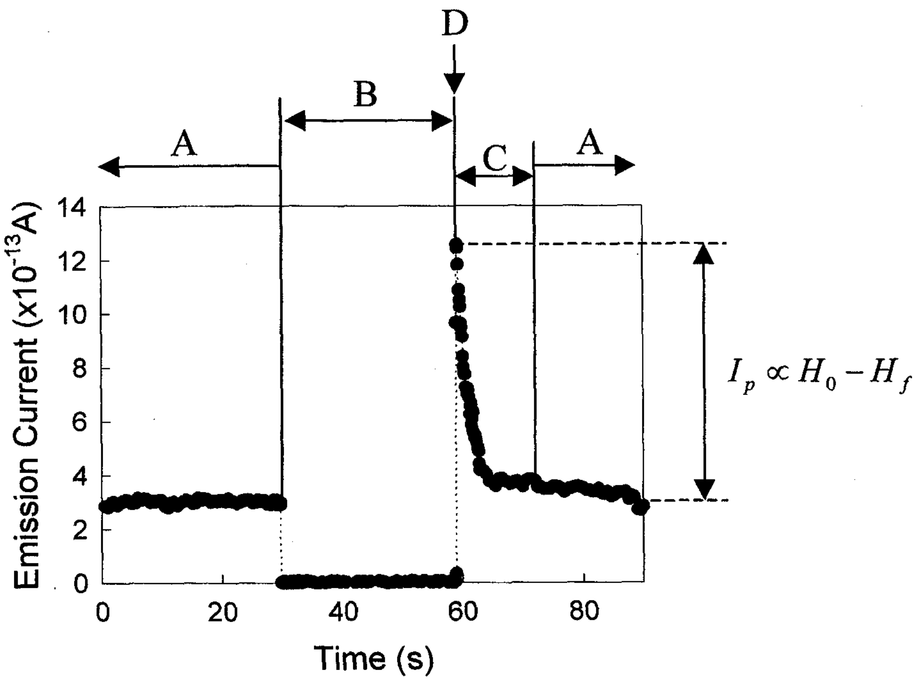

Figure 3-44 Typical emission property from the annealed W tip surface at 300 K. After the voltage interruption (region B), the tip voltage is reapplied at point D. Regions A and C show the regions of steady-state emission and of the decay in emission regions, respectively.

protrusion formed on (111) face. Therefore, I_p observed at the moment of application of tip voltage (*point D*) would cause the difference of "*b-peak*" between H_0 and H_f. When the high electric field is applied to the surface at *point D*, the structural transformation of the pyramid protrusion is considered to be triggered. At *region C*, since the height of the protrusion is lowered gradually by the surface diffusion of W atoms due to the high electric field, H_0 decreases to H_f and hence emission current would be decayed. Namely, the slow decay of I_p in *region C* reflects the reconstruction process of the pyramid protrusion formed on (111) face.

Based upon this emission model, the temperature dependence of the FSE described in Section 3.6.2 would be explained as follows: In order to apply this emission mechanism to the FSE phenomenon on the W tips, it is essential that the high electric field applied to the tip surface triggers the surface diffusion of W atoms. As discussed in Section 3.6.2 and 3.6.5, the thermally-activated structural transformation on the W tip surface, which was annealed at 800 K, took place at the temperatures between 200 and 400 K. This was proved by the fact that the potential barrier for surface diffusion of W atoms is quite low in this temperature range. Therefore, the high electric field applied to the surface assists the surface diffusion phenomenon, and I_p would be observed due to the field-triggered surface diffusion at the temperatures between 200 and 400 K. Thus, the temperature dependence of FSE from the W tip observed in this study can be explained qualitatively by the emission model proposed here. However, the applied voltage dependence described in Section 3.6.4 and the annealing temperature dependence in Section 3.6.3 have not been interpreted by this model. Moreover, the quantitative discussion regarding the FSE phenomenon, as well as the driving force of forming the pyramid structures at 300 K without electric field, has not been clarified in this study. In order to construct a concrete model of the FSE, further investigation will be needed in future.

3.7 Summary

In this chapter, the FSE properties from W tip surfaces were investigated using FIM and FEM. The experimental results on the FSE current, I_p, were summarized as follows:

1) FSE did not take place at an ideal W surface.
2) The annealing treatment 800 K to the ideal W tip caused FSE.
3) The FSE intensity showed temperature dependence.
4) The temperature dependence of FSE was independent of the annealing time, while it depended on the annealing temperature.
5) FSE showed the different applied voltage dependence from the steady-state field emission.

Moreover, the application of FIM and FEM technique to the FSE study provided the following results:

6) On the {111} crystal planes of the W tip, a pyramid protrusion was formed by the annealing treatment at 800 K.
7) The structural transformation of such a protrusion at the temperatures between 200 and 400 K was estimated by FEM.
8) The strong FSE signal from the (111) face, where the pyramid protrusions were expected, was identified by the *FSE-image* captured by CCD device.
9) The emission mechanism based upon such a structural transformation was proposed, and the temperature dependence of FSE was succeeded to explain qualitatively.

References

[1] "*Exo-Electron Emission from Abraded Metal Surfaces at High and Ultrahigh Vacuums*"; J. A. Ramsey, Journal of Applied Physics, vol. 37 (1966) 452 ~ 453.

[2] "*Investigation of Exo-Electron Emission of Clean Semiconductor Surfaces*"; J. Drenckhan, H. Gross and H. Glaefeke, Physica Status Solidi A, vol. 2 no. 4 (1970) K201.

[3] "*Exoelectron Emission from Aluminum in Ultrahigh Vacuum*"; V. I. Svitov and I. V. Krylova, Soviet Physics-Solid State, vol. 17 no. 9 (1975) 1858 ~ 1859.

[4] "*The chemical aspects of exoemission*"; I. V. Krylova, Russian Chemical Reviews, vol. 45 no. 12 (1976) 1101 ~ 1976.

[5] "*Storage Effect in Photo-stimulated Exoelectron Emission from Scratched Aluminum*"; H. Shigekawa and S. Hyodo, Japanese Journal of Applied Physics, vol. 21 no. 9 (1982) 1278 ~ 1282.

[6] "*Change of Energy-level Distribution of Photoemission Sources in Al and Zn Caused by Scratching*"; H. Shigekawa, R. Iwatsu, M. Okada and S. Hyodo, Japanese Journal of Applied Physics Part 1, vol. 22 no. 1 (1983) 42 ~ 45.

[7] "*Intensity vs. Time Profiles of Photostimulated Exoelectron Emission from Scratched Aluminum*"; H. Shigekawa and S. Hyodo, Japanese Journal of Applied Physics Part 1, vol. 22 no. 10 (1983) 1493 ~ 1495.

[8] "*Deformation Enhanced Photoemission from Aluminum I. Experimental Results*"; O. Buck, W. J. Pardee, F. J. Szalkowski and D. O. Thompson, Applied Physics, vol. 12 no. 4 (1977) 301 ~ 310.

[9] "*Exoelectron Emission Accompanying Phase Changes in Age-hardenable Aluminum Alloys*"; T. Górecki and C. Górecki, Japanese Journal of Applied Physics Supplement, vol. 24-4 (1985) 102 ~ 105.

[10] "*Field-Stimulated Exoelectron Emission from 99.9999% Pure Al*"; M. Tagawa, S. Takenobu, N. Ohmae and M. Umeno; Applied Physics Letters, vol. 53 no. 7 (1988) 626 ~ 627.

[11] "*The Trap-Level of Exoelectron and Field-Stimulated Exoelectron Emission of High Purity Al*"; M. Tagawa, M. Umeno, N. Ohmae and S. Takenobu, Japanese Journal of

Tribology, vol. 34 no.10 (1989) 1175 ~ 1184.

[12] "*Distribution of Trap Levels in Field-Stimulated Exoelectron Emission*"; M. Tagawa, K. Tsuzuki, M. Mori, N. Ohmae and M. Umeno, Applied Physics Letters, vol.61 no. 12 (1992) 1471 ~ 1473.

[13] "*Influence of Oxygen Adsorption on Field-Stimulated Exoelectron Emission from High-Purity Aluminum*"; M. Tagawa, M. Mori, N. Ohmae and M. Umeno, Applied Surface Science, vol.72 no. 3 (1993) 259 ~ 265.

[14] "*Temperature Dependence of the Field-Stimulated Exoelectron Emission*"; M. Mori, E. Ogawa, M. Tagawa, N. Ohmae and M. Umeno, Applied Surface Science, vol.76/77 (1994) 21 ~ 25.

[15] "*Field Ion Microscopy (Principles and Applications)*"; E. W. Müller and T. T. Tsong, (American Elsevier Publishing Company Inc., New York, 1969).

[16] "*Field Emission and Field Ionization*"; R. Gomer, (Harvard University Press, Cambridge, 1961).

[17] "*The Emission of Electrons under the Influence of Intense Electric Fields*"; M. S. Gossling, Philosophical Magazine, vol. 1 no. 3 (1926) 609 ~ 635.

[18] "*Electron Emission in Intense Electric Fields*"; R. H. Fowler and L. W. Nordheim, Proceedings of the Royal Society of London Series A, vol. 119 no. 781 (1928) 173 ~181.

[19] "*The Effect of the Image Force on the Emission and Reflection of Electrons by Metals*"; L. W. Nordheim, Proceeding of the Royal Society of London Series A, vol. 121 (1928) 626 ~ 639.

[20] "*Die Abhängigkeit der Feldelektronenemission von der Austrittsarbeit*"; E. W. Müller, Zeitschrift fur Physik, vol. 102 (1936) 734 ~ 761.

[21] "*Surface Electronic Properties*"; T. Kuroda, (The Nikkan Kogyo Sinbunnsya ltd., Tokyo, 1995) p. 245 [in Japanese].

[22] "*The Thermal Stability and Rearrangement of Field-Evaporated Tungsten Surfaces*"; D. W. Bassett, Proceedings of the Royal Society of London A, vol. 286 (1965) 191 ~ 203.

[23] "*The Work Function of Polycrystalline Tungsten Foil*"; B. J. Hopkins and J. C. Riviere, Proceedings of the Physical Society, vol. 81 no. 521 (1963) 590 ~ 592.

[24] "*Origin of the Field-Stimulated Exoelectron Emission from Tungsten Tip Surfaces*"; T. Shiota, M. Morita, M. Tagawa, N. Ohmae and M. Umeno, Ultramicroscopy, vol. 73 no.

1-4 (1998) 217 ~ 221.

[25] "*Simultaneous Adsorption of Hydrogen and Carbon Monoxide on Tungsten*"; Yu. K. Ustinov, Soviet Physics-Solid State, vol. 13 no. 2 (1971) 447 ~ 452.

[26] "*Surface Structure Dependence of O_2-W Adsorption System*"; M. Sato, Applied Surface Science, vol. 82/83 (1994) 532 ~ 536.

[27] "*Application of Field Emission to Chemisorption*"; R. Gomer, Surface Science, vol. 70 (1978) 19 ~ 31.

[28] "*Field Ion Microscope Studies of Single-Atom Surface Diffusion and Cluster Nucleation on Metal Surfaces*"; G. L. Kellogg, Surface Science Reports, vol. 21 (1994) 1 ~ 88.

[29] "*Atomic View of Surface Diffusion with and without a Driving Force, and Atomic Interactions*"; T. T. Tsong, P. Cowan and G. Kellogg, Thin Solid Films, vol. 25 (1975) 97 ~ 106.

[30] "*Surface Diffusion Measurements by Digitized Autocolleration of Field Emission Current Fluctuations*"; J. E. Whitten and R. Gomer, Review of Scientific Instruments, vol. 65 no. 12 (1994) 3707 ~ 3717.

[31] "*A Combined FIM, AES and LEED Study of the Structure and Composition of Ion Bombarded Tungsten Surfaces*"; J. M. Walls, A. D. Martin and H. B. Southworth, Surface Science vol. 50 (1975) 360 ~378.

[32] "*Field-Ion Microscope Observations of He Ion Bombardment Damage in Tungsten*"; J. M. Walls, R. M. Boothby and H. B. Southworth, Surface Science, vol. 61 (1976) 419 ~ 434.

[33] "*Combined FIM and TEM of Heavy Ion Damage in Tungsten*"; K. Stiller, Radiation Effects and Defects in Solids, vol. 115 (1990) 205 ~215.

[34] "*Study of Surface by Using New Tools*"; J. A. Becker, Solid State Physics, vol. 7 (Academic, New York, 1958) p.379 ~ 424.

[35] "*The Surface Potential of Hydrogen on Tungsten (100), (110) and (112) Single Crystal Surfaces*"; B. J. Hopkins and S. Usami, Surface Science, vol. 23 no.2 (1970) 423 ~ 426.

[36] "*The Clean Thermally Induced W(001) (1x1) to* $\left(\sqrt{2}x\sqrt{2}\right)$ *R 45 Degrees Surface Structure Transition and its Crystallography*"; M. K. Debe and D. A. King, Surface Science, vol. 81 no. 1 (1979) 193 ~ 237.

[37] "*A LEED Study of Structures Produced by H_2 on (100) W*"; K. Yonehara and L. D. Schmidt, Surface Science, vol. 25 no. 2 (1971) 238 ~ 260.

[38] "*Temperature and Field Effects on Atomic Arrangements of Clean Tungsten Tip Surfaces Observed by FIM*"; S. Nishigaki and S. Nakamura, Japanese Journal of Applied Physics, vol. 15 no. 1 (1976) 19 ~ 28.

[39] "*Anomaly of the Thermal-Field Emission and Total-Energy Distribution of the (012), (013), and (023) Tungsten Faces*"; J. K. Wysocki, Physical Review B, vol. 28 no. 2 (1983) 834 ~ 841.

[40] "*Multilayer Reconstruction and Vibrational Properties of W(001)*"; C. L. Fu and A. J. Freeman, Physical Review B, vol. 37 no. 5 (1988) 2685 ~ 2688.

[41] "*Monte Carlo Study of the W(001) Surface Reconstruction Transition Based on Total-Energy Calculations*"; L. D. Roelofs, T. Ramseyer, L. L. taylor, D. Singh and H. Krakauer, Physical Review B, vol. 40 no. 13 (1989) 9147 ~ 9154.

[42] "*Activation Energy for the Surface Migration of Tungsten in the Presence of a High-Electric Field*"; P. C. Bettler and F. M. Charbonnier, Physical Review, vol. 119 no. 1 (1960) 85 ~ 93.

[43] "*Surface Self-Diffusion of Nickel and Platinum*"; A. J. Melmed, Journal of Applied Physics, vol. 38 no. 4 (1967) 1885 ~ 1892.

[44] "*Photostimulated EEE Accompanying Structural Transformations in Metallic Glasses (Exoelectron Emission)*"; T. Górecki and C. Górecki, Japanese Journal of Applied Physics Supplement, vol. 24-4 (1985) 27 ~ 31.

[45] "*Role of Non-Stoichiometry in Exoelectron Oxide Emission 1. Emission Centers*"; V. S. Kortov, Japanese Journal of Applied Physics Supplement, vol. 24-4 (1985) 65 ~ 68.

[46] "*Reconstruction of the {111} Face on a Tungsten Tip Observed by means of a Scanning Field Emission Microscope (SFEM)*"; B. Barwinski and S. Sendecki, Applied Surface Science, vol. 119 no. 1-2 (1997) 111 ~ 116.

[47] "*Field-Emission Electron Spectroscopy of Single-Atom Tips*"; V. T. Binh, S. T. Purcell, N. Garcia and J. Doglioni, Physical Review Letters, vol. 69 no. 17 (1992) 2527 ~ 2530.

[48] "*An Atomic View of Surface Self-diffusion on the Tungsten Tip with or without High Fields*"; S. Nishigaki and S. Nakamura, Japanese Journal of Applied Physics, vol. 15 no. 9 (1976) 1647 ~ 1654.

Chapter 4

Field-Stimulated Exoemission from the Sputtered W Surface

4.1 Introduction

A surface defect has been considered to be one of the origins of exoemission. There have been a number of researches regarding TSE from the surface with such a defect. However, the quantitative relationship between the amount of surface defects and the exoemission intensity has not been clarified yet on TSE. Moreover, exoemission site has not been also identified. On the other hand, in the FSE experiments, the surface of a tip used as a sample can be characterized by FIM with an atomic resolution.

In this study, a W tip, which can be relatively easily imaged by FIM, was used as a sample of FSE study in order to elucidate a relationship between surface defects and FSE quantitatively. The introduction of surface defect was conducted by the ion bombardment with cathode sputtering technique. The controllability of the defect formation on the cathode sputtering is suitable for the FSE research. The presence of threshold energy of impinging ions to show FSE from the W tip surface was confirmed, and the relationship between FSE and the sputtering of the surface atoms are discussed.

4.2 Cathode Sputtering

A cathode sputtering is one of the methods of low-energy ion bombardment, and has been applied to the field emission studies. Before FEM was invented, Müller had already established the cathode sputtering method and investigated its effect when the field emitter was operated in a gas environment [1]. Also, there have been a number of reports regarding defect formation on a tip surface by the cathode sputtering with the energies from several hundreds eV to several keV. [2-4]. In the cathode sputtering, although the sample is restricted to a sharp tip, any kinds of gas can be used as a sputtering gas and the energy of the incident ions can be changed widely by adjusting the applied voltage to the sample. Moreover, FIM has been established as a method to evaluate the tip surface with an atomic resolution, as is discussed in Section 3.3. Therefore, the defects formed on the tip surface by the cathode sputtering can be characterized by FIM observation.

A principle of the cathode sputtering is shown in Figure 4-1. The vacuum chamber, in which a tip was installed, is evacuated up to UHV, and a desired sputtering gas is introduced into the UHV chamber. The negative high voltage is applied to the tip, and then electrons are emitted from the tip surface toward the anode screen. Since the mean free

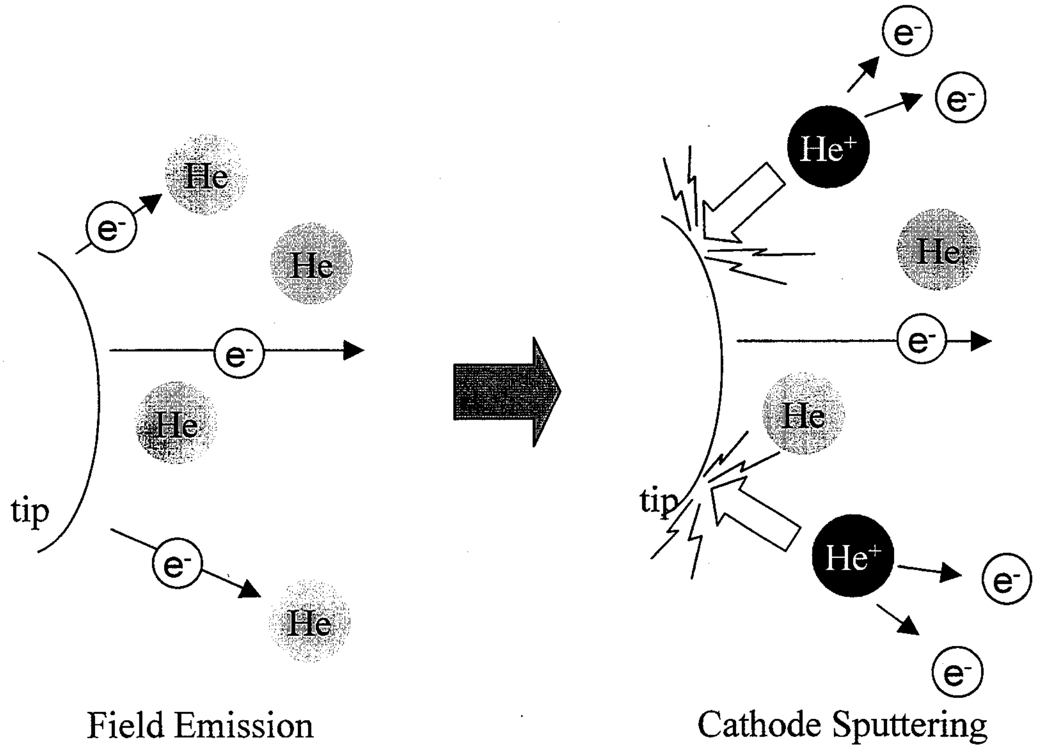

Figure 4-1 Schematics of the cathode sputtering process. He gas is used as a sputtering gas.

path in the chamber is smaller than the distance between the tip and screen, the collisions of field-emitted electrons with gas atoms are expected to occur. When the electron energy of the field-emitted electrons reaches a several hundreds eV, gas atoms are positively ionized due to the electron impact ionization. Such positive ions are attracted by the electric field to the tip, and bombard the tip surface.

The ion dose and ion energy of the cathode sputtering are estimated as follows: Walls et al. reported that the ion current could be estimated by using the field emission current I_F, the path length of the electrons L, and the ionization probability of the gas species σ [5]. According to their reports, the number of incident ions per unit time and area onto the tip during the cathode sputtering, n, is expressed by the following equation;

$$n = \frac{I_F}{e} \cdot L\sigma\left(\frac{273}{T}\right)P \tag{4-1}$$

where T, P and e are the gas temperature, the partial pressure of sputtering gas and the elementary electric charge, respectively. In this calculation, all of the ions are considered to be collected by the tip. However, Dranava et al. [6] pointed out that the fraction of ions impinging on the tip surface was given by $(3/7)\beta\pi r^2 L^{7/3}$, where β and r are the constant and the radius of curvature of tip apex, respectively. In this study, both equations are taken into account with the constants of $\sigma = 10^{-3}$ [7], $L = 5cm$, $P = 1.3\times10^{-2} Pa$, $\beta = 2.3\times10^{4} cm^{-4/3}$ [6] and $r = 30nm$. Using these values, the ion dose, N, per unit area of the tip surface is expressed;

$$N = 1.2\times10^{17} I_F t \tag{4-2}$$

where t represents the sputtering time in seconds.

The energy distribution of incident ions in the cathode sputtering attributes to the potential difference between the space where ions are formed and the tip surface. However, since high electric field is limited only at the area close to tip surface in the case of tip-screen configuration, it is considered that the average incident energy of ions are close to the tip voltage. Therefore, in this study, the voltage applied to the tip was used as the impinging energy of the sputtering ions.

4.3 Experiments

The experimental apparatus used in this study is shown in Figure 4-2, and this is a similar facility described in Section 3.4.2. The FIM/FEM observation chamber was evacuated by a turbo molecular pump, a titanium getter pump, an ion pump and a cryo pump. The ultimate pressure in the chamber attained to an order of 10^{-8} Pa. The measurement systems of emission current or FIM/FEM images were the same of those described in Section 3.4.2. The tip was cooled down to 185 K when liquid nitrogen was poured into the cold finger. A 99.95 % W-wire was used as a sample. The sample preparation followed the procedure described in Section 3.4.1. The cleaning of W tip surface was performed by field evaporation during the FIM observation. After the cleaning treatment, W tip surface was bombarded by low-energy He^+ ions. The ion bombardment over the tip surface was conducted using the cathode sputtering technique, and the detail of the sputtering is described below.

1) The pressure in the UHV chamber was confirmed to be lower than 10^{-8} Pa.
2) He gas, which was used as a sputtering gas, was introduced through variable leak

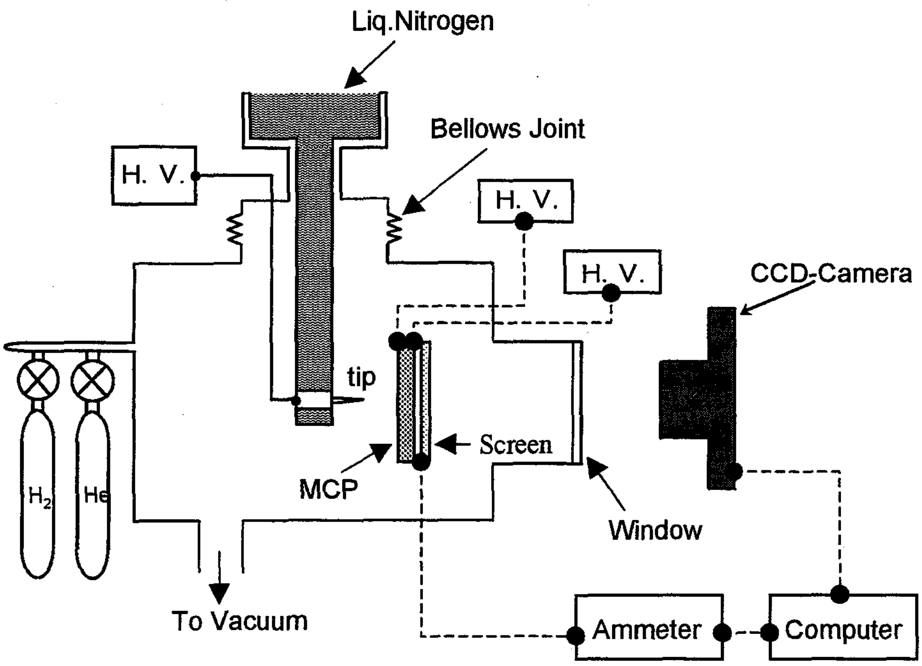

Figure 4-2 Schematics of the experimental facility used in this study.

valve (VLV) into the UHV chamber at a partial pressure of 1.3 x 10^{-2} Pa.

3) A proper negative voltage was applied to the tip and the cathode sputtering was carried out for 180 s.
4) As soon as the cathode sputtering was completed, He gas was evacuated and the pressure of the chamber was recovered to an order of 10^{-8} Pa.

FSE signal was detected by measuring the temporal enhancement of the emission current (I_p), as described in Section 3.4.3. Note that the difference of the experimental procedure was that a steady-state emission current was taken to be not 3 x 10^{-13} A, but 5 x 10^{-10} A. This is because the sensitivity of the current detection system used in this study is lower than that described in Section 3.4.

4.4 Results and Discussion

4.4.1 Effect of He Exposure on FSE

As described in the previous section, the cathode sputtering of a W tip surface in this study was carried out at 185 K in He gas atmosphere. Therefore, some He atoms, which are not ionized, would be adsorbed on the W surface because the tip was cooled down to 185 K. Since a gas adsorption on the metal surface has been considered as one of the origins of exoemission, the effect of He adsorption over the W tip surface on the FSE property was examined. The W tip was exposed to He gas with a partial pressure of 1.3 x 10^{-2} Pa for 180 s after the cleaning by field evaporation, which was the same condition as the cathode sputtering (see Section 4.3). Before the FSE measurement, He gas introduced into the UHV chamber was analyzed by the quadrupole mass spectroscopy (QMS). In order to avoid any damages of the filament attached in QMS, the measurement was carried out in the He gas atmosphere with a pressure of 1.3 x 10^{-3} Pa. The result is shown in Figure 4-3. No impurity in the He gas was detected. The FSE measurements were conducted before the He exposure, immediately after the He exposure, 1 hour and 2 hours after the He exposures. Figure 4-4 indicates the result of this experiment. The same measurements were repeated three times. The mean value and dispersion of the measured I_p are shown by

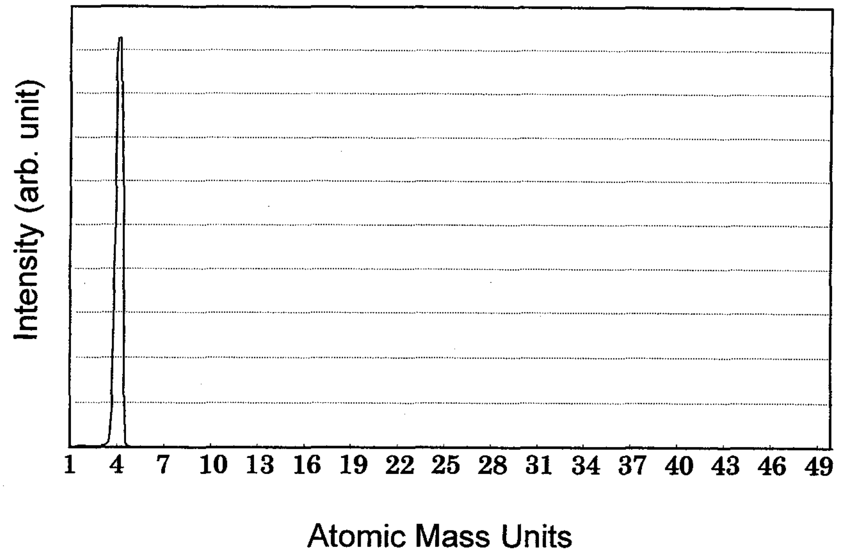

Figure 4-3 QMS spectrum in the He gas with a partial pressure of 1.3 x 10^{-3} Pa.

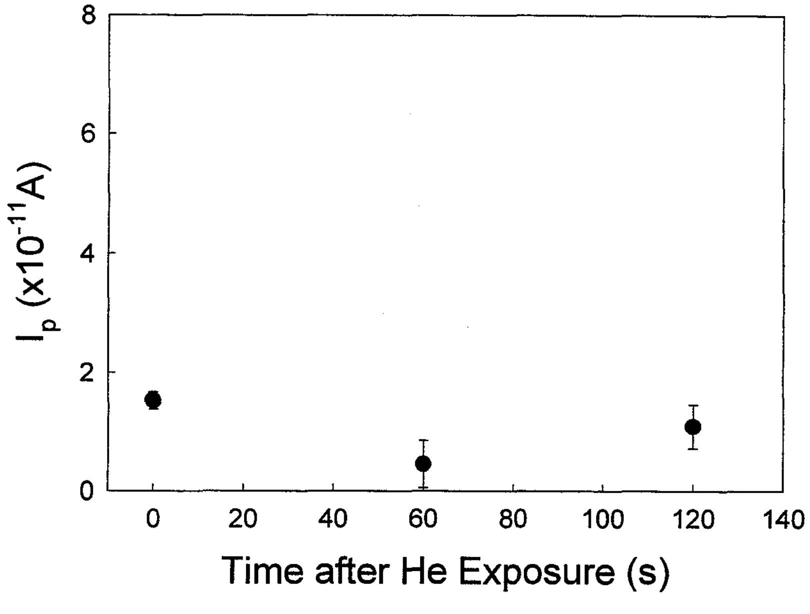

Figure 4-4 FSE intensities, I_p, from the W tip exposed to He gas without ion bombardment. The measurements were performed at 0, 60 and 120 s after the exposure in the UHV atmosphere.

symbols and error bars, respectively. From the Figure 4-4, it was found that I_p from W tips due to He exposure during the cathode sputtering process was lower than 1.5 x 10^{-11} A.

4.4.2 Incident Energy Dependence

The dependence of incident energies of He^+ ions upon I_p was examined. In this measurement, the enhancement of emission due to the He exposure of 1.5 x 10^{-11} A (see Figure 4-4) was subtracted from the FSE signal of ion-bombarded surfaces. The FSE intensities from the clean and the ion-bombarded W tip surfaces were measured, and the difference in FSE intensities was considered to be FSE. The results are shown in Figure 4-5. The measurements were repeated three times, and the mean values and dispersions of the collected data are represented by the symbols and error bars in the graph. I_p kept constant value of about 1 x 10^{-11} A until the incident energy of He^+ ions reached 500 eV. Since these I_p values were lower than that measured after He exposure, which was considered to be background level as described in Section 4.4.1, it was concluded that no FSE was detected at the incident energies from 390 to 500 eV. In contrast, a clear FSE signal I_p was observed and it increased with the incident energies of He^+ ions higher than 500 eV. When an ion with incident energy of E collides to a surface atom, maximum energy (E_t), which can be transferred from the incident ion to the surface atom, is provided by the following equation [8];

$$E_t = 4EMm/(M+m)^2 \qquad (4\text{-}3)$$

where m and M are the mass of the incident ion and the surface atom, respectively. According to the equation (4-3), the incident energy E of He^+ ions of 500 eV, which corresponds to the threshold of appearance of FSE, can transfer the energy of 41.6 eV to the surface W atom. The maximum energy transferred to the W atoms from the He^+ ions with the energy of 500 eV is very close to the sputtering threshold of the W atom which was reported to be 40 eV [9]. Actually, it was confirmed in this experiment that the vacancies at the W tip surface were created after the He^+ ion bombardment with the incident energy of 550 eV. The fact that FSE was observed due to the ion bombardment with an incident energy slightly higher than that required for the vacancy formation suggests that the FSE from W tips is related to the distortion of the atomic arrangements of W surface.

In this experiment, the He^+ ion dose of the ion bombardment at the energies lower than 500 eV, in which FSE was not observed, was estimated to be 1.4 x 10^{13} ions/cm^2 from the equation (4-2). In contrast, the He^+ ion dose of 1.2 x 10^{10} ions/cm^2 was introduced to the W tip surface with the incident energies from 500 to 570 eV. This is because the W tip surfaces were heavily damaged at the high dose of He^+ ions with the energies over 500 eV. These experimental results clearly indicate that the dose of He^+ ions is not a primary factor for appearance of FSE, but the incident energy is.

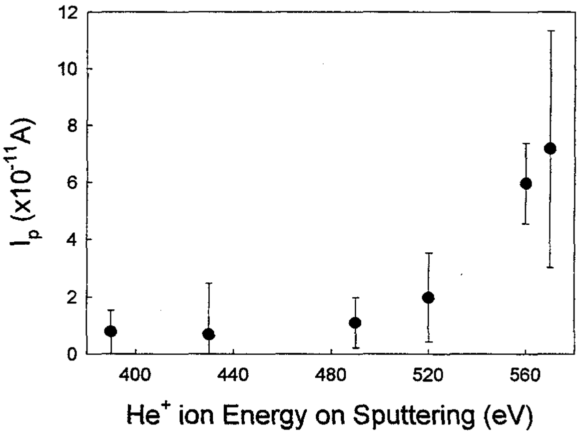

Figure 4-5 FSE from W surfaces bombarded by He^+ ions with energies ranging from 390 to 570 eV.

4.4.3 Decay of FSE

It has been recognized that the intensity of PSE from a mechanically damaged metal surface decayed with time in the range of a few hours to several tens hours [10-13]. In this study, the history of FSE intensities after the ion bombardment was also investigated. The measurements of FSE were made at 0, 60 and 120 s after He^+ ion bombardment with the incident energies of 390 and 560 eV at 185 K. The experimental results are shown in Figure 4-6. The filled and open circles indicate the results obtained from the ion-bombarded surfaces with the incident energies of 390 and 560 eV, respectively. The symbols and error bars in the graph show the mean values and dispersions of the data measured by the experiments repeated three times, respectively. Also, the time history of FSE from the W surface exposed to He gas atmosphere shown in Figure 4-4 is superimposed in Figure 4-6 and represented by filled triangles. A clear FSE signal I_p was not detected on the W surface ion-bombarded at 390 eV as well as the W surface without the ion bombardment. However, I_p from the W surface bombarded by He^+ ions with the incident energy of 560 eV was remarkable and decayed slowly with time. It was confirmed that

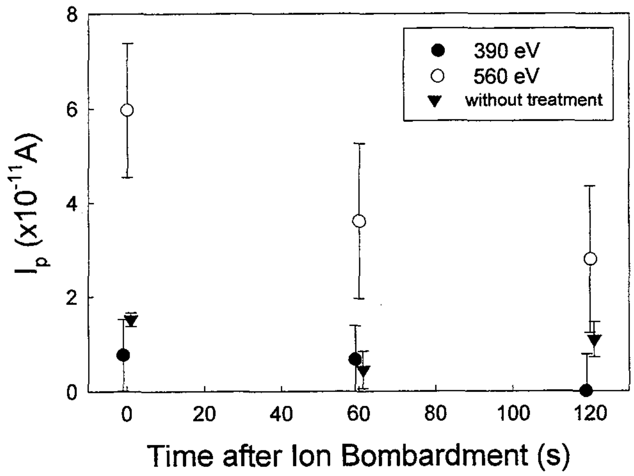

Figure 4-6 Variations of FSE from the ion-bombarded W surfaces at 390 and 560 eV, which were measured at 185 K.

FSE observed here had tendency to decay as well as PSE from mechanically treated metal surfaces [10].

This emission property becomes one of the keys to elucidate the mechanism of FSE from the ion-bombarded W surface. In order to apply the two-process model, which explain FSE phenomena from Al tips, it is essential that I_p depends on the interruption period of applied voltage. However, the dependence of I_p on the interruption was not observed in the case of FSE from the ion-bombarded W tip surfaces. The independence of I_p on the interruption period was also observed in FSE from the clean W tip surfaces after annealing at 800 K, as described in Section 3.6.2. Therefore, the decay of I_p with time, which is shown in Figure 4-6, may be explained by the emission mechanism based upon the diffusion of surface atoms as proposed in Section 3.6.7. In the experiment described in Section 3.6.2, I_p was only detected at the temperature range where the change of atomic arrangement on the W tip surface was expected. At this temperature, the activation energy for self-diffusion of W atoms was considered to become quite low, because the structural transformation of W surface could take place thermally even without a help of high electric field. Also, it has been reported that the high electric field applied to the tip surface, which was enough to emit electrons from the surface, reduced the activation energy for the surface diffusion of W atoms [14] and led to the field-induced tensile stress at the tip surface [15]. Therefore, we concluded that FSE from the annealed W tips was related to the surface diffusion of W atoms. According to this emission model, the decay of I_p observed here would be explained as follows: The low-energy ion bombardment, which is slightly higher than the threshold energy for sputtering a W atom, introduces the perturbation of the atomic arrangement of the W surface atoms. This perturbation makes the potential energy of W atoms high. Such W atoms locate the position energetically high, so that the high electric field, which reduces activation energy for surface diffusion, may induce the relaxation of the ion-bombarded surface. The electrons may be emitted by receiving the excess energy during this relaxation process and are detected as FSE signal I_p. The relaxation process may also be driven by the thermal activation process, and the number of perturbed atoms, thus, would decrease gradually with time. This mechanism can result in the decay of I_p observed in Figure 4-6.

4.4.4 Temperature Dependence

In order to verify the proposed mechanism that the decay of I_p was related to surface relaxation process as described above, the same experiment was conducted at 300 K as well as at 185 K. The W tip surface was bombarded at 300 K by He$^+$ ions with an incident

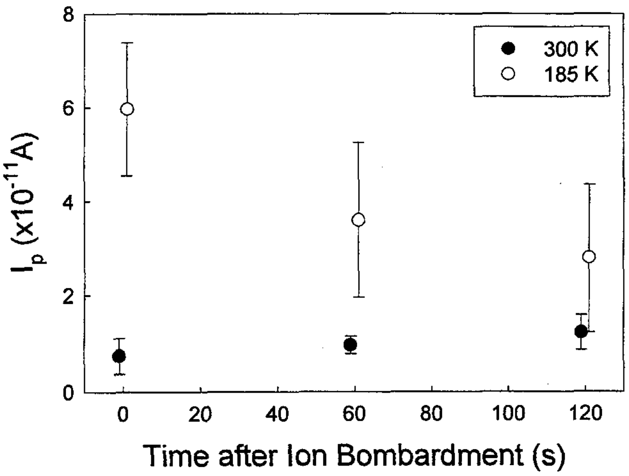

Figure 4-7 Comparison of FSE properties from560 eV ion-bombarded W surfaces at 300 and 185 K.

energy of 530 eV. The ion dose during the bombardment was 1.2 x 10^{10} ions/cm^2, which was the same as the previous experiment at 185 K shown in Figure 4-6. The experimental results at 300 K are shown in Figure 4-7. The filled circles indicate the data measured at 300 K, and the open circles are those obtained at 185. From Figure 4-7, it is obvious that no FSE signal was detected at 300 K.

The probability of the thermally driven surface diffusion, *P*, can be roughly estimated by the Arrehenius-type equation [14];

$$P = \omega \exp\left(-E_d / kT\right) \tag{4-4}$$

where ω and E_d are the pre-exponential factor and the activation energy for the surface self-diffusion of W atoms, respectively. The diffusion probability at 300 K calculated from the equation (4-4) was 6 ~ 10 orders of magnitude greater than that at 185 K, when E_d was estimated to be reference values from 0.57 to 0.96 eV [16-18]. During the cathode sputtering, He gas with a partial pressure of 1.3 x 10^{-2} Pa was introduced as a sputtering gas. In this experimental apparatus, it took at least 20 min to recover the pressure to an order of 10^{-8} Pa after the cathode sputtering. Therefore, the relaxation of W tip surface ion-bombarded at 300 K could be completed before the measurement of emission current. That is the positive reason why no I_p from the ion-bombarded surface was detected at 300 K, while obvious I_p was observed at 185 K. Also, this model is supported by the fact that the self-diffusion of W atoms took place at a temperature higher than 300 K [14,19].

4.5 Conclusion

FSE from the W tip surfaces bombarded by He^+ ions with energies ranging from 390 to 570 eV was investigated. It was found that FSE took place on the W surface ion-bombarded with energies higher than 500 eV, which corresponded to the sputtering threshold of a W atom. The FSE from the ion-bombarded surface depends strongly on the incident energy of He^+ ions and the tip temperature. The time history of I_p indicated a slow decay. All of these FSE properties can be explained by the emission model proposed in this study which relates to the surface diffusion of W atoms after the ion bombardment.

References

[1] "*Beobachtungen über die Feldemission und die Kathoden-zerstäubung an Thoriertem Wolfram*"; E. W. Müller; Zeitschrift fur Physik, vol. 106 (1937) 132 ~ 140.

[2] "*Study of Atomic Structure of Metal Surfaces in the Field Ion Microscope*"; E. W. Müller; Journal Applied Physics, vol. 28 no. 1 (1957) 1 ~ 6.

[3] "*Field Ion Microscope*"; K. M. Bowkett and D. A. Smith; (North-Holland, Amsterdam, 1970) p180.

[4] "*FIM Observation of Point Defect Clusters in Ion-implanted Tungsten Surfaces*"; N. Igata and S. Sato, Nanotechnology, vol. 4 no. 4 (1993) 213 ~ 217.

[5] "*Field Ion Microscope Observations of Helium Ion Bombardment Damage in Tungsten*"; J. M. Walls, R. M. Boothby and H. N. Southworth, Surface Science, vol. 61 no. 2 (1976) 419 ~ 434.

[6] "*Low-temperature Surface Migration of Tungsten Activated by Ion Bombardment*"; Zh. I. Dranova and I. M. Mikhailovskii; Soviet Physics-Solid Status, vol. 12 no. 1 (1970) 132 ~ 137.

[7] "*The Ionization of Helium, Neon, and Argon by Electron Impact*"; P. T. Smith, Physical Review, vol. 36 (1930) 1293 ~ 1302.

[8] "*Determination of Displacement Energy of Tungsten Atoms by Irradiating FIM Specimens with Inert Gas Ions*"; S. Tamaki and E. Sugata, Oyo Buturi, vol. 40 no. 4 (1971) 380 ~ 390 [in Japanese].

[9] "*Electron Irradiation and Recovery of Tungsten*"; H. H. Neely, D. W. Keefer and A. Sosin, Physica Status Solidi, vol. 28 (1967) 675 ~ 682.

[10] "*Spectral and Temporal Characteristics of Photostimulated Exoemission from Coldworked Metals*"; H. Käämbre, V. Bichevin, V. Sammelselg, H. Kelle, E. Asari and O. Saks, Applied Surface Science, vol. 136 no. 1-2 (1998) 55 ~ 61.

[11] "*Effect of Temperature on the Exoemission of Electrons from Abraded Aluminum Surfaces*"; W. T. Pimbley and E. E. Francis; Journal of Applied Physics, vol. 32 no. 9 (1961) 1729 ~ 1733.

[12] "*Intensity vs. Time Profiles of Photostimulated Exoelectron Emission from Scratched*

Aluminum"; H. Shigekawa and S. Hyodo, Japanese Journal of Applied Physics, vol. 22 no. 10 (1983) 1493 ~ 1495.

[13] "*Study for initial oxidation behavior of metals by photo-electron emission measurement*"; H. Masuda, S. Matsuoka and N. Nagashima, Corrosion Engineering, vol. 39 no. 7 (1990) 343 ~ 346.

[14] "*An Atomic View of Surface Self-diffusion on the Tungsten Tip with or without High Fields*"; S. Nishigaki and S. Nakamura, Japanese Journal of Applied Physics, vol. 15 no. 9 (1976) 1647 ~ 1654.

[15] "*Field Ion Microscopy (principles and applications)*"; E. W. Müller and T. T. Tsong, (American Elsevier Publishing Company Inc., New York, 1969).

[16] "*Atomic View of Surface Self-Diffusion : Tungsten on Tungsten*"; G. Ehrlich and F. G. Hudda; Journal of Chemical Physics, vol. 44 no.3 (1966) 1039 ~ 1049.

[17] "*Field Ion Microscope Studies of Transition Metal Adatom Diffusion on (110), (211) and (321) Tungsten Surfaces*"; D. W. Bassett and M. J. Parsley, Journal of Physics D, vol. 3 no. 5 (1970) 707 ~ 716.

[18] "*Surface Diffusion and Cluster Binding Energy of Individual Atoms on Tungsten Surfaces*"; T. T. Tsong, Physical Review B, vol. 7 no. 8 (1973) 4018 ~ 4020.

[19] "*The Thermal Stability and Rearrangement of Field-evaporated Tungsten Surfaces*"; D. B. Bassett, Proceedings of the Royal Society of London A, vol. 286 (1965) 191 ~ 203.

Chapter 5

Effect of Gas Adsorption on the Field-Stimulated Exoemision

5.1 Introduction

Adsorption of gases on the solid surface has been considered to be strongly related to exoemission phenomena. As described in Section 2.4, it has been reported that the exoemission takes place when oxygen molecule reacts with alkali metal or Mg surfaces. Also, it was confirmed that adsorption of oxygen and water on metal surfaces caused or enhanced PSE [1-3]. In contrast, there have been some reports that PSE was suppressed by the re-oxidation of deformed metal surfaces as shown in Section 2.2. Thus, the role of gas adsorption to the exoemission phenomena has not yet been made clear.

In FSE, the evaluation of the sample surface can be performed by FIM and FEM with an atomic resolution as described in Section 2.3, and especially using FEM, the electronic structure is obtainable with spatial resolution in a real space. Therefore, if FSE occurs, or is enhanced, due to gas adsorption, it is expected that the relationship between the change in electronic structure at the surface and FSE property may be clarified by using FEM and FIM. Actually, the effect of oxygen adsorption on FSE from Al tips was reported by Tagawa et al. and it was concluded that oxygen adsorption led to FSE enhancement [4]. Also, it was suggested from a temperature dependence of FSE from Al tips that hydrogen adsorption was one of the origins of FSE [5]. However, difficulty of imaging of the Al surface by FEM and FIM prevented further study.

In this chapter, a W tip was used as a specimen because of the easiness of imaging by FIM. The field-evaporated clean W tips were exposed to hydrogen or oxygen gases, and then FSE from the hydrogen- or oxygen-adsorbed W tip surfaces was measured. On the other hand, FSE from the annealed W tip surfaces was observed as shown in Section 3.6.

Therefore, it was examined whether or not the FSE intensity from the annealed W tip surfaces was enhanced due to adsorption of hydrogen or oxygen. The effect of water adsorption, as well as hydrogen or oxygen adsorption, on the FSE was also investigated. In the following sections, the details of the experimental procedure, results and the discussions are described.

5.2 Experimental

The same experimental apparatus explained in Section 3.4.2 was used in all of the experiments performed here. The W tip was prepared by the same procedure described in Section 3.4.1. In this study, hydrogen, oxygen and water were chosen as adsorbates. The exposure of hydrogen or oxygen was carried out by the following procedure:

1) The UHV chamber with a pressure of lower than 1.6×10^{-8} Pa was isolated from the vacuum pump by closing the metal valve.
2) Hydrogen or oxygen gas was introduced through VLV and kept at a partial pressure of $0.7 \sim 1.3 \times 10^{-6}$ Pa for a desired time, and then evacuated.
3) After the pressure recovered lower than 1.6×10^{-8} Pa, the FSE measurement was started.

In contrast, water exposure was carried out in the specimen preparation chamber, because the MCP attached in the FIM observation chamber may be damaged by the water adsorption. The procedure of water exposure is as follows:

1) The W tip was transferred using the transfer rod from the FIM observation chamber to the preparation chamber, and then the preparation chamber was separated from the FIM observation chamber by the gate valve.
2) Water vapor with a partial pressure of 5.3×10^{-5} Pa was introduced to the preparation chamber through VLV.
3) After the exposure, water vapor was evacuated, and then the tip was returned to the FIM observation chamber.
4) FSE from the water-exposed W tip surface was investigated.

The method to detect FSE signal was described in Section 3.4.3. Different from the case of the clean W tip surface, a large fluctuation in a steady-state field emission was measured in some cases. In order to eliminate the uncertainty due to the fluctuation in emission, the corrected data were analyzed by the following method: Steady-state field emission current in *Region A* in Figure 5-1 was fitted by the equation (3-30), which describes field emission current theoretically. The fitting results and experimental data are shown in Figure 5-1 by the open and filled circles, respectively. The 99 % confidence limit of the emission data was calculated in the *Region A*. A difference, I_d, between the calculated and experimental value at the point indicated by *B* is dealt as a FSE signal only when I_d exceeds the 99 % confidence limit of steady-state emission current in *Region A*.

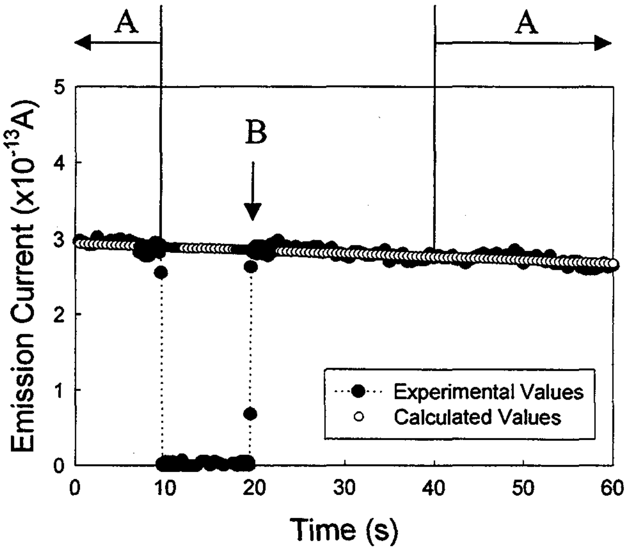

Figure 5-1 The method to measure FSE signal. *Region A* is considered as a steady-state field emission, and the negative voltage is reapplied at the point *B*. The filled and open circles show the experimental data and the fitting results by the equation (3-30), respectively.

5.3 Results and Discussion

5.3.1 Hydrogen Adsorption

Before the FSE measurement, the W tip used in this study was cleaned at 50 K by field evaporation during FIM observation. It was confirmed that no FSE signal from the clean surface was detected at 50 K. The exposure by 0.1 L of hydrogen gas was carried out at 50 K by the procedure described in the previous section and then the FSE from the W tip surface was measured. The exposure and measurement processes were repeated until the total exposure reached 2.0 L. Figure 5-2 (a) shows the result of hydrogen exposure. The work function change due to hydrogen adsorption was measured simultaneously, and the result is indicated in Figure 5-2 (b). The method to estimate the work function was the same of that performed in Section 3.5.2. Since the work function of a clean polycrystalline W surface was reported to be 4.5 eV [6], it was assumed that the mean work function of the initial W tip surface prepared by field evaporation was referred to be 4.5 eV. It was reported by Polizzoti et al. that when hydrogen was adsorbed at 80 K on the W tip surface which was prepared by field evaporation, the average work function over the hydrogen adsorbed W surface with a saturation hydrogen coverage attained to be 5.1 eV [7]. In this study, the average work function over the surface increased gradually with the hydrogen exposure, and it was saturated at about 5.1 eV in the exposure range higher than 0.7 L. The work function change indicated that the amount of hydrogen adsorption was saturated at the exposure of 0.7 L. On the other hand, I_d, which is the FSE signal, measured by the method described in Section 5.2, was smaller than the fluctuation level of steady-state field emission at all of the hydrogen exposures. The fluctuation was measured as a variation in the 99 % confidence limit. Therefore, it was concluded that FSE from the H-adsorbed W surfaces does not take place at 50 K even after the hydrogen adsorption.

The same experiments were performed at the tip temperatures at the temperatures of 150, 300 and 450 K. The experimental results on I_d, fluctuation of the steady-state field emission and the average work function as a function of the hydrogen exposure at 150, 300 and 450 K are shown in Figures 5-3, 5-4 and 5-5. In each figure, (a) and (b) indicate the I_d properties and the work function change, respectively. According to Polizzoti's report, when the W tip surface cleaned by the flashing method was covered with hydrogen, the

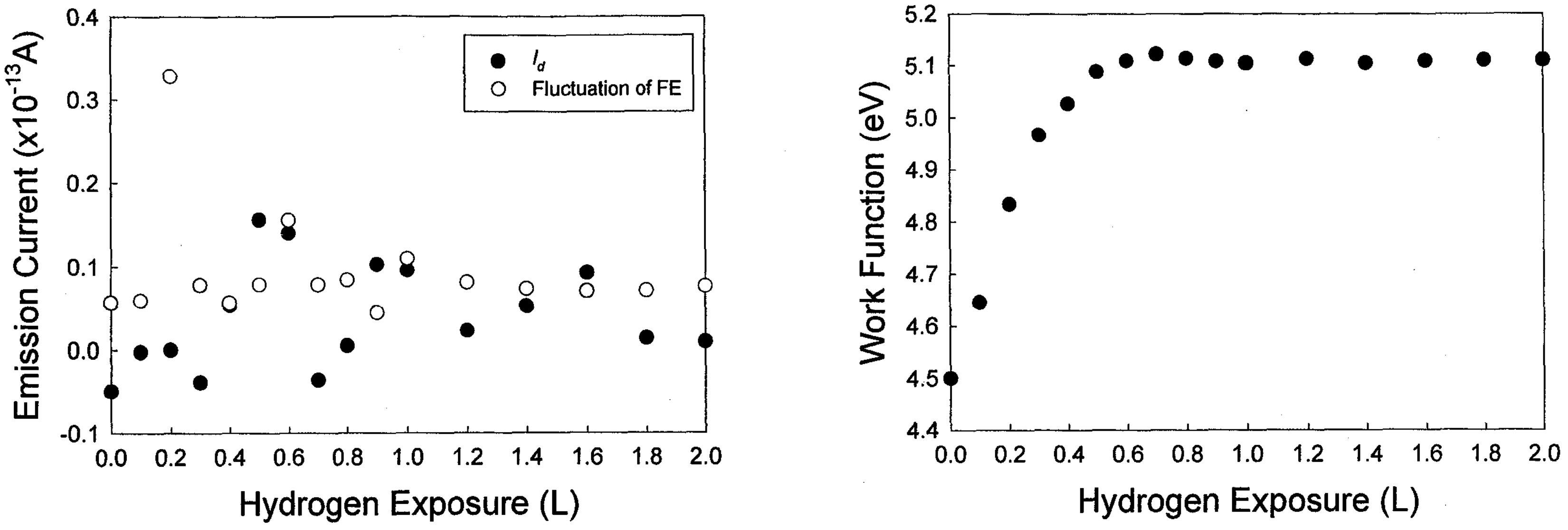

(a) I_d properties at 50 K

(b) mean work function change 50 K

Figure 5-2 Variations of I_d and the mean work function on the hydrogen-adsorbed W surfaces at 50 K as a function of hydrogen exposure; (a) and (b) show the I_d properties and the work function change, respectively.

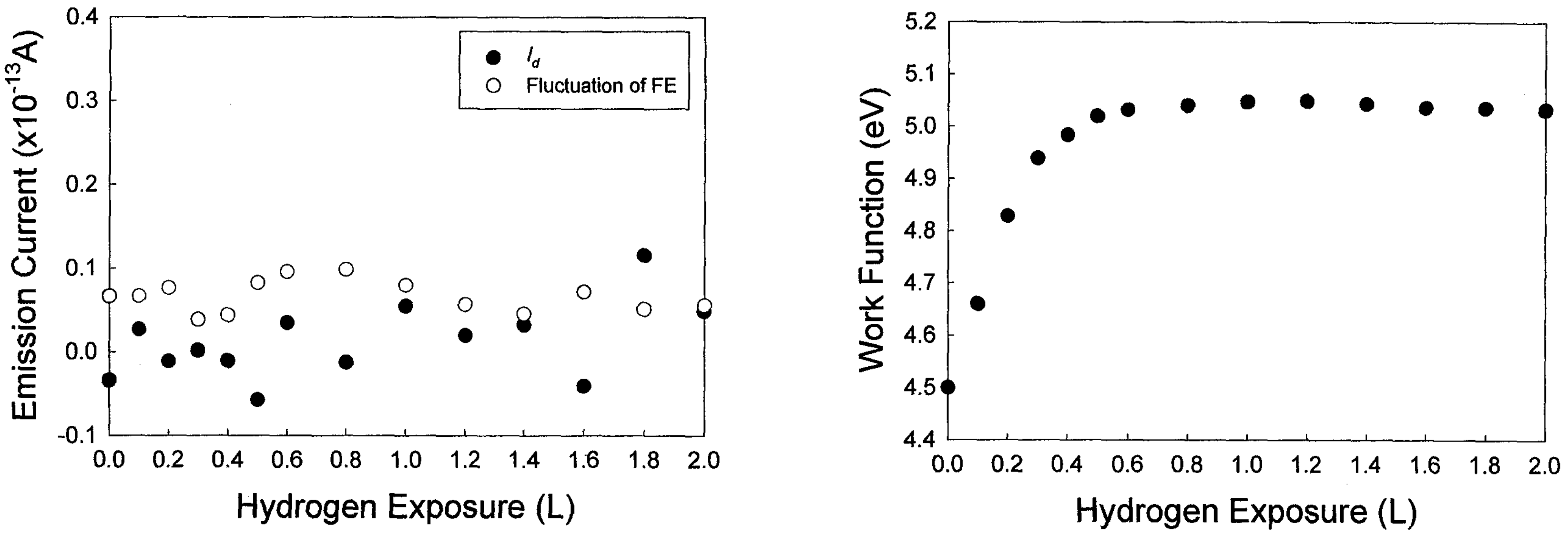

(a) I_d properties at 150 K

(b) mean work function change 150 K

Figure 5-3 Variations of I_d and the mean work function on the hydrogen-adsorbed W surfaces at 150 K as a function of hydrogen exposure; (a) and (b) show the I_d properties and the work function change, respectively.

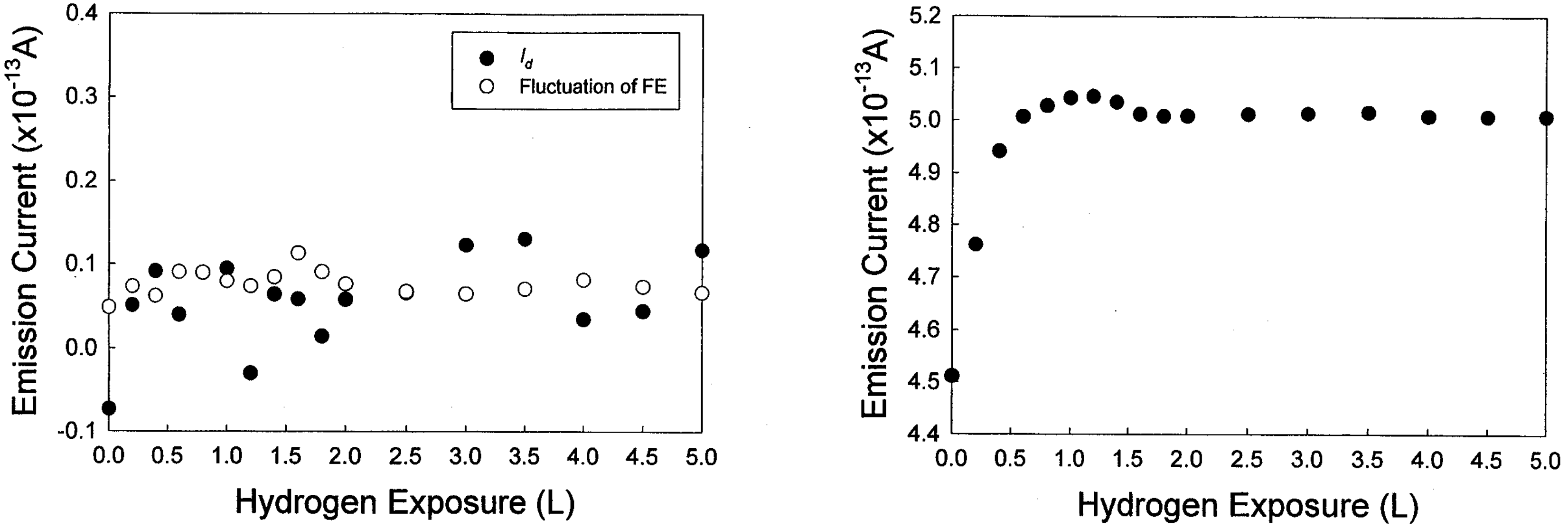

(a) I_d properties at 300 K

(b) mean work function change 300 K

Figure 5-4 Variations of I_d and the mean work function on the hydrogen-adsorbed W surfaces at 300 K as a function of hydrogen exposure; (a) and (b) show the I_d properties and the work function change, respectively.

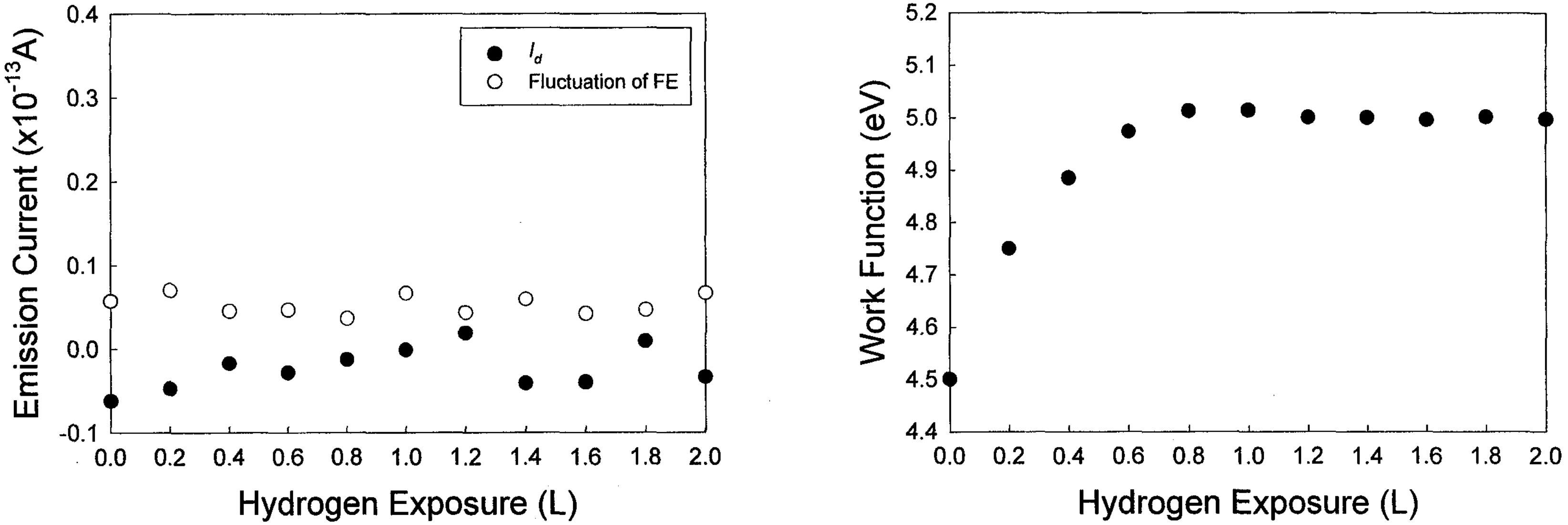

(a) I_d properties at 450 K

(b) mean work function change 450 K

Figure 5-5 Variations of I_d and the mean work function on the hydrogen-adsorbed W surfaces at 450 K as a function of hydrogen exposure; (a) and (b) show the I_d properties and the work function change, respectively.

average work functions at 150 and 300 K were reported to be 4.92 and 4.85 eV [7]. These work functions reported by Polizzoti et al. are slightly lower than those observed in Figure 5-3 and 5-4. However, the average work function of the W surface formed by field evaporation was 0.1 eV higher than that formed by the flashing method, when hydrogen was adsorbed sufficiently on these surfaces at 80 K. Therefore, it is considered that the work function change obtained in this study agrees with the previous report. The filled and open circles in Figures 5-3 (a) ~ 5-5 (a) represent I_d and fluctuation of the steady-state field emission measured by the method described in Section 5.2. It was found that clear FSE was not observed in all cases. From these results, although the adsorbed hydrogen has been considered to be one of origins of FSE from Al tips [5], it does not affect FSE from W tips at temperatures from 50 to 450 K.

In Section 3.5.2, appearance of a clear FSE signal, I_p, on a clean W tip after the annealing treatment was confirmed at around 300 K. In order to confirm the contribution of hydrogen adsorption to the FSE phenomenon, the effect of hydrogen exposures on I_p was examined at 320 K. The experimental result is shown in Figure 5-6. Obviously, I_p decreased rapidly with hydrogen exposure, and finally disappeared at the hydrogen exposure

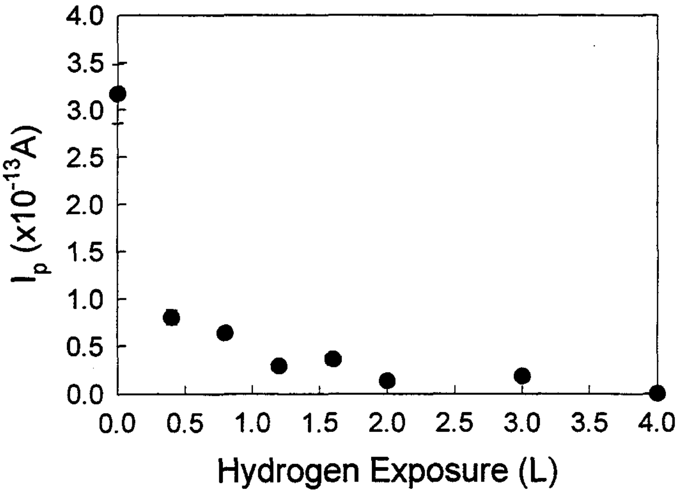

Figure 5-6 Effect of hydrogen exposure on I_p measured at 320 K.

at 4.0L. If I_p is induced by the hydrogen adsorption, I_p should increase with hydrogen exposure. However, as presented in Figure 5-6, hydrogen adsorption reduces I_p. Therefore, it is concluded that FSE on W tips is suppressed by the hydrogen adsorption on the tip surface.

5.3.2 Oxygen Adsorption

The oxygen adsorption has been considered to play an important role of exoemission phenomena. Actually, it was reported that the adsorbed oxygen was one of the origins of FSE from Al tips [4]. In this study, whether or not FSE takes place on oxygen-adsorbed W tip surfaces were identified, as well as the case of hydrogen.

The measurements of FSE from the oxygen-adsorbed W surfaces were performed at 50, 150, 300 and 450 K. Before the FSE measurement, a W tip was cleaned by the field evaporation at 50 K. The cleanliness of the W tip surface was evaluated by FIM image, and it was also confirmed by the fact that no FSE from such a W tip surface was detected at 50 K. After the confirmation of cleanliness, the tip temperature increased to the desired temperatures (50, 150, 300 and 450 K). The W tip was exposed to oxygen gas by the method described in Section 5.2. Figures 5-7 ~ 5-10 show the experimental results at the tip temperatures of 50, 150, 300 and 450 K, respectively. In the Figures 5-7 ~ 5-10, (a) and (b) illustrate the I_d properties and the variation of mean work function over the oxygen-adsorbed W tip surfaces. Moreover, in each figure labeled (a), the filled and open circles represent the fluctuation of the steady-state field emission current and I_d, respectively. At 50 K, as shown in Figure 5-7 (b), the work function of the W tip increased instantly by the oxygen exposures between 0.2 and 0.3 L, and kept constant in oxygen exposures higher than 0.6 L. However, I_d was smaller than the fluctuation of emission at all exposures. Therefore, it was concluded that, even though the oxygen adsorption occurred on the W tip, FSE was not enhanced by the oxygen adsorption. The same tendency was also observed in the experimental results at the temperatures of 150, 300 and 450 K, even though work function changes relatively slower.

Similar to the case of hydrogen adsorption, the effect of oxygen exposure on the FSE from the annealed W tip was also examined. Prior to the measurement, the W tip was

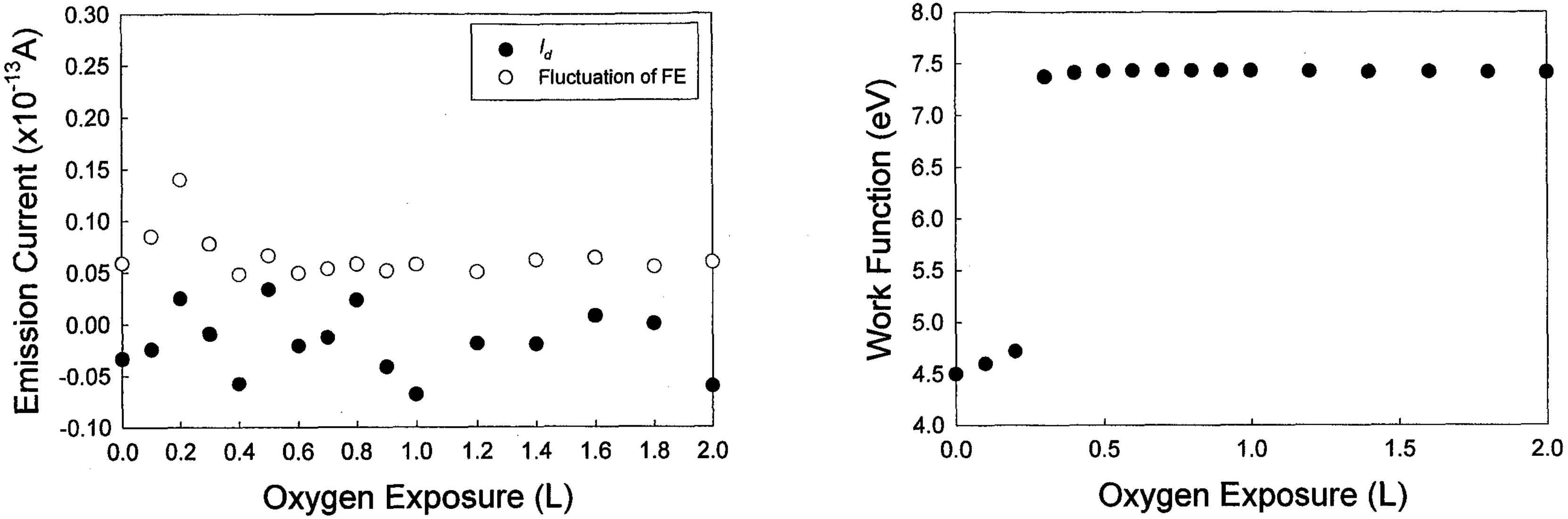

(a) I_d properties at 50 K

(b) mean work function change 50 K

Figure 5-7 Variations of I_d and the mean work function on the oxygen-adsorbed W surfaces at 50 K as a function of hydrogen exposure; (a) and (b) show the I_d properties and the work function change, respectively.

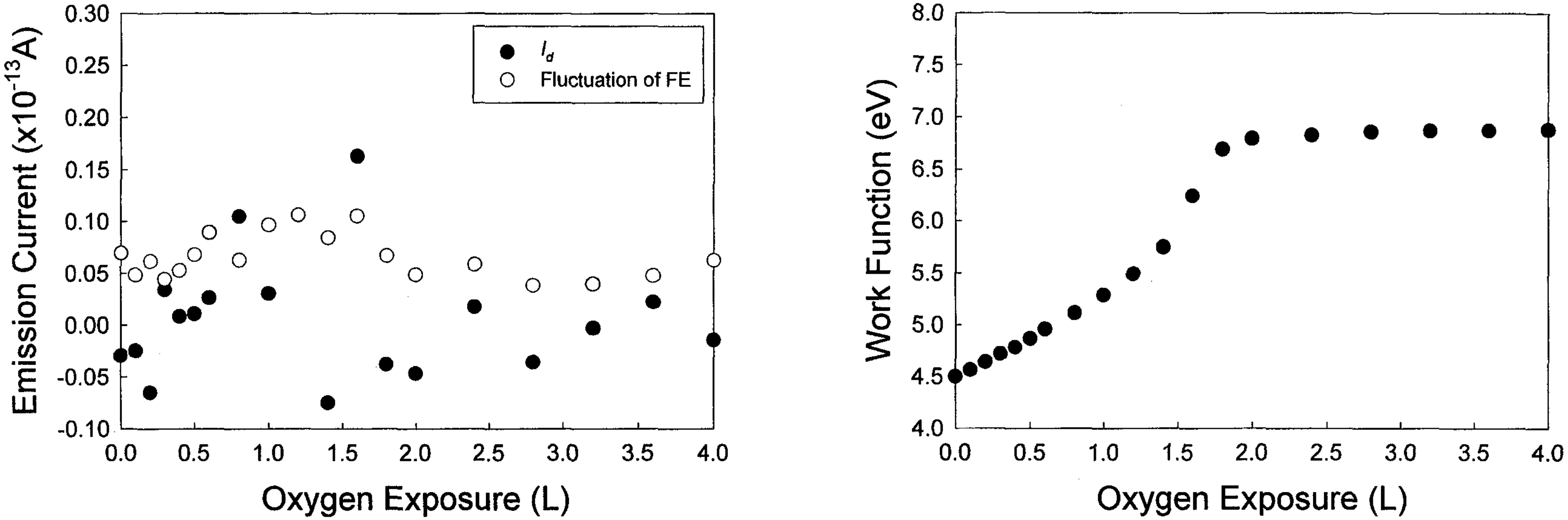

(a) I_d properties at 150 K

(b) mean work function change 150 K

Figure 5-8 Variations of I_d and the mean work function on the oxygen-adsorbed W surfaces at 150 K as a function of hydrogen exposure; (a) and (b) show the I_d properties and the work function change, respectively.

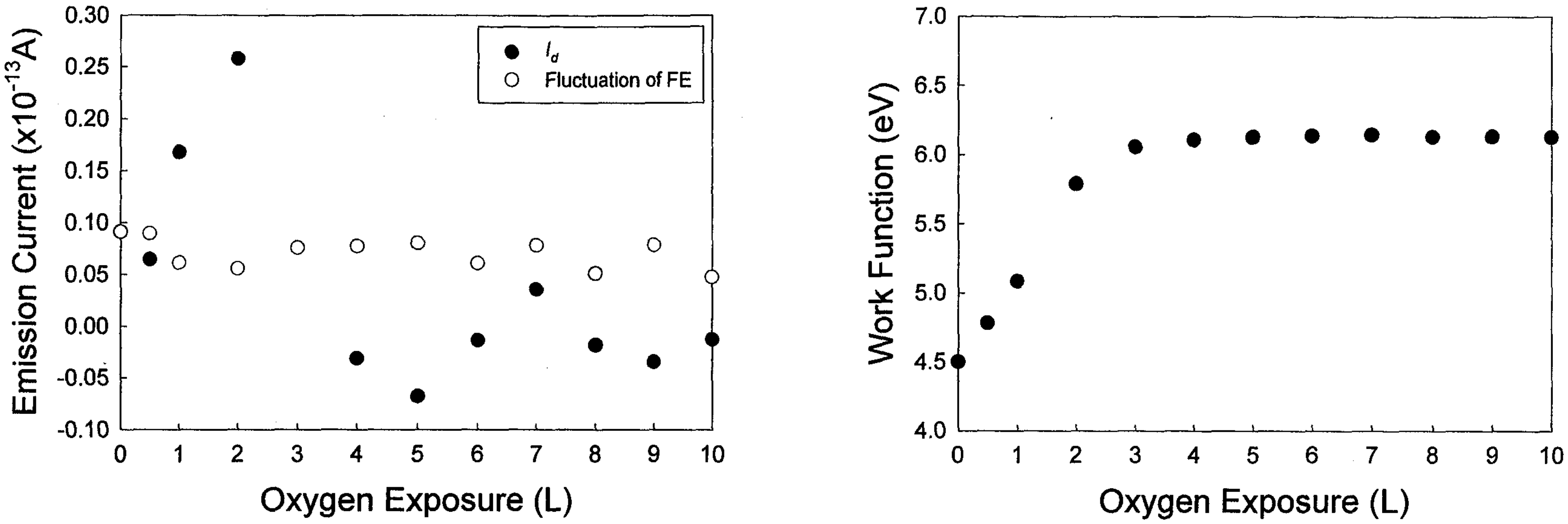

(a) I_d properties at 300 K

(b) mean work function change 300 K

Figure 5-9 Variations of I_d and the mean work function on the oxygen-adsorbed W surfaces at 300 K as a function of hydrogen exposure; (a) and (b) show the I_d properties and the work function change, respectively.

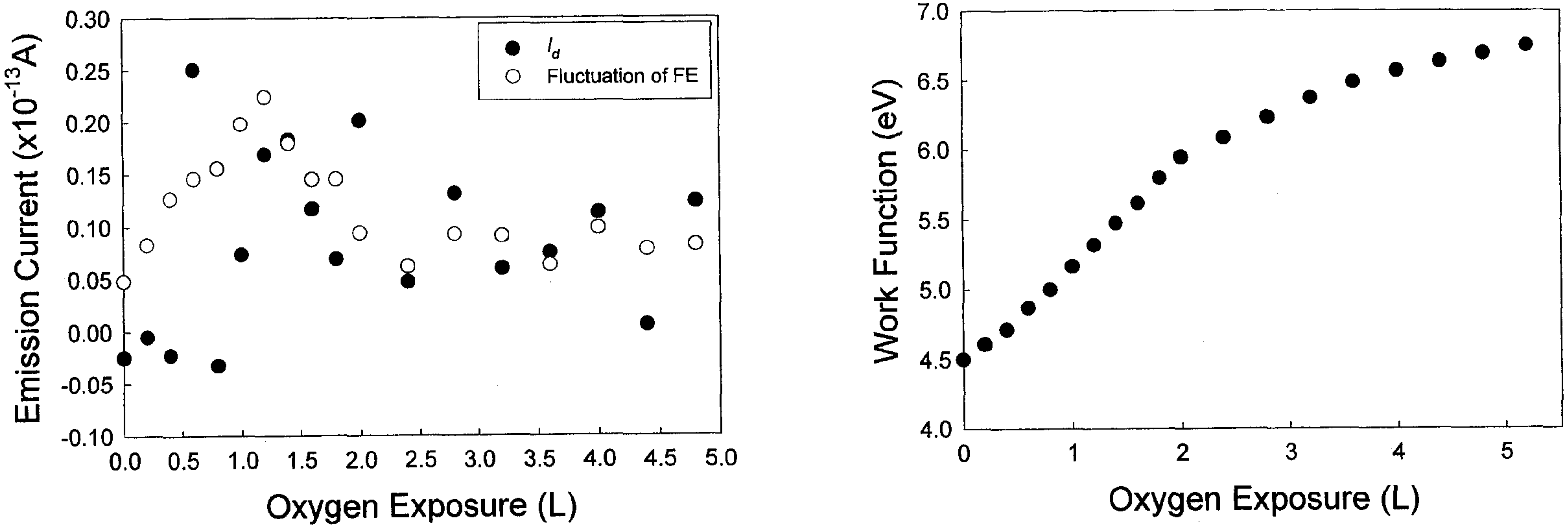

(a) I_d properties at 450 K

(b) mean work function change 450 K

Figure 5-10 Variations of I_d and the mean work function on the oxygen-adsorbed W surfaces at 450 K as a function of hydrogen exposure; (a) and (b) show the I_d properties and the work function change, respectively.

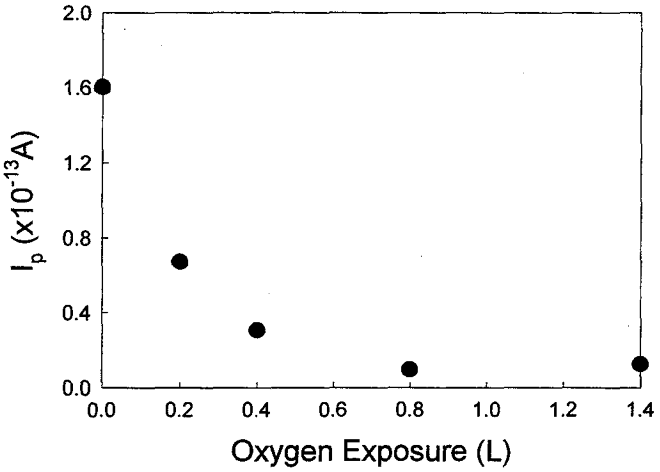

Figure 5-11 Effect of oxygen exposure on I_p measured at 320 K.

cleaned by field evaporation at 50 K. The annealing treatment of the clean W tip at 800 K for 60 s was carried out, and then the FSE signal, I_p, was measured at 320 K. Figure 5-11 indicates the result of the experiment. Although I_p was detected at the clean W tip surface, it decayed rapidly with the oxygen exposure and finally disappeared. This is the same tendency as the hydrogen exposure case. Therefore, it was concluded that the oxygen exposure suppressed FSE from the annealed W tip, while in case of Al the FSE was enhanced by oxygen exposure [4].

From these discussions, it was considered that the oxygen adsorption was not the origin of FSE from W tips, as well as the hydrogen adsorption described in the previous Section 5.3.1.

5.3.3 Water Adsorption

It has been believed that water, as well as oxygen, plays a crucial role on exoemission phenomena. In this section, the preliminary experiment regarding the contribution of water adsorption on FSE from the W tip was performed.

As described in Section 5.2, it was necessary that W tips were exposed to water vapor in the preparation chamber because of the limitation of our experimental set up. In order to transfer the W tips from the FIM observation chamber, the tip holder has to be a room temperature. However, the field evaporation during FIM observation can not be applied as a cleaning technique of the W tip surface at room temperature, because the tip should be cooled down to 50 K in order to observe with an atomic resolution using FIM. Therefore, in this study, the W tip surface was cleaned by the following process:

1) The W tip was cooled down to 50 K and cleaned by field evaporation during FIM observation.
2) After the cleanliness of the tip surface was confirmed on the FIM image, the clean W tip was held in UHV chamber with a pressure lower than 1.5 x 10^{-7} Pa for about 24 hours in order to recover the tip temperature to room temperature.
3) The W tip was annealed at 800 K as a cleaning process. This is because hydrogen, which is the main component of a residual gas, desorbs from W surfaces at temperatures higher than 800 K [7].

After the annealing treatment, the emission property was measured in UHV with a pressure of 1.5 x 10^{-7} Pa at room temperature with the negative voltage of -814.7 V. The five continuous measurements were performed before the water adsorption, and the results are shown in Figure 5-12. As shown in Figure 5-12, obvious and reproducible I_p was detected on the annealed W tip surface, which is similar to Figure 3-24. After the conformation of the I_p appearance, the W tip was exposed to water vapor by the procedure described in Section 5.2. The amount of the water exposure was 30 L. After the water exposure, the same measurements as shown in Figure 5-12 were carried out. Figure 5-13 shows the result of the experiments. I_p was enhanced only at the first measurement and recovered to the same I_p level of the annealed W tip which is shown in Figure 5-12. Although the water exposure may give rise to the clear enhancement of I_p, there might be some possibility that the residual gas of the preparation chamber or the impurity in the water vapor contributes to this I_p enhancement. Therefore, the residual gas in the preparation chamber was analyzed by QMS. Figures 5-14 (a) and (b) illustrate the QMS results in the preparation chamber measured at the residual gas atmosphere of 2.5 x 10^{-6} Pa and at water vapor atmosphere with a partial pressure of 6.5 x 10^{-5} Pa, respectively. It is clear from the Figures 5-14 (a) and (b) that pure water vapor was introduced during the water exposure process. Therefore, the impurity of water vapor was concluded not to relate the enhancement of I_p. Moreover, the

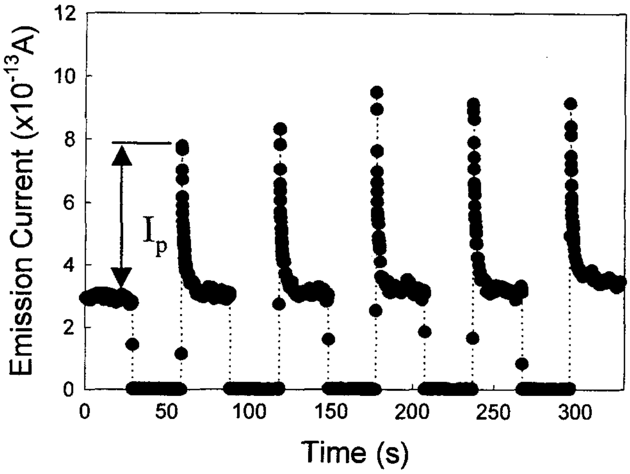

Figure 5-12 Five continuous measurements of I_p at room temperature from the W tip surface annealed at 800 K.

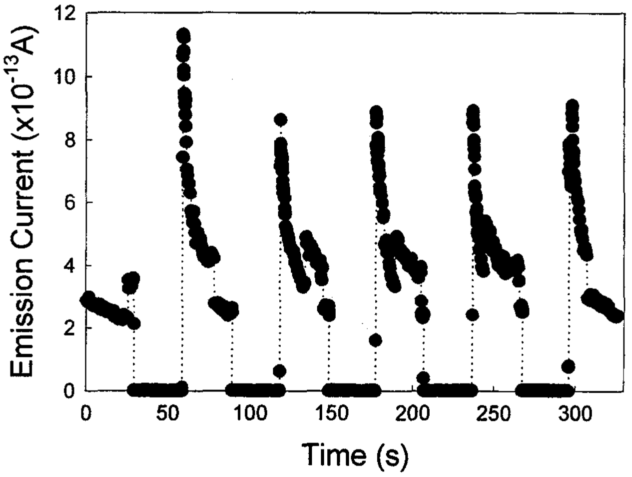

Figure 5-13 Five continuous measurements of I_p at room temperature from the W tip surface after 30 L exposure of water vapor.

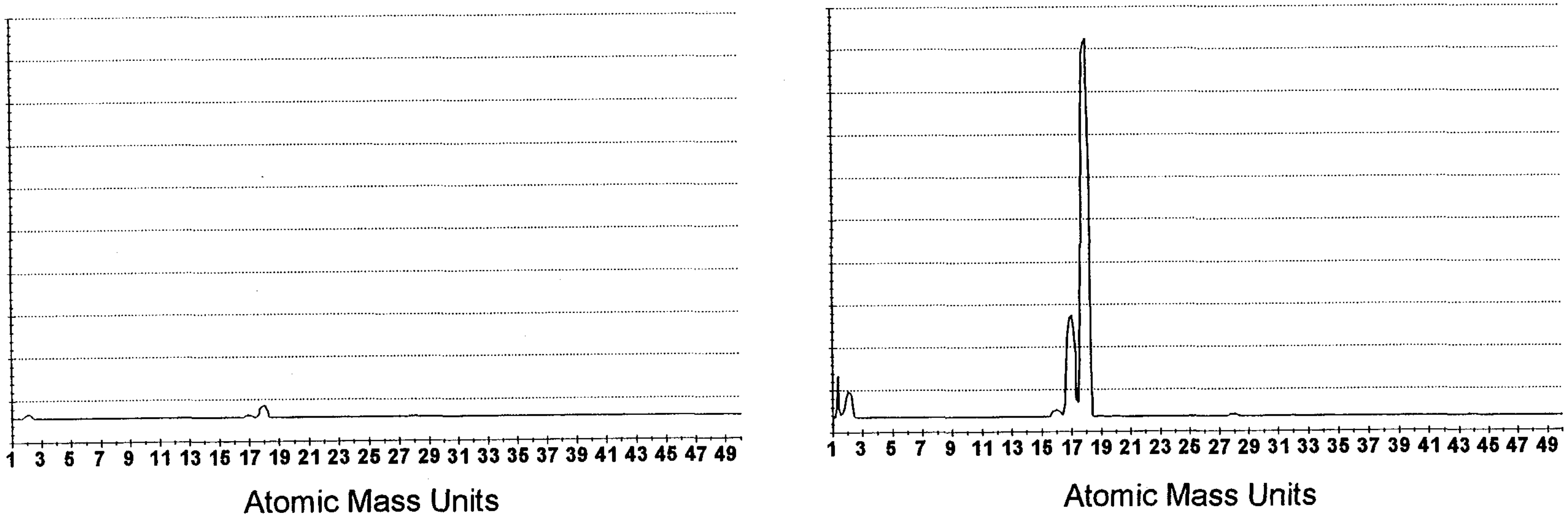

(a) residual gas (2.5 x 10^{-6} Pa)

(b) water vapor (6.5 x 10^{-5} Pa)

Figure 5-14 QMS spectra in the preparation chamber; (a) and (b) indicate the results of residual gas (2.5 x 10^{-6} Pa) and of water vapor (6.5 x 10^{-5} Pa) atmosphere, respectively.

emission property from the W tip exposed to the residual gas of the preparation chamber after the annealing at 800 K was measured (without water vapor introduction) in order to assess the effect of residual gas adsorption in the preparation chamber. The exposure to the residual gas was performed at 2.5 x 10^{-6} Pa for 100 s. The filled and open circles shown in Figure 5-15 represent the emission currents measured at room temperature in the FIM observation chamber and in the preparation chamber, respectively. From the Figure 5-15, I_p was suppressed due to the exposure to the residual gas in the preparation chamber. According to the results shown in Section 5.3.1, the suppression of I_p would be caused by the adsorption of hydrogen which is the residual gas in the preparation chamber. Therefore, it was concluded that the enhancement of I_p shown in the Figure 5-13 was assigned to the water adsorption. Thus, water adsorption on W surface plays clearly a different role from hydrogen and oxygen adsorption on FSE. In order to recognize the contribution of water adsorption to FSE in detail, further experiments will be needed in future.

5.4 Conclusion

The FSE properties of the hydrogen- and oxygen-adsorbed W tip surfaces were investigated in the temperature range between 50 and 450 K. Clear FSE signals were not detected both on the surfaces at all temperatures examined. Also, the contributions of hydrogen, oxygen and water adsorption to FSE from the W tip surfaces after annealing treatment were studied. Hydrogen and oxygen adsorption suppressed the FSE signal, I_p, while water adsorption enhanced. Thus, the preliminary result on the effect of the water adsorption on FSE suggested the contribution of water adsorption upon FSE from W surface. However, the detailed mechanism has not been clarified yet. In our previous experiment, holding clean W tips in UHV chamber for 15 hr led to the appearance of FSE [10]. From the results obtained here, it seems to be reasonable that the appearance of FSE in the previous experiment would be caused by the effect of adsorption of water from the residual gas in the UHV chamber.

References

[1] "*Early Stages in the Oxidation of Magnesium, Aluminium and Magnesium/Aluminium Alloys*"; G. C. Allen, P. M. Tucker, B. E. Hayden and D. F. Klemperer, Surface Sciece, vol. 102 (1981) 207 ~ 226.

[2] "*Exo-Electron Emission from Abraded Metal Surfaces at High and Ultrahigh Vacuums*"; J. A. Ramsey, Journal of Applied Physics, vol. 37 (1966) 452.

[3] "*Exoelectron Emission, Phenomena and Parameters*"; A. Scharmann, Proceedings of 4th International Symposium on Exoelectron Emission and Dosimetry, Liblice, (1973) 12 ~29.

[4] "*Influence of Oxygen Adsorption on Field-Stimulated Exoelectron Emission from High-Purity Aluminum*"; M. Tagawa, M. Mori, N. Ohmae and M. Umeno, Applied Surface Science, vol. 72 (1993) 259 ~ 265.

[5] "*Temperature Dependence of the Field-Stimulated Exoelectron Emission*"; M. Mori, E. Ogawa, M. Tagawa, N. Ohmae and M. Umeno; Applied Surface Science vol. 76/77 (1994) 21 ~ 25.

[6] "*The Work Function of Polycrystalline Tungsten Foil*"; B. J. Hopkins and J. C. Riviere, Proceedings of the Physical Society, vol. 81 no. 521 (1963) 590 ~ 592.

[7] "*Chemisorption on Perfect Surfaces; Hydrogen and Nitrogen on Tungsten and Rhodium*"; R. S. Polizzoti and G. Ehrlich, Journal of Chemical Physics, vol. 71 no. 1 (1979) 259 ~ 270.

[8] "*Binding States of Hydrogen on Tungsten*"; P. W. Tamm and L. D. Schmidt, Journal of Chemical Physics, vol. 54 no.11 (1971) 4775 ~ 4787.

[9] "*Observation of Ring Formation in the Field Electron Emission Image Pattern of Water Covered Field Emitters*"; J. Šotola, W. Drachsel and J. H. Block, Surface Science, vol. 266 (1992) 70 ~ 75.

[10] "*Origin of the Field-Stimulated Exoelectron Emission from Tungsten Tip Surfaces*"; T. Shiota, M. Morita, M. Tagawa, N. Ohmae and M. Umeno, Ultramicroscopy, vol. 73 no. 1-4 (1998) 217 ~ 221.

Chapter 6

First-Principles Calculational Study on Exoemission

6.1 Introduction

It has been pointed out by many researchers that defects, impurities, cracks and/or adsorption on a surface play an important role as an origin of exoemission phenomenon. Among a number of emission mechanisms of exoemission proposed, many of these models consider the presence of electron traps in a band gap or above the Fermi level [1-3]. However, since the identification of the traps for exoemission has not been successfully achieved, the origins of electron traps have not been clarified yet. This is probably due to the fact that the exoemission hardly takes place on a well-defined surface, and that it is a transient phenomenon. Therefore, it is difficult to use common surface analysis techniques with an atomic resolution, such as scanning tunneling microscope (STM). The relationship between exoemission phenomena and the status of the emitting surface has not been established yet.

On the other hand, recent improvement in the computational science has made it possible to calculate the electronic structure not only for a bulk, but also for a variety of surfaces. In the field of molecular science, the quantum chemistry method to simulate non-empirically reaction of molecules or excitation phenomenon has been developed. However, these methods were not always useful for the highly free system like a solid or a surface. The attempts to apply non-empirical first-principles calculation to a solid and a surface have been performed, and the calculational methods to approximate a real system, such as the density functional theory (DFT), have been established. Today, the non-empirical calculation of the electronic structures has become a powerful tool which can predict the electronic structure of the realistic systems.

Although many computational studies in the surface science have been reported, no computational study has been carried out with regard to the exoelectron emission. The first-principles calculation technique provides the electronic structure for the surface and it will be valuable for understanding the origins of exoelectron traps and for constructing emission models of exoelectrons. In this chapter, the electronic structures of a clean, oxygen-adsorbed, defective and stepped Al (001) surfaces were calculated by the first-principle calculation using ultrasoft pseudopotentials. A possible emission mechanism of exoelectrons from Al surface was proposed on the basis both of the computational results obtained in this study and of the experimental results reported previously. In Sections 6.2 ~ 6.4, the fundamentals of the first-principles calculation and the calculational method used in this study are described. The calculational results on clean, oxygen adsorbed, defective and stepped Al(001) surfaces are described in Sections 6.5 ~6.8. Moreover, on each surface, the relationship between the electronic structure and exoemission are discussed.

6.2 Fundamentals in Electronic Structure Calculation

6.2.1 Wave Function in Many-Body System

It is assumed that a field is formed by the force attributed to potential $V(\mathbf{r},t)$, which is shown by the equation (6-1);

$$\mathbf{F}(\mathbf{r},t) = -grad\,V(\mathbf{r},t) \tag{6-1}$$

In this field, the wave function $\varphi(\mathbf{r},t)$, which represents the action of single particle with the mass of m is provided as a solution of Schrödinger equation (including time) indicated by the following equation;

$$\left\{-\frac{\hbar^2}{2m}\nabla^2 + V(\mathbf{r},t)\right\}\varphi(\mathbf{r},t) = i\hbar\frac{\partial}{\partial t}\varphi(\mathbf{r},t) \tag{6-2}$$

If $\varphi(\mathbf{r},t)$ is obtained by solving Schrödinger equation (6-2), the possibility that single particle is observed in the small volume $d\mathbf{r}$ including the point $\mathbf{r}$ is proportional to $|\varphi(\mathbf{r},t)|^2 d\mathbf{r}$. This means that the possibility to find this single particle becomes larger at the place where φ

is greater and it becomes zero at $\varphi = 0$. Generally, $|\varphi(\mathbf{r},t)|^2 d\mathbf{r}$ is normalized as shown by $\iiint |\varphi(\mathbf{r},t)|^2 d\mathbf{r} = 1$ where the integrals are conducted in all regions in which single particle can exist.

Next, the system consisted of *N*-particles is considered. When position vector, mass and momentum of each particle are indicated by $\mathbf{r}_j$, m_j and P_j (j = 1 ~ N), Hamiltonian of this system is given by the following equation;

$$H = \sum_{j=1}^{N} \frac{P_j^2}{2m_j} + V(\mathbf{r}_1, \mathbf{r}_2 \cdots \mathbf{r}_N) \tag{6-3}$$

where $V(\mathbf{r}_1, \mathbf{r}_2 \cdots \mathbf{r}_N)$ is a sum of the potentials induced both by the external forces and by the internal forces between each particle. By replacing the momentum P_j in the equation (6-3) to $-i\hbar\nabla_j$, Hamiltonian based upon quantum mechanics is obtained as the equation (6-4);

$$H = -\sum_{j=1}^{N} \frac{\hbar^2}{2m_j} \nabla_j^2 + V(\mathbf{r}_1, \mathbf{r}_2 \cdots \mathbf{r}_N) \tag{6-4}$$

According to the equations (6-2) and (6-5), the wave function $\Psi(\mathbf{r}_1, \mathbf{r}_2 \cdots \mathbf{r}_N, t)$, which describes the actions of N-particles at the time *t*, is given by the following Schrödinger equation (6-5);

$$H\Psi = -i\hbar \frac{\partial \Psi}{\partial t} \tag{6-5}$$

Similar to the equation (6-3), the normalized solution indicated by the equation (6-6) means the possibility to find *j*th particle in the volume $d\mathbf{r}_j$ including $\mathbf{r}_j$ point:

$$\iiint |\Psi(\mathbf{r}_1, \mathbf{r}_2 \cdots \mathbf{r}_N, t)|^2 d\mathbf{r}_1 d\mathbf{r}_2 \cdots d\mathbf{r}_N = 1 \tag{6-6}$$

Since the wave function of many-body system is very complex, the interaction between each particle can not be described correctly. Therefore, $\Psi(\mathbf{r}_1, \mathbf{r}_2 \cdots \mathbf{r}_N, t)$ is generally shown by combining the wave function $\varphi_j(\mathbf{r}, t)$ of each particle.

Hereafter, a stationary state is considered as the simplest case. In the case of stationary state, the possibility of existence of single particle does not depend on time, and is shown by the following equation (6-7);

$$\Psi(\mathbf{r}_1, \mathbf{r}_2 \cdots \mathbf{r}_N, t) = e^{-iEt/\hbar} \Phi(\mathbf{r}_1, \mathbf{r}_2 \cdots \mathbf{r}_N) \tag{6-7}$$

From the equation (6-5), the Schrödinger equation is obtained as the following equation;

$$H\Phi(\mathbf{r}_1, \mathbf{r}_2 \cdots \mathbf{r}_N) = E\Phi(\mathbf{r}_1, \mathbf{r}_2 \cdots \mathbf{r}_N) \tag{6-8}$$

This equation provides solutions with a physical meaning against each eigen value E_j, and their solutions Φ_j are eigenfunctions. In the case that interactions between particles are negligible, Hamiltonian of the many-body system is represented by a sum of Hamiltonians of each particle as shown in the equation (6-9);

$$H = \sum_{j=1}^{N}\left(-\frac{\hbar^2}{2m_j}\nabla^2 + V_j(\mathbf{r}_j)\right) = \sum_{j=1}^{N} H_j \tag{6-9}$$

Then, the solution of the Schrödinger equation (6-8) can be written by the following;

$$\Phi(\mathbf{r}_1, \mathbf{r}_2 \cdots \mathbf{r}_N) = \phi(\mathbf{r}_1)\chi(\mathbf{r}_2)\cdots \tag{6-10}$$

From the equations (6-8) and (6-10), the equations (6-11-1) ~ (6-11-N) are obtained by a variable separation method.

$$H_1\phi(\mathbf{r}_1) = \varepsilon(\mathbf{r}_1) \tag{6-11-1}$$

$$H_2\chi(\mathbf{r}_2) = \varepsilon'(\mathbf{r}_2) \tag{6-11-2}$$

$$\vdots \qquad\qquad \vdots$$

$$\varepsilon = \varepsilon + \varepsilon' + \cdots \tag{6-12}$$

These equations (6-11-1) ~ (6-11-N) indicate the wave functions which describe action of each particle. By solving these equations, eigen values $(\varepsilon, \varepsilon' \cdots)$ and eigenfunctions $(\phi, \chi \cdots)$ against each Hamiltonian (H_j) can be calculated. Using the calculated eigen value and the eigenfunction of each particle, eigenfunction (Φ_n) and eigen value (E_n) of Hamiltonian (H) in the many-body system are represented by the equation (6-13),

$$\Phi_n(\mathbf{r}_1, \mathbf{r}_2 \cdots \mathbf{r}_N) = \phi_l(\mathbf{r}_1)\chi_m(\mathbf{r}_2)\cdots \qquad (l, m, n \cdots = 1,2,3 \cdots)$$

$$E_n = \varepsilon_l + \varepsilon'_m + \cdots \tag{6-13}$$

These discussions can be generally applied even if N-particles involve different kinds of particles. However, only electron is considered in this system, that is, mass and a function of potential V_j are same for all particles in this system. Therefore, the Hamiltonian and Schrödinger equation of the system can be redrawn as the equations (6-14) and (6-15),

$$H_j = -\frac{\hbar^2}{2m}\nabla^2 + V(\mathbf{r}_j) \tag{6-14}$$

$$\left\{-\frac{\hbar^2}{2m}\nabla^2+V(\mathbf{r}_j)\right\}\phi(\mathbf{r}_j)=\varepsilon\,\phi(\mathbf{r}_j) \tag{6-15}$$

After the normalized eigen values and eigenfunctions of the equation (6-15) are determined to be $\varepsilon_l, \varepsilon_l' \cdots$ and $\phi_l, \phi_l' \cdots$, the eigenfunction Φ and eigen value E of the many-electron system are provided by the following equations;

$$\Phi(\mathbf{r}_1, \mathbf{r}_2 \cdots)=\phi_l(\mathbf{r}_1)\,\phi_l(\mathbf{r}_2)\cdots \tag{6-16}$$

$$E=\varepsilon_l+\varepsilon_l'+\cdots \tag{6-17}$$

If all particles are the same, they can not be distinguished. Therefore, there exist *N!* eigenfunctions of the equation (6-8) against the eigen values shown by the equation of (6-17).

In the theory of quantum mechanics, since the orbit of single particle can not be pursued and the existence of the single particle is recognized as a possibility distribution of it, the particles with *N!* different functions can not be distinguished. Therefore, in the system containing a lot of same particles, it is accepted that the solutions of the Schrödinger equation, which meet the following requests, have a physical meaning;

1) In the case of Fermi particle, when arbitrary two particles are exchanged, the wave functions only with an opposite sign are accepted,
2) In the case of Bose particle, when arbitrary two particles are exchanged together, the unchanged wave functions are allowed,

where Fermi and Bose particles mean those following the Fermi and Bose distribution, respectively. For example, an electron, positron and neutron belong to the former, and photon is considered as the later. In the system consisted of two Fermi particles, where electron spin is not considered, wave functions are obtained as follows: When there are two particles denoted by $\mathbf{r}_1$ and $\mathbf{r}_2$, the wave function Φ of the system is provided by the equation (6-18),

$$\Phi(\mathbf{r}_1, \mathbf{r}_2)=C_1\phi_l(\mathbf{r}_1)\phi_l'(\mathbf{r}_2)+C_2\phi_l(\mathbf{r}_2)\phi_l'(\mathbf{r}_1) \tag{6-18}$$

where the constants C_1 and C_2 satisfy the following condition in order to normalize Φ;

$$|C_1|^2+|C_2|^2=1 \tag{6-19}$$

When these particles are exchanged, the equation (6-18) is rewritten as the following;

$$\Phi(\mathbf{r}_2, \mathbf{r}_1)=C_1\phi_l(\mathbf{r}_2)\phi_l'(\mathbf{r}_1)+C_2\phi_l(\mathbf{r}_1)\phi_l'(\mathbf{r}_2) \tag{6-20}$$

In the case of Fermi particle, the condition of $\Phi(\mathbf{r}_1,\mathbf{r}_2)=-\Phi(\mathbf{r}_2,\mathbf{r}_1)$ regarding the wave functions of (6-18) and (6-20) must be satisfied. From this relation, it is obtained that C_1 equals $-C_2$. According to the equation (6-19), C_1 and $-C_2$ are calculated to be $1/\sqrt{2}$. Therefore, the wave function of Fermi particle system is given by the following equation;

$$\begin{aligned}\Phi_F(r_1,r_2)&=\frac{1}{\sqrt{2}}\{\phi_l(\mathbf{r}_1)\phi_l'(\mathbf{r}_2)-\phi_l(\mathbf{r}_2)\phi_l'(\mathbf{r}_1)\}\\&=\frac{1}{\sqrt{2}}\begin{vmatrix}\phi_l(\mathbf{r}_1) & \phi_l'(\mathbf{r}_1)\\ \phi_l(\mathbf{r}_2) & \phi_l'(\mathbf{r}_2)\end{vmatrix}\end{aligned}\qquad(6\text{-}21)$$

On the other hand, in the case of Bose particle, the wave function of Bose particle system is obtained by the equation (6-22),

$$\begin{aligned}\Phi_B(r_1,r_2)&=\frac{1}{\sqrt{2}}\{\phi_l(\mathbf{r}_1)\phi_l'(\mathbf{r}_2)+\phi_l(\mathbf{r}_2)\phi_l'(\mathbf{r}_1)\}\\&=\frac{1}{\sqrt{2}}\begin{vmatrix}\phi_l(\mathbf{r}_1) & -\phi_l'(\mathbf{r}_1)\\ \phi_l(\mathbf{r}_2) & \phi_l'(\mathbf{r}_2)\end{vmatrix}\end{aligned}\qquad(6\text{-}22)$$

Moreover, when more than three Fermi particles are involved in the system, the equation (6-21) is transformed to the following equation;

$$\Phi_F(r_1,r_2\cdots)=\frac{1}{\sqrt{N!}}\begin{vmatrix}\phi_l(\mathbf{r}_1) & \phi_l'(\mathbf{r}_1) & \cdots\\ \phi_l(\mathbf{r}_2) & \phi_l'(\mathbf{r}_2) & \cdots\\ \vdots & \vdots & \ddots\end{vmatrix}\qquad(6\text{-}23)$$

This is named "Slater determinant", and even when the spin of an electron is taken into account, the wave functions of Fermi particle system are provided by the similar determinant.

6.2.2 Approximations

It has been proved in the previous part that the wave functions of many-body system without the interaction between each particle are provided by the Slater determinant. However, electrons interact each other as well as atomic nuclei in the real system. Hence, it is necessary to introduce further approximations in order to calculate the electronic structure of a real system. The approximation methods widely used are as follows:

1) Adiabatic Approximation (Born-Oppenheimer Approximation);

Since the mass of electron is smaller than that of atomic nucleus, it is considered that the electron follows the motion of atomic nucleus.

2) Mean Field Approximation;

The motion of an electron is restricted by the Pauli's principle because the electron follows Fermi statistics and Coulomb interaction. The effect of these interactions with an electron from other electrons can be replaced by an appropriate potential.

In the Born approximation, since atomic nuclei are considered to be the source of the external potentials defined by the following equation;

$$v_{\text{int}}(\mathbf{r}_j) = v(\mathbf{r}_j, \mathbf{R}_j) \tag{6-24}$$

where **r** and **R** show the position vectors of electron and atomic nucleus, respectively. Also, in the mean field approximation, the interaction of surrounding electrons with an electron is approximated by the potential $v_{ext}(\mathbf{r}_j)$. Therefore, the Schrödinger equation is indicated by the equation (6-25);

$$\begin{aligned} &\left\{-\frac{\hbar^2}{2m}\nabla^2 + v(\mathbf{r}_j)\right\}\phi_i(\mathbf{r}_j) = E\phi_i(\mathbf{r}_j) \qquad (i, j = 1\sim\mathrm{N}) \\ &v(\mathbf{r}_j) = v_{\text{int}}(\mathbf{r}_j) + v_{ext}(\mathbf{r}_j) \end{aligned} \tag{6-25}$$

where $\phi_i(\mathbf{r}_j)$ show the steady-state of each electron. According to the equations of (6-23) and (6-25), the many-body system involving *N*-electrons is converted to the Schrödinger equation of single electron.

The potential $v(\mathbf{r}_j)$, which is necessary for solving the Schrödinger equation (6-25), contains $v_{ext}(\mathbf{r}_j)$ formed by the other electrons. The $v_{ext}(\mathbf{r}_j)$ can be determined by the distribution of *N-1* electrons originated by the equation (6-25). On a calculation of electronic structure, the $v(\mathbf{r}_j)$ is constructed using a certain wave function $\phi(\mathbf{r}_j)$ as the first step. Then, the Schrödinger equation (6-25) is solved by the calculated $v(\mathbf{r}_j)$, and $\phi'(\mathbf{r}_j)$ is obtained. Using the $\phi'(\mathbf{r}_j)$, thus calculated, $v'(\mathbf{r}_j)$ can be calculated. Thus, $\phi_i(\mathbf{r}_j)$ is calculated by repeating these processes, and finally $\Phi(\mathbf{r}_1, \mathbf{r}_2 \cdots)$ is obtained. This calculation is called "self-consistent calculational method".

6.2.3 Bloch's Theorem

When a potential $\nu(\mathbf{r})$ has a periodicity shown by the equation (6-26), the wave function of single electron is expressed by the equation (6-27),

$$\nu(\mathbf{r}) = \nu(\mathbf{r} + \mathbf{R}) \tag{6-26}$$

$$\varphi_k(\mathbf{r}) = e^{-i\mathbf{k}\cdot\mathbf{r}} u_k(\mathbf{r}) \tag{6-27}$$

where **R** is the vector indicating the periodicity of the Bravais lattice. Since $u_k(\mathbf{r})$ has the same periodicity as the Bravais lattice, the following equation is appreciable;

$$u_k(\mathbf{r}) = u_k(\mathbf{r} + \mathbf{R}) \tag{6-28}$$

From the equations (6-27) and (6-28), the equation (6-29) is obtained;

$$\varphi_k(\mathbf{r} + \mathbf{R}) = e^{-i\mathbf{k}\cdot\mathbf{R}} \varphi_k(\mathbf{r}) \tag{6-29}$$

In the field of a periodical potential, a wave function can be represented by the plane waves and by the periodical part. Due to this periodicity, the calculation result on a unit cell provides the wave function of a perfect crystal.

6.3 Density Functional Theory

6.3.1 Basic Theory

The density functional theory (DFT) was formulated for the first time in 1964 by Hohenberg and Kohn [4]. The fundamental assumption is the development of the single electron density $n(\mathbf{r})$. However, it was pointed out later that $\nu(\mathbf{r})$ was not always determined by a physically meaningful $n(\mathbf{r})$. In this section, DFT will be explained simply using the formulation given by Levy [5]. According to this formulation method, the ground state in the field formed by the potential $\nu(\mathbf{r})$ can be decided regardless the status of spins and the degeneracy of the ground state.

Here, it is assumed that the single electron density $n(\mathbf{r})$ is obtained by a proper antisymmetric wave function $\psi^n(\mathbf{r})$. This limitation about $n(\mathbf{r})$ is named "*N*-representability". In contrast, even when $n(\mathbf{r})$ is provided, the only one $\psi^n(\mathbf{r})$ is not always determined. In the case of single electron, the wave function, $e^{i\mathbf{k}\cdot\mathbf{r}}\{n(\mathbf{r})\}^{1/2}$, decides the electron density, $n(\mathbf{r})$, which is independent of the wave number **k**. The antisymmetric wave function, which minimizes the expected value of a sum of the kinetic energy T and the interaction between electrons V_e, is defined as $\psi^n_{\min}(\mathbf{r})$, and a function of $F[n]$ is defined as follows:

$$F[n] = \min\left\{\left\langle\psi^n\middle|T+V_e\middle|\psi^n\right\rangle\right\} = \left\langle\psi^n_{\min}\middle|T+V_e\middle|\psi^n_{\min}\right\rangle \tag{6-30}$$

where $\langle\phi|H|\phi\rangle \equiv \int\phi^*(\tau)H\phi(\tau)d\tau$

Since $F[n]$ does not include the external potential $v(\mathbf{r})$, it is functional of $n(\mathbf{r})$. Using $F[n]$ defined by the equation (6-30), the basic theorem of DFT is expressed as follows:

1) Variational principle regarding the energy functional of the ground state;

   The energy functional $E[n]$ of $n(\mathbf{r})$, which satisfy N-representability, is defined as the following equation;

   $$E[n] = \int v(\mathbf{r})n(\mathbf{r})d\mathbf{r} + F[n] \tag{6-31}$$

   Then, the energy of the ground state, E_{gs}, is defined by the minimum of $E[n]$.

2) Possibility that the ground state is expressed by the density of single electron;

   E_{gs} is expressed as a functional of the single electron density $n(\mathbf{r})$ by the following equation;

   $$E_{gs} = \int v(\mathbf{r})n_{gs}(\mathbf{r})d\mathbf{r} + F[n_{gs}] \tag{6-32}$$

The antisymmetric wave function $\psi^{n_{gs}}_{\min}$, which minimizes the expected value of $T+V_e$ as shown by the equation (6-30), becomes the wave function of ground state ψ_{gs}. Thus, the energy and wave function of the ground state can be obtained only by understanding the single electron density $n(\mathbf{r})$, even though all wave functions of many-body system are not calculated.

6.3.2 Kohn-Sham Theory

As discussed above, if $F[n]$ is known, n_{gs} is determined from $E[n]$ shown by the equation (6-32). Therefore, in order to perform the calculation of an electronic structure, $F[n]$ has to be understood. $F[n]$ is consisted of two parts, indicating the kinetic energy T and the interactions between electrons V_e, as expressed by the equation (6-30). The Kohn-Sham theory describes about the part of the kinetic energy T.

In the Kohn-Sham theory, $F[n]$ is described as follows:

$$F[n]=T_s[n]+\frac{e^2}{2}\iint d^3r\,d^3r'\frac{n(\mathbf{r})n(\mathbf{r}')}{|\mathbf{r}-\mathbf{r}'|}+E_{XC}(n) \tag{6-33}$$

The first and second terms in the right side of the equation (6-33) show the kinetic energy of an electron and the Coulomb energy between electrons which is called "Hartree term", respectively. The third term $E_{XC}(n)$ includes all interactions except the kinetic and Coulomb energy, and called "exchange-correlation energy term". However, the kinetic energy $T_s[n]$ is defined in the virtual system with noninteracting electrons.

It is assumed that single electron density $n(\mathbf{r})$ is provided by the external potential $v(\mathbf{r})$ in the system without interactions as follows:

$$\left\{-\frac{\hbar^2}{2m}\nabla^2+v(\mathbf{r})\right\}\psi_i(\mathbf{r})=\varepsilon_i\psi_i(\mathbf{r}) \tag{6-34}$$

$$n(\mathbf{r})=\sum_i|\psi_i(\mathbf{r})|^2 \tag{6-35}$$

The Kohn-Sham theory defines the relation of $v(\mathbf{r})$ in the virtual system with the true potential in the real system of interacting electrons. From the equations (6-34) and (6-35), $T_s[n]$ is defined as the following equation:

$$T_s[n]=\sum_i\varepsilon_i-\int v(\mathbf{r})n(\mathbf{r})d\mathbf{r} \tag{6-36}$$

By substituting (6-36) and (6-33) into (6-31), the total energy is described by

$$E[n]=\sum_i\varepsilon_i-\int d^3r\,v(r)n(r)+\int d^3r\,v_{ext}(r)n(r)+\frac{e^2}{2}\iint d^3r\,d^3r'\frac{n(\mathbf{r})n(\mathbf{r}')}{|\mathbf{r}-\mathbf{r}'|}+E_{XC}(n) \tag{6-37}$$

The E[n] provides the minimum value of the total energy against the single electron density of the ground state in the system with the interactions, $n_{gs}(\mathbf{r})$.

Now, $n(\mathbf{r})$ which is slight different by $\Delta n(\mathbf{r})$ from $n_{gs}(\mathbf{r})$ is considered, that is:

$$n(\mathbf{r}) = n_{gs}(\mathbf{r}) + \Delta n(\mathbf{r}) = n_{gs}(\mathbf{r}) + \eta n'(\mathbf{r}) \qquad (6\text{-}38)$$

where η shows the constant. In order to conserve the number of electrons, $\Delta n(\mathbf{r})$ should meet the following condition:

$$\int \Delta n(\mathbf{r}) d\mathbf{r} = 0 \qquad (6\text{-}39)$$

By applying the variational principle to a total energy in the system of noninteracting electrons, the equation (6-40) is obtained:

$$T_s[n] + \int n(\mathbf{r}) v(\mathbf{r}) d\mathbf{r} = T_s[n_{gs}] + \int n_{gs}(\mathbf{r}) v(\mathbf{r}) d\mathbf{r} + O(\eta^2) \qquad (6\text{-}40)$$

From the equations (6-38) and (6-40), the equation (6-41) is led:

$$\delta T_s[n] = T_s[n] - T_s[n_{gs}] = -\int \Delta n(\mathbf{r}) v(\mathbf{r}) d\mathbf{r} + O(\eta^2) \qquad (6\text{-}41)$$

When a sum of the second and third term in the right side of the equation (6-33) is replaced by $G[n]$, the equation in the real system with the interactions corresponding to the equation (6-40) in the virtual system is shown by

$$T_s[n] + \int n(\mathbf{r}) v_{ext}(\mathbf{r}) d\mathbf{r} + G[n] = E_{gs} + O(\eta^2) \qquad (6\text{-}42)$$

The equation (6-42) is expanded by $\Delta n(\mathbf{r})$, and the following equation is led using the equation (6-41):

$$\begin{aligned} &\delta T_s[n] + \int \Delta n(\mathbf{r}) v_{ext}(\mathbf{r}) d\mathbf{r} + \int \frac{\delta G[n]}{\delta n(\mathbf{r})} d\mathbf{r} \\ &= \int \left\{ v_{ext}(\mathbf{r}) + \frac{\delta G[n]}{\delta n(\mathbf{r})} - v(\mathbf{r}) \right\} \Delta n(r) d\mathbf{r} + O(\eta^2) \qquad (6\text{-}43) \\ &= 0 + O(\eta^2) \end{aligned}$$

where $\delta G[n]/\delta n(\mathbf{r})$ shows the functional derivative of $G[n]$ against $n(\mathbf{r})$. When the equation (6-43) satisfy the condition indicated by the equation (6-39),

$$v(\mathbf{r}) = v_{ext}(\mathbf{r}) + \frac{\delta G[n]}{\delta n(\mathbf{r})} = v_{ext}(\mathbf{r}) + \int d^3 r' \frac{n'(\mathbf{r})}{|\mathbf{r} - \mathbf{r}'|} + \mu_{XC}(\mathbf{r}) \qquad (6\text{-}44)$$

$$\text{where } \mu_{XC}(\mathbf{r}) = \frac{\delta E_{XC}[n]}{\delta n(\mathbf{r})} \qquad (6\text{-}45)$$

The $\mu_{XC}(\mathbf{r})$ is labeled "exchange-correlation potential".

In summary of Kohn-Sham theory, by solving the following four equations, Kohn-Sham equations, ε_i and $n(\mathbf{r})$ can be determined.

$$\left\{-\frac{\hbar^2}{2m}\nabla^2 + v(\mathbf{r})\right\}\psi_i(\mathbf{r}) = \varepsilon_i\psi_i(\mathbf{r})$$

$$n(\mathbf{r}) = \sum_i |\psi_i(\mathbf{r})|^2$$

$$v(\mathbf{r}) = v_{ext}(\mathbf{r}) + \frac{\delta G[n]}{\delta n(\mathbf{r})} = v_{ext}(\mathbf{r}) + \int d^3r' \frac{n'(\mathbf{r})}{|\mathbf{r}-\mathbf{r}'|} + \mu_{XC}(\mathbf{r})$$

$$\mu_{XC}(\mathbf{r}) = \frac{\delta E_{XC}[n]}{\delta n(\mathbf{r})},$$

Then, a total energy can be calculated by the equation (6-37).

6.3.3 Local Density Approximation

The many-electron system is transformed to the effective single electron system by Kohn-Sham equations as described above. It is necessary to solve the Kohn-Sham equations that the functional deviation $\delta E_{XC}[n]/\delta n(\mathbf{r})$ which corresponds to exchange-correlation potential $\mu_{XC}(\mathbf{r})$ is required. This potential about the system of a homogeneous electron gas has been established. In the case that the electron density $n(\mathbf{r})$ is varying, if the variation of $n(\mathbf{r})$ is slow, it is approximated that $n(\mathbf{r})$ is locally uniform. Then, the exchange-correlation potential is indicated by the following equation:

$$E_{XC}[n] = \int \varepsilon_{XC}(n(\mathbf{r}))n(\mathbf{r})d\mathbf{r} \qquad (6\text{-}46)$$

where $\varepsilon_{XC}(n(\mathbf{r}))$ is the exchange-correlation energy per electron in the uniform electron gas of density $n(\mathbf{r})$. Therefore, the exchange-correlation potential is given by the equation (6-47):

$$\mu_{XC}(r) = \varepsilon_{XC}(n(r)) + n(r)\frac{d\varepsilon_{XC}(n)}{dn} \qquad (6\text{-}47)$$

The approximation shown by the equation (6-46) is a local density approximation (LDA). The results by LDA are precise only for the limiting case that spatial electron density is varying slowly. Therefore, the LDA calculation on the total energy shows relatively large error in especially inner-shell area of an atom. Therefore, an absolute value of energy calculated using LDA may not be correct, while the energy dispersion between two different states is exact. Now, there are many attempts beyond LDA, for example, generalized gradient approximation (GGA), self-interaction correction (SIC), and so on.

6.4 Pseudopotential Method

6.4.1 Fundamentals of Pseudopotentials

Though the states of inner-shell and valence electrons are the eigen states of the same Hamiltonian, valence electrons do not occupy the same states due to the Pauli's exclusion principle. Therefore, valence electrons feel a repulsive potential from the inner-shell electrons, as well as the attractive potential from the atomic nucleus. As a result, a part of the attractive potential is canceled by the repulsive potential at the inner-shell area, and hence, an effective weak potential is formed. This is called "pseudopotential". Thus, pseudopotential does not provide a strong attractive potential in the inner-shell area. In contrast, in the valence area, pseudopotential and true potential give the same eigen value. Therefore, the eigenfunction obtained by pseudopotential, which is called "pseudo wave function", is different from the true wave function in the inner-shell area and agrees with it in the valence area as shown in Figure 6-1. The pseudopotential method is one of the first principle calculations that the true potential is replaced by the pseudopotential and an

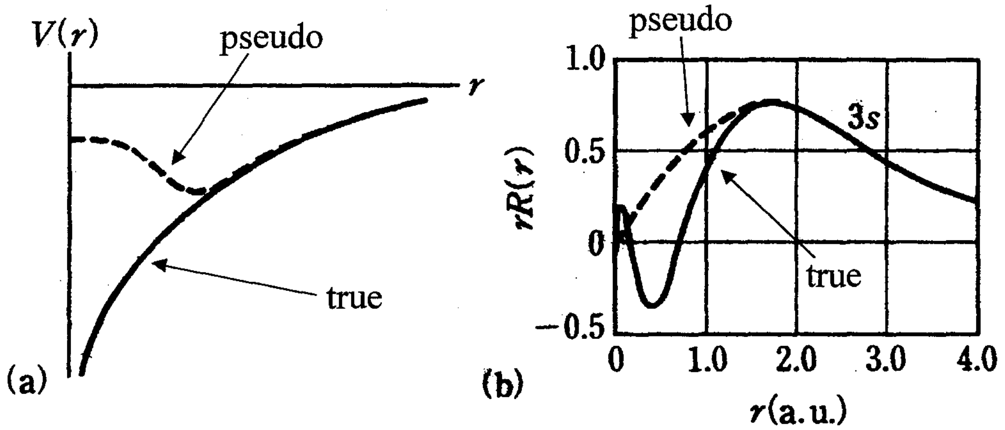

Figure 6-1 True and pseudopotential curves and wave functions; (a) and (b) show potential curves and wave functions.

electronic structure is calculated by expanding the wave function of the interatomic area (or outer-shell area) using plane waves.

In order to conduct a non-empirical calculation, an effective single-electron potential provided by single electron density has to be consistent with the true potential in the area of $r > r_c$, where r_c means the radius of the inner-shell area. For this purpose, it is necessary that norm of the pseudo wave function $\phi_{PS}(\mathbf{r})$ agrees with that of the true wave function $\phi_t(\mathbf{r})$ in the area of $r < r_c$. Therefore, a non-empirical pseudopotential has to satisfy the following conditions:

1) Wave function of valence electron does not vibrate in the area of $r < r_c$.
2) In the area of $r > r_c$, $\phi_{PS}(\mathbf{r})$ equals $\phi_t(\mathbf{r})$.
3) Norm-conservation constraint: $\int_{r<r_c} d^3r|\phi_{PS}(\mathbf{r})|^2 = \int_{r<r_c} d^3r|\phi_t(\mathbf{r})|^2$

Especially, the condition 3), norm-conservation constraint, is important for non-empirical pseudopotential method. The pseudopotential which satisfy this condition is called "norm-conserving pseudopotential" [6].

The pseudopotential can not be determined only by three conditions described above. In recent years, some attempts to promote efficiency for expanding the pseudo wave function using plane waves are performed. Such a pseudopotential is called "soft pseudopotential". In 1990, Vanderbilt proposed the pseudopotential which can be formed without norm-conservation constraint. This pseudopotential is called "ultrasoft pseudopotential" [7].

6.4.2 Ultrasoft Pseudopotential

In the pseudopotential method, wave function is expanded using plane waves. Thus, when a plane wave basis is applied, a lot of plane waves are needed on the calculation regarding the elements with a localized wave function, such as, oxygen atom, transition metals and so on. Therefore, a variety of ideas to reduce the number of plane waves by improving pseudopotential have been proposed. A number of researches are carried out in order to construct such a soft pseudopotential [7-10]. The ultrasoft pseudopotential constructed by Vanderbilt requires the smallest number of plane waves used for expansion of wave function compared to the other methods.

In order to soften a pseudopotential, it is necessary that the convergence of Fourier component in wave function raises. It has been pointed out by Hamann et al. [11] that the norm-conservation constraint of the wave function in the inner-shell area is an important condition for constructing a highly reliable pseudopotential. In order to realize the norm-conservation constraint in the inner-shell area, the wave functions of $2p$-electrons of oxygen atom or those for d-electrons of a transition metal must have a large amplitude in that area. Therefore, there is a limitation for softening the potential because of this norm-conversion constraint. However, when the state of single electron is calculated on the basis of a given potential, the norm-conversion constraint of the wave function is not needed actually. Vanderbilt added the condition to conserve a charge in the inner-shell area ($r < r_c$), when total energy and force acting on an atom was calculated by the constructed pseudopotential. Thus, it was suggested that the ultrasoft pseudopotential with a similar reliability to norm-conserving pseudopotential could be generated even without norm-conservation constraint by using the method proposed by Vanderbilt.

6.4.3 BB-VB Program

The program for calculating an electronic structure used in this study was BB-BV program. This program has been published by Tsukada Laboratory in the University of Tokyo. In this program, the band structure was calculated using plane wave basis and ultrasoft pseudopotential proposed by Vanderbilt. The stable position of each atom can be also determined by optimization of total energy. This program is composed of two calculation processes: the construction of the ultrasoft pseudopotential and the calculation of the electronic structure.

Figure 6-2 shows the algorithm of the BB-VB program. The calculation process is explained along with the algorithm as follows:

1) Construction of the pseudopotential

All-electron calculation, which means the calculation considering all electrons from 1*s* to the outermost orbital, is firstly performed for an isolated atom by the program "allel". Atomic number and arrangement of electrons are the input data, and

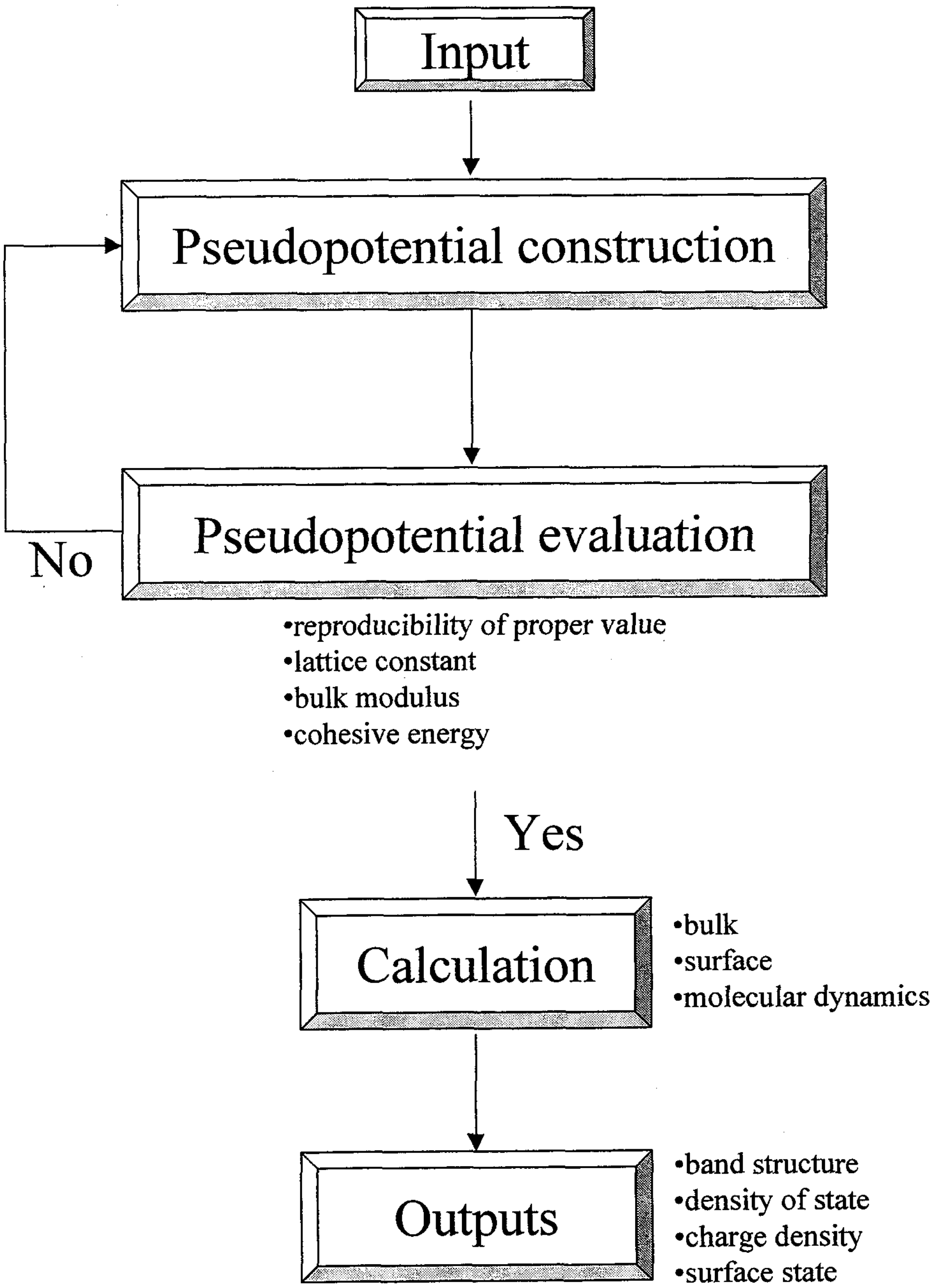

Figure 6-2 Algorithm of the calculation using BB-VB program.

the data necessary for the construction of pseudopotential and the energy of each orbital were calculated.

The pseudopotential of an ion is formed by the program "psv", and then one of the important parameters, cut-off radius, is also decided. When the cut-off radius is taken to be smaller, pseudopotential come closer to a real potential. However, since the area of approximation becomes smaller, the calculation time increases. Therefore, the cut-off radius is one of the important factors to construct pseudopotential providing good approximation with the reasonable calculation time.

Since the true and pseudo wave functions are calculated by the program "psv", the constructed pseudopotential can also be evaluated briefly. The detailed evaluation of the constructed pseudopotential is carried out by the following methods.

2) Evaluation of the constructed pseudopotential

The pseudopotential constructed by the method described above is evaluated in detail by examining reproducibility of eigen values, lattice constant, bulk modulus and cohesive energy. Each evaluation method is explained below:

<Reproducibility of eigen values>

This method is based on the comparison of the eigen value calculated by the pseudopotential and by the all-electron calculation. Regarding an certain electron arrangement, the orbital energies are calculated by the all-electron calculation program "allel". Then, the orbital energies on the same electron arrangement are also estimated by the pseudopotential calculation program "sllsd". The pseudopotential is evaluated from the comparison of these calculated results.

<Lattice Constant>

The calculation of an electronic structure of balk crystal is conducted by the program "cgmain" using the constructed pseudopotential. Total energy is calculated with a lattice constant as a parameter. The total energies thus obtained against a variety of lattice constants are fitted by a parabolic function, and the lattice constant, which gives the minimum total energy, is determined. The pseudopotential is evaluated by the comparison of the calculated lattice constant with the experimental data.

<Bulk Modulus>

Similar to the evaluation method by lattice constant, total energies were plotted against the volume of unit cell by the equation proposed by Murnaghan:

$$E(V) = \frac{B_0 V}{B_0'} \left\{ \frac{(V_0 / V)^{B_0'}}{B_0' - 1} + 1 \right\} + C \tag{6-48}$$

where E, V, B_0 and B_0' are the total energy, the volume of unit cell, the bulk modulus and differential of B_0.

<Cohesive Energy>

Total energies of an isolated atom and the atom in bulk crystal are calculated by the programs "sllsd" and "cgmain", respectively. The difference between these energies is considered to be cohesive energy, because it is defined as an energy for isolating each atom from a bulk crystal. Using the cohesive energy calculated here, further evaluation of pseudopotential is performed.

The generation of pseudopotential was repeated until the evaluation results show good approximation.

3) Calculation of electronic structure

After construction of the pseudopotential was completed, force against each atom, charge density and so on is calculated by the program "cgmain". Moreover, band structure, density of states (DOS), surface states and local density of states (LDOS) can be calculated using the outputs of "cgmain" by the following methods: Regarding the band structure, the energy of each band at *k*-points are calculated by the program "vboef", and a unit of energy output by "vboef" is transformed from Hartree (HR) to eV by the program "ngband". DOS can be obtained by running both programs "band" and "dos". Using the program "vbwfn", the charge density (CD) of an arbitrary band at an arbitrary *k*-point is calculated, and the spatial distribution of electrons can be also computed. Therefore, the surface states and LDOS can be calculated simultaneously.

6.5 Al (001) Clean Surface

6.5.1 Al Pseudopotential

Figure 6-3 shows the calculational results on the wave functions of 3*s* and 3*p* orbitals in an individual Al atom. The true wave function was obtained by calculating with all 13 electrons of an Al atom (all-electron method), and the pseudo wave function was calculated with the approximation using the pseudo-potential constructed in this study. The radius in the abscissa and the cut-off radius indicate the distance from the center of atomic nucleus and the radius of the inner-shell area, respectively. At the radius is smaller than the cut-off radius of 1.95 a.u. (1.03Å), both true wave functions of 3*s* and 3*p* orbitals show complicated

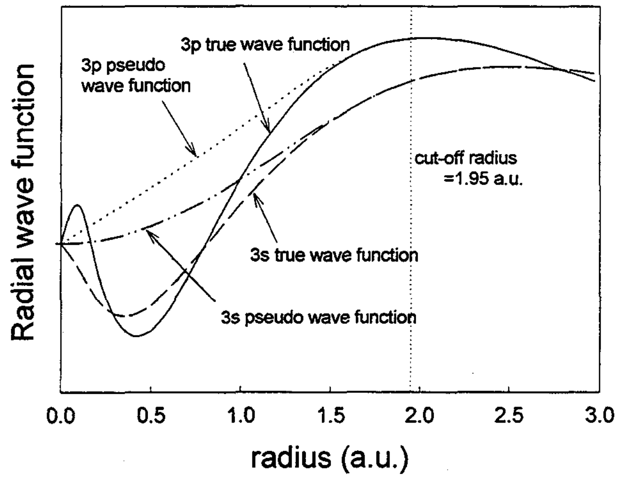

1 a.u. = 0.53 Å

Figure 6-3 True and pseudo wave functions of 3*p* and 3*s* orbitals in an Al atom; true and pseudo wave functions are calculated with all-electron method and with the approximations using pseudopotential, respectively.

Table 6-1 Comparison of the energies regarding 3*s* and 3*p* orbitals calculated by all-electron and pseudopotential methods.

Electron configuration	3*s* orbital energy		3*p* orbital energy	
	All-electron method	Pseudo-potential method	All-electron method	Pseudo-potential method
$3s^2 3p^1$	-0.287108	-0.287191	-0.102780	-0.102795
$3s^{0.5} 3p^0$	-1.046654	-1.030388	-0.795269	-0.783272
$3s^1 3p^1$	-0.576504	-0.574871	-0.362097	-0.361257
$3s^0 3p^2$	-0.602574	-0.599249	-0.384253	-0.382600
$3s^2 3p^0$	-0.547468	-0.547018	-0.336940	-0.336672

shapes, while the pseudo wave functions become smooth. On the other hand, at the radii lager than 1.95 a.u., both of the pseudo wave functions of 3*s* and 3*p* orbitals agree well with the true wave functions, respectively. It was found that the calculational results on the wave functions of 3*s* and 3*p* orbitals in the radii lager than 1.95 a.u. using the constructed pseudopotential are consistent with those of all-electron method.

The calculations on energies of 3*s* and 3*p* orbitals were conducted both by all-electron method and the pseudopotential method, with a variety of electron configurations in 3*s* and 3*p* orbitals. The results are summarized in Table 6-1. Both 3*s* and 3*p* orbital energies calculated by the pseudopotential method are consistent with those calculated by the all-electron method with the error of a few percent. Therefore, it was confirmed that the orbital energies calculated by the pseudopotential constructed in this study can provide the similar results of the all-electron method.

Since these results were calculated on an isolated Al atom, it was doubted whether or not the approximation by the constructed pseudopotential could reproduce the electronic structure of Al bulk. Therefore, the electronic structure of Al bulk was calculated using the pseudopotentials, and the calculational results were compared with those reported previously. In the calculation of the electronic structure of the Al bulk, it should be confirmed that the convergence of the total energy against input parameters of cut-off energy, lattice constant, bulk modulus and cohesive energy. Figure 6-4 shows the cut-off energy dependence of the total energy. The cut-off energy is one of the most important input parameters and directly influences to the number of plane-waves which consists of a wave function. The cut-off energy is taken to be as large as possible, with considering the approximation of the true wave

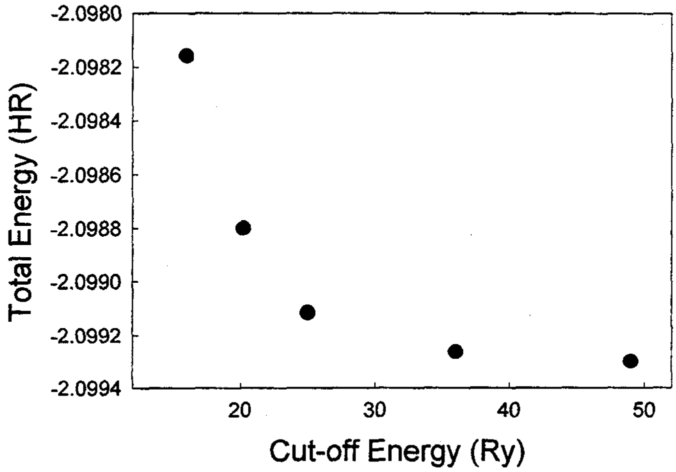

Figure 6-4 Total energy convergence against cut-off energy.

functions and the calculation time. In this study, the cut-off energy was determined to be 25 Ry from the convergence of the total energy shown in Figure 6-4, and this value was used in the following calculations on Al bulk.

The lattice constant, the bulk modulus and the cohesive energy of Al bulk were calculated using the constructed pseudopotential. The lattice constant was obtained as follows; the total energies were calculated with the different eight lattice constants as shown in Figure 6-5. Then, they were fitted by a square function, and the lattice constant was decided to be 7.519 a.u. (3.979Å) where the total energy became a minimum value. As for the bulk modulus, it was obtained to be 87 GPa by fitting the calculated value using Murnaghan's equation as shown in Figure 6-6. Table 6-2 shows the comparison of the calculated values with the experimental data [12]. It is important to evaluate the reliability of calculated results by comparing between the calculated and experimental values [12-15]. Especially, the reproducibility of lattice constant is the most important, and it is recognized that the calculation results are reliable if the relative error of a calculated value to the experimental data is within 1 % [15]. As for the bulk modulus, it is often reported that the error reaches several percent even in the case of reliable computations [15]. In this study, the errors of the calculated values on lattice constant and bulk modulus are within 1.02 % and 3.58 %, respectively. Note that the experiment was made at room temperature, while the

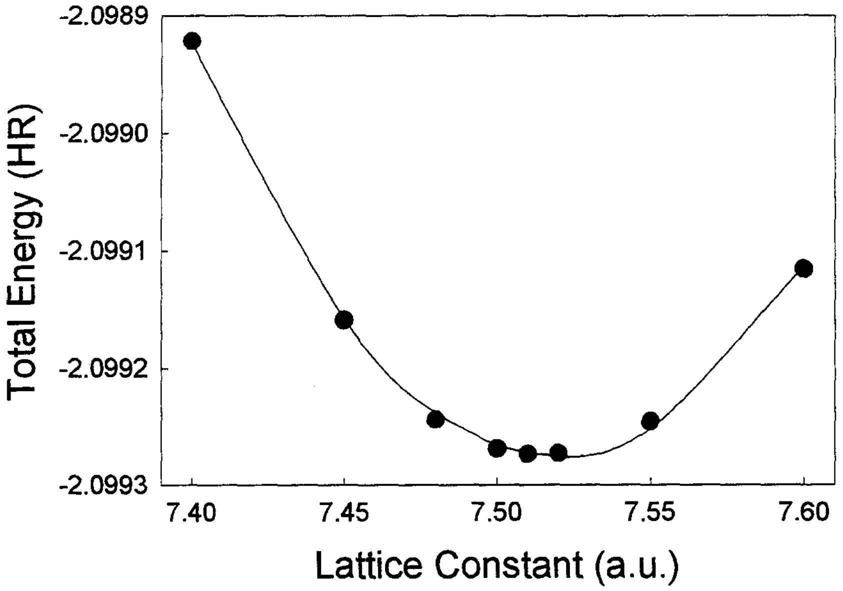

1 a.u. = 0.53 Å

Figure 6-5 Total energy convergence against lattice constant.

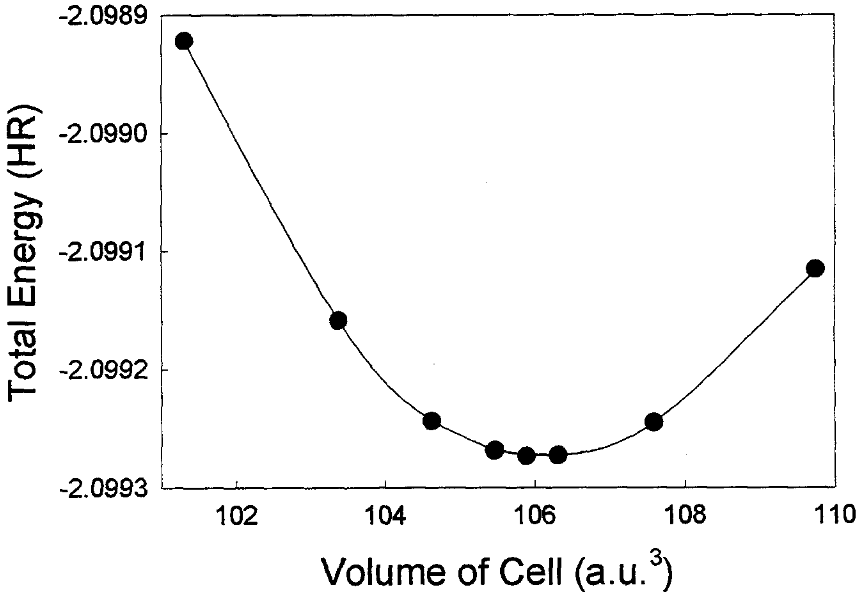

1 a.u. = 0.53 Å

Figure 6-6 Total energy convergence against bulk modulus.

Table 6-2 Comparison of lattice constant, bulk modulus and cohesive energy calculated and obtained experimentally.

	Lattice constant [Å]	Bulk modulus [GPa]	Cohesive enregy [Ry/atom]
Calculation	3.979	87	0.309
Experiment	4.02	84	0.25
Tolerance(%)	1.02	3.58	23.6

calculated values were those at 0 K. According to the report on thermal expansion of the Al lattice by Andrew [16], lattice constant decreased lineally with decreasing the temperature. It is expected that the lattice constant calculated here is 0.2 ~ 0.3 % smaller than that at room temperature. Therefore, our calculational results using the pseudopotential constructed here are considered to be reliable. On the other hand, the cohesive energy calculated in this study shows large error with the experimental data. This is attributed to LDA used in this calculation. Moreover, when an electronic structure is obtained by LDA, there is a problem that the calculation result on excited states is not reliable [17]. However, the electronic structure we need to know on this exoemission research is that at a few eV above the Fermi level (E_F), where the exoelectron traps are expected. Since the calculation using the LDA method can provide the electronic structure at around the ground states precisely, our theoretical consideration in this study considered to be reasonable and will give important information to clarify the mechanism of exoemission.

The band structures on the Al bulk calculated by the pseudopotential method are shown in Figure 6-7 (a). For comparison, the computational results reported previously by Singhal et al. [18] is also indicated in Figure 6-7 (b). The assignments in the abscissa correspond to those indicated in Figure 6-8. *K*, *W* and so on are the symmetry points in the first Brillouin Zone of a face centered cubic lattice. It has been recognized that the energy dispersion of the bands is trustworthy, even though the absolute energies calculated by LDA are meaningless [19]. Therefore, the longitude in Figure 6-7 (a) indicates the relative

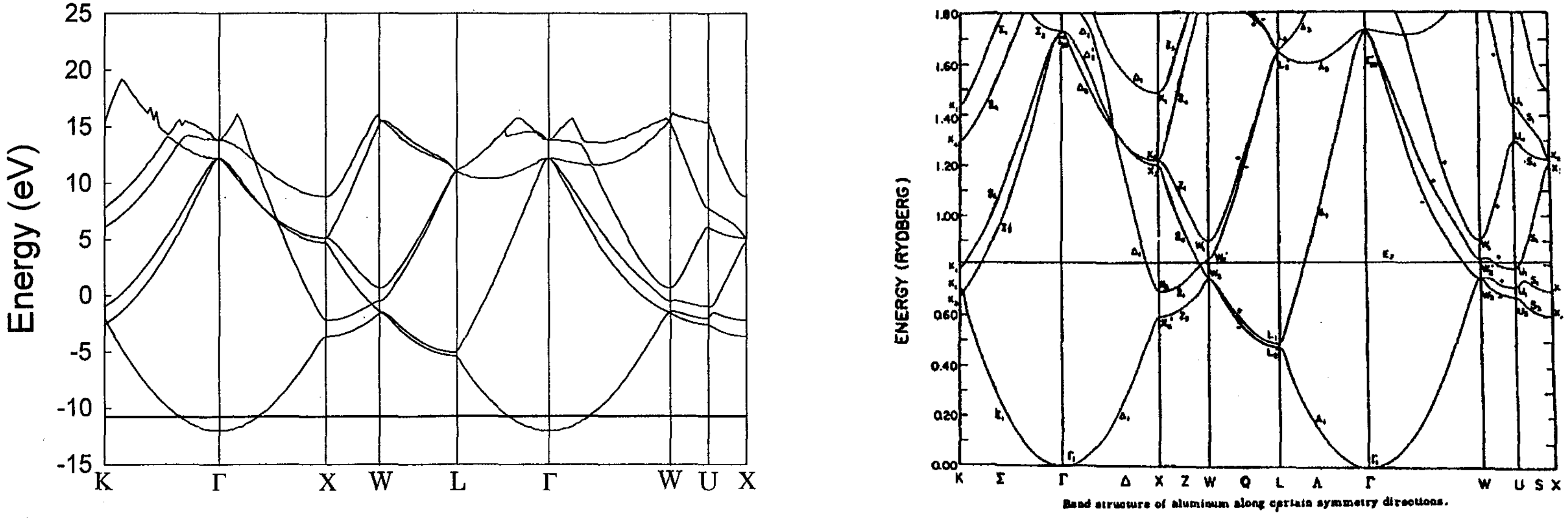

(a)

(b)

Figure 6-7 Band structures of Al bulk; (a) and (b) show the results calculated in this study and by Singhal [18], respectively.

energy to E_F. It is found that the band dispersion calculated in this study (Figure 6-7 (a)) is in very good agreement with that obtained by Shinghal et al. (Figure 6-7 (b)). In Figure 6-7 (a), the lowest band, which corresponds to 3*s* orbital, locates below E_F, while the second lowest band, 3*p* orbital, intersects E_F. This is caused by partly electron occupation of 3*p*, and one of the characteristic features of an electronic structure in a metal. From these results, it is concluded that our calculation result regarding Al bulk is trustworthy.

Also, the comparison of DOS of Al bulk was carried out. Figures 6-9 (a) and (b) show DOS obtained in this study and reported by Lee et al. [20], respectively. The abscissa of Figure 6-9 (a) were marked to be zero at E_F. It was found that our calculation gave the same results as that by Lee et al., *i.e.*, there exists three peaks in DOS at 4 eV below E_F, while the distribution of DOS from 6 to 12 eV below E_F is smooth which reflects free electron-like electronic states of Al bulk.

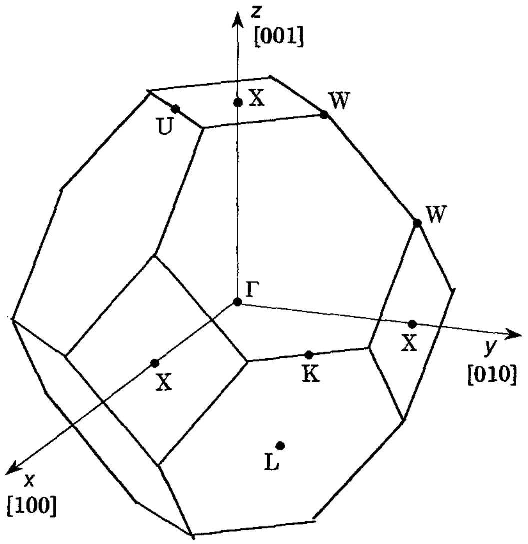

Figure 6-8 First Brillouin zone of face centered cubic (f.c.c.) lattice.

From these discussion, it was confirmed that the electronic structure of Al bulk can be reproduced by our calculation using the constructed pseudopotential.

6.5.2 Electronic Structure

A. Supercell Structures

It was confirmed in the previous section that our calculational results of the electronic structure on Al bulk using the constructed pseudopotential were reliable. However, since the exoemission took place on a solid surface, the calculation of electronic structure has to be performed regarding an Al surface. It has been known that the axis of an Al tip, which was used in the previous FSE experiment, has the orientation of [001] due to the anisotropy of the etching rate in electrochemical etching [21], and it was also confirmed by FIM experiment

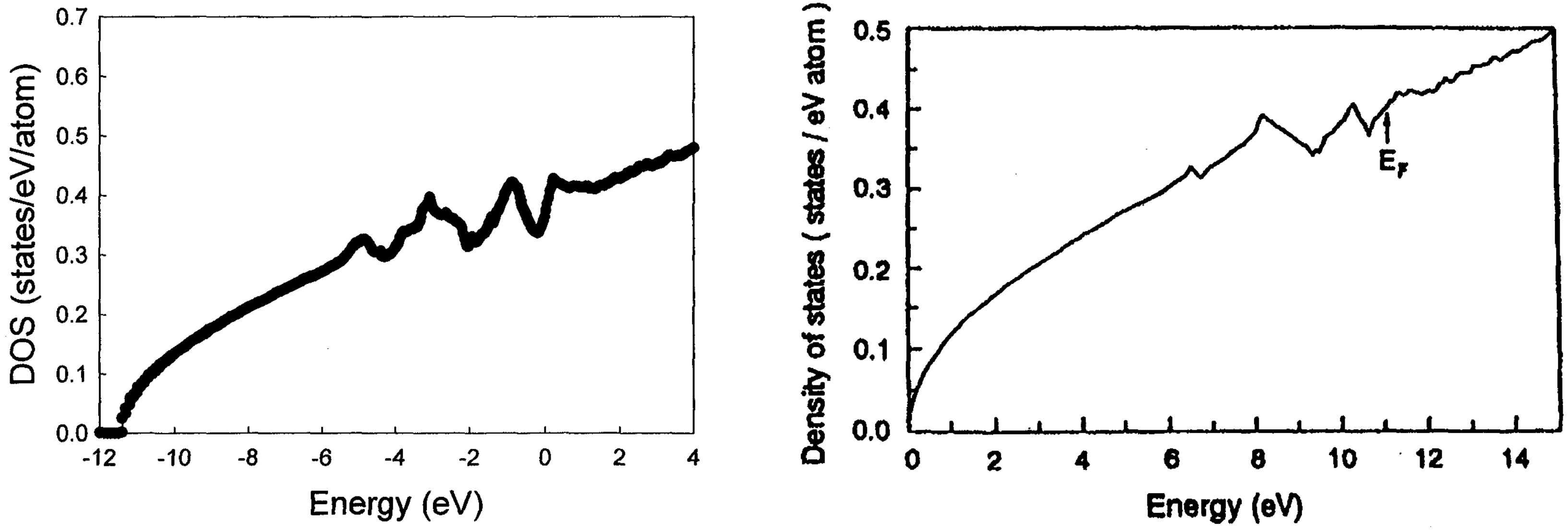

(a)

(b)

Figure 6-9 The calculated DOS of Al bulk; (a) is calculated in the present work, and (b) is reported by Lee et al. [20]

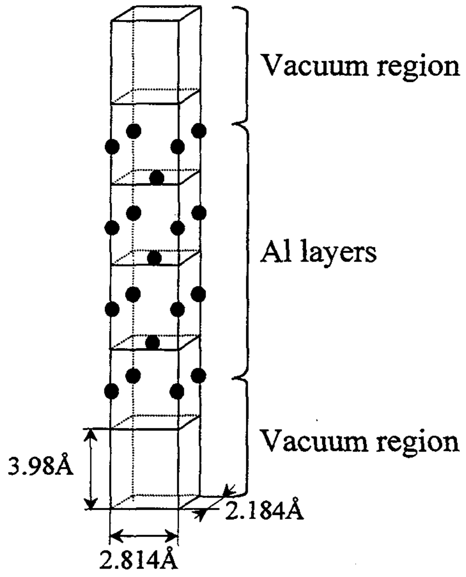

Figure 6-10 A supercell containing 7 layers of Al (001) and 5 layers of the vacuum regions. Mono-layer corresponds to 3.98Å (lattice spacing of Al (001)).

[22]. Therefore, in this theoretical study, the electronic structure of Al (001) surface was calculated.

Generally, in order to calculate the surface electronic structure by the first-principles calculation, supercells containing the slab of solid and the vacuum region are used [23-25]. Figure 6-10 shows the supercell that consisted of 7 layers of Al (001) and 5 layers of vacuum region. Note that a layer corresponds to lattice spacing of Al (001), 3.98Å, which was obtained by our calculation as described in the previous section. Before the calculation of electronic structure of Al (001) surface, it was necessary to confirm that the total energy was converged sufficiently against input parameters, that is, thickness of vacuum region, cut-off energy and number of sample k-point. The sample k-point means the calculated point in reciprocal space, and therefore, accuracy of the calculation becomes higher, as the number of sample k-point becomes greater. As for the thickness of vacuum region, if it is not enough large, an incorrect calculational result may be obtained because of the interaction of two opposite surfaces through vacuum region. Table 6-3 indicates the summary of the calculation results of the total energy convergence. In these calculations, the thickness of Al slab was taken to be 3 layers. In the LDA method, an absolute value of the calculated

Table 6-3 Total energy convergence against the input parameters of the thickness of vacuum region, cut-off energy and number of sample k-point.

Thickness of vacuum region [layers]	1	3	5
ΔE_{tot} [meV]	53.531	27.494	27.413

Cut-off energy [Ry]	16.0	25.0	36.0
ΔE_{tot} [meV]	28.85	27.41	27.04

Number of sample k-points	450	722	1058
ΔE_{tot} [meV]	37.99	27.41	24.17

energy is meaningless, while the energy dispersion is correct, as described in the previous section. In order to evaluate the convergence of total energy, the difference in the total energies between two different surfaces was compared. The energy difference, ΔE_{tot}, can be defined as the following equation,

$$\Delta E_{tot} = E_a - E_b \tag{6-49}$$

E_a: total energy on Al (001) without surface relaxation.

E_b: total energy on Al (001) with the first interlayer distance reduced by 3 % against Al (001) lattice spacing.

As shown in Table 6-3, ΔE_{tot} kept constant when the vacuum region exceeds over 3 layers thickness. Since the thickness of vacuum region was one of the most important parameters to affect the supercell size, it was determined to be 5 layers where the better-converged result was obtained. The convergences of ΔE_{tot} against variations of cut-off energy and number of sample k-point were checked as well with the supercell containing 3 layers of Al slab and 5 layers of vacuum region. As for the cut-off energy, 25 Ry was decided because ΔE_{tot} converged well with this cut-off energy. Number of sample k-point is the parameter relating directly to the calculation time. According to Kwak's report on the electronic structure of W (110) surface calculated by first-principles method [26], even 392 sample k-points gave well-converged results. Therefore, in this study, the calculation was performed at 722 k-points, with considering the convergence of ΔE_{tot} shown in Table 6-3 and the calculation time.

B. Surface Relaxation

In a bulk, an atom is stabilized due to interactions of coordinating atoms. However, since coordinating number in a surface is different from that of a bulk, an atom is unstable at the equilibrium position in the bulk. Therefore, the atom moves toward new equilibrium position, and the atomic structure at the surface is different from a bulk. The change of surface structure is categorized into surface relaxation and surface rearrangement. In the case of a metal, it has been known that surface relaxation takes place in most of metals. On the other hand, surface rearrangement was observed only on the clean surfaces of some metals, for example, W (001) [27] and Au (011) [28].

As for the Al surface, it has been reported that surface rearrangement does not take place and surface relaxation is only observed [29-33]. Table 6-4 summarizes the experimental reports on surface rearrangement of Al surfaces at (111) [22], (001) [33], or (110) [34,35] surfaces. The Δd_{mn} indicates the relative change of interlayer distance between *m th* and *n th* layers with regard to the lattice spacing of a bulk. On Al (001) surface studied in this study, surface relaxation was not observed [33]. The thickness of Al slab in the supercell was determined by comparing our calculation results on surface

Table 6-4 Surface relaxations on Al (111), (001) and (110) crystal planes

Crystal plane	Δd_{12} (%)	Δd_{23} (%)	Ref.
(111)	0.9 ± 0.5	N/A	Zingg [22]
(001)	0.0	N/A	Stampfl [33]
(110)	-8.5 ± 1.0 -8.6 ± 0.8	5.5 ± 1.1 5.0 ± 1.1	Taraschi [34] Ratsch [35]

relaxation structure with the experimental data.

The calculations were performed using the supercells containing 5 layers of vacuum region and Al slab raging from 5 to 9 layers. As described earlier, it is necessary that the cut-off energy and the number of sample k-point are determined on each system. Table 6-5 shows the calculation results on the total energy convergence against variations of cut-off energy and number of sample k-point. It was found that the difference in ΔE_{tot} of the calculational results with 578 and 882 k-points was about at least 6 meV. Though the convergence of E_{tot} calculated at 882 k-points may not be sufficient, 882 k-points were chosen as a calculation point, with considering a calculation time. Also, the difference of ΔE_{tot} in the cut-off energies of 25 and 36 Ry was found to be lower than 1 meV. Therefore, since it was considered that the cut-off energy of 25 Ry provided well-converged results, the cut-off energy was decided to be 25 Ry in this study.

The structure of surface relaxation was calculated using the cut-off energy of 25 Ry, 882 k-points and 5 layers of vacuum region as determined above. The calculational results are summarized in Table 6-6. Also, the calculational results reported by Cox et al. [36] and Bohnen et al. [37] and the experimental result by LEED [33] are shown in Table 6-6. It is found that Δd_{12} decreases as Al slab in a supercell becomes thicker. Δd_{12} was calculated to be 0.41 % when the Al slab was taken to be 9 layers, and it could reproduce the experimental value better than the other calculation results reported. From these results, the thickness of Al slab in this study was decided to be 9 layers.

The effect of surface relaxation on the electronic structure of Al surface was examined. Figures 6-11 (a) and (b) show the band structures of Al (001) surface with and without surface relaxation, respectively. The abscissa corresponds to the coordinate on surface Brillouin zone in reciprocal space as shown in Figure 6-12. There are some differences of energy dispersion between the band structures of the relaxed and the unrelaxed surfaces. Moreover, the comparison of charge distribution (CD) of valence electrons was performed on those surfaces. Figures 6-13 (a) and (b) illustrate the CD of unrelaxed and relaxed Al (001) surfaces, respectively. In this figure, the open circles indicate the Al atoms. The dark area corresponds to the area at high electron density. It was found that no remarkable change of CD was seen on both of the unrelaxed and relaxed surface. Finally, total DOS of the unrelaxed and relaxed surface were compared, and the calculational results on DOS are

Table 6-5 Total energy difference, ΔE_{tot}, calculated with variations of thickness of Al slab, cut-off energy and number of sample k-point.

Thickness of Al slab [layers]	Cut-off Energy [Ry]	Number of sample k-points	ΔE_{tot} [meV]
5	25.0	578	36.78
	25.0	882	30.36
	36.0	882	29.97
7	25.0	578	10.21
	25.0	882	16.11
	36.0	882	15.75
9	25.0	578	8.25
	25.0	882	10.36
	36.0	882	10.21

Table 6-6 The surface relaxation calculated in this study with variations of Al slab layer. For comparison, the results obtained by Cox, Bohnen and the LEED experiment are also shown.

Number of Al slab	Δd_{12}(%)	Δd_{23}(%)	Δd_{34}(%)	Δd_{45}(%)	
Al 3 lyaers	2.4				
Al 5 layers	2.5	0.06			
Al 7 layers	0.74	0.22	−0.66		
Al 9 layers	0.41	0.60	−0.66	−0.14	
Cox[39)	-0.44	-0.12	0.11	0.10	empirical method Al 11-layers
Bohnen[40)	1.2±0.4	0.2±0.4	-0.1±0.4		pseudo-potential method Al 15-layers
Experiment[31)	0				measured by LEED

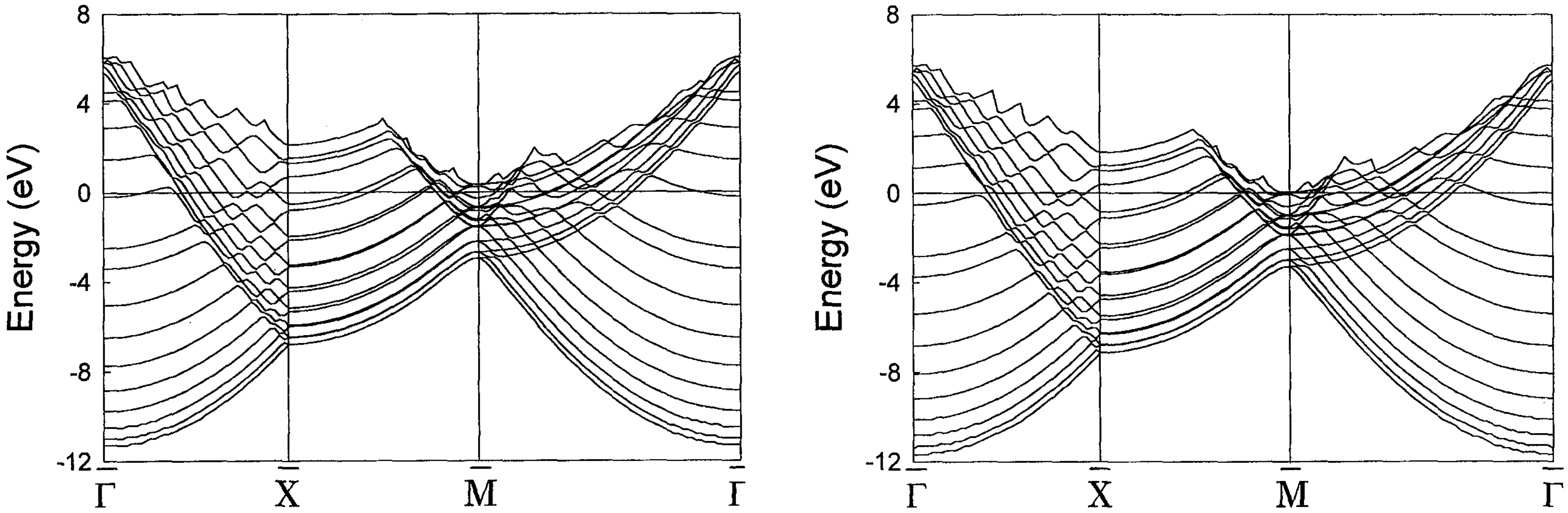

(a) unrelaxed surface

(b) relaxed surface

Figure 6-11 Band structures of Al surfaces with and without relaxation using supercell containing 9 layers of Al slab and 5 layers of vacuum region.

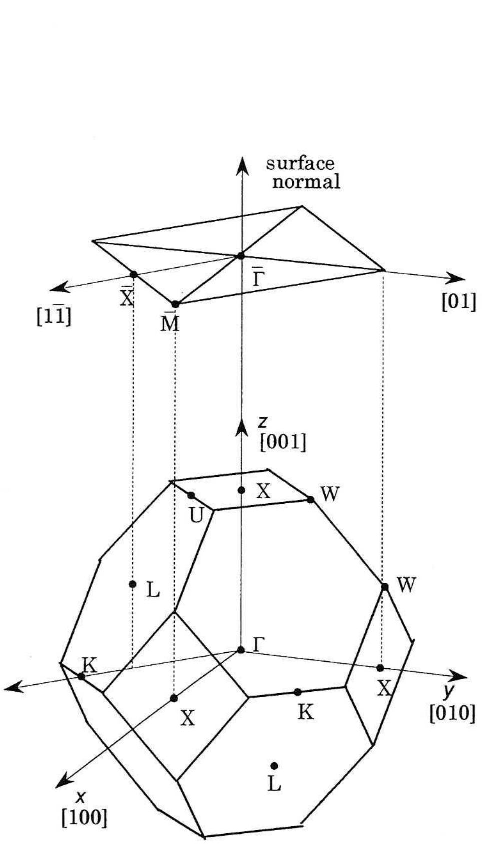

Figure 6-12 The (001) surface Brillouin zone of a f.c.c. lattice.

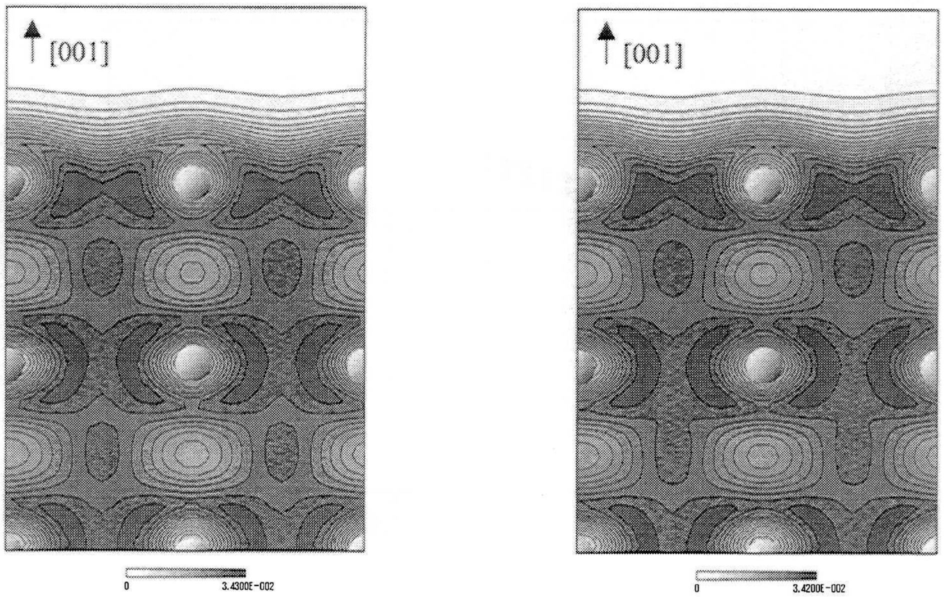

(a) unrelaxed surface

(b) relaxed surface

Figure 6-13 Charge density distribution of unrelaxed and relaxed Al (001) surfaces. Open circles show Al atoms.

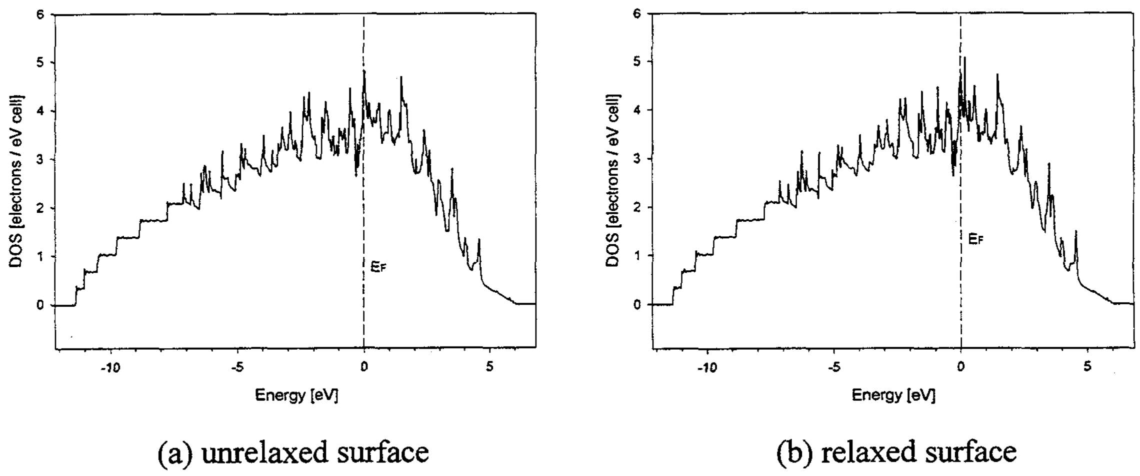

(a) unrelaxed surface (b) relaxed surface

Figure 6-14 Total DOS of the unrelaxed and the relaxed Al (001) surfaces, which demonstrate (a) and (b), respectively.

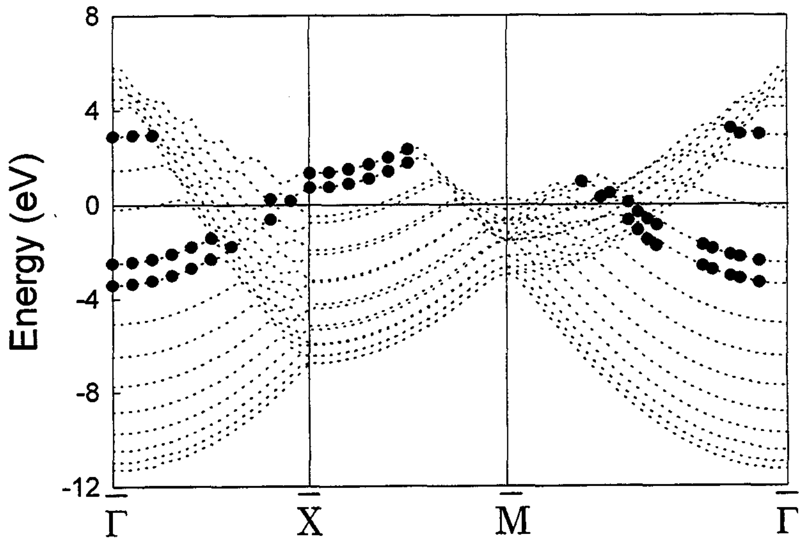

Figure 6-15 Surface states (filled circles) on Al (001) calculated by supercell containing 9 layers of Al slab and 5 Layers of vacuum region.

shown in Figures 6-14 (a) and (b). The energy shown in the horizontal axis is shifted to be $E_F = 0$. DOS of the Al (001) surface is quite different from that of Al bulk (Figure 6-9); there are fine structures near E_F which reflects the existence of surface states. However, the difference between the DOS of the unrelaxed and relaxed surfaces is not obvious. It is found from these calculational results that the electronic structure of the relaxed Al (001) surface is similar to that of the unrelaxed surface. Therefore, the surface relaxation calculated here (Table 6-6) would be caused by calculation errors. In this study, it is concluded that surface relaxation does not take place on Al (001), which agree with the experimental result by LEED.

C. Surface States

The surface states on Al (001) calculated in this study were also evaluated by comparing the experimental results. The supercell consisting of 9 layers of Al slab and 5 layers of vacuum region was used in this calculation. Figure 6-15 shows the computational result obtained in this study. The dotted lines and open circles illustrate the band structure as shown in Figure 6-11 and the surface states of Al (001), respectively. Surface states are defined as the states in which more than 60 % of electrons were localized within 2 layers from the outmost surface. The occupied level among the surface states can be measured experimentally by angle-resolved photoemission spectroscopy (AR-PES). The surface states on Al (001) experimentally examined by AR-PES were reported by Hansson et al. [38]. The experimental result is

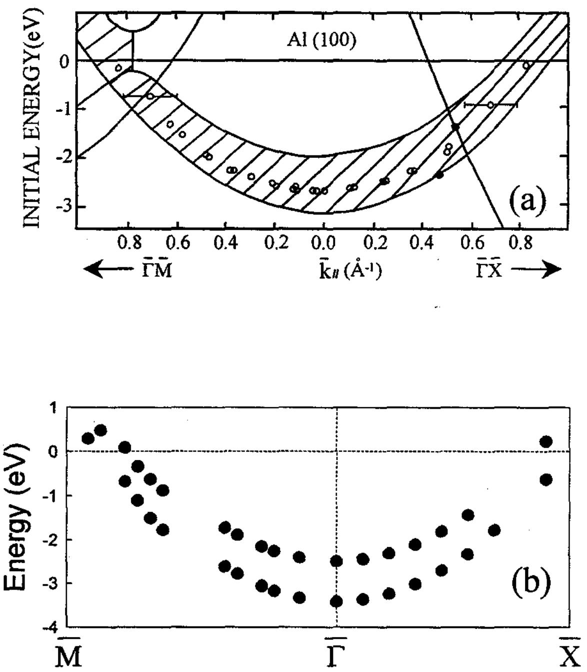

Figure 6-16 The occupied surface states on Al (001) observed by AR-PES (a) [Ref. 41] and those calculated in this study (b).

referred in Figure 6-16 (a), and the calculational result obtained in this study is also shown in Figure 6-16 (b). Although similar surface states appear below E_F in both Figures 6-16 (a) and (b), there exists a pair of surface states in the computational result. A similar result was reported by Krakauer et al. [39]. The pair of bands is considered due to the symmetric and anti-symmetric states [39]. At $\bar{\Gamma}$ point, the mean energy of a pair of surface states shown in Figure 6-16 (b) was calculated to be -2.95 eV, and it was consistent with that of the experimental value of -2.75 eV obtained by AR-PES [38]. It was concluded from these discussions that the calculational results in this study reproduced the electronic structure on Al (001) surface.

D. Discussion

It has been recognized that exoemission is related to the surface states induced by the perturbation on a solid surface, for example, adsorption, mechanically treatment, defect and so on [40-42]. However, the relationship between the origin of exoemission and the electronic structure on the surface has been not clarified yet. It was considered in the two-process model [43,44] that the trap levels of electrons were formed above E_F when an Al

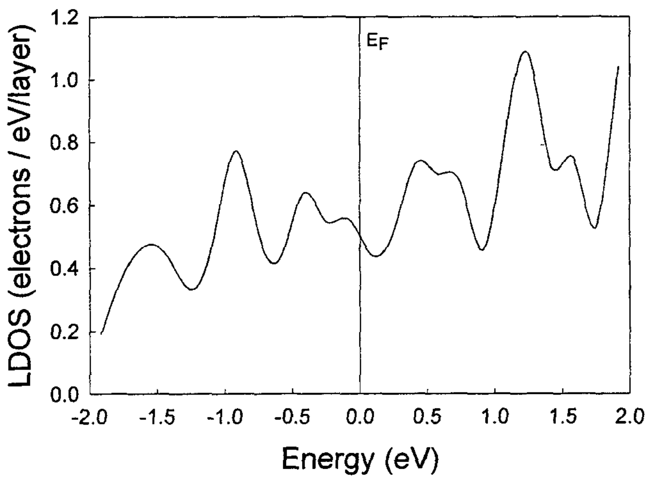

Figure 6-17 Calculated result on local density of states (LDOS) on Al (001) surface, which shows the energy distribution of electrons existing within 2 layers from the topmost surface.

surface was scratched. The electrons emitted from those traps were observed as a PSE of electrons. However, the trap levels have not been identified. Since the electronic structure on the surface can be obtained in the calculation, it will be possible to confirm whether or not the origin of exoemission is related to the electronic structure. At first, the possibility of exoemission from a clean Al (001) surface was discussed in this study.

In order to recognize the energy distribution of electrons at the surface, LDOS of Al (001) surface was calculated. The supercell used in this calculation contained 9 layers of Al slab and 5 layers of vacuum region. Figure 6-17 shows the calculational result. LDOS in this study is defined as the electronic state that exist within 2 layers from the outmost surface. It has been expected that trap levels of exoelectrons were formed above E_F [43,44]. From Figure 6-17, summits of the unoccupied states at 0.5 and 1.3 eV above E_F are considered as an origin of the trap level. According to classical statistical mechanics, the thermal energy received by electrons is estimated approximately to be several times higher than k_BT (k_B: Boltzmann's constant) [45]. Therefore, in order to excite the electrons from E_F to such states thermally, as assumed in two-process model, temperature of as high as several thousands degrees has to be introduced. However, exoemission of electrons was observed even at room temperature in the previous experiments. At room temperature, since k_BT equals 0.026 eV, the energy received by electron is considered to be too low to excite electrons to the trap level. It is concluded on the basis of the two-process model that exoemission from a clean Al (001) surface would not be observed, because such unoccupied states at 0.5 and 1.3 eV above E_F is too high to become traps of exoelectrons.

In summary, the Al pseudopotential constructed here is evaluated and it was concluded that the calculation on the electronic structure of Al (001) surface carried out in this study can reproduce the experimental results. Based upon two-process model, exoemission from a clean Al (001) surface would not take place since there is no activation energy to pump the electrons up to the trap levels.

6.6 Oxygen Adsorbed Al(001) Surface

6.6.1 Surface Structure Model

In order to calculate the electronic structure of oxygen-adsorbed Al (001) surface, the pseudopotential of oxygen atom must be constructed. The ultrasoft pseudopotential for oxygen atom was generated from the reference configuration of $2s^22p^4$ with a cut-off radius of 1.3 a.u. (0.7 Å) both for the *s* and *p* orbitals. The cut-off energy was taken to be 25 Ry. Thus, the method to construct the oxygen pseudopotential was the same as that of Al, while the evaluation was different. In general, a pseudopotential of a gas atom such as oxygen was not evaluated by the reproducibility of lattice constant but by the bond length of the molecule. The calculation of the bond length of an oxygen molecule was performed to evaluate the constructed pseudopotential of oxygen atom. In this calculation, the supercell with the size of 25 a.u. x 25 a.u. x 40 a.u. was used. The bond length was obtained from the most stable position of two oxygen atoms into the supercell. The most stable bond length was calculated to be 1.262 Å using the constructed oxygen pseudopotential. This is close enough to the experimental value of 1.207 Å [46]. Therefore, oxygen pseudopotential constructed in this study is considered to provide good approximation of the electronic property of oxygen atom.

The calculation of the electronic structure of oxygen-adsorbed Al (001) surface was conducted using the supercell containing 9 layers of Al slab as shown in Figure 6-18. As for the cut-off energy and the number of sample k-point, 25 Ry and 882 points were taken, which were the same as those in the calculation of Al. However, since oxygen atom is located on the Al surface, it is necessary that the thickness of vacuum region is evaluated individually.

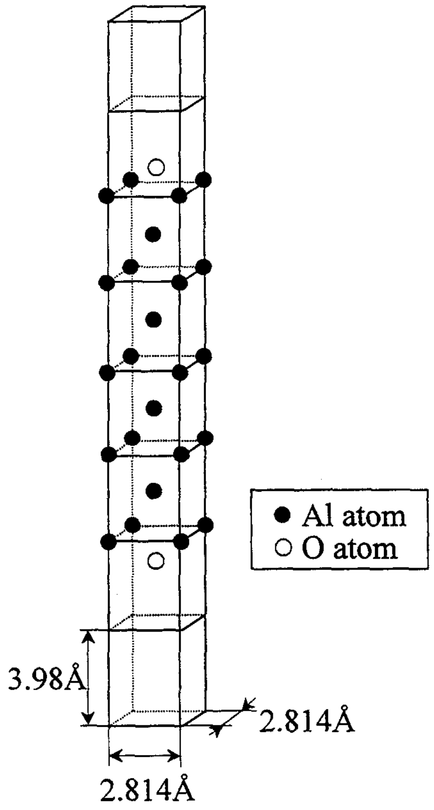

Figure 6-18 Supercell used in the simulation of oxygen-adsorbed Al (001) surface.

Table 6-7 Interaction between two oxygen atom with inter-atomic distance of 10 and 20 a.u.

Inter-atomic distance [a.u.]	Interactive force [HR/a.u.]
10.00	3.73×10^{-4}
20.00	4.46×10^{-6}

1 a.u. = 0.530 Å

Namely, the vacuum region has to be taken large enough to neglect the interaction with oxygen atoms on the counter surface. In order to determine the thickness of vacuum region, the interaction between isolated two oxygen atoms in the supercell was examined with different inter-atomic distance. Table 6-7 shows the interactive force between two oxygen atoms at the inter-atomic distance of 10 a.u. (5.29 Å) and 20 a.u. (10.58 Å). In the previous calculation to optimize the relaxed structure of Al (001), the interactive force became lower than 3.0×10^{-4} HR/a.u. when Al atom was in the most stable position. Based upon the same criterion, it is considered that the interaction between two oxygen atoms is small enough to neglect when the inter-atomic distance is 20 a.u. Therefore, the vacuum region was taken to be 7 layers, which corresponds to about 26 a.u. in the following calculations.

The adsorption site of oxygen atom on Al (001) surface was also important parameter to perform the calculation. Three sites shown in Figure 6-19 are considered as adsorption sites. There are many theoretical and experimental reports on the adsorption site of oxygen atom on Al (001) surface, and the conclusion was that oxygen atom was adsorbed at long-bridge site shown in Figure 6-19 [47,48]. In this study, the long-bridge site was chosen as an adsorption site of oxygen atom. On the other hand, there is no unified interpretation of the adsorption height of the oxygen atom at the long-bridge site. In this calculation, the adsorption height relative to the topmost Al atom (Δh_{ad}) was calculated from the total energy of the oxygen-adsorbed Al (001) surface. Figure 6-20 shows the calculated total energy for various adsorption heights of oxygen, Δh_{ad}. The total energy decreased with increasing Δh_{ad}, and it gave minimum value at Δh_{ad} = 0.589 Å. Namely, the stable position of the

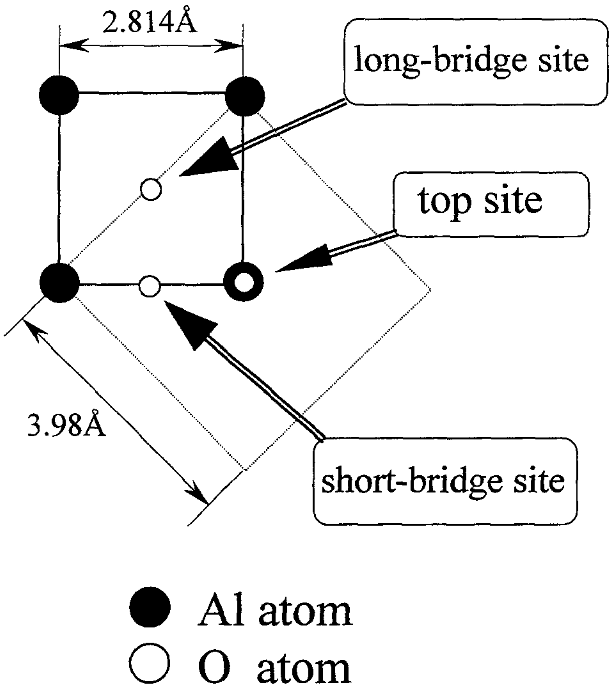

Figure 6-19 Adsorption sites of oxygen atom on Al (001) surface.

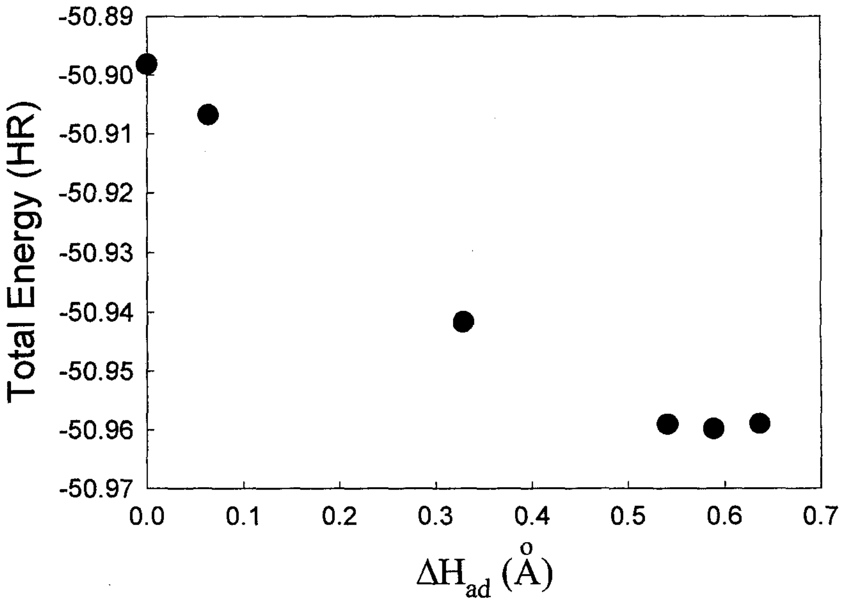

Figure 6-20 The change of the total energy of oxygen-adsorbed Al (001) surface with a variation of oxygen-adsorption height (Δh_{ad}).

adsorbed oxygen atom is calculated to be 0.589 Å higher than the topmost Al atom. The experimental results regarding the adsorption sites of oxygen atom on Al (001) through the work function measurements [49] or through the extended appearance-potential fine-structure analysis [50] suggested Δh_{ad} = 0 Å. The difference in Δh_{ad} = 0.589 Å and Δh_{ad} = 0 Å corresponds to that in bond length of 2.5 %. Also, the other computational results by the first-principles-based calculations were reported to be Δh_{ad} = 1.56 Å [51] or Δh_{ad} = 1.06 Å [52]. It was, therefore, concluded that the present results fitted the experimental results within the error of 2.5 %. Thus, Δh_{ad} = 0.589 Å was used in the following calculations.

6.6.2 Electronic Structure

The electronic structure of the oxygen-adsorbed Al (001) surface was calculated by the surface model constructed above in Section 6.6.1. Figure 6-21 demonstrates the band structure of the oxygen-adsorbed Al (001) surface. Compared with the band structure of a clean Al (001) surface, which is illustrated in Figure 6-11, new bands indicated by arrows are obvious. They are assigned to be O 2*s* and O 2*p* orbitals. Though three O 2*p* bands are seen in Figure 6-21, only two bands should appear for oxygen because of 4 electrons in O 2*p* orbital. The extra O 2*p* band in Figure 6-21 is considered due to the electron transfer from Al 3*s* or Al 3*p* to O 2*p* orbital. The similar results were also reported by Batra that electron in Al atom was transferred to oxygen atom when oxygen atom adsorption took place on Al (001) surface [53].

The surface states of the oxygen-adsorbed Al (001) surface were calculated by the same method described in Section 6.5.2.B. The surface states of the oxygen-adsorbed Al (001) are presented by filled circles in Figure 6-22. It was obvious from the comparison with the result on a clean surface shown in Figure 6-15 that the surface states were increased due to oxygen atom adsorption. The surface states attributed to O 2*p* orbital distribute at around 10 eV below E_F. According to the experimental results using photoemission, it was reported that the energy distribution of electrons in O 2*p* orbital was expanded to 10 eV below E_F when the oxygen atom was adsorbed on Al (001) surface [54,55]. The present result on the surface state of the oxygen-adsorbed Al (001) showed good agreement with the

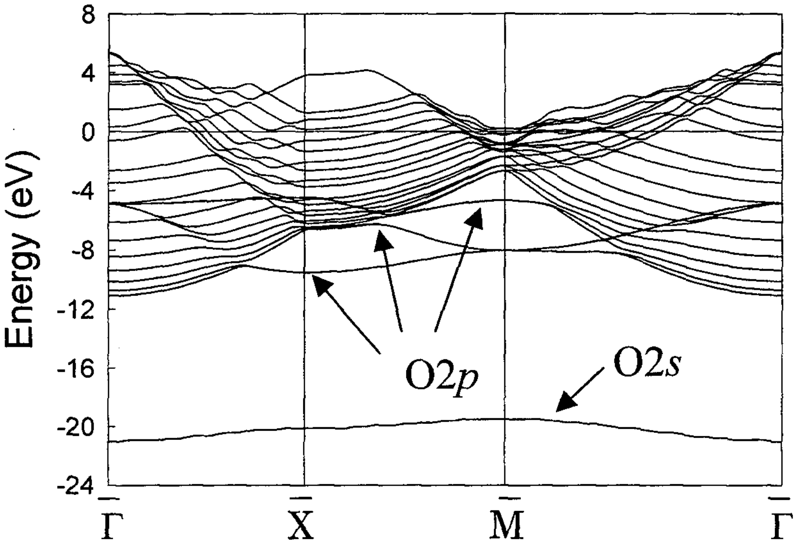

Figure 6-21 Band structures of oxygen-adsorbed Al (001) surface.

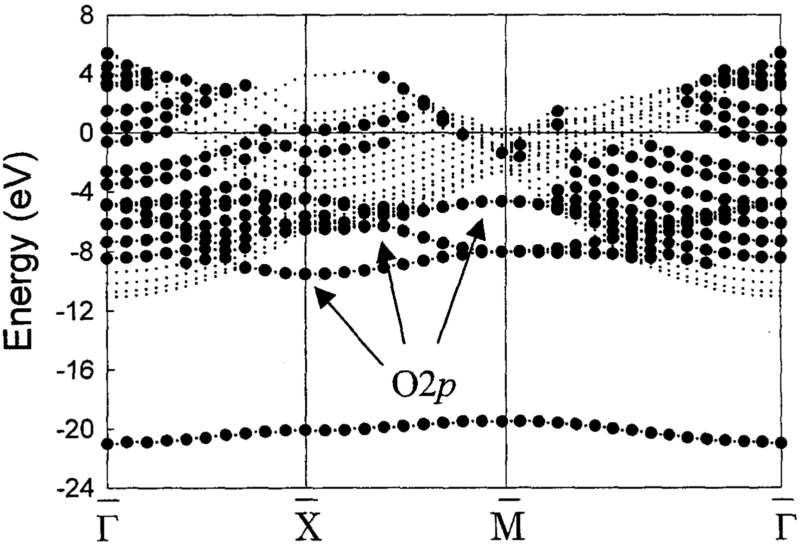

Figure 6-22 Surface states of the oxygen-adsorbed Al (001), which are shown by filled circles.

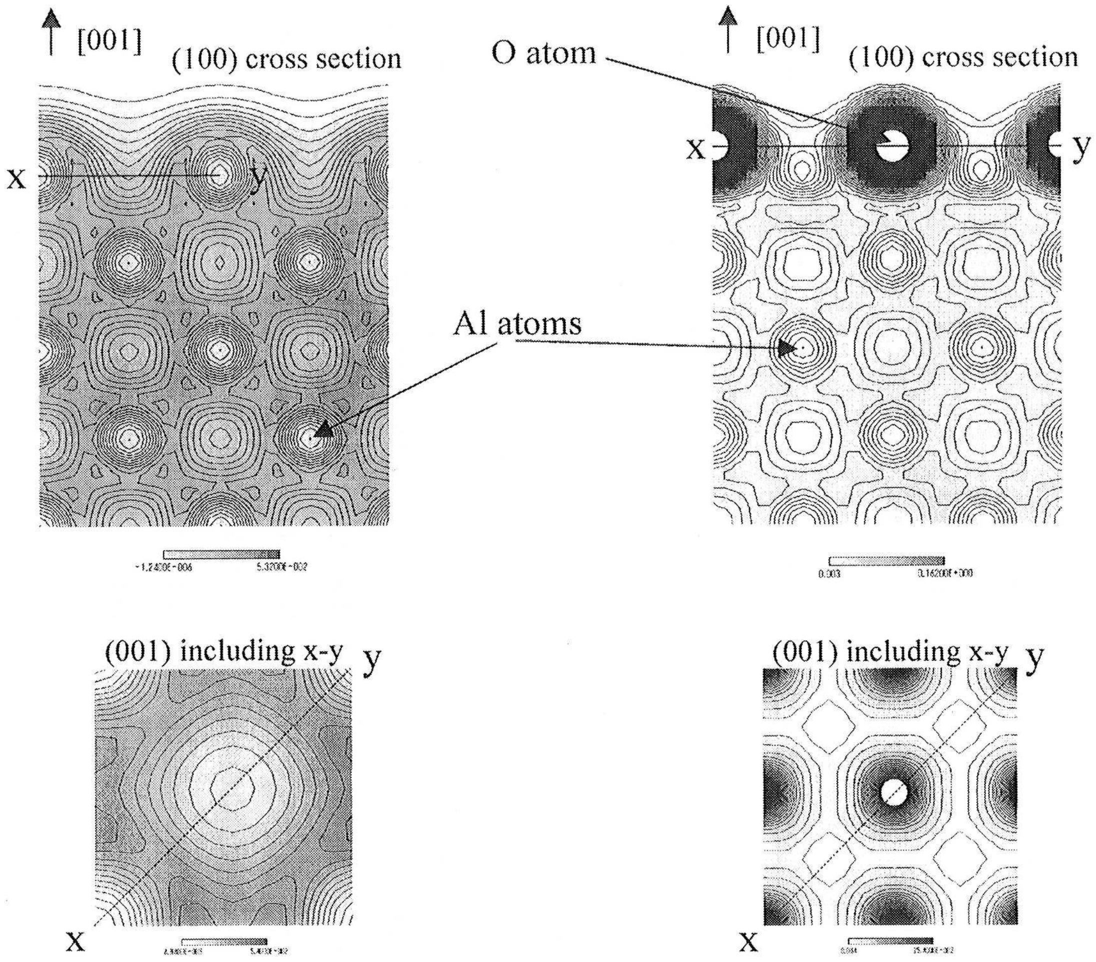

(a) clean surface

(b) oxygen-adsorbed surface

Figure 6-23 CD of the clean and oxygen-adsorbed surfaces; the higher and lower panels show the (100) cross section and the top view of the CD.

experimental results.

The CD on oxygen-adsorbed Al (001) surface was calculated by the method as described in 6.5.2.B and compared with that of a clean Al (001) surface. Figures 6-23 (a) and (b) illustrate (100) cross section of CD on the clean and the oxygen-adsorbed Al (001) surface, respectively. Two lower panels show the top view of CD at Al (001). It is found that CD increases around oxygen atoms. This increase of CD is caused by the surface states introduced by the oxygen adsorption as described above, and it is obvious that electrons are transferred from Al atom to oxygen atom.

6.6.3 Discussion

An emission mechanism of exoelectrons was constructed on the basis of the computational results of the first-principles calculation described above. The energy distribution of the surface states was examined at the clean and at the oxygen-adsorbed Al (001) surfaces by calculating LDOS. The results are indicated in Figure 6-24. The dotted and solid lines represent LDOS of the clean and oxygen-adsorbed Al(001) surface, respectively. E_{FC} and E_{FO} indicate the E_F of these surfaces. It was reported by Gresptad et al. that the work function of a clean Al (001) surface was 4.4 eV, *i.e.*, E_{FC} was decided to be located at 4.4 eV below vacuum level [56]. The E_F of the oxygen-adsorbed surface (E_{FO}) locates 0.6 eV higher than that of the clean surface (E_{FC}) due to the decrease in work function [57,58]. It is obvious in Figure 6-24 that both occupied and unoccupied surface states near E_F are increased by oxygen adsorption. It is widely known that exoemission due to gas adsorption on a metal surface is usually observed at the initial stage of the adsorption [59-61]. On the Al (001) surface, it was reported that islands of adsorbed oxygen atoms were formed at the initial stage of oxidation [57,62,63]. Since the formation of oxygen-islands leads to a local work function decrease as shown in Figure 6-24, the mean Fermi level (E_{FT}) over the partially oxidized surface moves from E_{FC} to E_{FO} depending on the fraction of the oxygen-islands. Therefore, even when the stimulating energy, which is lower than the mean work function, was introduced to Al (001) surface at the initial stage of oxygen adsorption, the electrons at the shadowed area in Figure 6-24 might be emitted as exoelectrons. This emission model was labeled the low work function patch (LWP) model. A similar emission

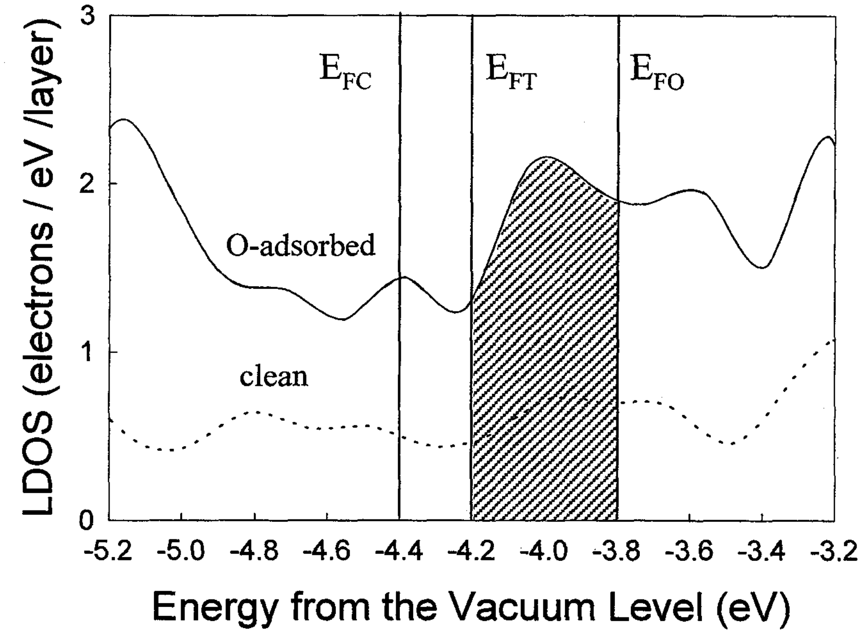

Figure 6-24 LDOS of the clean and oxygen-adsorbed Al (001) surfaces near E_F, which represent dotted and solid lines, respectively.

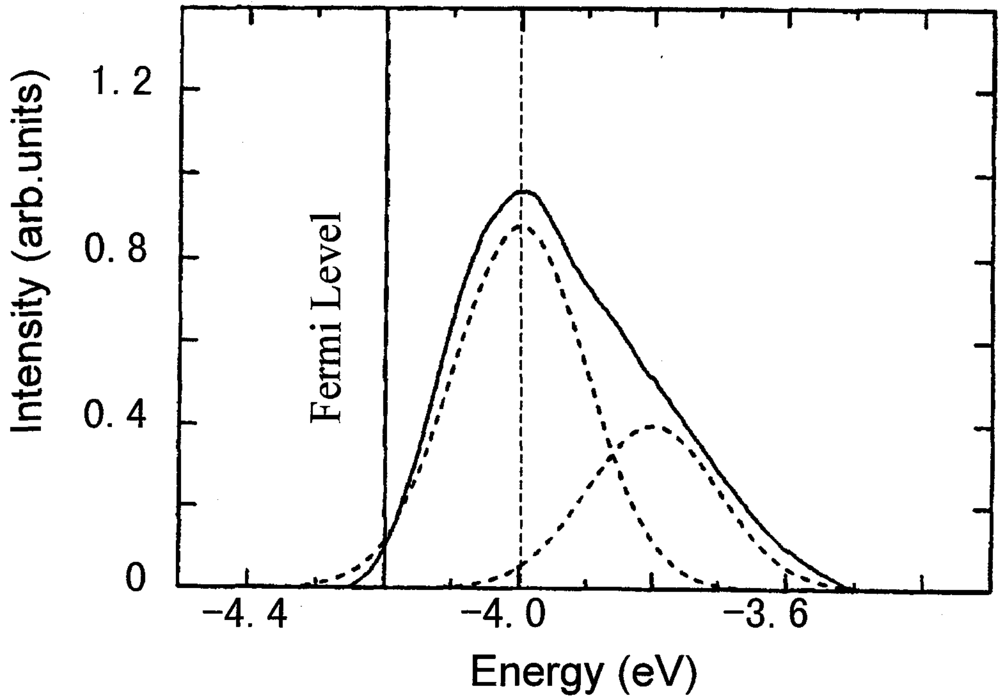

Figure 6-25 Total energy distribution of electrons emitted through FSE the Al tip surface annealed at 420 K for 30 min. [3]

mechanism of exoelectrons has been proposed for PSE from oxygen-adsorbed Mg surfaces [59]. However, we have demonstrated that the LWP model may be applied to exoemission from Al tip surface.

An attempt to compare the computational results obtained in this study with the previous experimental results has been made. The detail of the experiment has been reported in the literature [3], however, brief description is written here. In order to apply a high electric field in the order of 10^9 V/m, an electrochemically etched Al tip (99.9999% pure) was used as a sample. The total energy distribution (TED) of field stimulated exoelectrons from the Al tip surface were examined at room temperature in UHV of 4 x 10^{-10} torr. Figure 6-25 shows the TED of exoelectrons from the Al surface after annealing treatment. It shows bimodal spectrum, *i.e.*, peaks at 4.0 and 3.8 eV below the vacuum level were obvious before oxygen exposure. The oxygen exposure of 900 L led to a new peak at 3.6 eV and also enhanced the peak at 4.0 eV. The conclusion was that exoelectrons at 3.6 eV and 4.0 eV below the vacuum level originated from oxygen adsorption [3]. In that experiment, the Al tip was annealed at 420 K for 30 min. According to the report by Lauderback et al., it was found that small amounts of adsorbed oxygen atoms remained on the Al (001) surface even after the annealing treatment [64]. The mean work function of a polycrystalline Al surface, where small amounts of oxygen atoms remained, was measured to be 4.2 eV [65]. Thus, E_{FT} in our previous experiment was considered to be 4.2 eV below the vacuum level. From the literature [56], E_{FC} and E_{FO} were located to be 4.4 and 3.8 eV below the vacuum level, respectively. These values are reflected in Figure 6-24, and it is expected that an electron-filled states at the partially oxygen-covered Al(001) surface (shadowed area in Figure 6-24) indicate a peak at 4.0 eV below vacuum level. The peak position of the electron–filled state (4.0 eV) explains one of the peak positions in the total energy distribution of exoelectrons measured experimentally (Figure 6-25).

FSE is a phenomenon that exoelectrons are emitted from the surface where a high electric field (~10^9 V/m) is applied. This electric field is the same order of magnitude of that applied during the field emission or STM measurements. There is a possibility that the applied field to the surface during the FSE measurements may alter the electronic structure of the electron emitting surface. However, it has been confirmed that a similar phenomenon was observed even when Al surface was exposed to ultraviolet light on behalf of the high electric field [59]. Moreover, it has also been reported that the electron emission took place during the primary stage of oxidation of Mg even though the wavelength of the irradiating light was longer than the threshold of photoemission [59]. Grunberg also detected PSE during the oxidation of the abraded Al surfaces [66]. From these experimental results reported previously, we conclude that the effect of high electric field to the electronic structure of the Al surface may be negligible. Thus, we consider that it is reasonable to compare the experimental results on FSE from Al tips and the computational results reported herein.

As is described above, the LWP model based on the first-principles calculation explains the peak position of the exoelectrons emitted from the partially oxygen-adsorbed Al(001) surface. However, the LWP model can only be applicable to the stationary surface, and cannot describe the dynamics of the surface. This is the limitation of the LWP model which can not explain the dynamics of exoelectron emission such as storage effect [43,44]. In order to construct a concrete emission model including surface dynamics, a molecular dynamics study based on the first-principles calculation under the effect of a high electric field may be required in future.

In summary, a computational study with the first-principles calculation was carried out in order to elucidate the origin of exoelectrons from Al tips. It was shown that the first-principles calculation based on the ultrasoft pseudopotential can reproduce the lattice constant and the surface band structure of Al measured by the experiment. From the comparison of LDOS at the clean and at the oxygen-adsorbed surfaces, the low work function patch (LWP) model was proposed as the exoemission model. The LWP model explained the peak position in TED of exoelectrons emitted from Al tips. Even though the dynamic behavior of exoemission is impossible to describe by the current LWP model, the effectiveness of computational study on exoemissions has been demonstrated.

6.7 Defected Al(001) Surface

6.7.1 Supercell with a Point Defect

The supercell used in this calculation are shown in Figures 6-26 (a) and (b), which represent the models of a clean and defected Al(001) surface, respectively. These supercells contain 5 layers of Al slab and 5 layers of vacuum region, and are larger than that for the clean surface shown in Figure 6-10 so as to reproduce the effect of defect on the surface. In this calculation, the cut-off energy of 25 Ry and 338 k-points were used. In order to confirm that these parameters provide good approximation, the electronic structures of a clean Al(001) surface were calculated by the supercell shown in Figure 6-26 (a) and Figure 6-10 (or Figure 6-26 (c)). These supercells are labeled “*L-cell*” and “*S-cell*”, respectively. Table 6-8 shows the total energy per atom. It is found that the total energy calculated using *L-cell* is consistent with that using *S-cell*. Also, CD was calculated using both cells, and the results are shown in Figure 6-27 (a) and (b). No difference was observed between these two results. Therefore, it was confirmed that the parameters of the cut-off energy of 25 Ry and 338 k-points used in this calculation also provided a good approximation of the electronic structure on the clean Al (001) surface.

Table 6-8 Comparison of total energy per an atom calculated using *L-cell* and *S-cell*.

	Total Energy [HR / atom]
L-cell	−2.0911
S-cell	−2.0913

6.7.2 Results and Discussion

The electronic structures of the clean and defected Al(001) surfaces were calculated using the supercells shown in Figures 6-26 (a) and (b). Figures 6-28 and 6-29 illustrate CD

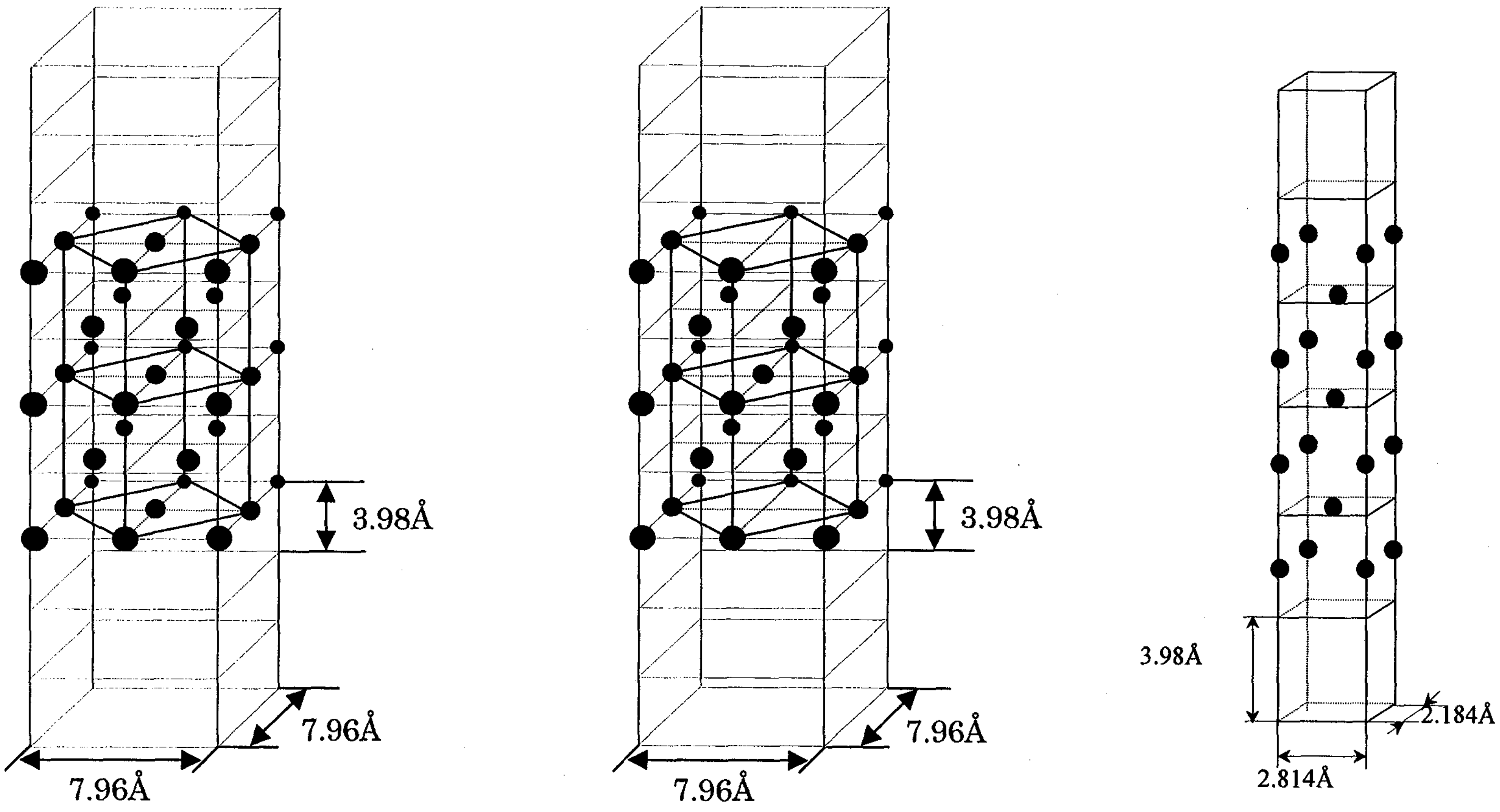

(a) clean surface model
(*L-cell*)

(b) defect surface model

(c) clean surface model
shown in Figure 6-10
(*S-cell*)

Figure 6-26 Supercells for the calculation of electronic structures on a clean and defected Al (001) surfaces; the clean and defected surfaces are shown in (a) and (b), respectively. (c) is the clean surface model shown in Figure 6-10.

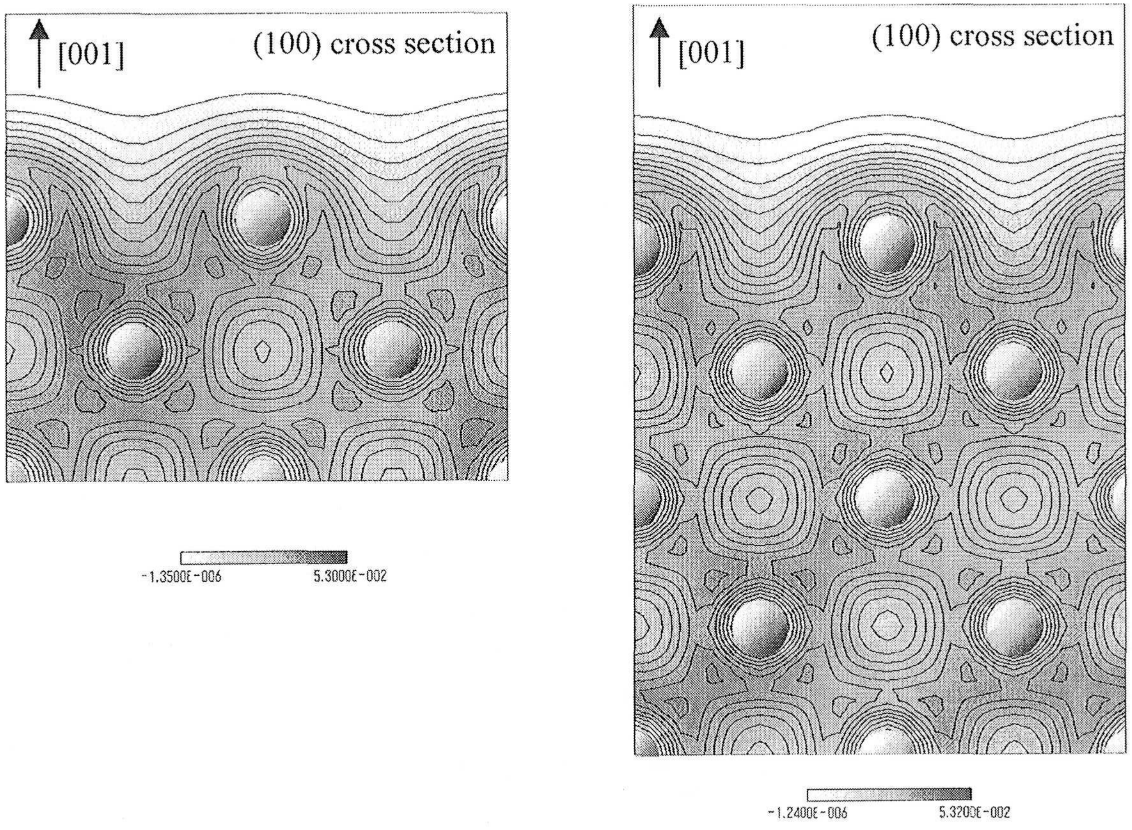

(a) *L-cell*

(b) *S-cell*

Figure 6-27 CD of the clean Al (001) surfaces calculated using *L-cell* and *S-cell*. Gray circles show Al atoms.

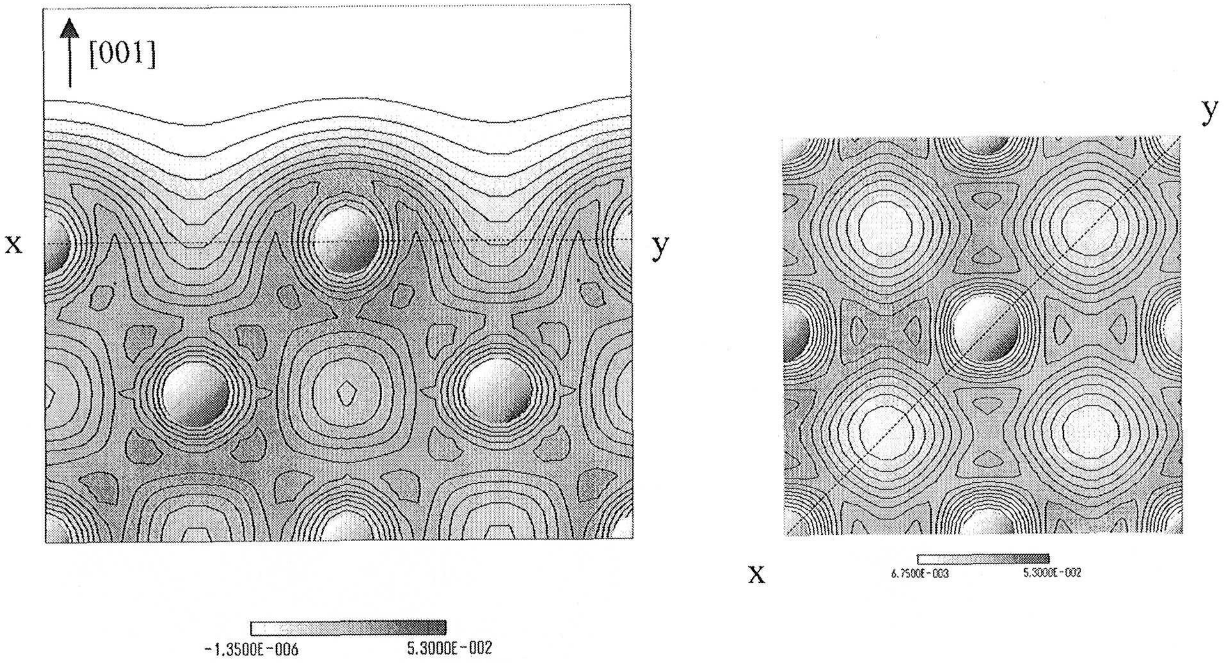

(a) (100) cross section

(b) (001) top view

Figure 6-28 CD of valence electrons on a clean Al (001) surface calculated using the surface structure model (supercell) shown in Figure 6-27 (a).

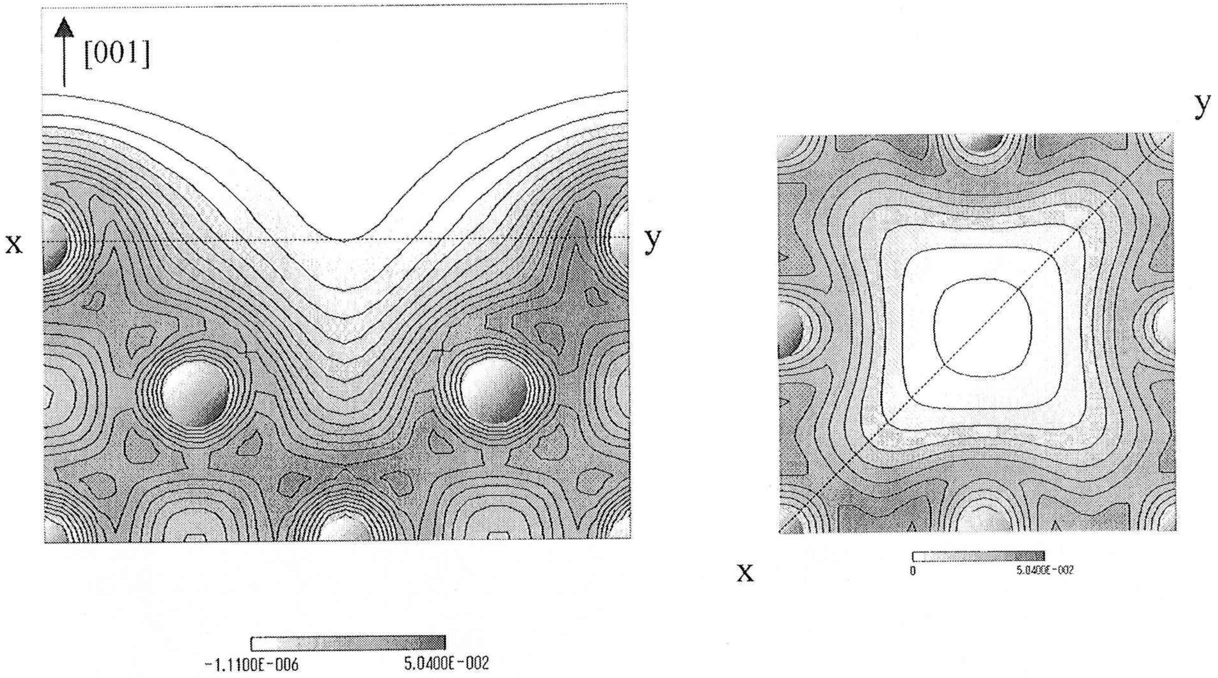

(a) (100) cross section

(b) (001) top view

Figure 6-29 CD of valence electrons on a defected Al (001) surface calculated using the surface structure model (supercell) shown in Figure 6-27 (b).

of valence electrons on the clean and defected surfaces, respectively. In the Figure 6-29, CD was reduced at the point defect. Except for the defect site, there is no obvious change on CD among these surfaces. However, LDOS of the defected surface, which are the states of electrons existing within 2 layers from the outmost surface, were different from that of the clean surface. The calculation results on LDOS of the clean and defect surface are shown in Figure 6-30. The dotted and solid lines correspond to LDOS of these surfaces, respectively. Though the difference of the unoccupied states between these surfaces was not clearly seen, the occupied states of the defected surface became obviously higher than that of the clean surface. It is considered that the introduction of point defect makes the surface energy high. Therefore, electrons with higher energy are increased, and consequently the occupied states of the defected surface near E_F would become higher than those of the clean surface. In order to recognize the distribution of electrons such high energies on the defected surface, CD was calculated. CD at the energies ranging from E_F to -0.15 eV is shown in Figure 6-31. Figures 6-31 (a), (b) and (c) demonstrate CD of the cross section of

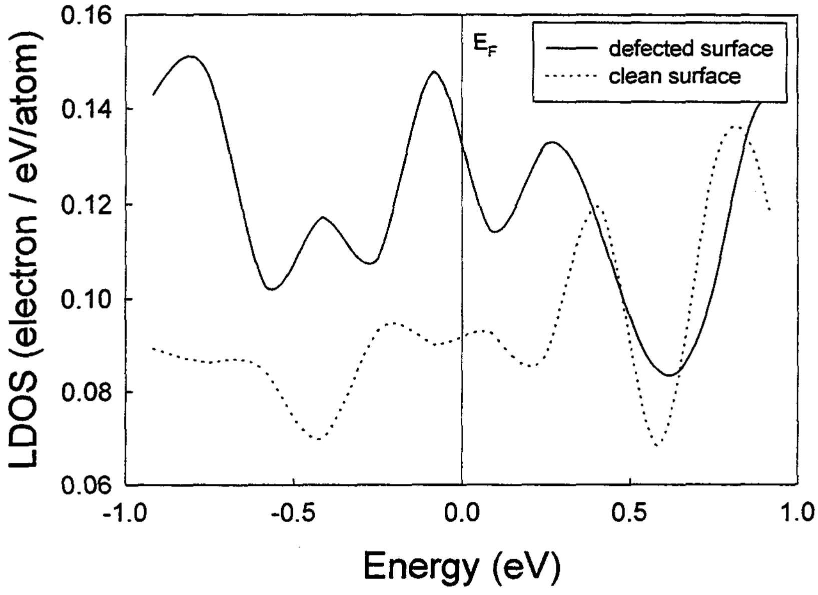

Figure 6-30 LDOS the clean and defected surfaces, which are represented by the dotted and solid lines. LDOS mean the states of electrons existing within 2 layers from the topmost Al layer.

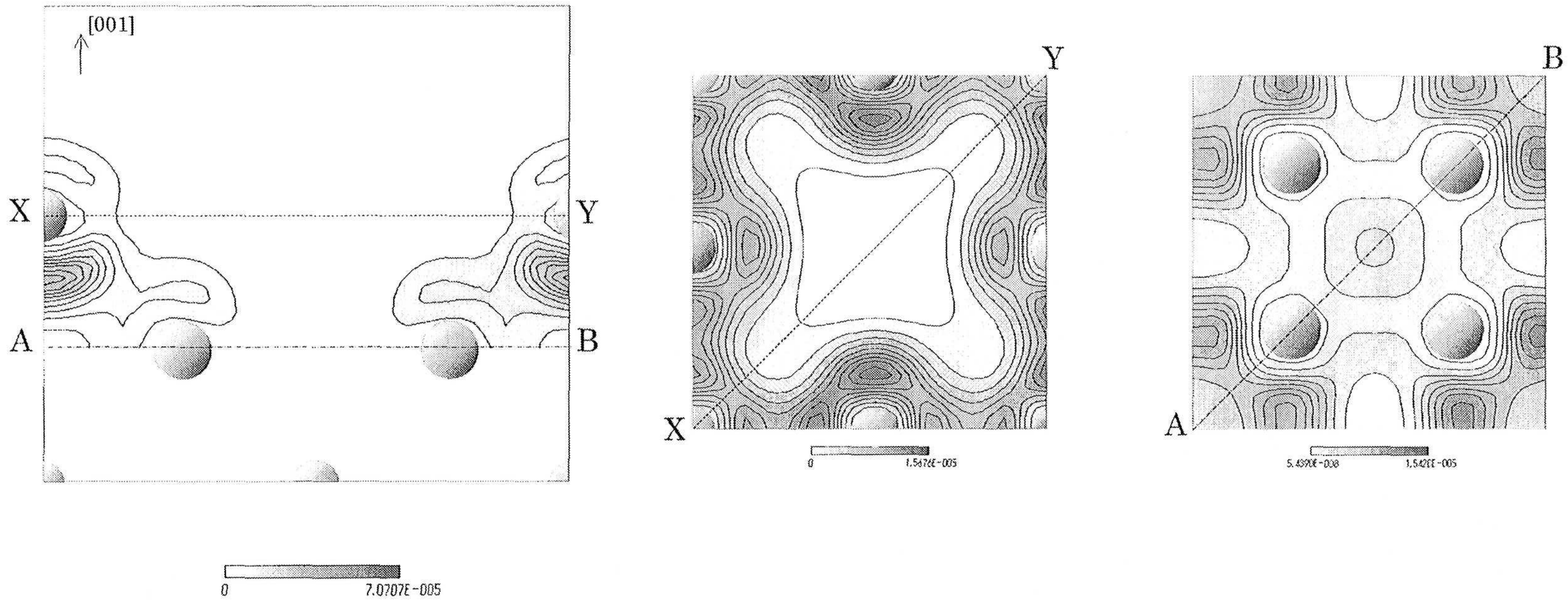

(a) (100) cross section

(b) (001) top view
(1st layer)

(c) (001) top view
(2nd layer)

Figure 6-31 CD of electrons with energies from E_F to -0.15 eV on the defected surface; (a) shows (100) cross section of the CD. (b) and (c) are top views of the (001) planes including X-Y and A-B lines, respectively.

(100), top view of the topmost (001) plane including X-Y line, and that of the second (001) plane including A-B line, respectively. From these figures, it is found that electrons with such higher energies do not exist at the point defect, while those electrons localize around the defect.

There is no report regarding the relationship between a point defect and exoemission property on an Al surface, and it was, however, reported by Buck et al. that PSE occurred at the Al surface sputtered by argon ions [67]. When the photoemission property from the ion-sputtered Al surface were compared with that of the well-annealed surface, it was found that the ion-sputtered surface enhanced the photoemission yield three times greater than well-annealed surface. They concluded that disorders on the surface induced by ion sputtering enhanced the photoemission yield. In our computational results, a point defect on Al(001) surface induced the enhancement of the electron-filled states near E_F. This calculational result obtained here explains the experimental result on the enhancement of photoelectron yield on the ion-sputtered surface. In summary, the increment of LDOS due to point defects on the surface was calculated in this study. The change in electronic structure may play a role as one of the origins of exoemission.

6.8 Stepped Al(001) Surface

6.8.1 Structure Model

The electronic structure was calculated at the surface with atomic steps parallel to [110] direction as shown in Figure 6-32. When electronic structure of the low index plane with steps is calculated, the structure model of the high index plane consisted of such steps is used generally, as shown in Figure 6-33 [67-70]. This facilitates the calculation due to high symmetry in a supercell. In this calculation, the supercell represented by the dotted line in Figure 6-33 was used. Namely, the electronic structure of Al(115) surface instead of stepped Al(001) surface was calculated. The parameters such as thickness of vacuum region, cut-off energy and the number of sample k-point were 13.4 Å corresponding to 6.7 layers of Al(001) lattice spacing, 25 Ry and 242 points, respectively. In order to obtain a

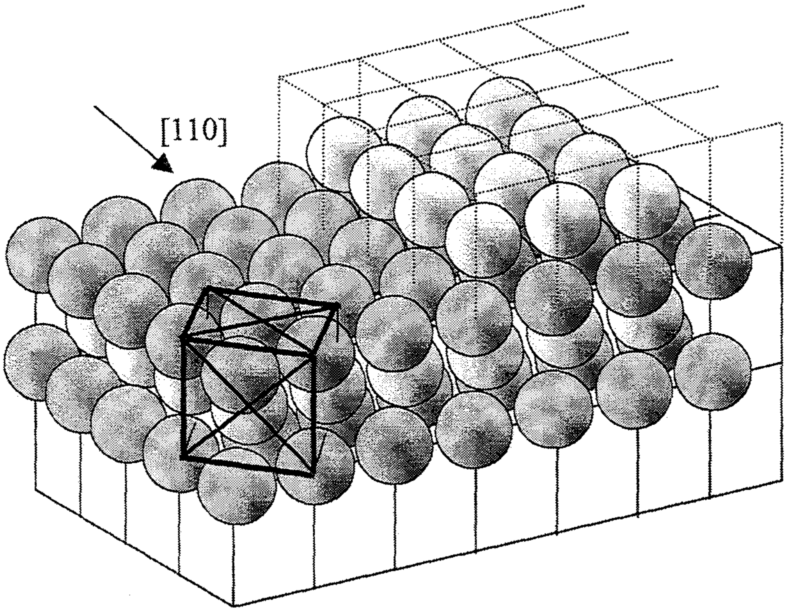

Figure 6-32 Structure model of the stepped Al (001) surface. Unit cell is indicated by solid lines.

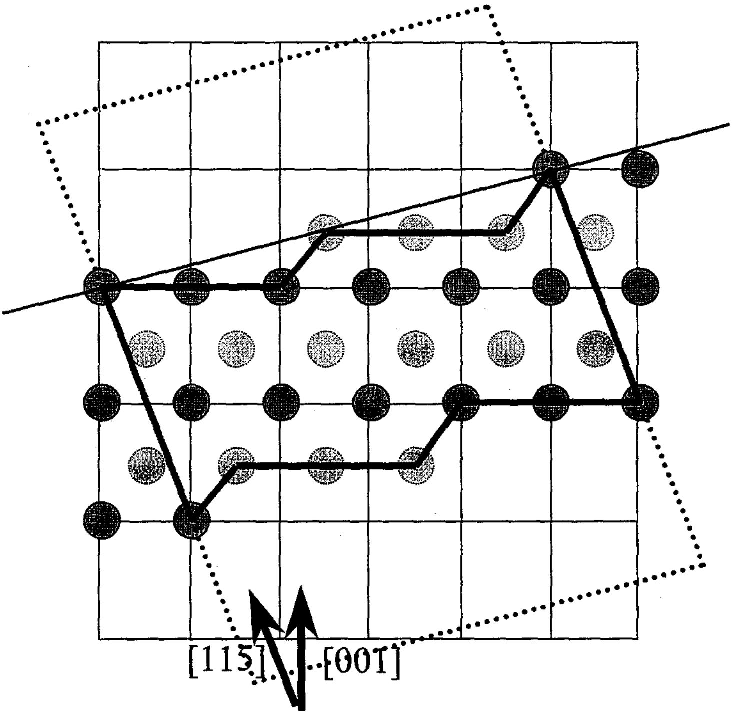

Figure 6-33 The side view of the stepped Al(001) surface model shown in Figure 6-32. Supercell used in this calculation is indicated by the dotted line.

good approximation, the total energy convergence against these parameters has to be confirmed. However, since the supercell used in this calculation was too large to evaluate the results by the methods explained in Section 6.5.2. Therefore, the computational results obtained by using the supercell were evaluated as follows.

In the case of face-centered cubic metal, the contribution of second nearest neighbor atoms to binding energy is weak. Therefore, if it is assumed that the binding energy depends on the number of nearest neighbor atoms, the change of surface energy can be estimated from the change of the counting nearest neighbor atoms on a surface. Based upon this assumption, the evaluation of the calculational result on the stepped Al(001) surface was applied. The results are summarized in Table 6-9, and all values are normalized by the number of the surface atom. The total energy difference between on Al bulk and on Al

Table 6-9 The evaluation of the reliability of the calculational results on the Al(001) stepped surface.

	ΔE (HR / atom)	ΔE_u (HR / atom)
Clean surface	0.0082	0.005125

	ΔE_{ex} (HR / atom)	ΔE_p (HR / atom)
Defected surface	0.0113	0.0111
Stepped surface	0.00939	0.00950

ΔE: the difference of total energies between the Al(001) bulk and the the clean Al (001) surface.

ΔE_u: the increased energy per one lost nearest-neighbor atom.

ΔE_{ex}: the energy difference between bulk and defected or stepped surface calculated by ΔE_u.

ΔE_p: the energy difference between bulk and defected or stepped surface obtained by the pseudopotential method.

(001) clean surface, ΔE, was calculated to be 0.0082 [HR]. When the one nearest-neighbor atom is removed, the increase of the total energy, ΔE_u, is estimated to be 0.005125 [HR]. Therefore, the total energy difference, ΔE_{ex}, between on the bulk and the defect surface was calculated by ΔE_u thus obtained, and compared with that, ΔE_p, calculated by pseudopotential method. It is found that both of the values are in good agreement, and therefore, this evaluation method of the energy convergence is considered to be reasonable. The same evaluation is applied to the calculational results on the stepped Al(001) surface. The ΔE_p between the clean and the stepped surfaces using the parameters described above is consistent with ΔE_{ex} between them. From this evaluation, it was confirmed that the vacuum region of 13.4 Å, the cut-off energy of 25 Ry and 242 k-points gave a well-converged result.

Moreover, further evaluation of our computational result was made by the comparison of CD in valence electrons. Figures 6-34 (a) and (b) show the CD of the stepped and clean Al(001) surfaces, respectively. Inside the second layer from the stepped surface, CD is similar to that of the clean surface. Therefore, our calculational result regarding the stepped surface is considered to be accurate.

6.8.2 Electronic Structure

The electronic structure of the stepped Al(001) surface was calculated by the pseudopotential method using the supercell shown in Figure 6-33. Figure 6-35 (a) demonstrates LDOS of the stepped and clean surfaces. The solid and dotted lines represent LDOS of these surfaces, respectively. LDOS of the stepped surface is defined as a state existing in the surface region outside the hatched area illustrated in Figure 6-35 (b). In the occupied state region, there was slight increase of LDOS just below E_F, which labeled '*A-peak*', while a great increment of LDOS at 0.4 eV above E_F was seen in unoccupied states, which labeled '*B-peak*'. In order to examine the origins of these increase in LDOS, the spatial distributions of electrons with the states labeled '*A*' and '*B*' were calculated. The computational result on the *A-peak* distribution is shown in Figure 6-36. It is found that

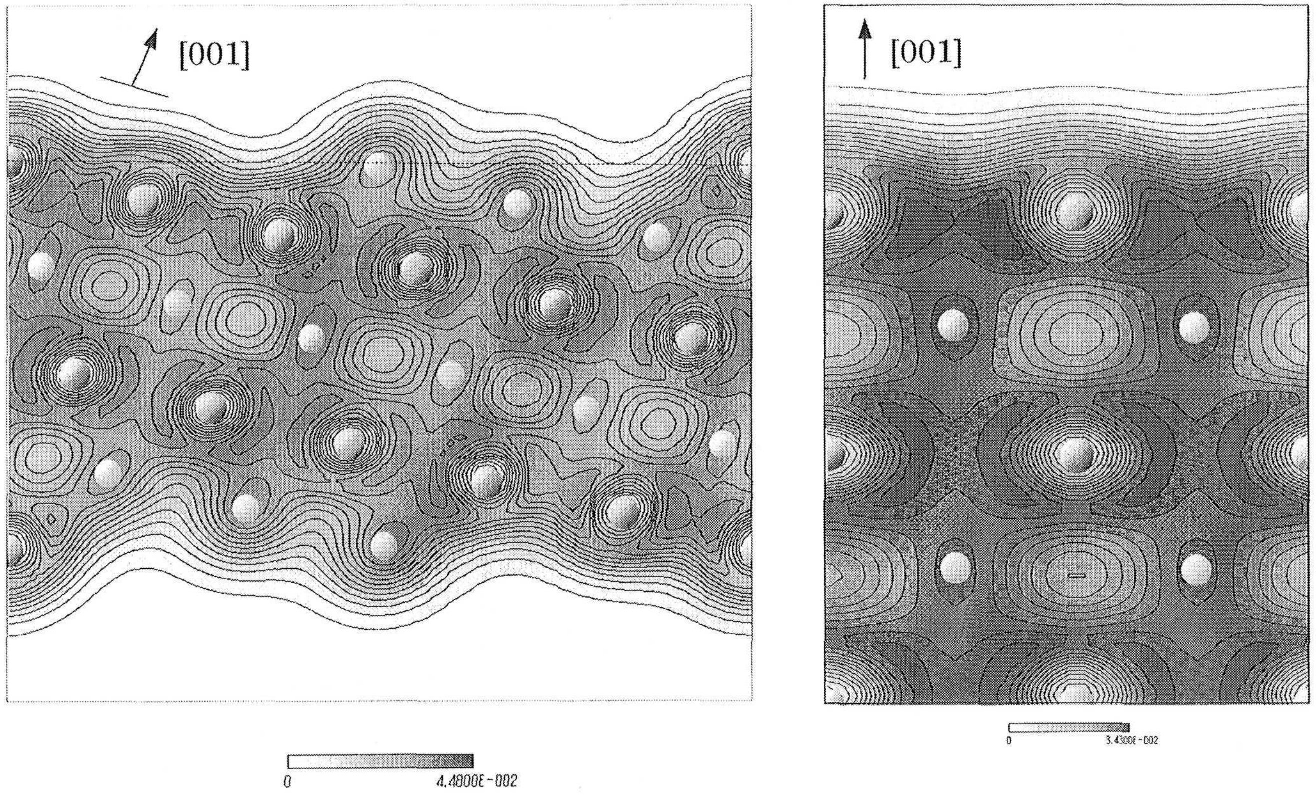

(a) stepped surface

(b) clean surface

Figure 6-34 CD of the stepped and the clean Al (001) surfaces.

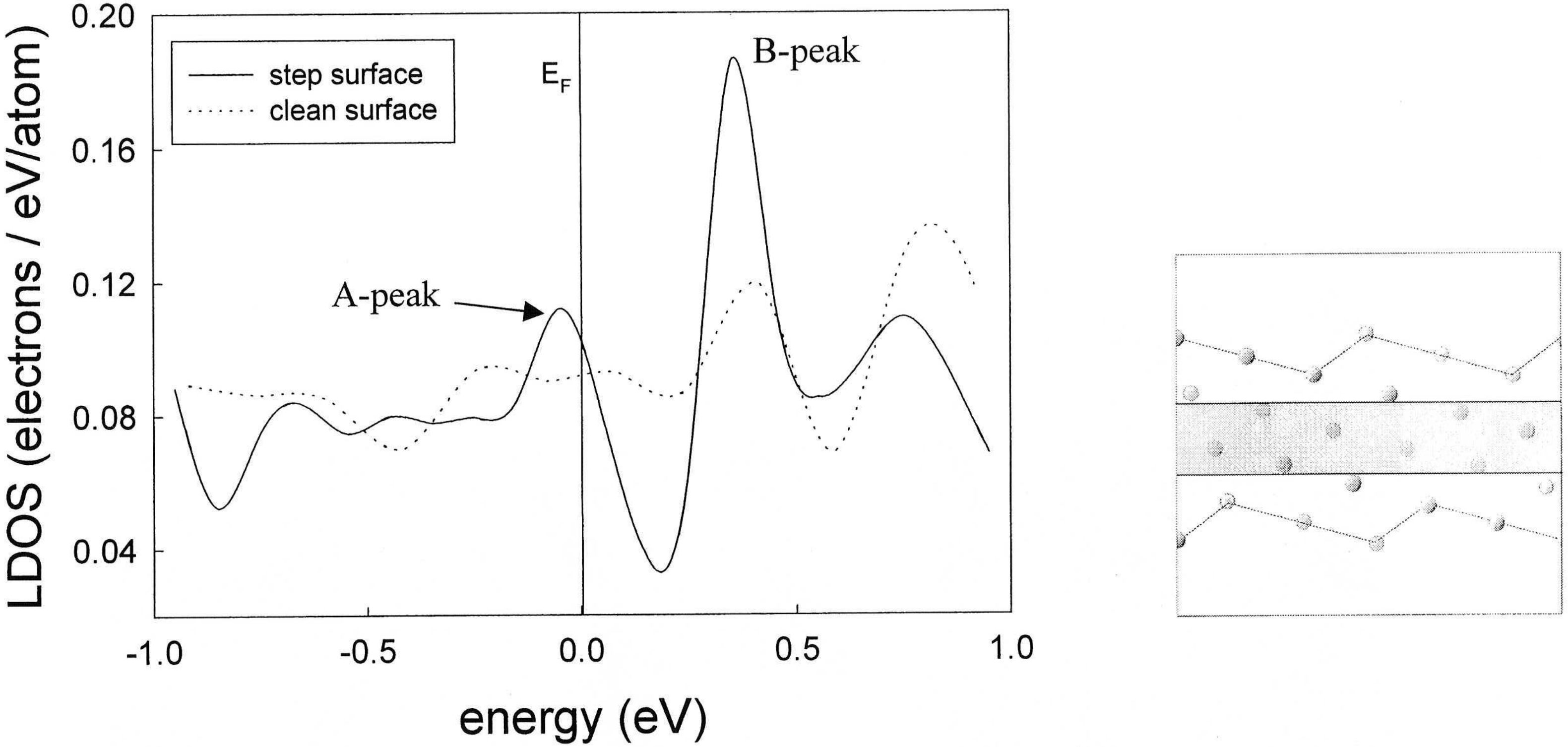

(a) LDOS of stepped and clean surfaces

(b) (100) cross section

Figure 6-35 LDOS of the stepped and clean surfaces, which are shown by solid and dotted lines. LDOS are the states of electrons existing in the unhatched area in (b).

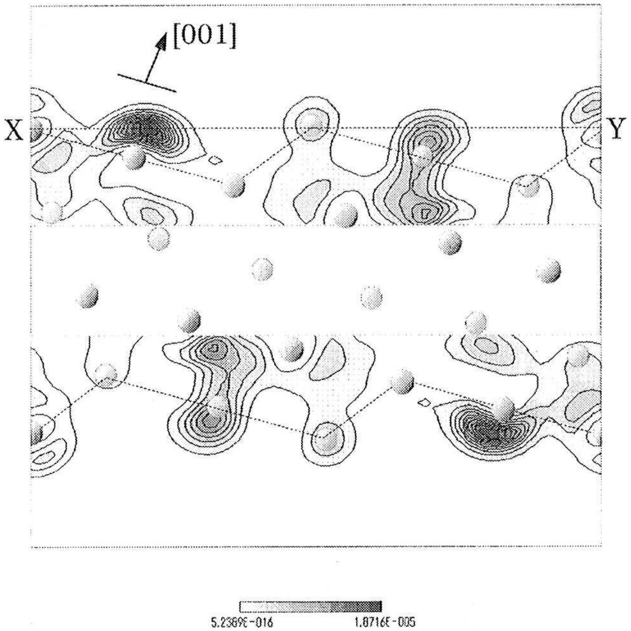

(a) (110) cross section

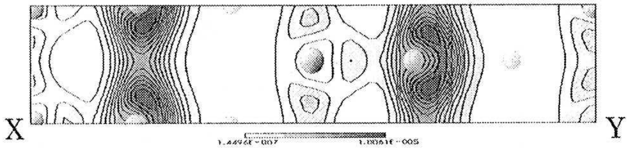

(b) (115) top view

Figure 6-36 CD of electrons with the states denoted by "A-peak" on the stepped Al(001) surface (Al(115) surface)

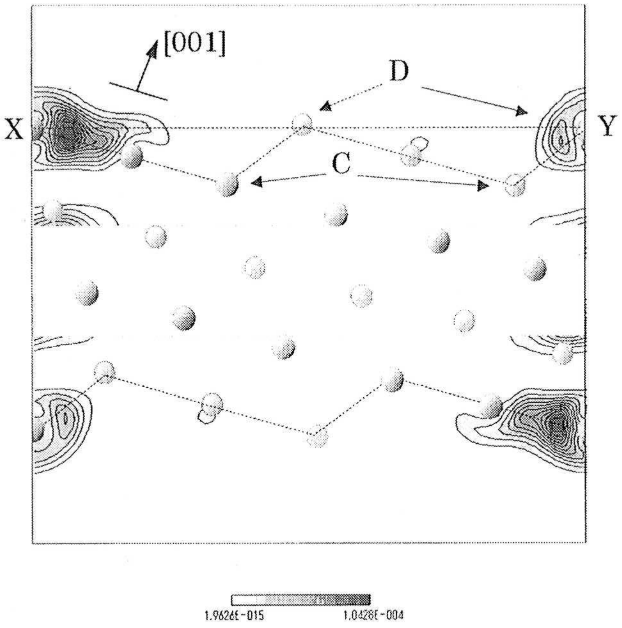

(a) (110) cross section

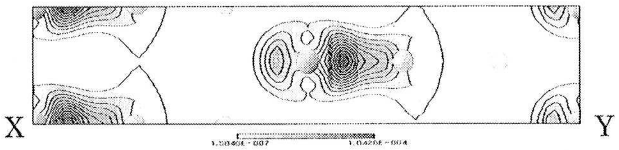

(b) (115) top view

Figure 6-37 CD of electrons with the states denoted by "B-peak" on the stepped Al (001) surface (Al(115) surface).

these states consisting the peak "*A*" exist mainly at a terrace region. On the other hand, unoccupied states, which consists the peak "*B*", localize clearly at steps as shown in Figure 6-37. Especially, these states distribute over not the bottom atoms of steps labeled '*C*', but the topmost atoms of steps labeled '*D*'. The *D-atoms* are less stable than the *C-atoms*, because *D-atoms* have 5 dangling bonds while *C-atoms* have 2. Therefore, it was recognized that *B-peak* in LDOS states were originated to unstable *D-atoms* located the steps.

6.8.3 Discussion

On the Al surfaces, many reports have been made on the PSE phenomena. Especially, regarding a scratched Al surface, PSE property has been examined in detail [71-77]. Since it is supposed that a scratched Al surface contains many atomic steps, which might be considered to be one of origins of PSE. In our computational results, the characteristic change of the electronic structure due to an atomic step on the Al(001) surface was obtained. In this part, the effect of steps on PSE was discussed.

PSE is the emission phenomenon observed even when the stimulating light energy is even lower than the threshold of photoemission (work function). At the beginning, it is necessary to understand the effect of the atomic step on work function. Though there has been no experimental study on work function of the stepped Al surface, it was theoretically reported by Ishida et al. that the work function decreased linearly with the step density [78]. The change of workfunction was calculated by the following equation,

$$\Delta\phi = 4\pi d_{\perp}\sqrt{x_w^2 + x_h^2}$$

where $d_{\perp}$, x_w and x_h represent the perpendicular component of dipole moment on a step, width of the step and height of the step, respectively. In the case of our surface structure model illustrated in Figure 6-33, $\Delta\phi$ was estimated to be 0.12 eV. Therefore, only when the atomic steps exist on the Al(001) surface, photoemission occurred by the stimulating energy 0.12 eV lower than workfunction. Moreover, in the case of PSE, two-photon photoemission process is also suggested. In our calculation results, the unoccupied state of Al(001) stepped surface at 0.4 eV above E_F increased greatly against that of the clean surface as shown in Figure 6-34 (a). The energy diagram of electrons on stepped Al(001) surface is

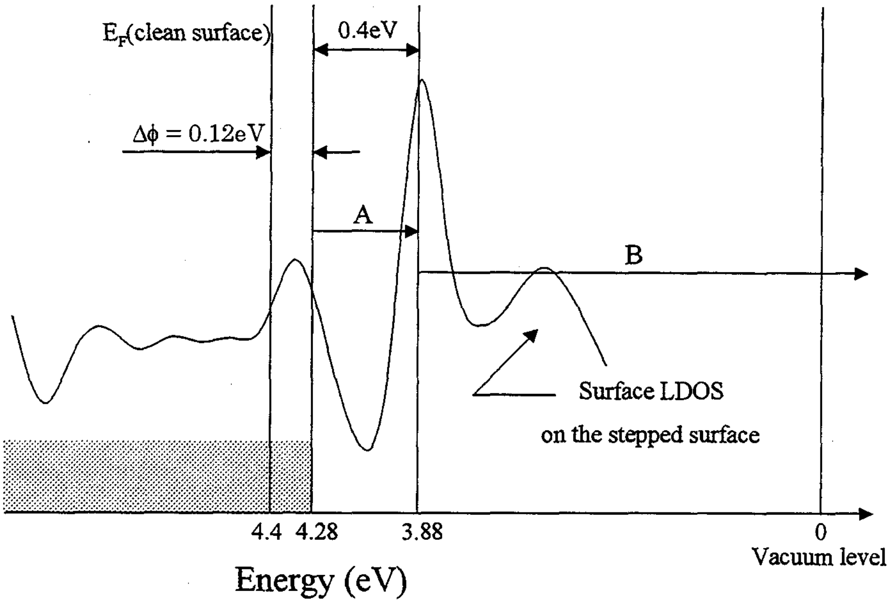

Figure 6-38 Emission model of PSE from the stepped Al surface based upon two-photon photoemission process.

illustrated in Figure 6-38. According to this figure, even when light with the energy larger than 3.88 eV, which is lower than the work function of clean Al(001) surface, is introduced, electrons which already pumped up to the unoccupied states (labeled '*A*') can be emitted to vacuum (labeled '*B*') through two-photon photoemission process. Actually, it was reported that the energy distribution of photoelectrons from the Al surface was shifted about 0.6 eV to lower energy due to scratching [72]. Moreover, it was observed that electron emission from the states induced by steps, which was located above the photoelectric threshold energy, took place on Si(111) 2x1 surface through two-photon photoemission process [79]. Therefore, the emission model proposed here, based upon two-photon photoemission process, is reasonable to explain PSE phenomenon from scratched Al surface, and it is concluded that the surface step is one of exoemission origins.

On the other hand, the tip surface, which is used as a specimen of FSE, is consisted of many Al(001) steps. Therefore, such steps may contribute to FSE from Al tips. According to experimental TED of exoelectrons from the Al tip shown in Figure 6-25, oxygen exposure caused the enhancement of the peak intensity at -4.0 eV below vacuum level. In contrast, the other peak intensity at -3.8 eV below vacuum level did not affect the oxygen exposure [3]. Therefore, the origin of this peak at -3.8 eV below vacuum level is considered to be intrinsic nature of the tip surface, for example, impurity, point defect, step and so on. In this calculational study, it was concluded that the surface steps on Al (001) surface induced the enhancement of the unoccupied states at –3.88 eV below vacuum level, with considering the decrease of work function due to the steps (see Figure 6-38). The peak position of unoccupied states induced by surface steps is close to the peak, which was not influenced by oxygen adsorption, in experimental TED of exoelectrons from Al tips. If electrons are excited from E_F to such unoccupied states and lifetime of trapped electron is log enough, the surface steps on Al (001) would be one of the origins of FSE from Al tips.

References

[1] "*A Note on Electron Transfer to Exoelectron Emission Sources from Scratched Aluminum*"; H. Shigekawa, Y. Fujiwara and S. Hyodo, Japanese Journal of Applied Physics, vol. 23 (1984) 1146.

[2] "*Detection of Surface States in GaAs and InP by Thermally Stimulated Exoelectron Emission Spectroscopy*"; S. S. Hullavarad, S. V. Bhoraskar and D. N. Bose, Journal of Applied Physics, vol. 82 (1997) 5597 ~ 5599.

[3] "*Influence of Oxygen Adsorption on Field-Stimulated Exoelectron Emission from High-Purity Aluminum*"; M. Tagawa, M. Mori, N. Ohmae and M. Umeno, Applied Surface Science, vol. 72 (1993) 259 ~ 265.

[4] "*Inhomogeneous Electron Gas*"; P. Hohenberg and W. Kohn, Physical Review, vol. 136 no. 3B, (1964) B864 ~ 871.

[5] "*Universal Variational Functionals of Electron Densities, First-Order Density Matrices, and Natural Spin-orbitals and Solution of the N-representability Problem*"; M. Levy, Proceedings of the National Academy of Sciences of the United States of America, vol. 76 no. 12 (1979) 6062 ~ 6065.

[6] "*Pseudopotentials That Work: from H to Pu*"; G. B. Bachelet, D. R. Hamann and M. Schluter, Physical Review B, vol. 26 (1982) 4199 ~ 4228.

[7] "*Soft Self-consistent Pseudopotentials in a Generalized Eigenvalue Formalism*"; D. Vanderbilt, Physical Review B, vol. 41 (1990) 7892 ~ 7895.

[8] "*Optimized Pseudopotentials*"; A. M. Rappe, K. M. Rabe, E. Kaxiras and J. D. Joannopoulos, Physical Review B, vol. 41 (1990) 1227 ~ 1230.

[9] "*Efficient Pseudopotentials for Plane-wave Calculations*"; N. Troullier and J. L. Martins, Physical Review B, vol. 43 (1991) 1993 ~ 2006.

[10] "*Optimized and Transferable Nonlocal Separable Ab-initio Pseudopotentials*"; J. S. Lin, A. Qteish, M. C. Payne and V. Heine, Physical Review B, vol. 47 (1993) 4174 ~ 4180.

[11] "*Norm-conserving Pseudopotentials*"; D. R. Hamann, M. Schluter and C. Chiang, Physical Review Letters, vol. 43 (1979) 1494 ~ 1497.

[12] "*Ab Initio Calculation of the Static Structural Properties of Al*"; Pui K. Lam and

Marvin L. Cohen, Physical Review B, vol. 24 (1981) 4224 ~ 4229.

[13] "*A Database of Structural Energies of Aluminium from Ab Initio Calculations*"; I. J. Robertson, D. I. Thomson, V. Heine and M. C. Payne, Journal of Physics, vol. 6 (1994) 9963 ~ 9972.

[14] "*Linearized Augmented-Plane-Wave Calculation of the Electronic Structure and Total Energy of Tungsten*"; Su-Huai Wei, Henry Krakauer and M. Weinert, Physical Review B, vol. 32 (1985) 7792 ~ 7797.

[15] "*Self-consistent Relativistic Calculation of the Energy Bands and Cohesive Energy of W*"; D. M. Bylander and Leonard Kleinman, Physical Review B, vol. 29 (1984) 1534 ~ 1539.

[16] "*First-Principles Calculations of the Thermal Expansion of Metal*"; Andrew A. Quong and Amy Y. Liu, Physical Review B, vol. 56 (1997) 7767 ~ 7770.

[17] "*Electronic Structure Calculation and Material Design System*"; H. Yoshida and K. Terakura, Solid State Physics, vol. 24 no. 3 (1989) 277 ~ 285.

[18] "*Self-Consistent Energy Bands in Aluminium. An Improved Calculation*"; S. P. Singhal and J. Callaway, Physical Review B, vol. 16 (1977) 1744.

[19] "*Recent development of band calculations*"; K. Terakura, vol. 31, (1996) 199 ~ 204.

[20] "*First-Principles Study of the Optical Properties and the Dielectric Response of Al*"; Keun-Ho Lee and K. J. Chang, Physical Review B, vol. 49 (1994) 2362 ~ 2367.

[21] "*Electropolithing*"; K. Mano, Syukyosya,1948 [in Japanese].

[22] "*On Imaging of Aluminium by Field Ion Microscopy*"; W. Zingg and H. Warlimount, Physica Status Solidi A, vol. 45 (1978) 117 ~ 122.

[23] "*Theoretical Analysis of the Electronic Structure of the Stable and Metastable C(2x2) Phases of Na on Al(001): Comparison with Angle-resolved Ultraviolet Photoemission Spectra*"; C. Stampfl, K. Kambe, R. Fasel, P. Aebi and M. Scheffler, Physical Review B, vol. 57 (1998) 15251 ~ 15260.

[24] "*Structural and Transport Properties of Aluminum Atomic Wires*"; Gianni Taraschi, Jose-Luis Mozos, C. C. Wan, Hong Guo and Jian Wang, Physical Review B, vol. 58 (1998) 13138 ~ 13145.

[25] "*Density-Functional Theory Calculations of Hopping Rates of Surface*

Diffusion"; C. Ratsch and M. Scheffler, Physical Review B, vol. 58 (1998) 13163 ~ 13166.

[26] "*First-Principles Study of the H-induced Reconstruction of W(110)*"; K. W. Kwak and M. Y. Chou, Physical Review B, vol. 53 (1996) 13734 ~ 13739.

[27] "*The Clean Thermally Induced W(001)(1x1) to* $\left(\sqrt{2}\times\sqrt{2}\right)R45°$ *Surface Structure Transition and its Crystallography*"; M. K. Debe and D. A. King, Surface Science, vol. 81 (1979) 193 ~ 237.

[28] "*Multilayer Distortion in the Reconstructed (110) Surface of Au*"; W. Moritz and D.Wolf, Surface Science, vol. 163 (1985) L655 ~ 665.

[29] "*R-Factor Analysis of the Effect of Non-structural Parameters in LEED, Applied to Al(111)*"; H. B. Nielsen and D. L. Adams, Journal of Physics C, vol. 15 (1982) 615 ~ 623.

[30] "*Perturbation Calculations of the c(2x2) Sodium Overlayer Structure on Al (001)*"; M. Van Hove, S. Y. Tong and N. Stoner, Surface Scienece, vol. 54 (1976) 259 ~ 268.

[31] "*Truncation-Induced Multilayer Relaxation of the Al(110) Surface*"; J. R. Noonan and H. L. Davis, Physical Review B, vol. 29 (1984) 4349 ~ 4355.

[32] "*Oscillatory Relaxation of the Al(110) Surface*"; J. N. Anderson, H. B. Nielsen, L. Petersen and D. L. Adams, Journal of Physical C, vol. 17 (1984) 173 ~ 192.

[33] "*Theoretical Analysis of the Electronic Structure of the Stable and Metastable c(2x2) Phases of Na on Al(001): Comparison with Angle-Resolved Ultraviolet Photoemission Spectra*"; C. Stampfl, K. Kambe, R.Fasel, P. Aebi and M. Scheffler, Physical Review B, vol. 57 no 24 (1998) 15251 ~ 15260.

[34] "*Structural and Transport Properties of Aluminum Atomic Wires*"; G, Taraschi, J. L. Mozos, C. C. Wan, H. Guo and J. Wang, Physical Reivew B, vol. 58 no. 19 (1998) 13138 ~ 13145.

[35] "*Density-Functional Theory Calculations of Hopping Rates of Surface Diffusion*"; C. Ratsch and M. Scheffler, Physical Review B, vol. 58 no. 19 (1998) 13163 ~ 13166.

[36] "*Modelling of Surface Relaxation and Melting of Aluminium*"; H. Cox, R. L. Johnston, J. N. Murrell, Surface Science, vol. 373 (1997) 67 ~ 84.

[37] "*First Principles calculation of lattice relaxation and surface phonons on Al(100)*"; K. P. Bohnen and K. M. Ho, Surface Science, vol. 207 no. 1 (1988) 105 ~ 117.

[38] "*Photoemission from Surface States and Surface Resonances on the (100), (110), and (111) crystal faces of aluminum*"; G. V. Hansson and S.A. Flodstrom, Physical Review B, vol. 18 (1978) 1562 ~ 1571.

[39] "*Linearized Augmented Plane-Wave Method for the Electronic Band Structure of Thin Films*"; H. Krakauer and M. Posternak, Physical Review B, vol. 19 (1979) 1706 ~ 1719.

[40] "*Characterization of Anodic Oxide Coatings on Aluminum by Tribostimulated Exoemission*"; D. L. Doering, T. Oda, J. T. Dickinson and P. Braunlich, Applied Surface Science, vol. 3 no. 2 (1979) 196 ~ 210.

[41] "*Thermally Stimulated Relaxation in Solids*"; H. Glaefeke, ed. P. Brabnlich, p. 225, Springer Verlag, Berlin (1979).

[42] "*Fracto-Emission Accompanying Adhesive Failure*"; J.T. Dickinson, M. K. Park, E. E. Donaldson and L. C. Jensen, Journal of Vaccum Science Technology, vol. 20 (1982) 436 ~ 469.

[43] "*Two-Process Model of PSEE from Scratched Metals*"; H. Shigekawa and S. Hyodo, Applied Surface Science, vol. 22/23 (1985) 361 ~ 368.

[44] "*Field-Stimulated Exoelectron Emission from 99.9999% Pure Al*"; M. Tagawa, S. Takenobu, N. Ohmae and M. Umeno, Applied Physics Letters, vol. 53 no. 7 (1988) 626 ~ 627.

[45] "*Solid State Electronics*"; T. Kanaji, S. Hongo and T. Urano, (edited by T. Kanaji, Shokabo, tokyo, 1995).

[46] "*CRC Hand Book of Chemistry and Physics*"; edited by R. C. Weast (CRC press, Inc., Florida, 1985-1986), F-166.

[47] "*Oxidation Kinetics of the Top Atomic Layer of Al(100) from Angle Resolved SIMS*"; S. A. Larson and L. L. Lauderback, Surface Science, vol. 284 (1993) 1 ~ 13.

[48] "*Initial Interaction of Oxygen with Aluminium Single Crystal Faces: a LEED, AES and Work Function Study*"; R. Michel, J. Gastaldi, C. Allasia and C. Jourdan, Surface Science, vol. 95 (1980) 309 ~ 320.

[49] "*Interaction of Oxygen with Clean Aluminum Surfaces by Measurement of Work Function Changes*"; R. L. Wells and T. Fort, Surface Science, vol. 33 (1982) 172 ~ 178.

[50] "*Extended Appearance-potential Fine-structure Analysis: Oxygen on Al(100)*"; M. L. den Boer, T. L. Einstein, W. T. Elam, R. L. Park, L. D. Roelofs, and G. E. Laramore, Physical Review Letters, vol. 44 (1980) 496 ~ 500.

[51] "*Self-Consistent Theory of the Chemisorption of H, Li, and O on a Metal Surface*"; N. D. Lang and A. R. Williams, Physical Review Letters, vol. 34 (1975) 531 ~ 534.

[52] "*Oxygen Chemisorption of a Small Aluminium Cluster*"; J. Harris and G. S. Painter, Physical Review Letters, vol. 36 (1976) 151 ~ 154.

[53] "*Electronic Structure of the Oxygen Overlayer on Al(100)*"; I. P. Batra and S. Ciraci, Physical Review Letters, vol. 39 (1977) 774 ~ 777.

[54] "*Chemisorption of O and H on the Free-Electron-like Metals, Al and Mg Studied by Photoelectron Spectroscopy*"; S. A. Foldtrom, L. G. Petersson and S. B. M. Hagstrom, Journal of Vacuum Science Technology, vol. 13 (1976) 280 ~ 282.

[55] "*Multiple Oxidation States of Al Observed by Photoelectron Spectroscopy of Substrate Core Level Shifts*"; S. A. Foldtrom, R. Z. Bacirach, R. S. Bauer and S. B .M. Hagstrom, Physical Review Letters, vol. 37 (1976) 1282 ~ 1285.

[56] "*Anisotropic Work Function of Clean and Smooth Low-Index Faces of Auminium*"; J. K. Grepstad, P. O. Gatland and B. J. Slagsvold, Surface Science, vol. 57 (1976) 348 ~ 362.

[57] "*Adsorption of Oxygen on Clean Single Crystal Faces of Aluminium*"; P. O. Gartland, Surface Science, vol. 62 (1977) 183 ~ 196.

[58] "*Self-consistent Linearized-Augmented-Plane-Wave-Method Determination of Electronic Structure*"; H. Krakauer, M. Posternak, A. J. Freeman and D. D. Koelling, Physical Review B, vol. 23 (1981) 1685 ~ 1691.

[59] "*Early Stages in the Oxidation of Magnesium, Aluminium and Magnesium/Aluminium Alloys. I. Exoelectron Emission and Long Wavelength Photoemission*"; G. C. Allen and P. M. Tucker, Surface Science, vol. 102 (1981) 207 ~ 226.

[60] "*Exoelectron Emission during Oxidation of Cs Films*"; A. Böttcher, R. Grobecker,

R. imbeck, A. Morgante, and G. Ertl, Journal of Chemical Physics, vol. 95 (1991) 3756 ~ 3766.

[61] "*Exoelectron Emission during the Oxidation of Na Films*"; A. Böttcher, R. Grobecker, T. Greber, A. Morgante and G. Ertl, Surface Science, vol. 280 (1993) 170 ~ 178.

[62] "*Interaction of Oxygen with Clean Aluminum Surfaces by Measurement of Work Function Changes*"; R. L. Wells and T. Fort, Surface Science, vol. 33 no. 1 (1972) 172 ~ 178.

[63] "*Oxygen Adsorption on Aluminium Single Crystal Faces Studied by AES, XPS and LEED*"; C. W. B. Martinson and S. A. Flodstrom, Surface Science, vol. 80 (1979) 306 ~ 316.

[64] "*An AES and SIMS Study of the Effect of Temperature on the Interaction of Oxygen with Al(100)*"; L. L. Lauderback and S. A. Lawson, Surface Science, vol. 233 (1990) 276 ~ 282.

[65] "*An Electron Spectroscopic Investigation of the Interaction of Methanol with Polycrystalline Aluminum*"; J. W. Rogers Jr., R. L. Hance, and J. M. White, Surface Science, vol. 100 (1980) 388 ~ 406.

[66] "*A Study of the Structure of Abraded Metal Surfaces*"; L. Grunberg and K. H. R. Wright, Proceedings of the Royal Society of London A, vol. 232 (1955) 403 ~ 423.

[67] "*Deformation Enhanced Photoemission from Aluminum 1. Experimental Results*"; O. Buck, W. J. Pardee, F. J. Szalkowski and D. O. Thompson, Applied Physics, vol. 12 (1977) 301 ~ 310.

[68] "*Phonons on Stepped Surfaces*"; P. Knipp, Physical Review B, vol. 43 (1991) 6908 ~ 6923.

[69] "*Ab Initio Calculations of the Atomic and Electronic Structure of Diamond (111) Surfaces with Steps*"; G. Kern and J. Hafner, Physical Review B, vol. 58 (1998) 2161 ~ 2169.

[70] "*Structure and Vibrations of the Vicinal Copper (211) Surface*"; C. Y. Wei, Steven P. Lewis, E. J. Mele and Andrew M. Rappe, Physical Review B, vol. 57 (1998) 10062 ~ 10068.

[71] "*Storage Effect in Photostimulated Exoelectron Emission from Scratched*

Aluminum"; H. Shigekawa and S. Hyodo, Japanese Journal of Applied Physics, vol. 21 (1982) 1278 ~ 1282.

[72] "*Change of Energy-level Distribution of Photoemission Sources in Al and Zn Caused by Scratching*"; H. Shigekawa, R. Iwatsu, M. Okada and S. Hyodo, Japanese Journal of Applied Physics, vol. 22 (1983) 42 ~ 45.

[73] "*Intensity vs. Time Profiles of Photostimulated Exoelectron Emission from Scratched Aluminum*"; H. Shigekawa and S. Hyodo, Japanese Journal of Applied Physics, vol. 22 (1983) 1493 ~ 1495.

[74] "*An Improved Method for Determining the Emission Rate and Source Population of PSEE*"; H. Shigekawa and S. Hyodo, Japanese Journal of Applied Physics, vol. 22 (1983) 1627.

[75] "*A Method for Determining the Activation Rates of PSEE Centers in Scratched Aluminium by Varying the Stimulation Intensity*"; H. Shigekawa, Y. Ando, A. Kumagai and S. Hyodo, Japanese Journal of Applied Physics, vol. 24 (1985) 1240.

[76] "*Two-process Model for a Comprehensive Interpretation of Photostimulated Exoelectron Emission*"; H. Shigekawa and S. Hyodo, Japanese Journal of Applied Physics Supplement, vol. 24-4 (1985) 21 ~ 26.

[77] "*PSEE-Related Phenomena Indicative of the Meaning of Two-process Model Parameters for Mechanically Deformed Aluminium*"; H. Shigekawa, Y. Fujiwara, Y. Ando, A. Kumagai and S. Hyodo, Japanese Journal of Applied Physics Supplement, vol. 24-4 (1985) 122 ~ 124.

[78] "*Calculation of the Electronic Structure of Stepped Metal*"; H. Ishida and A. liebsch; Physical Review B, vol. 46 no. 11 (1992) 7153 ~ 7156.

[79] "*Low-Energy Laser Photoelectron Study of Defect States on Cleaved Si(111)2x1 Surfaces*"; M. Yamada, J. Kanasaki, N. Itoh and R. T. Williams, Surface Science vol. 349 (1996) L107 ~ 110.

Chapter 7

Concluding Remarks

Exoemission phenomenon has been studied for about a century since it was discovered. The various investigations on this phenomenon have been performed in order to apply exoemission to the industrial field. Particularly, the applications to radiation dosimetry, non-destructive testing of the surface and surface analysis have been expected greatly. However, the exoemission has not been utilized contrary to such highly industrial expectations, since the relationship between the exoemission properties and the status of the emitting surface has not been elucidate in detail. Most of the studies on the exoemission reported previously were performed in macroscopic view, and the quantitative discussions were not achieved. In order to interpret the exoemission phenomena quantitatively, it is essential to identify the emitting surface with extremely high resolution. In the FSE study, the specimen surface can be evaluated by FIM and FEM with atomic resolution. The attempt to apply the surface analyses with atomic resolution such as FIM and FEM to the exoemission research have never been performed, and this study is the world's first report on such experiments. From the measurements of FSE from the annealed W surfaces, the following results were obtained;

1) FSE does not occur on the ideal W surface prepared by field evaporation.
2) The annealing treatment of the W tip at 800 K leads to FSE at around 300 K. This FSE phenomenon indicated a good reproducibility.
3) The FSE from the annealed W tip shows a temperature dependence. Namely, the FSE was observed at the temperature between 200 and 450 K, and the intensity of the FSE showed a summit at around 300 K.
4) The peak temperature depended not on the annealing time, but on the annealing temperature.
5) The applied voltage dependence of FSE was different from that of the steady-state field

emission.

Using FIM and FEM, the electron-emitting surface could be identified with atomic resolution, and the results are as follows:

6) The pyramid protrusions were formed on {111} faces of the W tip surface by the annealing treatment at higher than 800 K.
7) The structural transformation of such pyramid protrusions took place at the temperatures between 200 and 400 K. Namely, it was considered that the height of such a protrusion was lowered when the tip temperature was increased from 200 to 400 K. The temperature where this structural transformation occurred was in a good agreement with that of FSE.

Moreover, the spatial distribution of FSE from the annealed W tip was investigated by FSE-images, and the following results were obtained:

8) The intensity of the FSE from the annealed W tip surface was strongest at the (111) faces. Also, it was found that the intensities of FSE at the {111} faces and its surroundings attained to 94 % of the total FSE intensity.

From these results shown in (6) ~ (8), the emission mechanism based upon the surface diffusion of W atoms were proposed. The proposed model of FSE could explain the temperature dependence of FSE qualitatively well.

The FSE properties from the W surface, which was bombarded by low-energy He^+ ions, were investigated, and the results are as follows;

9) FSE was observed at the W surface bombarded by the He^+ ions with energies higher than 500 eV, which was slight higher than sputtering threshold. The FSE intensity increased with increasing the energy of the He^+ ion.
10) The intensity of FSE from the ion-bombarded W tip surface decayed with time at 185 K.
11) After ion-bombardment of the W tip surface, FSE was observed at 185 K, but not at 300 K.

These results obtained in this experiment were successfully explained by the emission model, which was based upon the surface diffusion of W atoms. It was confirmed that the emission model could also explain the FSE properties from the ion-bombarded W surfaces.

The FSE properties from the gas-adsorbed W surface were studied. The experimental results are summarized;

12) Although hydrogen or oxygen was adsorbed on the clean W surfaces prepared by the field evaporation, FSE did not appear.
13) FSE from the annealed W tip surface was suppressed by the exposure of hydrogen as well as oxygen.
14) It was confirmed that water exposure enhanced the FSE intensity.

The detailed of this phenomenon has not been made clear yet. Hence, it will be one of the future works.

The first-principles calculation was carried out in the exoemission study. The electronic structures of the clean, the oxygen-adsorbed, the defected and the stepped Al (001) surfaces were calculated by the pseudopotential method, and the attempts to explain the experimental results on FSE, as well as PSE, from Al surface were performed.

15) The surface states, surface relaxation and DOS of the clean Al (001) surface calculated by pseudopotential method were in good agreement with that reported previously. It was confirmed that the calculational results obtained in this study was trustworthy.
16) From the calculation of the electronic structure of the oxygen-adsorbed Al (001) surface, the stable position of an adsorbed oxygen atom on the surface could be determined. Moreover, it was found that oxygen adsorption enhanced electron density with energies near E_F, and these electrons existed around adsorbed oxygen atom.
17) The LWP model was proposed, and the experimental results on FSE from Al tips could be explained.
18) The surface model with point defects was constructed, and the electronic structure of such a surface was calculated. It was clear from the calculational result that point defects on Al (001) surface caused the enhancement of electron-filled states. The relationship between the FSE, PSE or TSE properties and such an electronic structure has remained unclear.
19) It was found from the calculational results that the occupied states near E_F and unoccupied states at 0.4 eV above E_F were enhanced by the steps on Al (001) surface. Especially, the unoccupied states were increased dramatically, and the relationship of such states with FSE and PSE was discussed. As a result, it was suggested that the surface step became one of the origins of FSE and PSE. However, the detailed

mechanism has not been elucidated yet.

Although the emission mechanism from the Al surface with point defects and steps has not been clarified in detail, the previous experimental result on FSE from Al tips was successfully explained by the LWP model qualitatively. However, the LWP model can not describe the dynamic behavior at the surface, the further study based upon molecular dynamics calculation is mandatory.

Throughout the FSE studies described in this thesis, a number of new aspects on exoemission are uncovered. Since many of these findings are the cutting edge of exoemission research, the correlation of FSE results obtained in this study with conventional PSE or TSE results requires future work. However, the attitude of this thesis for clarifying the relationship between exoemission and movement of individual surface atom and for combining the experimental results with computational results is a pioneering work in the new age of exoemission studies with atomic resolution.

Acknowledgments

The author is most grateful to Professor Masataka Umeno of Osaka University for his continuous advice, suggestion and encouragement throughout this work, and for his careful reading of this thesis.

The author expresses his gratitude to Professor Masakazu Aono and Professor Yoshizo Takai of Osaka University for their careful reading of this manuscript, comments and suggestions.

Special thanks are given to Professor Shigenori Kanaya, Professor Shunichi Fukuzumi, Professor Mikiji Miyata, Professor Syozo Yanagida, Professor Masaaki Yokoyama and Professor Yoshiki Ichioka of Department of Material and Life Science, Osaka University.

The author is thankful to Associate Professor Kiyoshi Yasutake and Dr. Takayoshi Shimura of Osaka University for their appropriate comments and suggestion.

Thanks are due to Professor Nobuo Ohmae and Associate Professor Masahito Tagawa of Kobe University, for their considerable discussion and impressive suggestion during this work and the preparation of this thesis.

The author would like to express his gratitude to Associate Professor Nobuyuki Shima of Himeji Institute of Technology for providing the BB-VB program used in this study, and for discussion on the calculational results.

The authors are grateful to Dr. Osamu Matsuda of Hokkaido University and Dr. Takeshi Uenoyama of Matsushita Electric Corporation for providing suggestions for first-principles calculation.

The suggestion and discussion on our computational studies by Professor Hideaki Kasai of Osaka University are acknowledged.

The discussion with Dr. Katsumi Nagaoka of Waseda University is gratefully acknowledged.

The author is grateful to my co-workers, Mr. Shinji Kibi, Mr. Ryo Yamamoto and Mr. Kenji Dokuni for their helpful assistance on the experiments, and to Mr. Masashi Morita and Mr. Ryosuke Ito for their helpful work on the calculational studies.

Finally, grateful acknowledgment is given to all of the members at Applied Surface Science Laboratory, Department of Material and Life Science, Osaka University.